

**HYBRID POLYMERIC MATERIALS COMPRISING CLAY NANOTUBES,
PHOTOTHERMAL AGENTS AND PHASE CHANGE MATERIALS FOR FOOD,
WATER AND ENERGY APPLICATIONS**

by

Cüneyt Erdinç TAŞ

Submitted to the Graduate School of Engineering and Natural Sciences
in partial fulfillment of the requirements for the degree of

Doctor of Philosophy

Department of Material Science and Engineering Program

Thesis Advisor: Asst. Prof. Hayriye ÜNAL

Thesis Co-Advisor: Asst. Prof. Serkan ÜNAL

SABANCI UNIVERSITY

23 FEBRUARY 2021

Cüneyt Erdinç Taş, a Ph.D. student of Sabancı University Faculty of Engineering and Natural Sciences student ID 21986, successfully defended the dissertation entitled “Hybrid polymeric materials comprising clay nanotubes, photothermal agents and phase change materials for food, water and energy applications”, which he prepared after fulfilling the requirements specified in the associated legislations, before the jury whose signatures are below.

APPROVED BY:



Date of Approval : 23 February 2021

© Cüneyt Erdinç TAŞ 2021

All Rights Reserved

ABSTRACT

HYBRID POLYMERIC MATERIALS COMPRISING CLAY NANOTUBES, PHOTOTHERMAL AGENTS AND PHASE CHANGE MATERIALS FOR FOOD, WATER AND ENERGY APPLICATIONS

Cüneyt Erdinç TAŞ

Doctor of Philosophy, 2021

Material Science and Engineering

Thesis Advisor: Asst. Prof. Hayriye ÜNAL

Thesis Co-Adviser: Asst. Prof. Serkan ÜNAL

Keywords: Halloysite Nanotubes, Polydopamine Coating, Food Packaging, Nanoparticle Separation, Waterborne Polyurethane, Solar to Thermal Energy Conversion, Phase Change Materials

In this thesis, different fundamental solutions have been offered on the concepts of "saving food", "saving water" and "saving energy" by preparing hybrid composite systems comprising different combinations of clay nanoparticles, photothermal agents and phase change materials.

For the protection of food products, two main approaches were presented to prolong the shelf life of packaged food in the marketing and transportation stages. The first solution offered was the design of active food packaging materials with halloysite nanotubes having ethylene scavenging properties for the storage of fruits and vegetables. The second solution offered was the design of a food packaging material comprising halloysite nanotubes loaded with phase change materials that can buffer temperature fluctuations during the cold-chain

transportation of food products. The particle quality of halloysite nanotubes were determined to play a critical role in these studies, which has led to an in-depth investigation of the effect of homogeneous size distribution and agglomeration-free quality of halloysite nanotubes on their loading/surface functionalization capacity and efficiency as reinforcing fillers in polymer nanocomposites. A novel three-step nanoparticle separation method was developed based on the surface modification of halloysite nanotubes with polydopamine, resulting in agglomeration-free halloysite nanotubes sorted in different size ranges.

The surface modification of particles with polydopamine was further extended to a new material design that utilizes the light to thermal energy conversion capability of polydopamine. Waterborne polyurethane particles synthesized in the form of aqueous dispersions were coated with polydopamine, resulting in hybrid polydopamine-polyurethane dispersions. Films cast from these dispersions intrinsically showed light to thermal energy conversion ability and were demonstrated to have a huge potential in water purification by solar driven evaporation.

Promising results obtained with polydopamine-polyurethane hybrid films led us to produce a multifunctional hybrid material that has solar to thermal energy conversion, thermal energy storage and thermal buffering properties. As a preliminary work to reach this goal the shape-stable latent heat storage concept was examined by using a zeolitic shape stabilizer and phase change materials. The acquired knowledge from this study was utilized to prepare form-stable phase change films by using the photothermal polydopamine-polyurethane polymer matrix and PEG4000 as phase change materials. In this study, PEG4000 was directly integrated into the polymer matrix at different ratios by dissolving in the aqueous polydopamine-polyurethane dispersion, resulting in form-stable phase change films, which present unique energy storage properties and have strong potential as thermoregulating materials.

ÖZET

GIDA, SU VE ENERJİ UYGULAMALARI İÇİN KİL NANOTÜPLERİ, FOTOTERMAL AJANLAR VE FAZ DEĞİŞİM MALZEMELERİ İÇEREN HİBRİT POLİMERİK MALZEMELER

Cüneyt Erdinç TAŞ

Doktora Tezi, 2021

Malzeme Bilimi ve Mühendisliği

Tez Danışması: Dr. Öğr. Üyesi Hayriye ÜNAL

Eş Danışman: Dr. Öğr. Üyesi Serkan ÜNAL

Anahtar Kelimeler: Halloysit Nanotüpleri, Polidopamin Yüzey Kaplama, Gıda Paketleme, Nanopartikül Ayırma, Su Bazlı Poliüretan, Güneş Enerjisinden Termal Enerjiye Dönüşüm, Faz Değişim Malzemeleri

Bu tezde, kıl nanoparçacıkları, fotermal ajanlar ve faz değişim malzemelerin birleşiminden oluşan hibrit kompozit sistemler hazırlanarak, "gıda güvenliği", "temiz suyun korunması" ve "enerji tasarrufu" kavramlarına farklı temel çözümler sunulmuştur.

Gıda ürünlerinin korunması alanında, pazarlama ve nakliye aşamalarında gıdaların ambalaj malzemeleri içerisinde raf ömürlerinin uzatılması hedefi için iki ana yaklaşım ele alınmıştır. Sunulan çözümlerden biri, meyve ve sebzelerin depolanması sırasında korunması için, etilen tutuculuk özelliğine sahip halloysit nanotüpleri ile aktif gıda ambalaj malzemelerinin tasarlanmasıdır. Sunulan diğer çözüm ise, gıda ürünlerinin soğuk zincir ile taşınması aşamasında sıcaklık dalgalanmalarına karşı termal tamponlama özelliğine sahip faz değişim malzemesi/halloysit sistemi içeren gıda ambalaj malzemesi elde edilmesidir. Halloysit

nanotüplerinin merkezde olduğu bu çalışmalar, partikül kalitesinin nanotüp performansı üzerindeki etkisinin düşünülmesine yol açmıştır. Homojen boyut dağılımına ve aglomerasyonsuz kaliteye sahip halloysit nanotüplerinin lümen yükleme kapasitesi, yüzey fonksiyonlanması ve takviye dolgu maddesi olarak nanokompozit film malzemelerine katkısını araştırmak amacıyla; halloysit nanotüp yüzeylerinin polidopamin tabakası ile kaplanması, ultrasonikasyon ile su ortamına dağıtılmmasını ve santrifüj ile boyut derecelendirilmesini içeren yeni bir üç aşamalı nanopartikül ayırma yöntemi geliştirilmiştir.

Polidopamin yüzey kaplaması üzerine yapılan detaylı çalışma, polidopamin tabakasının ışığı termal enerjiye dönüştürme kabiliyetinden yararlanarak yeni bir malzeme tasarımi fikrine neden olmuştur. Bu açıdan, su bazlı poliüretan, emülsyon formunda sentezlenmiş ve polidopamin ile su bazlı poliüretan partiküllerinin yüzeyleri kaplanmıştır. Elde edilen polidopamin-poliüretan dispersyonları ile, ışiktan termal enerjiye dönüşüm özelliğine sahip ve ikincil partikül ilavesi içermeyen döküm filmler hazırlanmış ve fotermal performansları sistematik olarak incelenmiştir.

Polidopamin- poliüretan filmlerinden elde edilen ümit verici sonuçlar, güneşten termal enerjiye dönüşüm, termal enerji depolama ve termal tamponlama özelliklerine sahip çok işlevli hibrid polimerik malzemeler geliştirilmesi konusunda yol gösterici olmuştur. Bu çok fonksiyonlu malzemelerin geliştirilmesi hedefinin ilk aşaması olarak, gizli ısı depolama kavramı, zeolitik bir yapı ve farklı faz değişim malzemeleri kullanılarak incelenmiştir. Bu çalışmadan elde edilen bilgiler, fotermal kabiliyete sahip polidopamin-poliüretan polimer matrisi ve faz değişim malzemesi olan PEG4000 içeren özgün şekil-kararlı faz değişim filmleri hazırlanmasında kullanılmıştır. Bu çalışmada, PEG4000 ikincil destek malzemesi içerisine enkapsüle edilmeden, polimer matrisine doğrudan entegre edilmiş ve bu sayede, oldukça basit bir yöntemle enerji depolama özelliği gösteren, ısı regülasyonunda kullanım için yüksek potansiyele sahip özgün, form-kararlı faz değişim kaplama filmleri elde edilmiştir.

"You cannot hope to build a better world without improving the individuals. To that end, each of us must work for our own improvement and, at the same time, share a general responsibility for all humanity, our particular duty being to aid those to whom we think can be most useful." (Marie Curie)

*To "the woman" who enabled me to be
awarded a Ph.D.*

ACKNOWLEDGEMENTS

I would like to thank my advisor, Asst. Prof. Hayriye Ünal, for her unbelievable contributions to my Ph.D. adventure. I would like to thank her for supporting me not only with scientific advice but also for allowing me to improve myself in terms of scientific creativity, productivity and letting me develop my imagination for different scientific approaches. I believe that she has perfectly taught me the way of how to bring up a Ph.D. by not putting me in an already drawn frame and encouraging me to produce new ideas.

I would like to thank my co-advisor, Asst. Prof. Serkan Ünal, for leading me to learn a wide range of polymer applications from membrane preparation to polymer processing and gain the point of view to be able to think about every detail of a scientific study. I would like to emphasize that, throughout my doctoral education, I have always felt him behind me, and he allowed me to focus on only my research without thinking about any other challenges that I may encounter.

I would like to thank my Ph.D. dissertation jury and Ph.D. progress committee member, Prof. Bahattin Koç, for his great contribution to my studies. I would like to thank Prof. Cemil Alkan and Assoc. Prof. Derya Yüksel İmer for being my dissertation jury member and for all of their contributions to my thesis.

I would like to thank, Assoc. Prof. Fevzi Çakmak Cebeci, not only for being my dissertation jury member but also for all of his contributions to my scientific career. He has been guided me from the very beginning of my Ph.D. education to the end. It has been priceless to feel that "Fevzi Hoca" is there to consult for anything. He also contributed greatly to the improvement of my teaching ability as a teaching assistant of his course.

I would like to thank Prof. Yusuf Menceloglu for being a part of every important stage of my life and all of his contributions to my personal career. He was there during my M.Sc. defense, he was there during my Ph.D. qualification oral exam, he was there at my wedding

ceremony, he was there during my Ph.D. dissertation presentation. I hope, he will be there throughout my life.

I would like to thank Ekin Berksun and Deniz Köken for their indescribable contribution to my studies, in private. I would also like to thank my research group members, Ayşe Durmuş Sayar, Necdet Özçelik, Sarp Kolgesiz, Öykü Demirel and Sena Yüce for their friendship and scientific contributions.

I would like to thank, Assoc. Prof. Erdal Ertaş, Dr. Hakan Bildirir, Dr. Öznur Karaoğlu, Ömer Faruk Çeven, Burçin Yıldız and Turgay Gönül for their great contribution to my Ph.D. thesis and their supports. We would like to thank Prof. İlknur Dag and her team at Eskisehir Osmangazi University Central Research Laboratory, Application and Research Center for their contributions in cryo-TEM imaging.

I would like to thank Dr. Murat Özbulut for his great friendship and undefinable patience to Buket-Erdinç-Billur trio conversations.

I would like to thank Dr. Emine Billur Sevinış Özbulut for her endless name and all contributions to my life. It should be noted that she has indescribable contribution to every single point of this thesis. I believe that it is not easy to gain this kind of personal friendship, the fellowship of the science and companionship with a person. If any person has Billur in his/her laboratory or is making anything with her, that means he/she is a lucky person. Therefore, I feel that I am luckier than anyone because Billur is a part of my life. I would like to thank Billur for making me lucky.

I would like to thank Buket Alkan Taş for making my life a real life. I believe that if this thesis became a better thesis, it has been because of her contributions to my studies. Moreover, I would like to thank her for being a person who has a special viewpoint on all subjects, making science her manner of life, fixing my failures, being behind me, next to me, in front of me. More importantly, I would like to thank her for choosing me as her life partner and making my dreams real. Also, many thanks to Bedriye Alkan and Sinan Alkan who are the reason of making my dreams real.

Furthermore, I would like to present my deepest gratitude to my parents, Emine Canan Taş and Ahmet Taş and also my brother Hasan Eren Taş for their love and support throughout my whole life.

Finally, I am thankful to TUBITAK for providing me scholarship (TUBITAK 213M542; TUBITAK 113Y350; TUBITAK 113O872; TUBITAK 216M012) during my thesis.

February 2021

Cüneyt Erdinç TAŞ

TABLE OF CONTENT

ABSTRACT.....	VII
ÖZET	IX
ACKNOWLEDGEMENTS	XIII
TABLE OF CONTENT.....	XVII
ABBREVIATIONS.....	XXI
SYMBOLS.....	XXIII
LIST OF TABLES	XXV
LIST OF FIGURES	XXVII
CHAPTER 1: GENERAL INTRODUCTION.....	1
1.1. Dissertation overview and objectives.....	1
1.2. Review on the functional components of the polymeric hybrid materials.....	4
1.2.1 HNTs	4
1.2.2 Photothermal agents	8
1.2.3 PCMs for latent heat storage	12
1.3. Dissertation structure.....	23
CHAPTER 2: HALLOYSITE NANOTUBES/POLYETHYLENE NANOCOMPOSITES FOR ACTIVE FOOD PACKAGING MATERIALS WITH ETHYLENE SCAVENGING AND GAS BARRIER PROPERTIES	25
2. 1. Abstract	25
2. 2. Introduction	26
2. 3. Materials and Methods	28
2.3.1. Preparation of HNT/PE nanocomposite films.....	28
2.3.2. Imaging of HNTs and HNT/PE nanocomposites	28
2.3.3. Thermal characterization.....	29
2.3.4. Mechanical characterization.....	29
2.3.5. Characterization of ethylene scavenging properties	29
2.3.6. Characterization of barrier properties	30
2.3.7. Experiments on food samples	30
2.3.8. Statistical analysis	31
2. 4. Results and Discussion.....	32
2.4.1 Structural, thermal, and mechanical properties of HNT/PE nanocomposite films	32
2.4.2 Ethylene scavenging properties of HNT/PE nanocomposite films.....	36

2.4.3 Gas barrier properties of HNT/PE nanocomposite films.....	40
2. 5. Conclusions.....	43
CHAPTER 3: THERMALLY BUFFERING POLYETHYLENE/HALLOYSITE/PHASE CHANGE MATERIAL NANOCOMPOSITE PACKAGING FILMS FOR COLD STORAGE OF FOODS ..	45
3. 1. Abstract.....	45
3. 2. Introduction.....	46
3. 3. Materials and Methods	48
3.3.1 Chemicals	48
3.3.2 Preparation of HNT/PCM nanohybrids	48
3.3.3 Preparation of PE-HNT/PCM nanocomposite films	48
3.3.4 Characterizations	49
3. 4. Results and Discussions.....	50
3.4.1 The design of nanocomposite food packaging films	50
3.4.2 HNT/PCM nanofillers for thermal buffering.....	51
3.4.3 PE-HNT/PCM nanocomposite films	57
3.4.4 Cold storage applications of PE-HNT/PCM nanocomposite films	60
3. 5. Conclusions.....	61
CHAPTER 4: PURIFICATION AND SORTING OF HALLOYSITE NANOTUBES INTO HOMOGENEOUS, AGGLOMERATION-FREE FRACTIONS BY POLYDOPAMINE FUNCTIONALIZATION	63
4.1. Abstract.....	63
4.2. Introduction.....	64
4.3. Materials and Methods	66
4.3.1. Chemicals	66
4.3.2. Three-step separation of HNTs.....	66
4.3.3. Functionalization of HNT surfaces with sodium dodecyl sulfate	67
4.3.4. Loading of HNTs with carvacrol.....	67
4.3.5. Preparation of polyethylene-HNT nanocomposite films.....	67
4.3.6. Characterization Methods	68
4.4. Results and Discussions.....	69
4.5. Conclusion	84
CHAPTER 5: WATERBORNE POLYDOPAMINE/POLYURETHANE PHOTOTHERMAL POLYMER MATRIX FOR LIGHT-TO-HEAT CONVERSION	87
5.1. Abstract.....	87
5.2. Introduction.....	88
5.3. Materials and Methods	90
5.3.1. Chemicals	90
5.3.2. Synthesis of waterborne polyurethane dispersion	90
5.3.3. Preparation of PDA-WPU dispersion	91
5.3.4. Preparation of PDA-WPU films	91
5.3.5. Characterization.....	91
5.4. Results and Discussions.....	94

5.4.1.	Synthesis and particle size distribution of PDA-WPU dispersions	94
5.4.2.	Physicochemical and morphological properties of PDA-WPU films.....	97
5.4.3.	Thermal properties of PDA-WPU films	99
5.4.4.	Mechanical properties of PDA-WPU cast films.	100
5.4.5.	Light-to-heat conversion in PDA-WPU films.....	101
5.4.6.	Solar-driven water evaporation capacity of PDA-WPU-based container..	107
5.5.	Conclusions	109

CHAPTER 6: IMPROVED LATENT HEAT STORAGE PROPERTIES THROUGH MESOPORE-ENRICHMENT OF A ZEOLITIC SHAPE STABILIZER111

6.1.	Abstract	111
6.2.	Introduction	112
6.3.	Materials and Methods	114
6.3.1.	Chemicals	114
6.3.2.	General procedure for the synthesis of ZSM-A	114
6.3.3.	General procedure for the synthesis of ZSM-B	114
6.3.4.	General procedure for preparation of PCM composites	114
6.3.5.	Characterizations.....	115
6.3.6.	Solar simulator experiments.....	115
6.4.	Results and Discussions	116
6.4.1.	Comparison of shape stability of ZSM-5, ZSM-A and ZSM-B PCM composites.....	116
6.4.2.	Thermal energy storage performance of ZSM-B based PCM composites	123
6.4.3.	Latent heat storage performances of ZSM-B based PCM composites under solar irradiation	127
6.5.	Conclusions	129

CHAPTER 7: WATERBORNE POLYDOPAMINE- POLYURETHANE/POLYETHYLENE GLYCOL PHASE CHANGE COMPOSITES FOR SOLAR-TO-THERMAL ENERGY CONVERSION131

7.1.	Abstract	131
7.2.	Introduction	132
7.3.	Materials and Methods	134
7.3.1.	Chemicals	134
7.3.2.	Synthesis of WPU dispersion.....	134
7.3.3.	Preparation of PDA-WPU dispersion	135
7.3.4.	Preparation of PDA-WPU/PCM films	135
7.3.5.	Characterizations.....	135
7.4.	Results and Discussions	139
7.4.1.	Synthesis and characterization of WPU and PDA-WPU dispersions/cast films	139
7.4.2.	Preparation and characterization of shape-stable PDA-WPU/PCM composite films	141
7.4.3.	Thermal properties of PDA-WPU/PCM composite films	146
7.4.4.	Shape stability and thermal reliability of PDA-WPU/PCM composite films	148

7.4.5. Solar-to-thermal energy conversion and storage performance of PDA-WPU/PCM films	149
7.4.6. Demonstration of PDA-WPU/PCM 1:1 composite film as a solar heat storage-release material effective under cold weather conditions.....	152
7.5. Conclusions.....	154
CHAPTER 8: OVERALL CONCLUSIONS AND FUTURE PERSPECTIVES.....	155
8. 1. Overall conclusions	155
8. 2. Future perspectives	157
REFERENCES	159
VITA OF CÜNEYT ERDİNÇ TAŞ.....	195

ABBREVIATIONS

HNT	: Halloysite Nanotubes
PE	: Polyethylene
PEG	: Polyethylene glycol
PDA	: Polydopamine
WPU	: Waterborne Polyurethane
LA	: Lauric Acid
SDS	: Sodium dodecyl sulphate
EDA	: Ethylenediamine
HDI	: Hexamethylene diisocyanate
AEAS	: Sodium 2-[(2-aminoethyl) amino] ethane sulphonate
TRIS	: Tris(hydroxymethyl)aminomethane
PCM	: Phase Change Material
OTR	: Oxygen Transmission Rate
WVTR	: Water Vapor Transmission Rate
TEM	: Transmission Electron Microscopy
SEM	: Scanning Electron Microscopy
TGA	: Thermogravimetric Analysis
DSC	: Differential Scanning Calorimetry
UTM	: Universal Testing Machine
IGA	: Intelligent Gravimetric Analyzer

TD	: Maximum Weight Loss
T0.1	: 10% Weight Loss
FTIR	: Fourier Transform Infrared
DLS	: Dynamic Light Scattering
YM	: Young's Modulus
TS	: Tensile Strength
EB	: Elongation at Break
FSPCM	: Form-Stable Phase Change Material
OM	: Optical Microscopy
XRD	: X-ray Diffraction Patterns

SYMBOLS

T_m	: Melting temperature
T_c	: Crystallization temperature
ΔH_m	: Heat of Fusion
X_c	: Relative Degree of Crystallinity
w_t	: Weight Fraction
μm	: Micrometer
g	: Gram
$^{\circ}\text{C}$: Celsius Degree
T_g	: Glass Transition Temperature
kV	: Kilovolt
N	: Newton
min	: Minute
h	: Hour
J	: Joule
SUN	: The value corresponding to 100mW/cm^2
rpm	: Revolutions per Minute
W	: Watt
mL	: Milliliter
\AA	: Armstrong
θ	: Theta

$^{\circ}K$: Kelvin Degree

M : Molar

P : Intensity of the Applied Light Irradiation

A : Area

η : Solar to Thermal Energy Storage Efficiency

LIST OF TABLES

Table 1. Thermal stability parameters of PE and HNT/PE nanocomposites.....	34
Table 2. Calorimetric parameters of PE and HNT/PE nanocomposite films obtained from the second heating cycle.	35
Table 3. Transition temperatures and enthalpies of pure PCMs and HNT/PCM nanohybrids.	54
Table 4. Mechanical properties of neat PE and PE-HNT/PEG nanocomposite films.....	58
Table 5. Thermal properties of PE-HNT/PEG nanocomposite films in the melting transition range of PEG400 and PEG600.	58
Table 6. Thermal decomposition, glass transition temperature and thermal conductivity values of WPU and PDA-WPU films. Values having a different letter (a–d) within the same column are significantly different.....	99
Table 7. Comparison of light to thermal energy conversion performance of PDAPU (6mg/ml)/72h with photothermal materials presented in the literature for different applications.	106
Table 8. TGA Results of ZSM-B Based PCM Nanocomposites.....	120
Table 9. The long-term stability of the prepared ZSM-B composites.....	122
Table 10. Comparison of phase change temperature and latent heat of ZSM-B-LA65 and ZSM-B-PEG70 with other literature studies which are in similar concept.	124
Table 11. Solar simulator results.	128

LIST OF FIGURES

Figure 1. SEM images (A) and crystal structure (B) of HNTs.....	5
Figure 2. Theories on PDA structure and formation.	10
Figure 3. Schematic of phase transitions in PCMs.....	13
Figure 4. (A) Melting temperatures and (B)latent heat of fusion values of paraffin type PCMs.	15
Figure 5. (A) Melting temperatures and (B) latent heat of fusion values of non-paraffin type PCMs.	16
Figure 6. (A) Melting temperatures and (B) latent heat of fusion values of fatty acid type PCMs.	17
Figure 7. (A) Melting temperatures and (B) latent heat of fusion values of salt hydrate type PCMs.	18
Figure 8. (A) Melting temperatures and (B) latent heat of fusion values of salt hydrate type PCMs for specified compositions.....	19
Figure 9. (A) Melting temperatures and (B) latent heat of fusion values of polyethylene glycol PCMs with various molecular weights.	20
Figure 10. (A, B): TEM images of HNTs at different magnifications; (C, D): SEM images of HNT/PE nanocomposites loaded with 1 wt % HNTs; (E, F): SEM images of HNT/PE nanocomposites loaded with 5wt%.....	32
Figure 11. Mechanical parameters of 500 HNT/PE nanocomposite films at varying HNT loadings. Values in the same group sharing a common letter are not significantly different.	36
Figure 12. Ethylene adsorption isotherms of HNTs (a) and PE and HNT/PE (5 wt.% HNT) films (b) as generated by gravimetric analysis.	38
Figure 13. a Photographs of banana samples packaged with PE films and HNT/PE films containing 5 wt.%HNTs. b Firmness of tomato samples packaged with PE films and HNT/PE films containing 5 wt.% HNTs. Values sharing a common letter are not significantly different.....	39
Figure 14. Oxygen transmission rate (OTR) (a) and water vapor transmission rate (WVTR) (b) of nanocomposite films at different HNT loading ratios. Values sharing a common letter are not significantly different.....	41

Figure 15. Total aerobic count on chicken surfaces packaged with neat PE films (red) and HNT/PE nanocomposite films loaded with 1 wt.% HNTs (green). Values sharing a common letter are not significantly different.....	42
Figure 16. Time-based weight loss of strawberries packaged with neat PE films (red) HNT/PE films loaded with 1 wt.% HNTs (green). Values sharing a common letter are not significantly different.....	43
Figure 17. The design of nanocomposite films.....	51
Figure 18. a) Photographs of HNT/PEG nanohybrids for different PCM impregnation ratios, b) SEM images of raw HNTs and HNT/PEG-M nanohybrids containing 30-40 wt.% PCM (scale bars represent 200 nm), c) Thermogravimetric analysis of raw HNTs and HNT/PCM nanohybrids containing 30 wt.% PCMs. Inset: PCM ratios as calculated by weight loss differences between nanohybrids and raw HNTs.....	53
Figure 19. DSC curves of HNT/PCM nanohybrids.....	54
Figure 20. a) Accelerated DSC heating/cooling cycles of HNT/PEG-M nanohybrids, inset: total $\Delta H_m/s$ calculated for the -20°C to 20°C temperature range, b) FT-IR spectra of raw HNTs and HNT/PEG-M nanohybrids before and after heat application at 160°C for 5 min, inset: photographs of HNT/PEG-M nanohybrid powders before and after heat treatment.	56
Figure 21. Time-temperature curves of neat PE film and PE-HNT/PEG nanocomposite films at -18°C which were taken to room temperature. Inset: Tabulated data showing elapsed time for the frozen films to reach 0°C, 10°C, 15°C and thickness of films. Values with different letters in the table (a-d) within the same column are significantly different.....	59
Figure 22. a) Photographs of packaged meatball samples, b) Time-temperature profiles of meatballs packaged with standard neat PE and PE-HNT/PEG-M films, curves constructed for frozen meatballs taken to room temperature (c) Time-temperature profiles of meatballs packaged with standard neat PE and PE-HNT/PEG-M films, curves constructed for chilled meatballs taken to room temperature. Time values with different letters in each graph (a-g) are significantly different.....	61
Figure 23. Coating of HNTs with polydopamine (a), FT-IR (b) and TGA (c) analysis of raw HNTs and PDHNTs.....	70
Figure 24. Schematic representation of the three-step separation protocol for HNTs.....	71
Figure 25. Yields of grade 1, grade 2 and grade 3 PDHNTs obtained at 2000, 6000 and 11000 rpm centrifugation, respectively, in comparison to yields of raw HNTs obtained by centrifugation at the same velocities. a) two-step separation protocol; polydopamine coating and centrifugation, b) three-step separation; polydopamine coating, ultrasonication and centrifugation.....	72
Figure 26. a) Photographs of grade 1, grade 2 and grade 3 PDHNTs, b) TGA analysis of separated PDHNTs.....	74
Figure 27. SEM and DLS characterization of raw HNTs and separated PDHNTs. a) representative SEM images at 10K magnification, b) representative SEM images at 100K magnification, c) nanotube length distributions histograms from SEM image analysis, d) size distribution histograms obtained by DLS.....	76

Figure 28. a) Photographs and b) TGA analysis of Raw HNTs and separated HNTs (Grade - 1,2,3) after polydopamine coating removed.....	77
Figure 29. Analysis of grade 1, grade 2 and grade 3 HNTs following the removal of the polydopamine coating by heat-treatment, a) representative SEM images at 10K magnification, b) representative SEM images at 100K magnification, c) nanotube length distributions histograms from SEM image analysis, d) size distribution histograms obtained by DLS, e) Aqueous dispersions of HNTs after six hours of storage at room temperature.	78
Figure 30. XRD analysis of raw HNTs; grade 1, grade 2, and grade 3 HNTs following the removal of the polydopamine coating.	80
Figure 31. Functionalization yields of separated HNTs of different quality grades along with raw HNTs calculated by TGA analysis. a) Yields of loading with carvacrol (b) Yields of covalent functionalization with SDS.	81
Figure 32. FT-IR spectrum of SDS functionalized raw HNTs and separated HNTs (Grade 1,2,3).	82
Figure 33. a) SEM images of surfaces of nanocomposite films composed of LDPE and HNTs, b) Mechanical parameters of HNT/LDPE nanocomposite films containing different quality grade HNTs in comparison to neat LDPE films.	84
Figure 34. Structure of synthesized WPU and the synthesis pathway for PDA-WPU particles.	94
Figure 35. Particle size distribution (a), z-average diameter (b) and zeta potential (c) values of WPU and PDA-WPU dispersions by DLS analysis (Values sharing a common letter (a–c) within the same bar are not significantly different). TEM images of WPU and PDA-WPU solid particles (d).	96
Figure 36. Photographs (A) contact angle values (B) and cross-section SEM images (C) of WPU and PDA-WPU films.	97
Figure 37. FT-IR analysis of WPU and PDAPU films.....	98
Figure 38. Mechanical properties of WPU and PDA-WPU films. Values in the same group sharing a common letter (a-c) are not significantly different.	101
Figure 39. Time-temperature profiles (a), solar irradiation cycles (b) and thermal camera images (c) of WPU and PDA-WPU films under sunlight at 1SUN and 3SUN irradiance.	102
Figure 40. Time-temperature profiles (a), NIR laser light irradiation cycles (b) and thermal camera images (c) of WPU and PDA-WPU films under 808 nm laser light at 800 mW/cm ² irradiance.	104
Figure 41. Photographs and solar-irradiation based time-temperature profiles of WPU and PDA-WPU (6mg/ml)/72h cast in the form of a container (A), experimental setup of water evaporation experiment under solar simulator (B), thermal camera images of WPU and PDA-WPU (6mg/ml)/72h container filled with water and exposed to sunlight for 60 min (C), water mass loss (D) and evaporation rates (E) of water in WPU and PDA-WPU containers under 3 SUN solar irradiance.....	108
Figure 42. A basic description of desilication of ZSM-5. M ⁺ can be H ⁺ , Na ⁺ or K ⁺ depending on the composition of the parent zeolite and the applied base.	116

Figure 43. Gas absorption measurement of ZSM-A, ZSM-B and ZSM-5.....	117
Figure 44. NL-DFT predictions for pore size distributions of the zeolitic materials, and relative pore size contributions near 1.3 nm, 3.1 nm, and 5.1 nm derived from the NL-DFT calculations as inset.....	117
Figure 45. Schematic representation of the composite preparation.	118
Figure 46. The physical states of prepared ZSM-X/PCM composites before (A) and after (B) heat treatment.	118
Figure 47. TGA Analysis of (A) ZSMB/LA (40%,60%,65% loading ratio), (B)ZSMB/PEG (40%,60%,70%).	119
Figure 48. DSC curves of the thermal cycle for (a) ZSMB/LA65, (c) ZSMB/LA70; (b-d) their enthalpy and transition temperature changing graphs.....	121
Figure 49. DSC curves of accelerated thermal cycles for (A) ZSM-B-LA65 and ZSM-B-PEG70 (B). The insets show the full measurements for each case.	122
Figure 50. FT-IR analysis of accelerated thermal cycles for (A) ZSM-B-LA65 and ZSM-B-PEG70 (B) end of 45 cycles.....	123
Figure 51. DSC curves of (a) ZSMB/LA and (b) ZSMB/PEG during melting and solidifying process; Enthalpies of melting and solidifying of (c) ZSMB/LA and (d) ZSMB/PEG with different PCM contents.	125
Figure 52. Heat loss percentages of (A) ZSMB/LA and (B) ZSMB/PEG composites.....	126
Figure 53. Thermal behavior of (A-B) ZSMB/LA65 and (C-D) ZSMB/PEG70 composites under solar simulator irradiation.	127
Figure 54. Experimental setup for the evaluation of thermoregulation properties of PDA-WPU/PCM films.	138
Figure 55. Synthesis of PDA-WPU particles (A), DLS diagram (B) and Z-Avg size and zeta potential values (C) of WPU and PDA-WPU.	140
Figure 56. FT-IR spectrum of WPU and PDA-WPU cast films.	141
Figure 57. Preparation of PDA-WPU/PCM cast films and photographs of films at different PDA-WPU:PCM ratios.	142
Figure 58. Surface and cross-section SEM images of PDA-WPU and PDA-WPU/PCM with different PEG4000 contents.	143
Figure 59. XRD spectra of PDA-WPU, PEG4000 and PDA-WPU/PCM films with different PEG4000 contents (A). Mechanical parameters (B) and thermal properties (C) and thermal conductivity values (D) of WPU, PDA-WPU and PDA-WPU/PCM film composites.	145
Figure 60. DSC curves (A), melting (B) and solidifying (C) temperatures with onset, peak and offset points, and melting/solidifying enthalpies (D) of PEG4000 and PDA-WPU/PCM film composites.	147
Figure 61. The physical states of prepared PDA-WPU/PCM composite films before and after heat treatment (A) and DSC curves of consecutive thermal cycles for thermal reliability of films (B).	149

Figure 62. Thermal behavior of film samples under 150 mW/cm² solar light irradiation (A). Thermal camera imaging of film samples at 20 min solar irradiation (B). Energy storage efficiencies of PDA-WPU/PCM composite films (C).....151

Figure 63. Thermal camera images (A) and thermal behavior graph (B) of film samples in the cold environment. Temperature changing inside of beakers having film samples (C).153

CHAPTER 1: General Introduction

1.1. Dissertation overview and objectives

Sustainability is undoubtedly a very critical issue for the earth and the life of living beings. Within this framework, the safety of food products, protection of clean water resources and decreasing the consumption of energy that is obtained from harmful materials such as fossil fuels should be priority targets to be considered. With this motivation, different hybrid materials comprising inorganic and organic components were designed, which can be utilized in food safety, water evaporation, solar to thermal energy conversion and thermal energy storage applications.

For the food safety subtitles, an active food packaging material with ethylene scavenging and gas barrier properties was designed by polyethylene and halloysite nanotubes (HNT). In the literature, it is possible to find different strategies to prolong the shelf life of products by using chemical applications, but consumer preferences are strongly against such chemical treatments. To add ethylene scavenging property into a packaging system, ethylene oxidizing materials such as potassium permanganate or metal catalysts can be used by immobilization on an inert substrate^{1,2}. However, this approach has limited acceptance due to toxicity-based concerns and regulations against their food-contact applications. To create barrier property on the packaging material, montmorillonite (MMT) nanoclay can be considered to reduce the gas permeability of the material³. But the strong hydrophilic character and natural, platy, nanolayered structure of MMT mostly requires chemical organo-modifications or the use of compatibilizers to improve their compatibility with low surface energy polymers such as polyolefins which are mostly the choice of polymeric matrix for food packaging applications. To overcome these problems, we have designed a flexible packaging material comprising HNTs which are safe, cost-effective, abundant, relatively hydrophobic, and more compatible with low surface energy polymers. In this way, we have demonstrated, for the first-time, HNT/polyethylene (HNT/PE) nanocomposites with ethylene adsorption and gas barrier

properties as food packaging films that can improve the quality and shelf life of perishable food products.

The second approach to food safety was to protect food products during the cold-chain transportation stage. As known, in the case of a short-term or long-term cold chain failure during transportation, temperature fluctuations can cause deterioration of temperature-sensitive food products. To develop a solution that slows temperature increases in cold foods in the case they are exposed to higher temperatures, we designed for the first-time flexible packaging films with a combination of phase change materials, HNTs, and PE polymer matrix. The design consisted of impregnation of HNTs with multiple polyethylene glycol PCMs with melting transitions at cold chain temperatures and incorporation of these nanofillers into the PE polymer matrix. This idea provided the development of a material that has thermal buffering capacity in a broad temperature interval and has the ability to retard temperature increases in cold-stored food products.

Our findings obtained from HNT-based food packaging studies and extensive utilization of HNTs in countless purposes in the literature provoked us to focus on the quality of nanotubes in terms of inhomogeneous size distribution and agglomeration tendency. As known, dispersing nanoparticles into a system is a very critical issue to obtain a nanocomposite of optimal performance. Here, homogeneous length size and agglomeration-free features of nanoparticles can be an important point that should be kept in view. HNTs naturally exist in a wide range of lengths and diameters depending on their deposits and have a tendency to agglomerate, thus cannot be individually dispersed in aqueous solutions and polymers. Different nanoparticle separation and purification methods can be found in the literature such as separation by filtration⁴, gel electrophoresis⁵, size exclusion chromatography⁶ and viscosity grading with centrifugation⁷. However, some of these techniques are not suitable for all nanoparticle systems or require the use of co-chemicals to increase the viscosity of the medium or colloidal stability, as in the viscosity grading method. In order to offer a suitable size separation technique for HNTs, a facile method was developed to obtain HNTs that are uniform in size and shape while preserving or improving their inherent properties. The protocol consists of the coating of HNTs with a polydopamine layer, followed by their ultrasonication and centrifugation at varying velocities for size-based separation. While this polydopamine functionalization based three-stage separation technique has been

demonstrated to be effective for size separation of HNTs, it can be easily applied to different nanoparticles due to the ease of functionalization of any surface with polydopamine.

Acquired knowledge from the polydopamine functionalization study was used to offer a new material design in the concept of light to thermal energy conversion applications. A novel polyurethane polymer matrix having light to thermal energy conversion capability was produced by coating polyurethane solid particle surfaces with polydopamine. With this strategy, a final photothermal polymeric material was obtained without incorporation of any nanoparticles. Ultimately, many disadvantages arising from adding secondary materials into the end-product such as toxicity, incompatibility, increased cost, and difficulties in processing were eliminated. While the designed material can be utilized in various different light-driven applications, its light-driven water evaporation performance was investigated as a critical potential.

The polymeric matrix which has light to thermal energy conversion ability has opened a way to prepare a multifunctional product that combines photothermal, energy storage and thermal buffering properties in a single system and can be used for important energy applications.

As a preliminary work to reach this goal, the latent heat storage phenomenon was specifically studied by using a zeolitic type inorganic framework. In this context, the effect of mesopore enrichment on phase change material (PCM) uptake of the zeolite and in turn the final latent heat storage properties were examined. Comparing latent heat storage and shape stabilizing performance of pristine microporous zeolite with its post-synthetically modified versions having altered porosity enabled us to examine specifically the effect of pore size on latent heat storage properties. In addition to the shape stabilizer effect, the effect of different PCMs on loading and latent heat storage properties were also investigated.

Detailed studies on latent heat storage, thermal buffering, light to thermal energy conversion and polydopamine functionalization allowed the development of a final multifunctional polymeric material comprising all critical properties in the concept of thermal management. To exhibit a composite system which is in the final usage form, waterborne polydopamine-polyurethane as photothermal matrix and PEG4000 as phase change material was dissolved into water dispersion stage, and the blended mixtures were directly poured onto a mold without using any other encapsulator for casting film preparation. In the end, shape-stable

latent heat storage, thermal buffering, and light to thermal energy conversion performance of the obtained composite were directly analyzed as a material that was ready to use in the practical real-life application as an end-product.

1.2. Review on the functional components of the polymeric hybrid materials

In this thesis, polymeric hybrid materials were developed by the combination of different functional components including HNTs as inorganic encapsulation agents, polydopamine as a photothermal surface functionalization agent, and PCMs as latent heat storage agents.

1.2.1 HNTs

i) General view

HNTs are natural clay minerals that have attracted great attention in green nanotechnology in recent years. One of the remarkable properties of HNTs is their natural hollow tubular nanostructure. Because of their unique natural form, they are accepted as eco-friendly nanotubes with low cost, presenting countless advantages such as non-toxicity, biocompatibility (EPA 4A listed material), high aspect ratio, high thermal stability, superior loading rates to other carriers, high adsorption capacity and regeneration ability.⁸ Due to these unique properties, HNTs have been utilized in many different application fields such as reinforcing of nanocomposites⁹, encapsulation of active components¹⁰, water purification¹¹, drug delivery¹², cancer cell isolation¹³, tissue engineering¹⁴, dentistry materials¹⁵ and cosmetics¹⁶.

Physical properties of HNTs show variation depending on the mining deposits from which they are obtained. However, generally the external diameter of the HNTs ranges from 40 to 70 nm and the nanotube length ranges from 500 to 1000 nm¹⁷. The typical average surface area of HNTs is 62 m²/g, pore volume is ~ 1.25 mL/g, refractive index is - 1.54 and specific gravity is- 2.53 g/cm³⁸.

As to the chemical form of HNTs, they have an empirical chemical formula of Al₂Si₂O₅ (OH)₄ .nH₂O resembling kaolin¹⁸. The outer and inner surfaces of the HNTs consist of siloxane (Si–O–Si) and octahedral array groups (Al–OH), respectively. Generally, the multilayer tubular walls of HNTs are composed of 15 ~ 20 aluminosilicate layers having a layer spacing of 10 Å or 7 Å for the hydrated or dehydrated HNTs, respectively¹⁹.

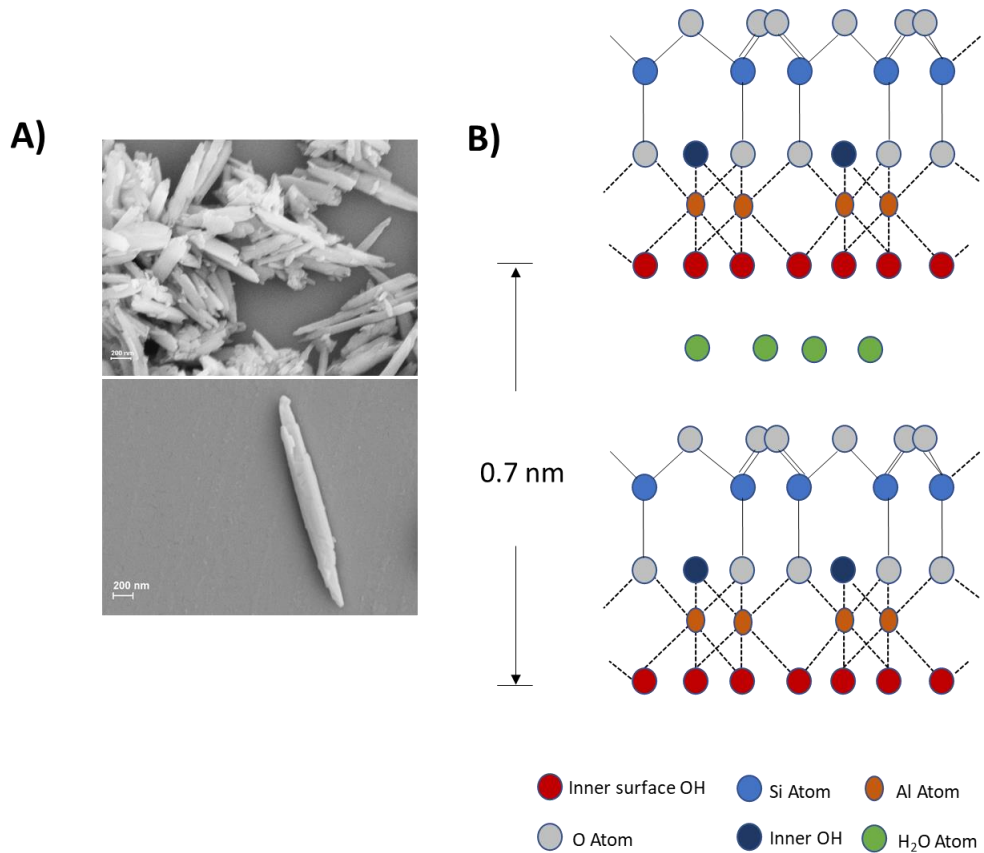


Figure 1. SEM images (A) and crystal structure (B) of HNTs.

HNTs compose of tetrahedral and octahedral sheets of Al, Si, O ions and OH groups organized into two-dimensional structures. Oxygen anions settle at the four corners with silicon at the center of the tetrahedron sheet and a hexagonal arrangement forms where three corners of each tetrahedron are shared with other nearby tetrahedra. A part of the octahedral sheet occurs in the perpendicular direction of the oxygen existing at the fourth tetrahedron corner. Al cation at the center and eight oxygens at the corners create the octahedral sheets and each octahedron connects sideways with octahedra nearby and vertically with the tetrahedron by sharing an oxygen (Figure 1B)²⁰.

ii) HNTs as gas adsorbents

In this thesis, one of the properties of HNTs that was utilized to create a food packaging nanocomposite film with ethylene scavenging behavior was its gas adsorption capacity. HNTs exhibit gas adsorption performance owing to their tubular porous structure and high surface area with pores between the aluminosilicate layers. These excellent properties present a way to use them in gas adsorption systems^{20,21}. Furthermore, alternative surface charges on their inner and outer surfaces supply a chance to tune the surface properties, thus enhancing their adsorption capabilities for various adsorbate molecules²². The natural structure of HNTs does also allow the enhancement of gas adsorption capacities via different strategies. Palantöken et al. presented a novel and simple method based on a cryoscopic technique to expand the HNT lumens via frozen water molecules entrapped in HNT lumens²³. Gaikwad et al. enhanced the adsorption capacity of HNTs by alkaline treatment and tested the ethylene adsorption performance of nanotubes for food-packaging applications²⁴. Ultimately, it can be accepted that HNTs are very good candidates for being used as gas adsorbent materials.

iii) HNTs as containers for active component loading

The inner lumens of HNTs enable them to be loaded with active components due to their suitable hollow diameter. Fundamentally, loading is performed with cyclic vacuum pumping in/out for the replacement of the air in the internal cavities with liquid active materials. The replacement of the inner air with a liquid substance can be observed with the revealing of bubbles at the surface of the dispersion. Although the proper lumen diameter of around 15 nm generates a very high capillary force that provides pushing the solution into the tubes, the application of cyclic air pumping is still necessary for reaching the efficient loading capacity. Active components in the liquid form can be loaded directly into HNTs. In the case of material in the solid form, the substance can be dissolved in a suitable solvent and loaded into HNTs. For example, water, alcohol, or acetone are usually used as the solvent for the drug loading. Following the loading procedure, obtained HNT/drug nanohybrids are washed with water to remove the adsorbed drug. This protocol can be applied for any kind of substance loading. Many kinds of materials can be loaded into HNTs such as drugs¹⁴, proteins²⁵, DNA^{26,27}, antimicrobial agents^{28,29}, pesticides^{30,31}, phase change materials^{32,33} etc.

iv) Halloysite nanotubes as reinforcing fillers

The surface structure of HNTs consisting of fewer surface hydroxyl groups provides a better dispersibility than other silicates such as montmorillonite and kaolinite in polymer matrices³⁴. Moreover, having a lower surface charge due to the presence of siloxane groups on the outer surface makes them more compatible with low surface energy polymers such as polyolefin type polymers³⁵. HNTs can be dispersed into polymeric matrices by a direct melt-blending method. Besides, HNTs can be embedded into melted polymers using industrial double-screw extruders resulting in nanocomposites with well-dispersed nanotubes. Reinforcing effects of HNTs on polymeric nanocomposite films arise from rod-like and high aspect ratio structures of HNTs and the unique surface chemical properties. More importantly, different examinations point out that HNTs include only traces of heavy metals which is much lower than standards of the restriction of harmful substances of the European Union. Thus, this conclusion makes HNTs a type of ‘green’, unique and promising reinforcing filler for thermoplastics¹⁰. Because of these advantages, HNTs have been incorporated into a great number of polymer matrices³⁶. In addition, since HNTs are intrinsically impermeable to gases, they create a tortuous path for gas molecules and inhibit their diffusion throughout the matrix; therefore, an acceptable barrier property can be added to the prepared nanocomposite film.

v) Surface modification of HNTs

Although HNTs have significant advantages that allow them to be used in countless applications, some disadvantages such as heterogeneous size distribution, surface charge and formation of hydrogen bonds reduce their affinity to a certain extent. Surface modification of HNTs with a suitable agent expands the range of potential applications. The natural structure of HNTs can cause weak compatibility with other materials due to poor intermolecular forces like van der Waals forces and hydrogen bonding³⁷. In order to make HNTs more compatible with the system in a desired application, surface modification may be very critical. Surface modification improved the performance of HNTs in different application leading to HNT composites with improved mechanical³⁸, improved sustained release properties³⁹, improved dispersion stability⁴⁰, improved dye removal properties⁴¹, improved catalyst properties⁴² and improved enzyme immobilization capacity⁴³. For such

goals, HNT surface can be modified with different chemicals. HNTs can be modified with a surfactant thanks to electrostatic interactions that provide a better dispersion stability^{44,45}. HNT surface can be modified with small molecules reacting with the hydroxyl groups of the HNT surface (intercalation modification) and the dispersion capability of nanotubes in a polymer matrix can be enhanced⁴⁶. HNT surfaces can also be coated with polymers directly⁴⁷ or via free radical modification of hydroxyl groups on the inner or outer surfaces⁴⁸. With these strategies, HNTs become more applicable in desired applications and a better nanotube performance can be obtained.

1.2.2 Photothermal agents

The photothermal effect is an important phenomenon based on converting light energy to thermal energy by using photothermal conversion materials. By taking advantage of this concept, various effective solutions can be offered to many vital application areas such as solar water evaporation⁴⁹, chemo-photothermal therapy⁵⁰, the photothermal killing of bacteria⁵¹, controlled release⁵², self-healing^{53,54} and shape memory materials⁵⁵.

Photothermal materials can be classified into four main categories, that are metallic nanostructures, inorganic semiconductor materials, carbon-based light-absorbing materials and polymeric materials⁵⁶. Light absorption is the fundamental process of photothermal generation, however, different types of photothermal agents can exhibit higher light-to-heat conversion ability than the other one because of some specific features. For example, metallic nanostructures present intense photothermal property due to surface plasmon resonance (SPR) effects, which is an electromagnetic resonant oscillation, that was first demonstrated by Gustav Mie⁵⁷. Inorganic semiconducting materials show photothermal property thanks to the bandgap between the valence and conduction band⁵⁸. As for carbon-based structures, the photothermal property is provided by the black body of material, which can theoretically absorb all incident light radiations; thus, enable effective light to heat energy conversion⁵⁹⁻⁶¹.

Polymeric materials can display photothermal properties generally through conjugated π -electron systems, in which the π electrons are delocalized and thus materials present high light absorption⁶². Conjugation induces the rapid promotion of an electron from the ground

state to the excited state. Then, the excited electron jumps back to the ground state by releasing thermal energy via nonradiative decay^{63,64}. Extensively investigated photothermal polymers can be mainly listed as polythiophene⁶⁵, polyaniline⁶⁶, polypyrrole⁶⁷, and polydopamine⁶⁸. In this thesis, polydopamine has been selected and utilized as an effective photothermal agent and also as a surface coating material.

Polydopamine

Polydopamine (PDA) is a mussel-inspired smart coating material. The coating of a surface with PDA layer is a uniquely adaptable and simple surface functionalization method which was firstly reported by Messersmith et al. in 2007⁶⁹. Following the first introduction of PDA, it has become an attractive and powerful tool for modification of surfaces due to its versatile character. As a result of its impressive structure, PDA have located a broad potential use in the biomedical, energy, consumer, industrial and military applications⁷⁰. Important features of PDA can be listed as strong NIR absorbance capacity, good biocompatibility, the feasibility of functional group modification and most importantly, its strong adhesion property and its ability to be coated on almost all substrate surfaces⁷¹.

i) Chemistry of PDA

Polydopamine basically consists of catechol groups on the polymer backbone. Oxidation polymerization in an aqueous solution is the most widely used procedure for the production of PDA⁷⁰. The dopamine monomer can be oxidized with oxygen as the oxidant and spontaneously self-polymerized at the alkaline conditions around pH 8.5 without the need for any complicated or harsh reaction conditions⁷¹. One of the critical points of PDA coating reaction that must be emphasized is that the concentration of dopamine monomer in the system should be higher than 2 mg/mL to create a PDA film on substrates. The thickness of the PDA film on the substrate can be controlled by adjusting the concentration of dopamine monomer or the polymerization time⁷².

Although it is a very remarkable material that is being utilized in many different studies, interestingly, its molecular structure is still under discussion and various structures have been proposed. The general acceptance is that the dopamine units or 5,6-dihydroxyindole derivatives are covalently linked via C–C bonds. As a strong prediction, PDA formation

occurs via several dehydrogenation steps generating *o*-quinone units by being cyclized to indole moieties and/or form C – C bonds. Monomers link each other between catechol or *o*-quinone moieties or via the pyrrole ring of indole units. PDA polymer backbone has been proposed to be composed of oligomers, most probably up to octamers, instead of high molecular weight polymers. The supramolecular structure of PDA likely forms via hydrogen bonding and π -stacking. The polymer configuration is completely regulated by hydrogen bonding, π -stacking and charge transfer between dihydroxyindole and indoldione monomers (Figure 2)⁷³⁻⁷⁵.

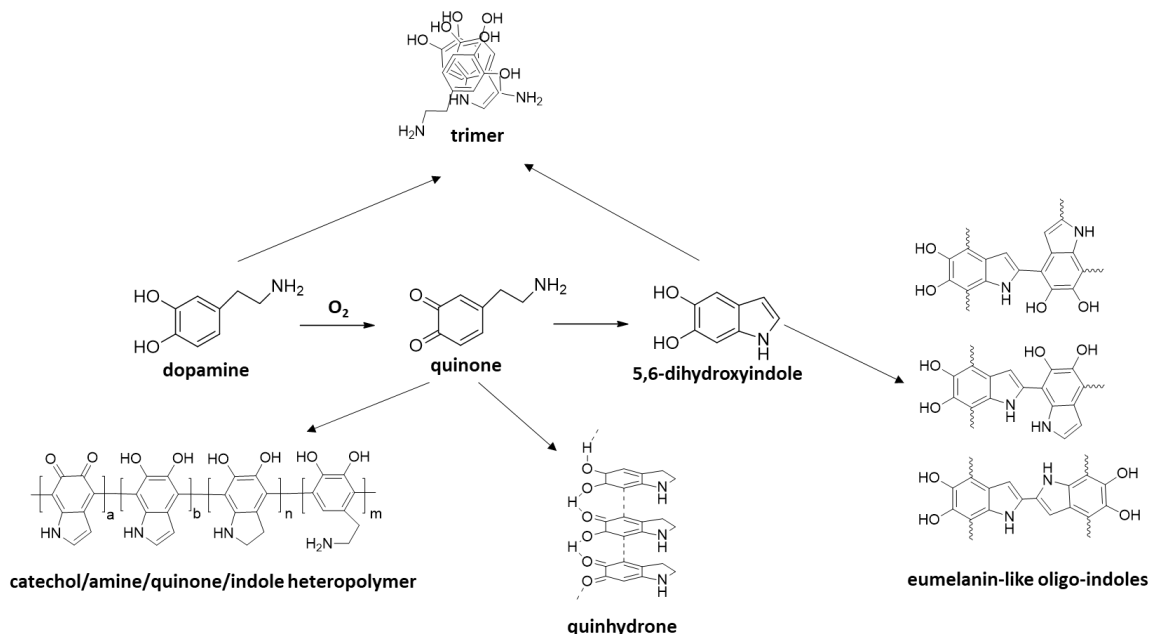


Figure 2. Theories on PDA structure and formation.

ii) Applications fields of PDA

Spectacular features of PDA have been transferred to several types of materials to utilize the various functions of PDA in desired applications. Easy manufacturing of PDA coating has opened a way to fabricate countless multifunctional substrates for specific properties. Grafting of various materials onto PDA coatings has been achieved by means of chemical reactions, abilities of PDA coating in the second reaction step, chelating, etc. Such that, from DNA⁷⁶, proteins⁷⁷, enzymes⁷⁸, living cells⁷⁹, to PEG⁸⁰, polysaccharides⁶⁹, hydroxyapatite⁸¹,

noble metal nanoparticles⁸², graphene oxide⁸³ and polymers⁸⁴ different surfaces have been modified with PDA to obtain chemically reactive, bio- interactive and bio-resistant surfaces. PDA has also been applied to hydrogels in the concept of injectable drug delivery depots, tissue engineering scaffolds, medical devices, sensors and separation systems⁸⁵. Some other PDA-derived hybrid systems can be found in the literature for the application of synthetic membranes⁸⁶ and microfluidic systems⁸⁷.

In order to reveal extensive utilization of PDA, the fields that were impacted by PDA technology can be categorized as, biomedical, water treatment, sensing and energy applications. In biomedical science, PDA has been used for the purpose of cell adhesion⁸⁸, encapsulating, patterning⁸⁹, induced toxicity attenuation of materials⁹⁰, antimicrobial surfaces⁹¹, tooth demineralization⁹², tissue engineering⁹³, reendothelialization of vascular devices⁹⁴, photothermal therapy⁹⁵, in vivo cancer diagnosis⁹⁶, bioimaging⁸⁷ and drug delivery⁹⁷. As to applications in water treatment, separation of heavy metals⁹⁸, organic pollutants⁹⁹ and bacteria from water¹⁰⁰, water/oil separation¹⁰¹ and seawater desalination¹⁰² studies have been conducted by preparing PDA-based systems. In the concept of sensing applications, the advantages of PDA have been benefited for the detection of small organic molecules¹⁰³, biomolecules¹⁰⁴ and heavy metal ions¹⁰⁵.

iii) PDA in energy applications

Among a wide range of applications of PDA, energy related applications of PDA-based systems are attracting great attention. Characteristic properties of PDA such as high carbon content, adhesion capability, hydrophilic character and behavior as a reducing agent make PDA a favorable component in hybrid materials for energy applications. PDA has been applied in various energy applications such as Li-Ion batteries¹⁰⁶, dye-sensitized solar cells¹⁰⁷, supercapacitors¹⁰⁸, electrocatalysts¹⁰⁹, photocatalysts¹¹⁰ and chemical catalysts¹¹¹.

In this thesis, the PDA coating was used to prepare a material having light to thermal energy conversion properties. PDA exhibits photothermal property by converting light energy to heat likely via nonradiative relaxation and molecular vibrations in the polymer chain¹¹². In the concept of light to thermal energy conversion, PDA assisted systems have been employed in water purification¹¹³⁻¹¹⁵ or vapor generation^{116,117} applications by coating the substrate surface with the PDA layer. Besides, photothermal therapy, which is another critical

application field of light to thermal energy conversion, has been also designed with different PDA-based hybrid systems¹¹⁸. Moreover, indirect photo-driven systems such as energy storage¹¹⁹⁻¹²¹, self-healing¹²² and shape memory¹²³ studies have been also conducted with PDA-containing composites.

1.2.3 PCMs for latent heat storage

Renewable energy has become a more and more vital subject day by day, mainly due to the constant increase in the level of greenhouse gases and economic problems arising from fuel prices. This critical situation has become a driving force for scientists to focus on research relating to energy. While it is critical to find solutions for benefiting from renewable energy sources to produce energy it is also very important to develop proper ways to store the produced energy. One of today's challenges is to be able to convert and store energy in suitable forms.

Different types of energy namely mechanical, electrical and thermal energy can be stored when utilizing appropriate methods. Mechanical energy storage basically involves gravitational energy storage, pumped hydropower energy storage, compressed air energy storage and flywheels. As to electrical energy storage, the method is carried out by converting stored chemical energy into electrical energy with a battery that can be charged by connecting to a source of direct electric current. Thermal energy storage can be performed by following strategies such as sensible heat, latent heat and thermochemical¹²⁴. In this thesis, thermal energy storage via latent heat phenomenon has been studied as the energy storage method.

i) Latent heat storage materials

Latent heat storage is based on the thermal energy transfer that happens when a PCM reaches its phase transition temperature, namely, changing from solid to liquid or liquid to the solid phase. During the melting transition, thermal energy is stored by PCMs and the stored energy is released when the material reaches its solidifying temperature. With this loop, thermal energy is stored and released in PCMs (Figure 3).

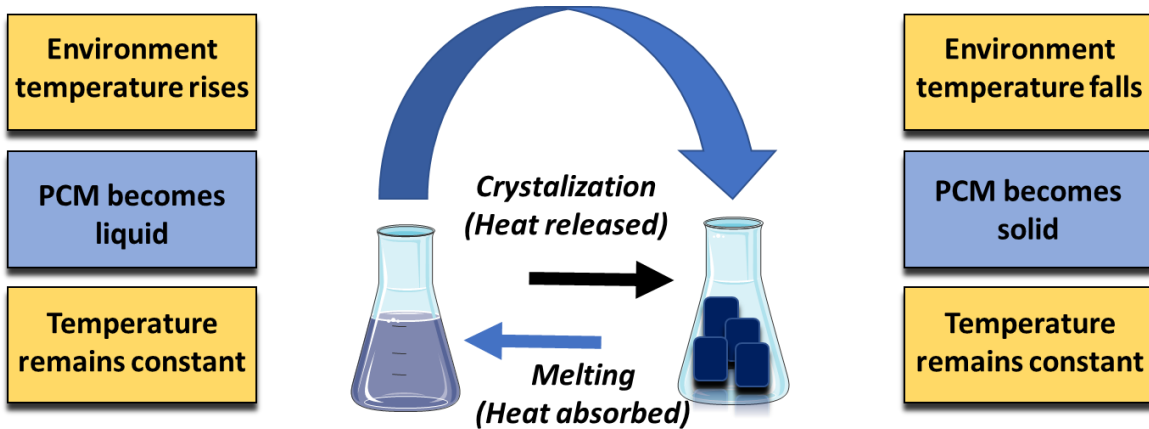


Figure 3. Schematic of phase transitions in PCMs.

Although this strategy is a smart idea for thermal energy storage/release in a simple and safe way, PCMs must exhibit certain desirable thermodynamic, kinetic, chemical properties along with cost-effectiveness and easy availability. These requirements can be summarized as follows. (i) PCMs should have a suitable phase-transition temperature, high latent heat of transition and good heat transfer in terms of their thermal properties; (ii) as their physical properties, PCMs should present favorable phase equilibrium, high density, small volume change, and low vapor pressure considering small size containers and containment problems; (iii) PCM should have low supercooling and sufficient crystallization rate; (iv) desired chemical properties of PCMs can be listed as long-term chemical stability, compatibility, no toxicity and non-flammability; (v) finally, abundance, availability and cost-effectiveness are the desired economical parameters of PCMs¹²⁵.

PCMs can be classified as organic, inorganic, and eutectic substances, which present different transition temperatures.

Paraffins: Paraffins are simple alkanes with a chemical formula of $\text{CH}_3-(\text{CH}_2)_n-\text{CH}_3$. Fundamentally, they have a large amount of latent heat and their melting point increases with chain length¹²⁶. The melting points and latent heat of fusion values of paraffins are presented in Figure 4.

Non-paraffins: Numerous non-paraffin organic phase change materials can be listed. These substances can be subtitled into two main categories as fatty acids and other non-paraffin

organic molecules like esters, alcohols, and glycols. Some important properties of these materials are high heat of fusion, inflammability, low flash points, instability at high temperatures, low thermal conductivity and toxicity¹²⁷. Among these materials, fatty acids, which have a general chemical formula of $\text{CH}_3(\text{CH}_2)_n\text{COOH}$, stand out due to their high heat of fusion values, reproducible melting/freezing behavior and freeze with no supercooling¹²⁸. Melting transition temperatures and latent heat of fusion values of some non-paraffin organic and fatty acid PCMs are presented in Figure 5 and Figure 6.

Salt hydrates: Salt hydrates are evaluated under the category of inorganic PCMs and their general formula is $\text{XY}\cdot\text{nH}_2\text{O}$. The most important properties of salt hydrates are high latent heat of fusion per unit volume, relatively high thermal conductivity, small volume changes during melting, not showing very corrosive behavior, compatibility with plastics and slight toxicity. They have some critical disadvantages for use in PCM systems such as incongruent melting behavior due to supersaturation and higher supercooling degrees¹²⁹. Melting transition temperatures and latent heat of fusion values of some salt hydrate PCMs are presented in Figure 7.

Eutectics: Eutectics are defined as combinations of two or more components at the minimum-melting. Each component melts and freezes harmoniously composing a mixture of the crystals of constituents during crystallization. Eutectics freeze to a special crystal mixture and frequently melt/freeze without segregation. Both components liquefy together during the melting process without separation¹³⁰. Melting transition temperatures and latent heat of fusion values of some eutectic PCMs are presented in Figure 8.

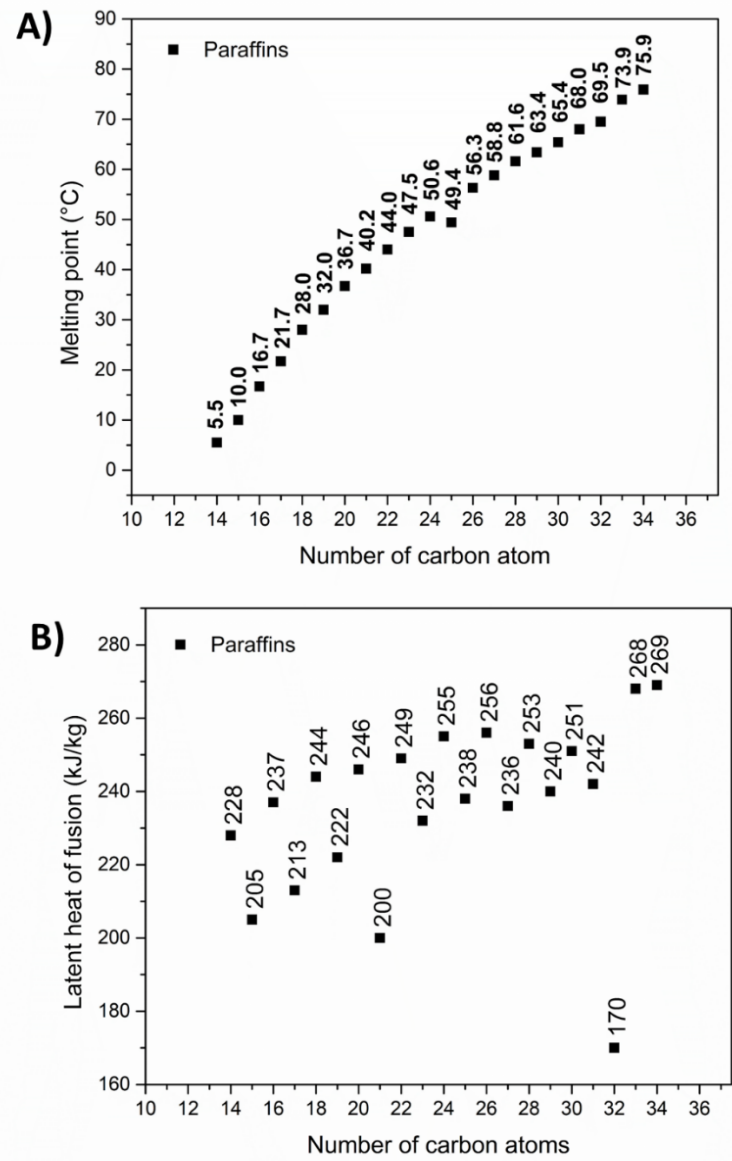


Figure 4. (A) Melting temperatures and (B)latent heat of fusion values of paraffin type PCMs.

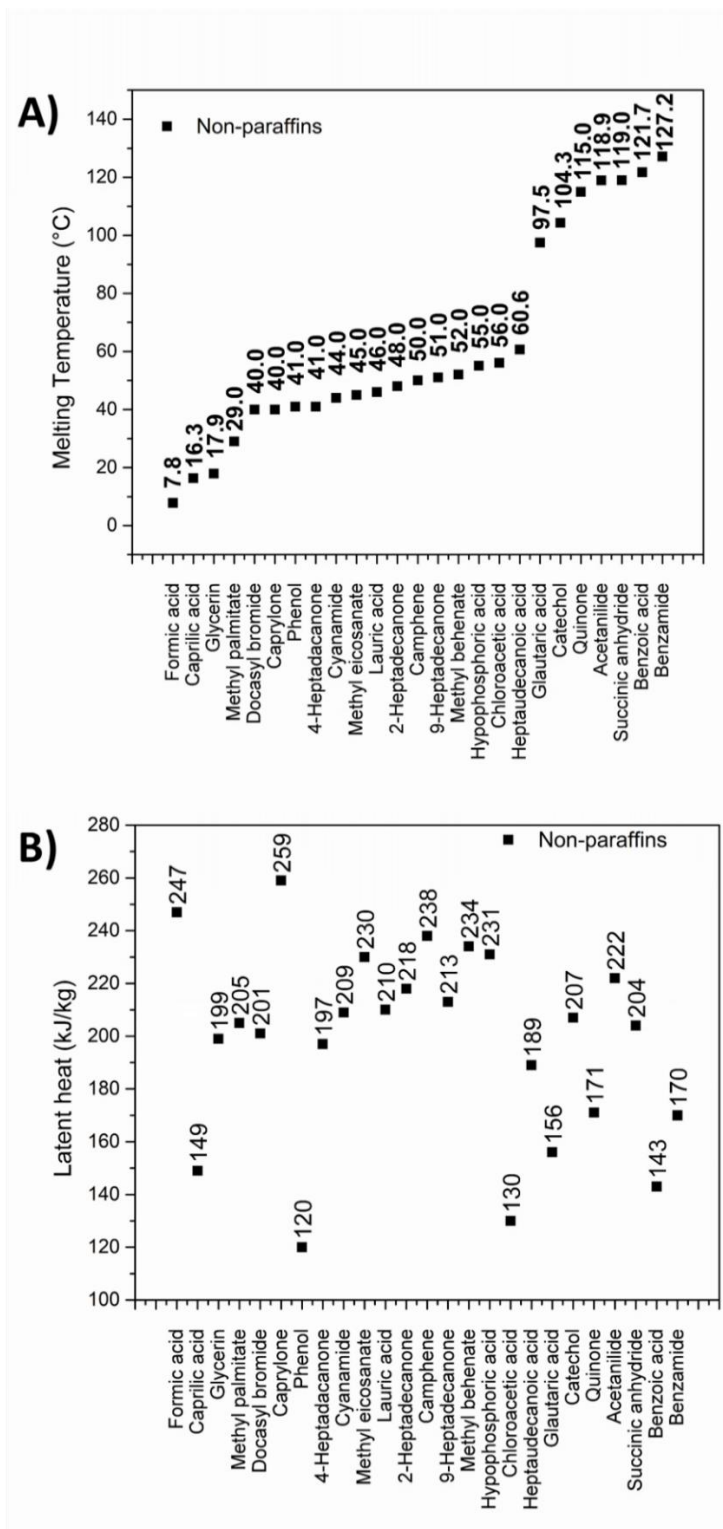


Figure 5. (A) Melting temperatures and (B) latent heat of fusion values of non-paraffin type PCMs.

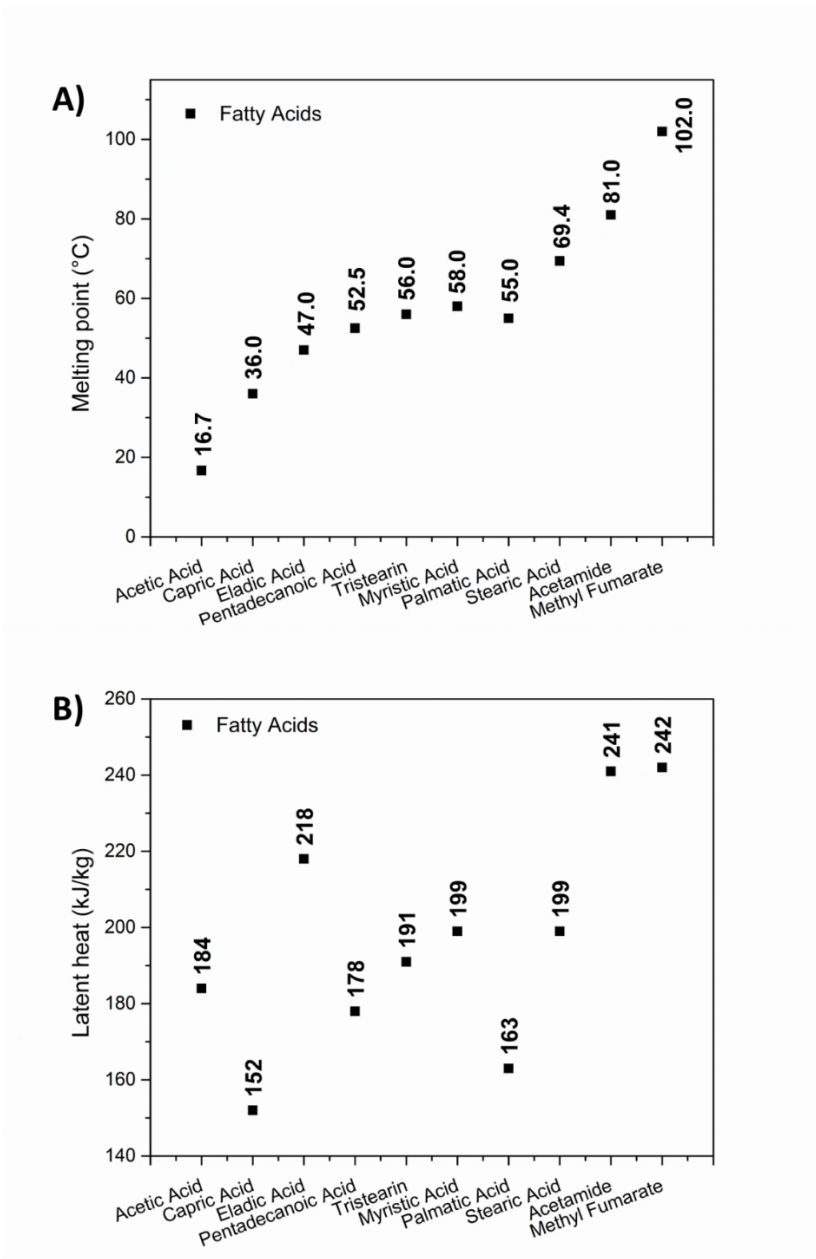


Figure 6. (A) Melting temperatures and (B) latent heat of fusion values of fatty acid type PCMs.

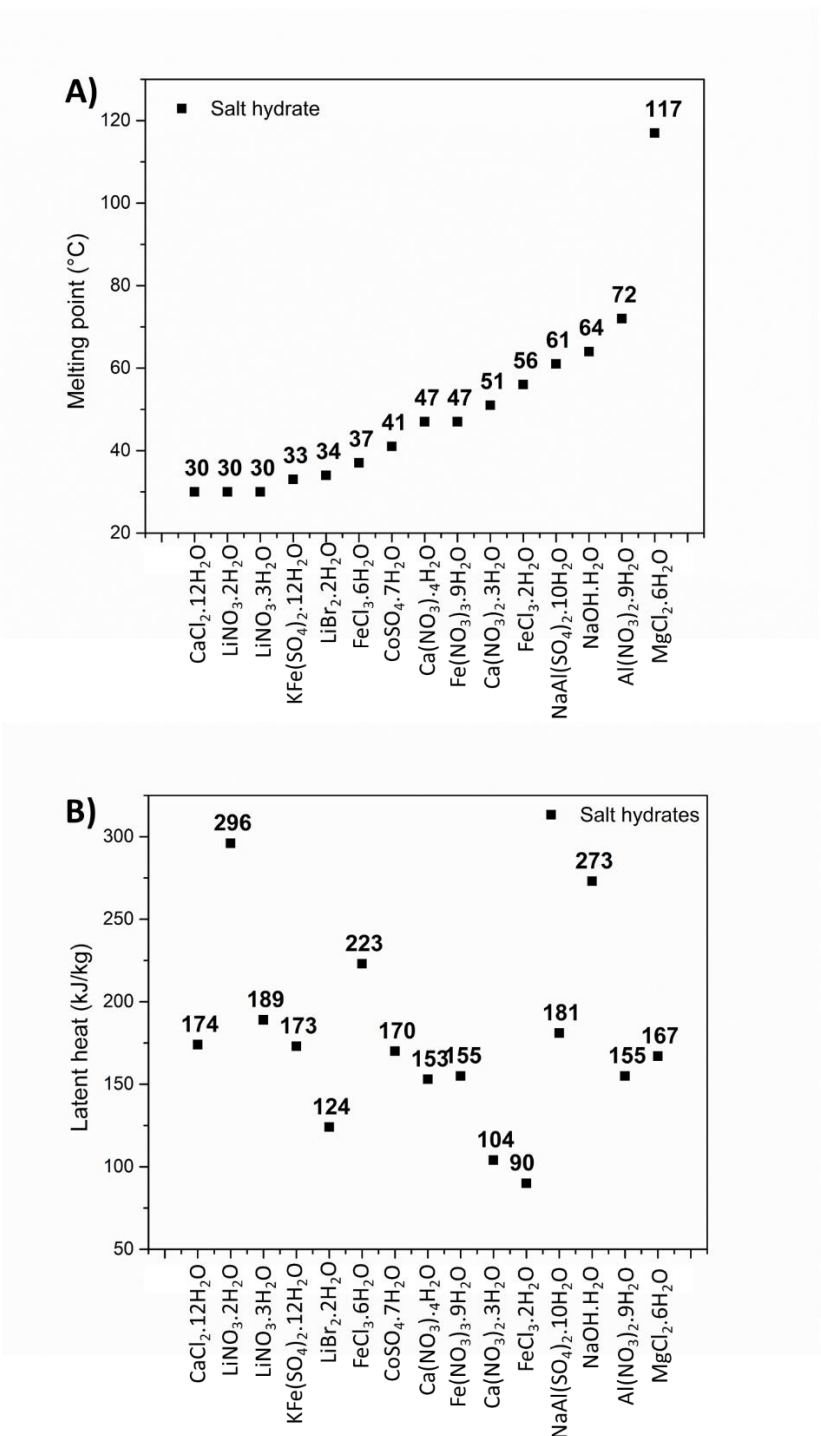


Figure 7. (A) Melting temperatures and (B) latent heat of fusion values of salt hydrate type PCMs.

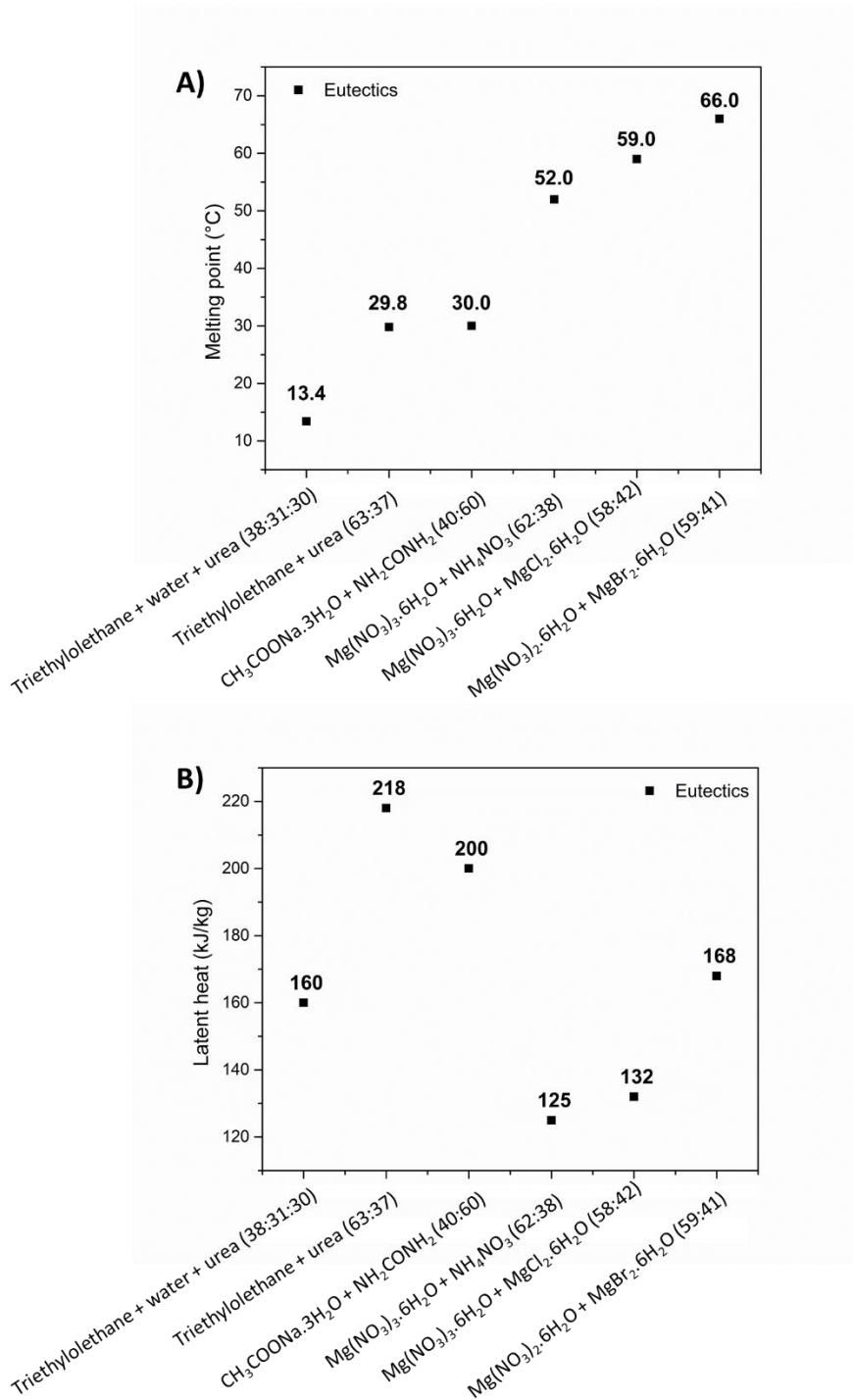


Figure 8. (A) Melting temperatures and (B) latent heat of fusion values of salt hydrate type PCMs for specified compositions.

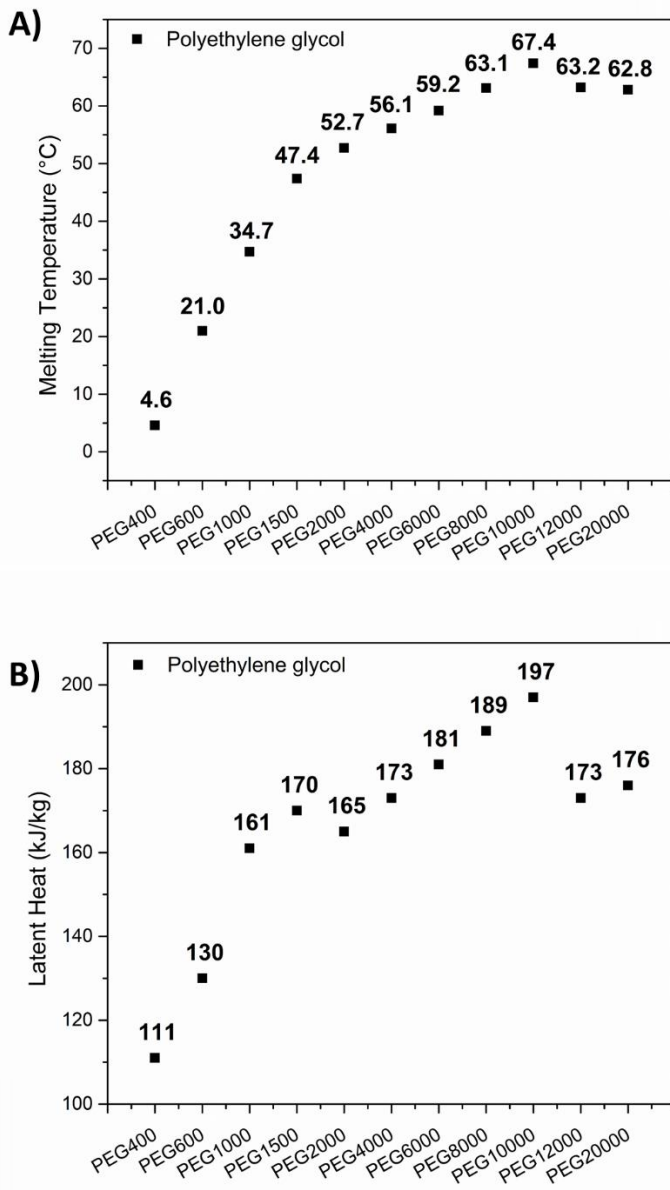


Figure 9. (A) Melting temperatures and (B) latent heat of fusion values of polyethylene glycol PCMs with various molecular weights.

Polyethylene glycol: Polyethylene glycol (PEG) is a type of polyether compound which has a general chemical formula of $\text{H}-(\text{O}-\text{CH}_2-\text{CH}_2)_n-\text{OH}$. PEG is a hydrophilic molecule that is being accepted as a low toxicity and used in a variety of products. As a promising solid-liquid organic PCM, PEG has desirable characteristics for use in PCM-based studies such as high phase change enthalpy, chemical-, biodegradation- and thermal stability, low vapor

pressure and non-corrosiveness. Moreover, a wide range of melting transition temperatures can be derived from the PEG by tuning its molecular weight^{131,132}. Melting transition temperatures and latent heat of fusion values of PEG PCMs with various molecular weights are presented in Figure 9.

ii) Shape-stabilization of PCMs

One of the important issues that should be considered in the practical application of PCMs is their shape stability. When the solid-liquid PCM-based systems are evaluated, the critical problem arises from the change of the physical state when the temperature of the PCM reaches its melting point. When the PCM is converted to its liquid form, leakage of the PCM may occur. Many serious damages such as contamination or device failure (i.e., for electronic-based equipment) can arise by the leakage of organic PCMs. The most intelligent and relatively simple way to overcome this problem is that entrapping the PCMs in a supporting matrix, which is called as shape-stabilization.

Different strategies can be used to create a shape-stable phase change composite system. One of them is shape-stabilization by microencapsulation which was firstly introduced by Barret K. Green in the 1950s¹³³ and became a very important technique for the commercialization of PCMs. In the concept of microencapsulation, PCMs can be stabilized in an organic shell using various materials such as melamine-formaldehyde resin¹³⁴, acrylic resins¹³⁵, urea-formaldehyde resin¹³⁶, poly (urea–urethane)¹³⁷ and polyurea¹³⁸. Another technique is the encapsulation of PCMs into an inorganic shell via rigid shell-forming materials such as silica¹³⁹, titania¹⁴⁰, calcium carbonate¹⁴¹ and zinc oxide¹⁴². Moreover, shape stabilization of PCMs can be carried out by preparing organic-inorganic hybrid shells. For this purpose, hybrid systems can be created by introducing inorganic additives such as silver nanoparticles¹⁴³, iron nanoparticles¹⁴⁴ and silicon nitride¹⁴⁵ into organic shells.

Shape-stable PCM composites can be obtained by directly embedding PCMs into polymer matrices. Polyacrylates¹⁴⁶⁻¹⁴⁸, polyolefins¹⁴⁹⁻¹⁵¹, styrenic block copolymers¹⁵²⁻¹⁵⁴, polysaccharides¹⁵⁵⁻¹⁵⁷ and polyurethanes¹⁵⁸⁻¹⁶⁰ can be given as examples of shape-stabilization of PCMs by a polymer matrix.

Improvements in nanoscience have also introduced new methods for the preparation of shape stable PCMs systems. In the literature, there are many studies conducted with nanoparticles

to form shape stable PCM nanocomposites. In these studies, carbon materials have an attractive place to produce PCM nanocomposites due to their excellent theoretical thermal conductivity¹⁶¹. Studies utilizing graphene nanoparticles¹⁶²⁻¹⁶⁴, boron nitride nanosheets¹⁶⁵⁻¹⁶⁷ and carbon nanotubes¹⁶⁸⁻¹⁷⁰ can be given as examples of the shape-stabilization of PCMs by nanomaterials. In addition to nanoparticle-based shape-stable PCM nanocomposites, porous materials are also important materials to obtain efficient PCM composites due to their critical advantages such as superior absorption, large surface area and wide pore size distribution.

Shape-stable PCM composites have been created with porous carbon¹⁷¹⁻¹⁷³, graphite scaffolds¹⁷⁴⁻¹⁷⁶, polyurethane foams¹⁷⁷⁻¹⁷⁹ and silica scaffolds¹⁸⁰⁻¹⁸².

The last material group that can be considered for shape-stabilization of PCMs is clay minerals as they exhibit many critical parameters required for PCM systems. There are many studies that utilized clay minerals such as diatomite¹⁸³, sepiolite¹⁸⁴, bentonite¹⁸⁵, perlite¹⁸⁶, SiO₂¹⁸⁷, attapulgite¹⁸⁸, vermiculite¹⁸⁹, fly ash¹⁹⁰, zeolite¹⁹¹ and halloysite³² due to their natural porous structure, excellent absorbability, high thermal stability, thermal conductivity.

iii) Applications of shape-stabilized PCMs

The main ability of PCMs, which is to absorb and release heat in the form of latent heat during their phase transition process, has made them smart materials for thermoregulation or thermal management. The availability of PCMs with phase transitions at almost any temperature range made them favorable for various thermal management applications. As explained in this section, PCM-based systems have been subjected to countless scientific studies because of their unique application potential. Besides numerous scientific studies on PCMs, it is also possible to find different commercial products that can be examples of real applications of shape stable PCMs. These real-life applications can be exemplified as wallboards, blankets, and panels for buildings, textiles, thermal interface pads for electronic equipment, automotive industry, heat storage boards, heat pouches for therapeutic use, cooling vests, heat therapy packs and passive thermal control packaging¹⁹².

In conclusion, PCMs have great potential in latent heat energy storage. Moreover, PCM technology can contribute to solutions to vital environmental risks posed by fossil fuel-based

energy. For example, the combination of PCMs and solar harvesting materials have great potential for developing solar driven applications in a wide range such as cookers, water heaters and heat storage tanks. Thus, focusing on PCM systems and trying to overcome weak points of PCM-based materials as well as offering materials that are cheap, environmentally friendly and easily applicable to industrial productions can provide a crucial step to protect our earth and for sustainability.

1.3. Dissertation structure

This thesis is composed of a total of eight-chapters including a general introduction and conclusions chapters. Six interconnected chapters consist of four published and two unpublished journal articles. All chapters are presented with a journal article format involving an abstract, experimental, introduction, results and discussions and conclusions sections. All references have been merged under the "references" section.

A brief summary of each chapter is as follows:

Chapter 1: The dissertation overview, objectives, structure and general introduction to materials used in the thesis were presented.

Chapter 2: The study of halloysite nanotubes/polyethylene nanocomposites for active food packaging materials with ethylene scavenging and gas barrier properties were presented. Prepared HNT/PE nanocomposite films were investigated in terms of their fundamental mechanical and thermal properties for various HNT content in the nanocomposite films. Ethylene scavenging and gas barrier properties, as well as the effect of film samples on the freshness of different food products were studied.

Chapter 3: The study of thermally buffering polyethylene/HNT/PCM nanocomposite packaging films for cold storage of foods were presented. Nanohybrids of PCMs and HNTs were prepared and embedded into polyethylene matrix. Thermal buffering performance of prepared nanocomposite films was investigated on food samples. This work has generated the background of other PCM-based studies in this thesis.

Chapter 4: The study of purification and sorting of Halloysite Nanotubes into homogeneous, agglomeration-free fractions by PDA functionalization was presented. In this study, a new and a facile three-step separation protocol, that allows the sorting of HNTs into

agglomeration-free fractions was reported. Effect of varying agglomeration-states and particle sizes on surface functionalization yields, lumen loading capacity and reinforced polymer properties were investigated.

Chapter 5: The study of waterborne polyurethane/PDA photothermal polymer matrix for light to thermal energy conversion was presented. In this study, waterborne polyurethane particles synthesized in emulsion form was coated with PDA. Films cast from polyurethane/PDA dispersions were investigated in terms of their light to thermal energy conversion performances under solar and laser light irradiations. Furthermore, the polyurethane/PDA polymer matrix was studied in terms of its solar-driven water-evaporation properties to evaluate of the potential of these materials in solar-driven water purification applications.

Chapter 6: The study of improved latent heat storage properties through mesopore-enrichment of a zeolitic shape stabilizer was presented. In this study, siliceous ZSM-5 was used as a shape stabilizer for molecular and polymeric phase change materials and investigated in terms of its critical PCM parameters including latent heat storage performances, melting/solidifying enthalpies, transition temperatures, heat loss percentages and thermal behavior under sunlight. The knowledge acquired from this study has been a bridge between chapter 5 and chapter 7.

Chapter 7: The study on polyurethane/PDA/PEG photothermal form-stable phase change composite films was presented. In this study, a PCM was directly added into the polyurethane/PDA polymer matrix resulting in form-stable phase change films. In addition to their fundamental characterizations such as thermal, mechanical, morphological properties; form stability, thermal conductivity, reliability for repeated thermal application, melting/solidifying enthalpies, and transition temperatures of the PCM in the films were investigated. Developed phase change films were tested in terms of their thermal behavior under solar light irradiation and their thermoregulation properties.

Chapter 8: In this chapter, the overall conclusions were provided for all chapters and potential future studies were discussed.

CHAPTER 2: Halloysite Nanotubes/Polyethylene Nanocomposites for Active Food Packaging Materials with Ethylene Scavenging and Gas Barrier Properties

Reference Publication: Cüneyt Erdinç Taş, Saman Hendessi, Mustafa Baysal, Serkan Ünal, Fevzi Ç. Cebeci, Yusuf Z. Menceloglu and Hayriye Ünal, "Halloysite Nanotubes/Polyethylene Nanocomposites for Active Food Packaging Materials with Ethylene Scavenging and Gas Barrier Properties", *Food and Bioprocess Technology*, 2017, 10.4: 789-798.

2. 1. Abstract

Novel polymeric active food packaging films comprising halloysite nanotubes (HNTs) as active agents were developed. HNTs which are hollow tubular clay nanoparticles were utilized as nanofillers absorbing the naturally produced ethylene gas that causes softening and aging of fruits and vegetables; at the same time, limiting the migration of spoilage-inducing gas molecules within the polymer matrix. HNT/polyethylene (HNT/PE) nanocomposite films demonstrated larger ethylene scavenging capacity and lower oxygen and water vapor transmission rates than neat PE films. Nanocomposite films were shown to slow down the ripening process of bananas and retain the firmness of tomatoes due to their ethylene scavenging properties. Furthermore, nanocomposite films also slowed down the weight loss of strawberries and aerobic bacterial growth on chicken surfaces due to their water vapor and oxygen barrier properties. HNT/PE nanocomposite films demonstrated here can greatly contribute to food safety as active food packaging materials that can improve the quality and shelf life of fresh food products.

2. 2. Introduction

There exists an increasing demand for food products that can maintain their quality for a longer time to prevent economic losses and health issues caused by food spoilage. Although the treatment of food products with chemical preservatives prolongs the shelf life of food products, consumer preferences are strongly against such chemical treatments. Active food packaging systems which include materials that can interact with food offer a solution to this dilemma. Active components embedded into food packaging materials can remove undesired molecules causing spoilage, release molecules that can improve the quality of food, or regulate the atmosphere within the packaging environment for optimum conditions that retain the freshness and safety of the food.^{193,194}

One of the desired features of active food packaging materials designed for the storage of fruits and vegetables is the ethylene scavenging behavior. Ethylene is a plant hormone released by climacteric fruits which is associated with the ripening and aging of food products.¹⁹⁵ When not removed from the packaging headspace, the excess ethylene produced by the food leads to increased respiration rates resulting in senescence and shorter shelf life. Attempts to develop ethylene scavenging packaging systems include utilization of ethylene oxidizing materials such as potassium permanganate or metal catalysts immobilized on an inert substrate.^{1,2} These ethylene capturing materials are usually used in the form of sachets that are placed inside the packaging, but they find limited acceptance due to toxicity-based concerns and regulations against their food-contact applications. While there are some reported packaging products claiming ethylene scavenging properties based on finely dispersed minerals such as zeolites, clays, and Japanese oya incorporated into films,^{196,197} there are no or limited scientific studies reporting their direct ethylene absorbing capacities and their effects on food samples.

Another objective of active food packaging is the development of packaging materials that demonstrate limited permeability against gases such as oxygen, carbon dioxide, and water vapor, thus extend the quality and shelf life of packaged products. While multilayer polymer films and direct polymer blending ensures desired barrier properties, higher production costs and problems associated with recycling limit economically viable utilization of these films. On the other hand, polymer nanocomposites prepared by the dispersion of nanofillers within

a polymer matrix provide a viable option for preparing packaging materials with barrier properties. Nanoparticles such as clay and silicate nanoparticles that are intrinsically impermeable to gases create a torturous path for gas molecules and inhibit their diffusion throughout the matrix.^{198,199} Studies on polymer/clay nanocomposites with barrier properties mostly focused on montmorillonite (MMT) nanoclay which has been demonstrated to result in nanocomposites with reduced gas permeability.^{3,200-203} However, strong hydrophilic character and natural, platy, nanolayered structure of MMT mostly requires chemical organo-modifications or the use of compatibilizers to improve their compatibility with low surface energy polymers such as polyolefins which are mostly the choice of polymeric matrix for food packaging applications.

In this work, we utilized halloysite nanotubes (HNTs) to prepare nanocomposites of polyethylene as food packaging materials demonstrating both ethylene scavenging and barrier properties. HNTs are natural aluminum silicate nanoparticles presenting hollow tubular nanostructures. While their nanoscale lumens feature HNTs as multifunctional nanoparticles for drug delivery and controlled release studies,^{14,204-206} their relative low cost compared with other tubular nanostructures such as carbon nanotubes and large abundance render them appropriate nanofillers for polymeric nanocomposite applications. The fact that HNTs possess a lower surface charge due to the presence of siloxane groups on the outer surface renders them relatively hydrophobic and more compatible with low surface energy polymers eliminating the need for intercalation or exfoliation.³⁵ Incorporation of HNTs into polymeric matrices have been studied not only with the aim of obtaining active agent releasing films or coatings^{204,207-209} but also to benefit from the reinforcing abilities of HNTs as clay nanoparticles to improve physical properties of polymers such as mechanical strength, thermal stability, and fire retardancy.⁹ Here, we studied for the first time ethylene adsorption capacities and barrier properties of HNT/polyethylene (HNT/ PE) nanocomposites to obtain food packaging films that can improve the quality and shelf life of perishable food products such as fruits, vegetables, and meats. While HNTs incorporated into PE matrix as hollow clay nanoparticles act as adsorbents that remove the naturally produced ethylene gas from the packaging headspace and slow down reactions leading to spoilage of fruits and vegetables, they also provide a torturous path for the migration of gases such as oxygen and water vapor further retaining the freshness of food products packaged with HNT/PE nanocomposites.

2.3. Materials and Methods

2.3.1. Preparation of HNT/PE nanocomposite films

Low-density PE (LDPE) granules (PETİLEN F2-12: density at 23 °C, 0.918–0.920 g cm⁻³; melt flow rate (190 °C 2.16 kg⁻¹), 2.1⁻³ g 10 min⁻¹; film quality (ASTM D-1238), A) were supplied from PETKİM Petrokimya A.Ş. They were used as received and dried at 70 °C overnight before compounding. HNTs mined from reserves in Balıkesir, Turkey was kindly provided by ESAN Eczacıbaşı, Turkey, as purified and pretreated by ball mill homogenization to reduce their agglomerate sizes approximately to 65 µm. Mixtures of HNTs and LDPE granules prepared at desired ratios were fed into a twin-screw extruder (Zamac, Mercator) with a screw diameter of 12 mm and L/D ratio of 40 and processed at 165–185 °C (650 rpm). Nanocomposites emerging from the extrusion die were cooled in a water bath and pelletized. Subsequently, nanocomposites were blown into 55–60-µm-thick films using a single screw extruder (Scientific Laboratory Ultra Micro Film Blowing Line Type LUMF-150 with LE8-30/C, LabTech Engineering) at 150–160 °C, at a screw speed of 80 rpm. Thicknesses of films were determined using a digimatic micrometer (Mitutoyo Quicmike, no. 99MAB041M).

2.3.2. Imaging of HNTs and HNT/PE nanocomposites

Transmission electron microscopic (TEM) analysis of HNTs was performed using JSM-2000FX (JEOL, Japan) at an operating voltage of 160 kV, using a 200-mesh copper grid (Formvar film).

Scanning electron microscopy (SEM) analysis of HNT/PE nanocomposite films were performed using LEO Supra 35VP Scanning Electron Microscopy on cryofractured surfaces of impact specimens at an acceleration voltage of 15 kV and under high vacuum. A thin layer of gold was sputter-coated onto the fractured surface to avoid charging on exposure to electron beam during SEM analysis.

2.3.3. Thermal characterization

Thermal stability and HNT content of nanocomposite films were determined by thermogravimetric analysis (TGA) on a DTG-60H (Shimadzu, USA) instrument. Samples of HNT/PE nanocomposites weighing approximately 20 mg were heated in an alumina pan from 30 to 800 °C at a rate of 10 °C min⁻¹ under nitrogen flow. Resulting temperature-dependent weight loss percentages were analyzed using TA-60WS Collection software.

Differential scanning calorimetry (DSC) analysis was carried out with a TA Q2000 (TA Instruments, USA) instrument under nitrogen atmosphere. Samples were heated from 30 to 190 °C at a heating rate of 10 °C min⁻¹ to eliminate any previous thermal history, and then cooled to 30 °C at a cooling rate of 10 °C min⁻¹. Samples were heated again to 190 °C at a heating rate of 10 °C min⁻¹. On the basis of recorded DSC thermograms, melting temperature (T_m), crystallization temperature (T_c), heat of fusion (ΔH_m), and relative degree of crystallinity (X_c) were determined. X_c was calculated by using the Eq. 1,

$$X_c = \Delta H_m^{\circ} / \Delta H_m (1 - w_t), \quad Eq. 1$$

where ΔH_m is the specific melting heat, calculated by the integration of the area under the crystallization peak, ΔH_m° is the theoretical specific melting heat of 100% crystalline PE, which is taken as 293 J g⁻¹,²¹⁰ and w_t is the weight fraction of HNTs.

2.3.4. Mechanical characterization

Mechanical properties of HNT/PE nanocomposite films were tested on a universal testing machine Zwick Roell Z100 UTM, with a load cell of 200 N and a crosshead speed of 12.5 mm min⁻¹ according to the testing method determined by ASTM D1708–10, the standard test method for tensile properties of plastics by use of micro-tensile specimens. Dog-bone test specimens had an overall length of 38 mm, overall width of 15 mm, narrow section width of 5 mm, and grip distance of 22 mm. An average of at least five replicates of each sample was reported.

2.3.5. Characterization of ethylene scavenging properties

Adsorption experiments were performed by using Hiden Isochema Intelligent Gravimetric analyzer (IGA-003) with ethylene gas. The IGA has a fully automatic microbalance system

that allows the direct measurement of the weight change of HNT, PE, and HNT/PE nanocomposites as a function of time, gas pressure, and the sample temperature. The long-term stability of microbalance is 0.1 µg with a weighing resolution of 0.2 µg and temperature stability of 0.2 °C. Approximately, 50 mg of sample was placed in a stainless-steel reactor and sealed.

Before introducing ethylene, gas flow samples were outgassed at 80 °C for 24 h under 10^{-6} mbar vacuum. For ethylene adsorption on HNTs and HNT/PE nanocomposite films, 1-h maximum equilibrium time was adjusted, and linear driving force mass transfer model was used as computer control prediction to get asymptotic uptake of ethylene at room temperature for every pressure point up to 1 bar, with 100 mbar intervals. The density of HNT/PE nanocomposites and HNT were taken as 0.91 and 2.59 g cm⁻³, respectively.

2.3.6. Characterization of barrier properties

Oxygen transmission rate (OTR) of HNT/PE nanocomposite films were evaluated by using Labthink TOY-C2 Film- Package Oxygen Permeability Tester (designed in accordance with ASTM D3985, ASTM F1307, and ASTM F1927). The oxygen gas permeability tests were performed at 25 °C and 0% RH conditions by using high-purity nitrogen gas as carrier gas (purity, >99.999%) and high-purity oxygen gas as testing gas (purity, >99.9%). Water vapor transmission rate (WVTR) of HNT/PE nanocomposite films were determined by using Labthink TSY-T3 Water Vapor Permeability Tester (designed in accordance with ASTM E96 and ASTM D1653). Measurements were performed at 38 °C with 90% relative humidity.

2.3.7. Experiments on food samples

Banana, tomato, and strawberry samples were collected from local markets and selected to be free of visual defects and uniform in terms of weight/shape. They were packaged with nanocomposite and control films using a thermal bag sealer, stored at room temperature for a set period of time.

A set of five bananas were packaged with each film (nanocomposite and control), resulting in approximately 20 × 10- cm packages. Packaged banana samples along with a set of bananas that were not packaged were photographed every day to determine the changes in their appearances and color until bananas in the control set appeared to be overripe.

A set of five tomatoes were packaged with each film (nanocomposite and control), resulting in approximately 10×10 - cm packages. Samples were stored until the tomatoes in the control set appeared to lose their firmness. The firmness of tomatoes was determined using a penetrometer (Model GY3) equipped with an 8-mm probe which measures the force required to penetrate into the pared tomato. Firmness values were reported as an average of five measurements obtained from individual tomatoes.

A set of five strawberries were packaged with each film (nanocomposite and control), resulting in approximately 5×5 -cm packages. Weight loss of strawberries packaged with nanocomposite and control films were determined by weighing them every day and determining the ratio of the weight of the sample to the initial weight until strawberries in the control set appeared to lose their integrity. Weight loss values were reported as the mean of five measurements obtained from individual strawberries.

Chicken samples were collected from a local butcher shop and were cut into 3×3 -cm pieces that weigh approximately 8 g. Oxygen barrier properties of prepared nanocomposite films were determined by measuring the total aerobic count on surfaces of cut chicken samples packaged with nanocomposite films and control neat PE films. A set of six cut chicken samples were packaged with each film (nanocomposite and control film) resulting in approximately 6×6 -cm packages and were stored at 4°C . The initial total aerobic count was determined on three samples that were not packaged with any films. At the end of 24- and 48-h time periods, three samples from each set were unpacked and the total aerobic count was measured. Bacteria on the chicken surface were collected with a moistened sterile cotton swab and released into 1 mL sterile phosphate buffer by vortexing for 30 s. Bacterial suspensions were then serially diluted and plated onto tryptic soy broth agar. Plates were incubated at 30°C for 24 h followed by colony counting.

2.3.8. Statistical analysis

Results were expressed as mean \pm standard error of at least three replicates. Statistical significance of differences between means was assessed by one-way ANOVA with Tukey's test at a confidence level of $p < 0.05$ using OriginPro software v.8.5. (OriginLab Corporation, USA).

2.4. Results and Discussion

2.4.1 Structural, thermal, and mechanical properties of HNT/PE nanocomposite films

HNTs that were utilized for nanocomposite preparation were supplied in the form of 65- μm -sized agglomerates, which individually demonstrated hollow, open-ended structures with diameters of 15–40 nm and lengths of 200–1000 nm as shown in representative TEM images (Figure 10 A, B). HNT/PE nanocomposite films loaded with 1, 3, and 5 wt.% HNTs were prepared by melt compounding the HNT powder and PE granules using a twin-screw extruder followed by blown film extrusion. Cryocut cross-sections of nanocomposite films were investigated by SEM. Nanocomposites prepared at 1 wt.% HNT loading presented a homogeneous distribution of finely dispersed HNTs (Figure 10 C, D). At 5 wt.% HNT loading, in addition to finely dispersed HNTs, larger aggregates of HNTs were also visible (Figure 10 E, F). Apparently, at higher loadings, the dispersion quality of HNTs within the PE matrix diminished resulting in larger HNT aggregates.

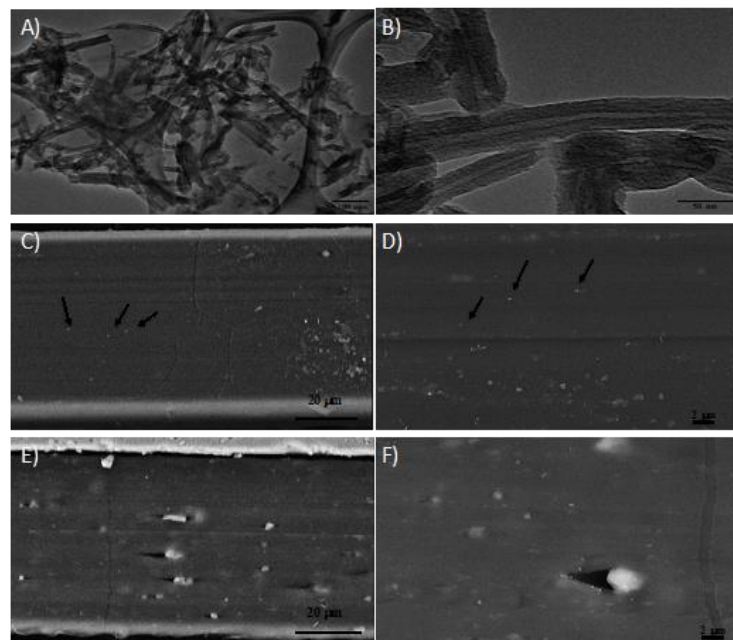


Figure 10. (A, B): TEM images of HNTs at different magnifications; (C, D): SEM images of HNT/PE nanocomposites loaded with 1 wt % HNTs; (E, F): SEM images of HNT/PE nanocomposites loaded with 5wt%.

Prepared HNT/PE nanocomposite films were tested for their thermal stability and HNT content using thermogravimetric analysis. Temperature-dependent weight loss curves of nanocomposite films obtained under inert atmosphere were analyzed by comparing temperatures at which 10% weight loss (T_{0.1}) and maximum weight loss (TD) were observed. Table 1 demonstrates that the nanocomposite film containing 1 and 3 wt.% HNTs have thermal decomposition temperatures that are similar to the thermal decomposition temperature of the neat PE film (less than 0.8% relative difference in TD). An improvement in thermal stability as mostly seen in other clay polymer nanocomposites at similar clay nanoparticle loadings²¹¹⁻²¹³ was not observed. HNTs which are inferior insulators for heat transfer compared with other silicate nanolayers due to their tubular structure²¹⁴ did not introduce a stabilizing effect to the polymer matrix at this low loading ratio, but rather, the thermal stability of the PE was retained. Only when the HNT content was increased to 5 wt.% that a slight destabilization of the polymer matrix was observed (2.1% relative decrease in TD). Probably, at 5 wt.% HNT loading, the dispersion of HNTs was less uniform due to aggregation of nanoparticles which disfavored the entrapment of volatile products, thus facilitated the degradation of the PE matrix. Another potential reason for the destabilization at higher HNT loading might be the known catalytic effect of clay nanoparticles on the degradation of polymers at higher loadings.^{215,216} The weight percentage of char at 800 °C corresponds to the amount of remaining HNTs in the nanocomposite as PE matrix itself presents almost a total weight loss at this temperature. While the char percentage increased with the HNT loading of the nanocomposite as expected, values varied slightly from theoretical char yields that were calculated according to char contents of individual nanocomposite components at 800 °C. For the nanocomposite containing 1 wt.% HNTs, the actual char yield was higher than the theoretical value, indicating a hindrance of the escape of polymer degradation products due to well-dispersed HNTs. For larger HNT loadings such as 3 and 5 wt.%, the opposite was valid where measured char content was lower than theoretical values, indicating a less-uniform dispersion of HNTs within the PE matrix. Thus, results of TGA studies indicated that 1 wt.% HNT loading is optimal to obtain thermally stable HNT/PE nanocomposites with well-dispersed HNTs.

Table 1. Thermal stability parameters of PE and HNT/PE nanocomposites.

	T _{0.1} (°C)	T _D (°C)	% char at 800°C TGA analysis	% char at 800°C theoretical
PE	441	473	0.28	-
HNT/PE 1%	440	474	1.71	0.78
HNT/PE 3%	439	477	1.71	2.34
HNT/PE 5%	435	463	3.40	3.9

Thermal properties of prepared nanocomposite films were further studied with differential scanning calorimetry (DSC). Calorimetric parameters of neat PE along with HNT/PE nanocomposites are summarized in Table 2. While melting and crystallization temperatures were not affected by the HNT loading, crystallization enthalpies and percent crystallinity values were dependent on the HNT loading. It was shown that the crystallinity value for the HNT/PE nanocomposite film containing 1 wt.% HNT was higher than the crystallinity of neat PE film, whereas, for HNT loadings of 3 and 5 wt.%, crystallinity values presented a decreasing trend. While 1 wt.% HNT loading provided a nucleating effect that induced crystallization of the PE chains as seen in similar cases with HNT/polymer nanocomposites,²¹⁷⁻²¹⁹ at higher loadings, a decreased quality in the state of HNT dispersion within the PE matrix was expected to lead to the loss of nucleation efficiency. Similar trends were reported previously for HNTs and nanoparticles acting as nucleating agents in semi-crystalline polymers in general.^{218,220} Similar to results obtained from thermal stability experiments, 1 wt.% HNT loading was demonstrated to be optimal for improved crystallinity, which is expected to improve the gas barrier properties of nanocomposite films.

Table 2. Calorimetric parameters of PE and HNT/PE nanocomposite films obtained from the second heating cycle.

	T_m (°C)	ΔH_m (J g ⁻¹)	T_c (°C)	ΔH_c (J g ⁻¹)	%crystallinity
PE	102.69 ± 0.49 a	36.04 ± 0.88 a	97.73 ± 1.03 a	45.36 ± 1.71 a	15.48 ± 1.43 a,b
HNT/PE 1%	103.73 ± 0.50 a	39.11 ± 1.40 b	98.33 ± 0.02 a	54.44 ± 1.38 b	18.58 ± 0.96 c
HNT/PE 3%	103.46 ± 0.43 a	35.21 ± 1.80 a, c	98.34 ± 0.62 a	49.78 ± 1.35 c	16.99 ± 0.46 a
HNT/PE 5%	103.86 ± 1.16 a	33.16 ± 1.50 c	98.05 ± 0.07 a	45.67 ± 1.37 a, c	15.59 ± 0.47 b

Values sharing a common letter (a-c) within the same column are not significantly different

Mechanical properties of HNT/PE nanocomposite films were also characterized. Figure 11 demonstrates that HNT/PE nanocomposite films containing 1, 3, and 5 wt.% HNT did not have significant variations in mechanical properties compared with neat PE films. A distinct effect in Young's modulus, tensile strength, and elongation at break values as a function of the HNT loading ratio was not observed ($p > 0.05$). While HNTs have been previously reported as reinforcing agents improving the mechanical properties of some polymers,²²¹⁻²²³ nanocomposites of HNTs and high-density PE were reported to have no improvement in mechanical properties when compatibilizers were not used.²²⁴ The fact that the incorporation of HNTs did not introduce any mechanical deterioration at tested loading ratios is important since nanocomposite films obtained in this work were as durable as neat PE, which meets mechanical property requirements for use as food packaging materials.

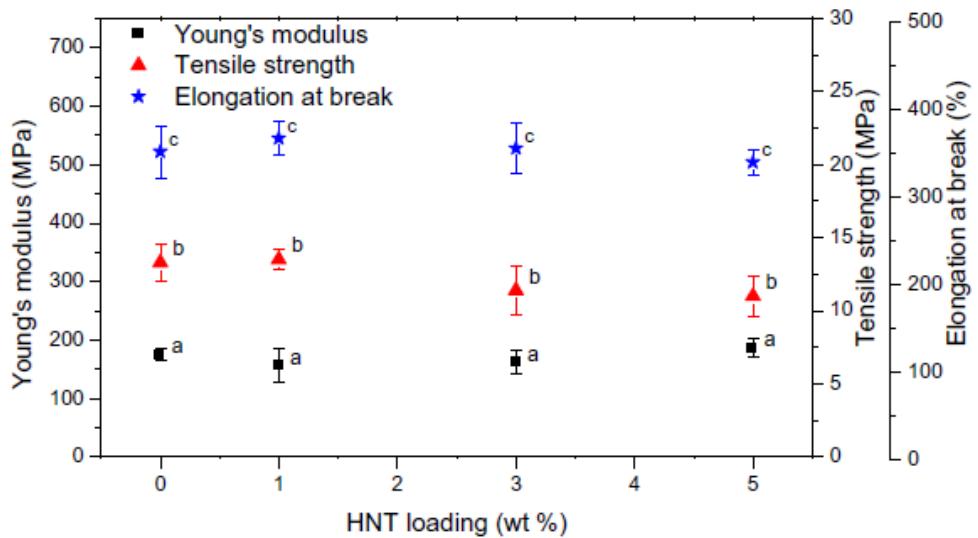


Figure 11. Mechanical parameters of 500 HNT/PE nanocomposite films at varying HNT loadings. Values in the same group sharing a common letter are not significantly different.

2.4.2 Ethylene scavenging properties of HNT/PE nanocomposite films

Ethylene scavenging properties of HNT/PE nanocomposite films were analyzed in order to evaluate the potential of these films for utilization as food packaging films that improve the shelf life of fruits and vegetables. The ethylene scavenging capacity of HNTs was determined by static sorption experiments conducted on a gravimetric microbalance system through a generation of ethylene sorption isotherms at room temperature. Following a 24-h degassing of HNTs, ethylene gas was introduced at set pressures and the weight gain that occurs due to ethylene adsorption was measured. Figure 12 depicts ethylene adsorption isotherms for HNTs and HNT-loaded PE films. As seen in Figure 12a, at 1 bar pressure, HNTs can adsorb up to 0.75 wt.% ethylene gas which corresponds to 6.36 mL of ethylene gas adsorption per each gram of HNTs. Apparently, the hollow structure of HNTs along with their large aspect ratio allowed the adsorption of ethylene gas in large amounts. This result demonstrated that HNTs have a larger ethylene adsorption capacity than some other ethylene adsorbing agents that were previously reported in the literature (4.16 mL g^{-1} ; palladium promoted ethylene scavengers)¹ or currently available on the market (3 mL g^{-1} ; Sensitech Ryan®). To evaluate the effect of HNTs as ethylene-adsorbing nanofillers within a polymer matrix, the ethylene

adsorption capacity of HNT/PE nanocomposite films was determined in comparison with neat PE films. Figure 12b demonstrates that nanocomposite films containing 5 wt.% HNTs had a 0.067% ethylene adsorption capacity at 1 bar pressure which corresponds to 0.56 mL ethylene adsorption for 1 g of food packaging film. Considering that ethylene gas release from most climacteric fruits and vegetables is in the range of 1–100 mL kg⁻¹ h⁻¹,²²⁵ prepared nanocomposite films are expected to have the ability to remove naturally produced ethylene gas from packaging headspace and improve the shelf life of fresh produce. HNT/PE nanocomposite films demonstrated larger ethylene adsorption capacity than neat PE films under the same adsorption conditions, indicating that ethylene scavenging properties were significantly enhanced by HNTs. At 1 mbar pressure, the presence of 5 wt.% HNTs improved the ethylene adsorption capacity of PE films by 20% which is a significant improvement considering parts per million level of ethylene sensitivity of fruits and vegetables.

Ethylene scavenging properties of HNT/PE nanocomposite films were evaluated on banana samples. Ripening processes of bananas are known to be highly dependent on the ethylene gas secreted by bananas where the ethylene gas allows green bananas to turn yellow and dark brown as they ripen.²²⁶ Thus, food packaging films that can capture the ethylene gas present in the headspace can slow down the ripening of bananas. Figure 13a presents photographs of bananas packaged with HNT/PE nanocomposite films containing 5 wt.% HNTs in comparison with bananas that were not packaged and bananas that were packaged with neat PE films taken at the beginning and at the end of an 8-day-long incubation period at room temperature. While unpackaged bananas and bananas packaged with the neat PE film turned yellow and developed several brown spots, bananas packaged with HNT/PE films revealed a significant difference where they stayed free of brown spots and retained their green color. Apparently, HNT/PE film slowed down the ripening of banana by adsorbing the ethylene gas secreted by the banana to a higher extent than the neat PE film.

Like bananas, tomatoes are also climacteric fruits for which the postharvest ripening occurs via the produced ethylene gas. Thus, the ripening of packaged tomatoes as measured by the firmness of fruit samples is highly dependent on whether the ethylene gas produced by tomatoes can be removed from the headspace by the packaging material. Figure 13b demonstrates the firmness of tomatoes wrapped with neat PE film and HNT/PE nanocomposite film containing 5 wt.% HNTs after 10 days of incubation at room temperature

in comparison with the initial firmness of tomatoes. While tomatoes wrapped with neat PE film lost initial firmness by 72% on average at the end of 10 days, tomatoes wrapped with HNT/PE nanocomposites mostly retained their firmness where their firmness decreased by only 16%. At the end of this 10-day time period, control tomato samples that were not wrapped with any films were deteriorated and their firmness was not measurable. Thus, HNT/PE films were demonstrated to be effective ethylene scavenging food packaging materials that can improve the shelf life of packaged tomatoes as well.

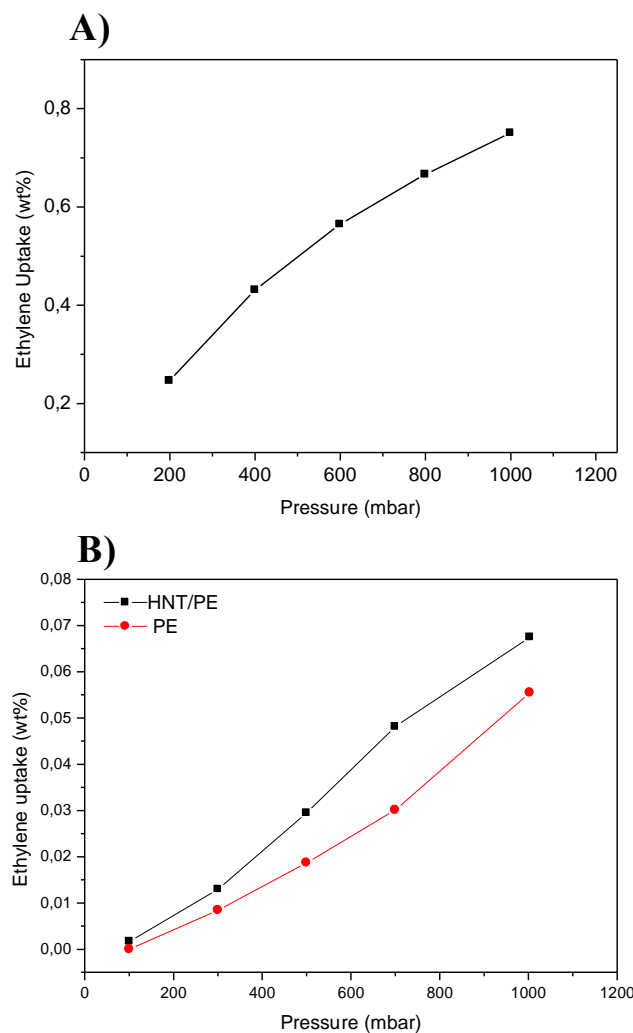


Figure 12. Ethylene adsorption isotherms of HNTs (a) and PE and HNT/PE (5 wt.% HNT) films (b) as generated by gravimetric analysis.

Experiments on tomato firmness and banana ripeness were also repeated with HNT/PE nanocomposite films containing 1 wt.% HNTs but results that are not significantly different than neat PE films were obtained (data not shown). The additional ethylene scavenging capacity provided by 1 wt.%HNTs was not significant enough. Although structural and thermal characterization of HNT/PE nanocomposite films demonstrated that 5 wt.% HNT content resulted in poorer quality in terms of dispersion of nanoparticles within the polymer matrix, apparently, this ratio was not disadvantageous in terms of the ethylene scavenging capacity of nanocomposite films; instead, it was critical to provide the necessary ethylene scavenging environment to improve the shelf life of bananas and tomatoes.

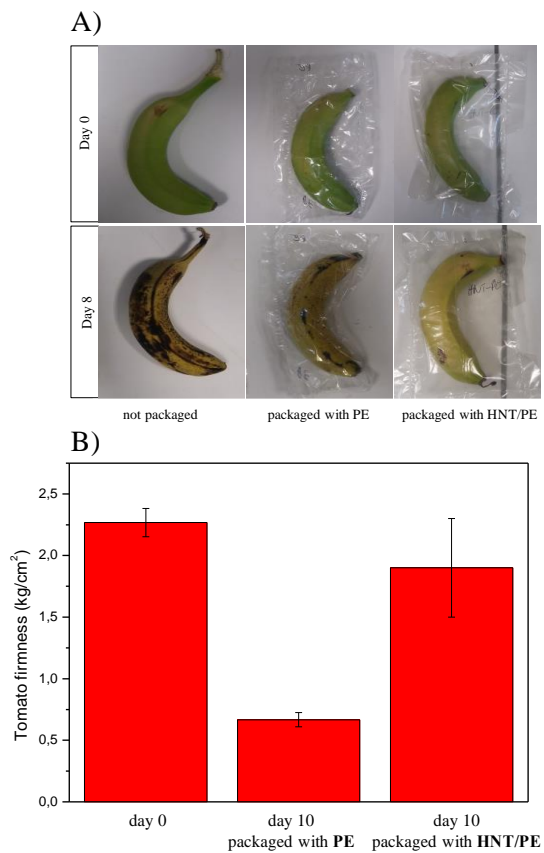


Figure 13. a Photographs of banana samples packaged with PE films and HNT/PE films containing 5 wt.%HNTs. *b* Firmness of tomato samples packaged with PE films and HNT/PE films containing 5 wt.% HNTs. Values sharing a common letter are not significantly different.

2.4.3 Gas barrier properties of HNT/PE nanocomposite films

Barrier properties of HNT/PE nanocomposites were determined by measuring the OTR and WVTR of prepared films (Figure 14). OTR and WVTR values were expected to decline due to the presence of nanofillers as they create a torturous path for the diffusion of gas molecules. When PE matrix was loaded with 1 wt.% HNTs, resulting nanocomposite films demonstrated 22% and 32% decrease in OTR and WVTR, respectively. Increased HNT loading did not improve barrier properties; conversely, nanocomposite films containing 5 wt.% HNTs presented significantly higher oxygen and water permeability compared with neat PE films. While at low HNT loadings well-dispersed HNTs acted as barriers slowing down the diffusion of gas molecules, at higher loadings, aggregates of HNTs formed voids within the film that allowed the fast permeation of gases and overcame the barrier effect. Furthermore, the hydrophobic nature of HNTs might also have caused increased water vapor permeability of HNT/PE nanocomposite films at higher HNT loadings. Similar to results obtained pertaining to nanocomposite films with optimum mechanical and thermal properties, 1 wt.% HNT loading was found to be optimum to obtain food packaging films with the highest barrier properties against oxygen and water vapor.

Oxygen barrier properties of HNT/PE nanocomposite films were evaluated indirectly by measuring the aerobic bacterial growth on chicken surfaces packaged with these films. Aerobic bacterial growth on packaged food depends highly on the oxygen concentration within the packaging headspace and can be inhibited by packaging materials with oxygen barrier properties. Figure 15 demonstrates total aerobic plate count per unit surface area of chicken samples packaged with HNT/ PE nanocomposite films prepared with 1 wt.% HNTs and neat PE films measured after incubation at 4 °C for different time periods. Chicken samples packaged with HNT/PE nanocomposite films presented significantly lower total aerobic count than chicken samples packaged with control films both after 24- and 48-h incubation. Limited oxygen concentration within the packaging headspace inhibited the growth of bacteria on packaged chicken samples. This result demonstrated that prepared HNT/PE nanocomposites with enhanced oxygen barrier properties can be utilized as food packaging materials for food samples that will stay safer in environments with limited oxygen concentration.

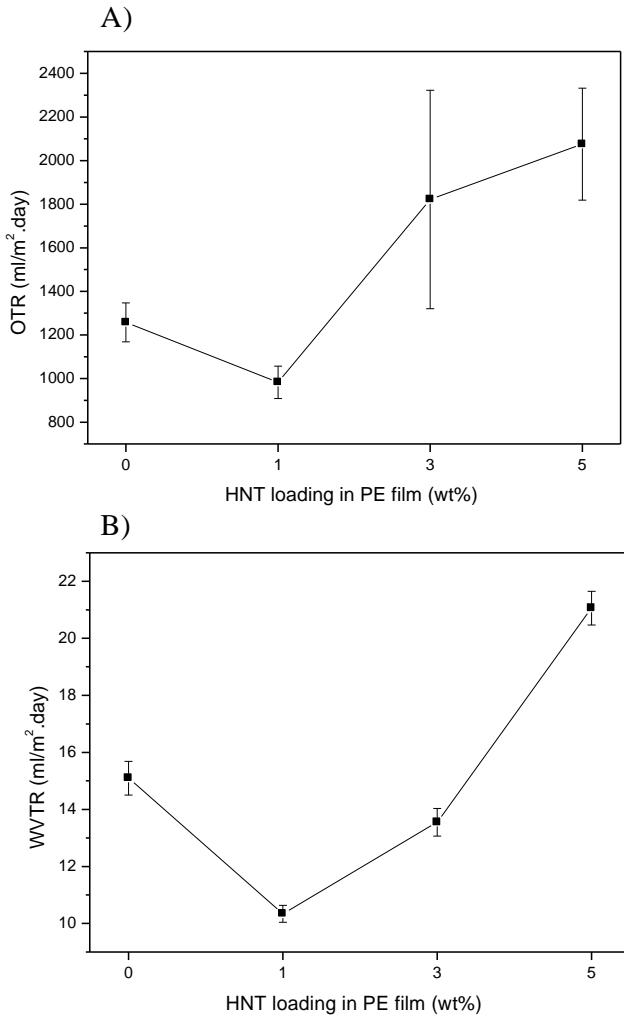


Figure 14. Oxygen transmission rate (OTR) (a) and water vapor transmission rate (WVTR) (b) of nanocomposite films at different HNT loading ratios. Values sharing a common letter are not significantly different.

As a demonstration of water vapor barrier properties of HNT/PE nanocomposite films, time-based water loss of strawberry samples packaged with HNT/PE films and neat PE films were determined. Strawberries are highly perishable fruits, and one of the indices determining the fruit quality during storage is the amount of weight loss that occurs due to transpiration. Packaging materials presenting limited permeability against water vapor allow strawberries to retain their weight during storage. Figure 16 demonstrates that at the end of day 6, strawberries packaged with HNT/PE nanocomposite films containing 1 and 5 wt.% HNTs presented 53% and 31% lower weight loss than strawberries packaged with neat PE film,

respectively. The presence of HNTs dispersed within the PE matrix inhibited the diffusion of water vapor through the packaging film; thus, loss of strawberry humidity was prevented to a larger extent. The relationship between HNT loading and water vapor barrier properties obtained by WVTR measurements of films was regenerated by the strawberry weight loss experiment where nanocomposite films containing 1 wt.% HNTs presented better water vapor barrier properties than nanocomposite films containing 5 wt.% HNTs. HNT/PE nanocomposite films were shown to be effective food packaging materials for food samples that require water vapor barrier packaging for improved shelf life.

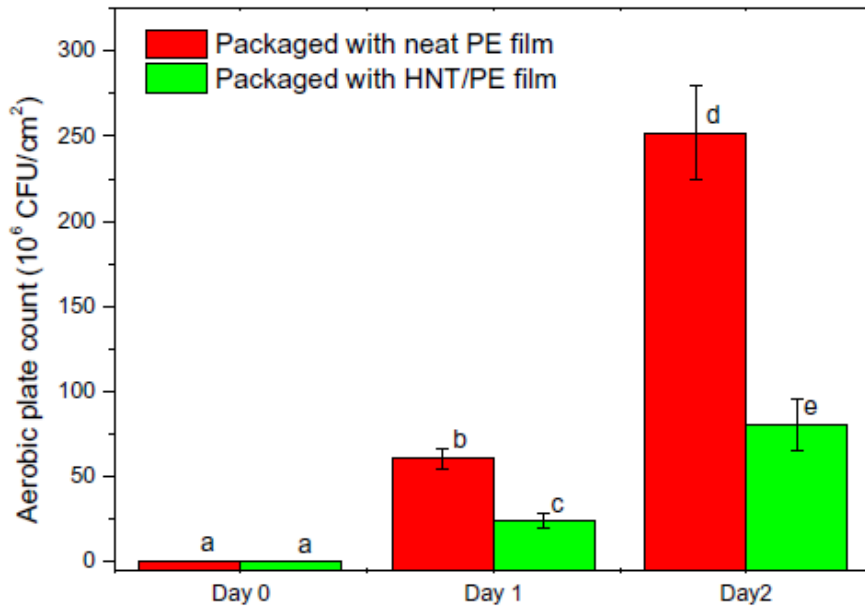


Figure 15. Total aerobic count on chicken surfaces packaged with neat PE films (red) and HNT/PE nanocomposite films loaded with 1 wt.% HNTs (green). Values sharing a common letter are not significantly different.

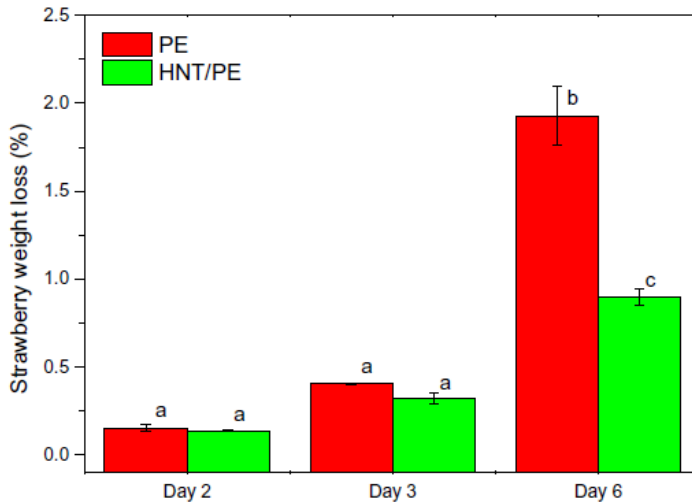


Figure 16. Time-based weight loss of strawberries packaged with neat PE films (red) HNT/PE films loaded with 1 wt.% HNTs (green). Values sharing a common letter are not significantly different.

2. 5. Conclusions

Nanocomposite films of HNTs and PE were prepared as potential active food packaging materials. While incorporation of HNTs significantly increased the ethylene adsorption capacity of PE films, it also introduced a tortuous path for the diffusion of oxygen and water vapor, which slowed down processes that lead to senescence of food products. Prepared HNT/PE films with 5 wt.% HNT content were shown to present optimal ethylene scavenging capacity as demonstrated by improved shelf life of bananas and tomatoes packaged with these films. Furthermore, HNT/PE films with 1 wt.% HNT content presented optimal oxygen and water vapor barrier properties as demonstrated by the improved shelf life of strawberries and fresh-cut chicken samples packaged with these films. Utilization of HNTs as natural, nontoxic, and cost-effective nanofillers were shown to result in potentially multifunctional active food packaging materials that can greatly contribute to food safety.

CHAPTER 3: Thermally Buffering Polyethylene/Halloysite/Phase Change Material Nanocomposite Packaging Films for Cold Storage of Foods

Reference Publication: Cüneyt Erdinç Taş and Hayriye Ünal, ‘‘ Thermally buffering polyethylene/halloysite/phase change material nanocomposite packaging films for cold storage of foods’’, *Journal of Food Engineering*, 292, (2021), 110351.

3. 1. Abstract

Controlling temperature fluctuations during storage and transportation of cold chain food products is pivotal in maintaining food safety and food quality. Here, nanocomposite flexible food packaging films that prolong the time that frozen or chilled food products stay cold are demonstrated. Nanohybrids of phase change materials (PCMs) and halloysite nanotubes (HNTs) were utilized as nanofillers with thermal buffering performance. Halloysite nanotubes (HNTs) were impregnated with PEG400 and PEG600 at 30 wt. % without leakage resulting in a mixture of nanohybrids that present consecutive melting transitions in the temperature range of -22°C to 22°C. Resulting nanohybrids were demonstrated to be thermally reliable over 21 cycles and heat stable at melt processing conditions required for polymeric nanocomposite applications. Incorporation of the mixture of HNT/PEG400 and HNT/PEG600 nanonybrids into polyethylene (PE) matrix by melt compounding resulted in flexible nanocomposite films of approximately 60 µm thickness that have acceptable mechanical properties for use in food packaging applications and present a broad melting transition from -17°C to 26°C with a latent heat of 2.3 J/g. Due to their temperature buffering capacity, the rate of thawing of frozen nanocomposite films at room temperature was more than two times lower than the rate of thawing of neat PE films. Frozen meat samples packaged with nanocomposite films reached 4°C 18 minutes later than samples packaged with standard PE films. Similarly, nanocomposite films delayed the warming of chilled samples for 20 minutes relative to neat PE films. Nanocomposite films composed of PCM

impregnated HNTs demonstrated here are the first examples of flexible food packaging films with significant thermal buffering capacity in cold chain temperatures and have a great potential to enhance food quality and food safety in cold-chain storage and transportation.

3.2. Introduction

1.3 billion tonnes of food, which corresponds to one-third of global food production is wasted annually all over the world according to estimates of Food and Agricultural Organization of United Nations^{227,228}. While most of the food waste occurs at the production and consumer levels, problems encountered during cold chain transportation of perishable and high-value food products also cause significant economic loss and risks in terms of food safety. As most of the processes that lead to loss of the food freshness including microbial growth²²⁹ or release of spoiling molecules such as ethylene from foods¹⁹⁵ are accelerated at higher temperatures, many food products require transportation under refrigerating, chilling or freezing conditions to ensure food safety and food quality.

Microbiological activity in foods slows down at temperatures below 8°C^{230,231}, therefore keeping the storage temperature below 8°C is crucial for cold chain transportation²³². Specifically, food products such as meat and fish are preferentially transported either frozen at temperatures below 0°C or chilled at temperatures of 1-2°C²³³. However, in the case of a short-term or long-term cold chain failure, temperature fluctuations can cause deterioration of the food product. Storage solutions that slow temperature increases in cold foods in the case they are exposed to higher temperatures, can counteract temperature fluctuations and significantly decrease the amount of food lost during cold chain transportation^{234,235}. While standard polymeric food packaging materials play an effective role in protecting foods against external influence due to their unique properties such as gas barrier, mechanical strength and durability²³⁶, they are mostly limited in terms of their thermal insulation capacity and they do not provide any protection against thermal fluctuations in food products during cold chain transportation except they are utilized as secondary packaging. Polymeric food packaging materials that are designed to have thermal buffering and temperature regulating properties can serve as a safety assurance in cold storage of perishable foods.

Phase change materials (PCMs) are substances that absorb and release large amounts of latent heat during their melting/solidifying transitions. PCMs have been used in many heat storage-related applications due to their large energy storage capacity, chemical stability, and low cost^{125,237,238}. By using different PCMs such as fatty acids²³⁹, paraffins²⁴⁰, salt hydrates²⁴¹ and polymeric materials²⁴², shape-stable PCM composites can be prepared via different strategies like encapsulation²⁴³ or impregnation methods²⁴⁴. Although PCMs have been generally utilized in latent heat storage applications²⁴⁵, their energy absorption capacities can also be utilized to improve the thermal buffering capacity of food packaging materials to prolong the time it takes the chilled food to reach the ambient temperature. There have been limited number of distinctive studies on the utilization of PCMs to keep food products cold in the literature. These studies involved utilization of composites of PCMs in the form of refrigerator panels²⁴⁶⁻²⁴⁸, insulator bags and containers²⁴⁹⁻²⁵², trays²⁵³, foams²⁵⁴ and bubble wrap liners²⁵⁵. However, there have not been any studies that focused on composites of PCMs in the form of flexible packaging films. Flexible packaging films with temperature buffering properties that are cost-effective and easily applicable to industrial manufacturing processes can effectively provide protection for perishable foods requiring cold chain transportation.

Here we studied for the first time the incorporation of shape stable PCMs into nanocomposite flexible films to obtain packaging materials with thermal buffering capacity at cold chain temperatures. Halloysite nanotubes (HNTs), which are aluminum silicate nanoparticles with hollow tubular nanostructures, were chosen as shape stabilizing agents for the encapsulation of PCMs. due to their considerable advantages such as low cost compared to other tubular structures, availability in abundance and compatibility with low surface energy polymers²⁵⁶. The objective of this study was impregnation of HNTs with multiple polyethylene glycol PCMs with melting transitions at cold chain temperatures and incorporation of these nanofillers into polyethylene (PE) polymer matrix to yield flexible packaging films with thermal buffering capacity in a broad temperature interval, which can retard temperature increases in cold-stored food products.

3.3. Materials and Methods

3.3.1 Chemicals

Halloysite nanotubes (mined from reserves in Balıkesir, Turkey) were provided by ESAN, Eczacıbaşı. Polyethylene glycol (PEG) 400 (Mw: 380-420 g/mol) and methanol (HPLC grade) were purchased from Sigma-Aldrich Inc. PEG600 (Mw: 570-630 g/mol) was purchased from Merck Chemical Ltd. Low-density polyethylene (LDPE) granules (PETİLEN: F2-12) were provided by Petkim Petrokimya A.Ş., Izmir, Turkey.

3.3.2 Preparation of HNT/PCM nanohybrids

HNTs were impregnated with PEG400 and PEG600 PCMs by a typical solvent assisted impregnation method with vacuum treatment²⁵⁷⁻²⁵⁹. The desired amount of PCM materials (30-40 wt. % relative to HNTs) were dissolved in 10 ml of methanol; HNTs, which were dried in a vacuum oven at 150°C for 24 hours were added into PCM-methanol mixture. Mixtures were kept in an ultrasonic bath for 20 min, transferred into water bath at 70°C and methanol was removed from the system by reducing the pressure to 0.2 kPa. Obtained HNT/PCM powders were further dried in a vacuum oven for 24 hours at 40°C. For the preparation of nanocomposite films, HNT/PEG400 and HNT/PEG600 PCM nanohybrids were mixed at a weight ratio of 1:1 and are labeled as HNT/PEG-M.

3.3.3 Preparation of PE-HNT/PCM nanocomposite films

PE-HNT/PCM nanocomposite films were prepared via pre-mixing by melt extrusion process followed by blown film extrusion²⁶⁰. Briefly, a mixture of PE pellets and HNT/PEG-M nanohybrids at a ratio of 20 wt.% (HNT/PCM-M: PE = 20:80) was fed into a twin-screw extruder with a screw diameter of 12 mm and L/D ratio of 40 (Zamak, Mercator). Extrusion process was carried out at a temperature range of 165-180°C with a twin-screw speed of 300 rpm. The melt of the mixture emerging from the extrusion die was cooled in a water bath and pelletized. Finally, prepared granule mixture was blown into 55-60 µm thick films using a single screw extruder (Scientific Laboratory Ultra Microfilm Blowing Line Type LUMF-150 with LE8-30/C, LabTech Engineering) at 150 – 160 °C with a screw speed of 80 rpm. In addition to PE-HNT/PEG-M films, nanocomposite films containing only HNT/PEG400

nanohybrids (PE-HNT/PEG400) and films containing only HNT/PEG600 nanohybrids (PE-HNT/PEG400) at 20 wt.% concentration were prepared as controls.

3.3.4 Characterizations

Nicolet IS10 Fourier Transform Infrared (FTIR) spectroscopy with an ATR system was used for the chemical analysis of raw HNTs and HNT/PCM nanohybrids. Impregnation amount of the PCM in the composite system was measured with Shimadzu Corp. DTG-60H (TGA/DTA) by heating samples to 1000°C with a rate of 20°C/min under nitrogen. The percentage of impregnated PCM was calculated as the difference between the total weight loss of raw HNTs and the total weight loss of HNT/PCM nanohybrids recorded at 25°C to 1000°C²⁶¹.

SEM visualization was performed using Zeiss LEO Supra 35VP scanning electron microscope (SEM). Samples in powder form were visualized by depositing samples onto SEM stubs via a double-sided carbon adhesive tape. Samples in film form were mounted onto the SEM holder. All samples were coated with Au-Pd prior to imaging. Secondary electron images of Au-Pd coated samples were obtained at 6 kV for samples in powder form and at 5 kV for samples in film form.

Thermal properties of the PCM nanohybrids were investigated by DSC (Thermal Analysis MDSC TAQ2000) by constructing heating and cooling cycles from -50°C to 40°C at a heating rate of 10°C/min under nitrogen.

Thermal reliability of HNT/PEG-M nanohybrid powders were analyzed with accelerated DSC cycles by placing 5-8 mg of nanohybrid powder into a regular DSC pan and performing 21 consecutive cycles in the temperature range of -40°C to 25°C with a heating rate of 20°C/min under nitrogen for each cycle^{262,263}. All enthalpy calculations were performed with the TA Universal Analysis Software.

To test whether HNT/PEG-M nanohybrids would stay stable during the melt extrusion process, 0.3 g HNT/PEG-M was kept in an oven at 160°C for 5 min (melt compounding process conditions) and powders were analyzed with FT-IR before and after heat treatment.

Mechanical properties of nanocomposite films were determined by a universal testing machine Zwick Roell Z100 UTM with a load cell of 200 N and a crosshead speed of 12.5

mm min⁻¹ according to the ASTM D1708–10 testing method. Dog-bone test specimens had an overall length of 38 mm, overall width of 15 mm, narrow section width of 5 mm and grip distance of 22 mm. An average of at least four replicates of each sample was reported. Thicknesses of nanocomposite films were measured with a digimatic micrometer (Mitutoyo Quicmike, no. 99MAB041M).

Time-temperature profiles of nanocomposite films were constructed by recording the temperatures of the outer surface of a film roll weighing 6 g with a K-Type surface contact thermocouple. Measurements were taken on three different spots on the film roll in triplicates, averages of temperatures and standard errors were reported. Rolls of PE-HNT/PCM and neat PE films were kept at -18°C for 24 hours, then, samples were taken out of the deep-freezer and thermal profiles were followed at room temperature by recording the temperature of film rolls every five seconds.

Meatballs samples of equal weight (35 g) were simply wrapped two-fold with packaging films of equal weight (1.2 g) without vacuum application. Wrapped meatballs were kept at -18°C or 4°C for 24 hours, then, samples were taken out of the deep-freezer/refrigerator and thermal profiles were followed at room temperature by recording the temperatures of the outer surface with a K-Type surface contact thermocouple every minute. Measurements were taken on three different spots on the wrapped meatballs in triplicates, means of temperatures and standard errors were reported.

Statistical significance of differences between means was assigned by one-way ANOVA with Tukey's test at a confidence level of $p < 0.05$ using OriginPro software v.9. (OriginLab Corporation, USA).

3.4. Results and Discussions

3.4.1 The design of nanocomposite food packaging films

PCMs utilized for the preparation of flexible packaging film materials with thermal buffering capacity at cold chain temperatures were polymeric PEG400 and PEG600, which present broad melting transitions in the temperature range of -26.8°C to 14.5 °C and -3.8°C to 31.1°C, respectively. With the aim of obtaining packaging materials that present melting transitions at the temperature intervals of both PCMs and absorb latent heat in the range of -

26.8°C to 31.1°C, a mixture of HNTs impregnated with PEG400 and HNTs impregnated with PEG600 was incorporated into the PE polymer matrix (Figure 17). Nanocomposites of HNTs and PE have been demonstrated to result in food packaging films with various functionalities such as antimicrobial, ethylene scavenging and gas barrier properties^{29,260}; however, there have not been any studies focusing on nanocomposites of PCM impregnated HNTs for food packaging applications.

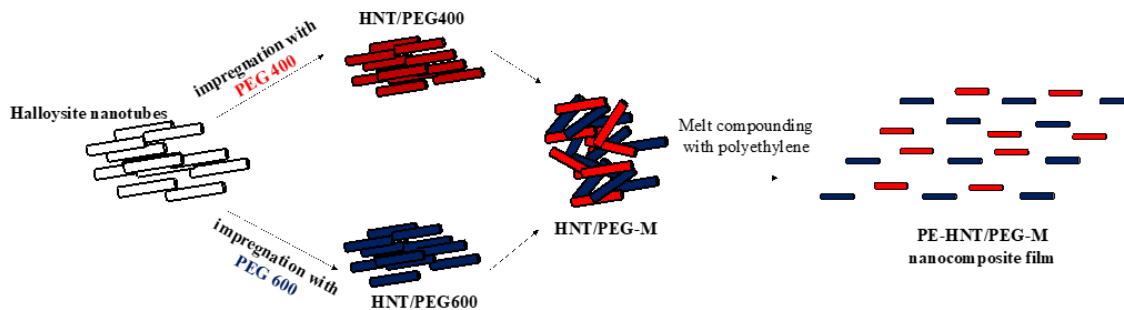


Figure 17. The design of nanocomposite films.

3.4.2 HNT/PCM nanofillers for thermal buffering

HNT/PEG400 and HNT/PEG600 nanohybrids prepared by the impregnation of HNTs were investigated in terms of their maximum impregnation capacity. In the case that shape stabilizers are loaded with PCMs above their maximum impregnation capacity, PCMs may leak out of the shape stabilizer resulting in hybrids that remain wet¹⁹². The maximum impregnation capacity of HNTs without any leakage of liquid PEG400 and PEG600 was determined by monitoring the appearance of nanohybrids at increasing PEG400 and PEG600 ratios using a previously reported method³² and found to be 30 wt.% (Figure 18A). While nanohybrids containing 40 wt.% PCM appeared wet and oily, nanohybrids containing 30 wt.% PCM were dry demonstrating that all PCM was entrapped within HNTs without any leakage. Physical mixture of HNT/PEG400 and HNT/PEG600 nanohybrids for 30 wt.% and 40 wt.% PCM content were also evaluated with SEM (Figure 18B). While HNT/PEG-M with 40 wt.% PCM content presented large chunks of HNTs potentially due to excess PCM on the surface of HNTs, HNT/PEG-M with 30 wt.% PCM content presented individual HNT/PEG-M nanohybrids. SEM images demonstrated that 40 wt.% PCM content was above the impregnation capacity of HNTs and it would not be possible to disperse these nanohybrids in PE matrix via the extrusion process. Besides, SEM images confirmed that HNTs retained

their nanotubular structures following the PEG/400 and PEG/600 impregnation. Although hybrids of HNTs and PCMs with melting transitions below room temperature were not reported before, the impregnation capacity obtained here is in agreement with previous studies that reported maximum impregnation capacities of HNTs in the range of 30-50 wt.%^{32,264}.

The impregnation of nanohybrids prepared at a 30 wt.% PCM ratio was confirmed with TGA analysis that allows the calculation of the actual PEG400 and PEG600 content of nanohybrids based on the total weight loss differences between raw HNTs and HNT/PCM nanohybrids (Figure 18C). Actual impregnation ratios derived from TGA analysis were in good agreement with the theoretical value of 30 wt.% demonstrating that the impregnation was successfully performed²⁶⁵.

Thermal behavior of HNT/PEG400 and HNT/PEG600 nanohybrids along with their mixtures (HNT/PEG-M) was investigated by DSC (Figure 19, Table 3). The melting transition of HNT/PEG-M nanohybrids exhibited a wide temperature range from -21.8°C to 21.7°C by covering melting transition temperature ranges of both HNT/PEG400 and HNT/PEG600 nanohybrids. Thus, the temperature range in which HNT/PEG-M nanohybrids can perform thermal buffering was expanded relative to temperature ranges for HNT/PEG400 and HNT/PEG600 nanohybrids alone due to the physical mixture of both nanohybrids. Melting enthalpies of HNT/PEG400, HNT/PEG600, and HNT/PEG-M nanohybrids were found to be 22.5 J/g, 24.8 J/g and 23.4 J/g, respectively. These results were 33% (for HNT/PEG400) and 36% (for HNT/PEG600) lower than theoretical enthalpies of PCM composites, probably due to the interference of the crystallization of PEG400 and PEG600 with the mesoporous HNT matrix. The crystal arrangement and orientation of PEG chains were restricted by the steric effects, mesoporous confinement and surface adsorption which declined the regularities of crystal regions; thus, the actual enthalpies were found to be much lower than theoretical enthalpies^{258,266}.

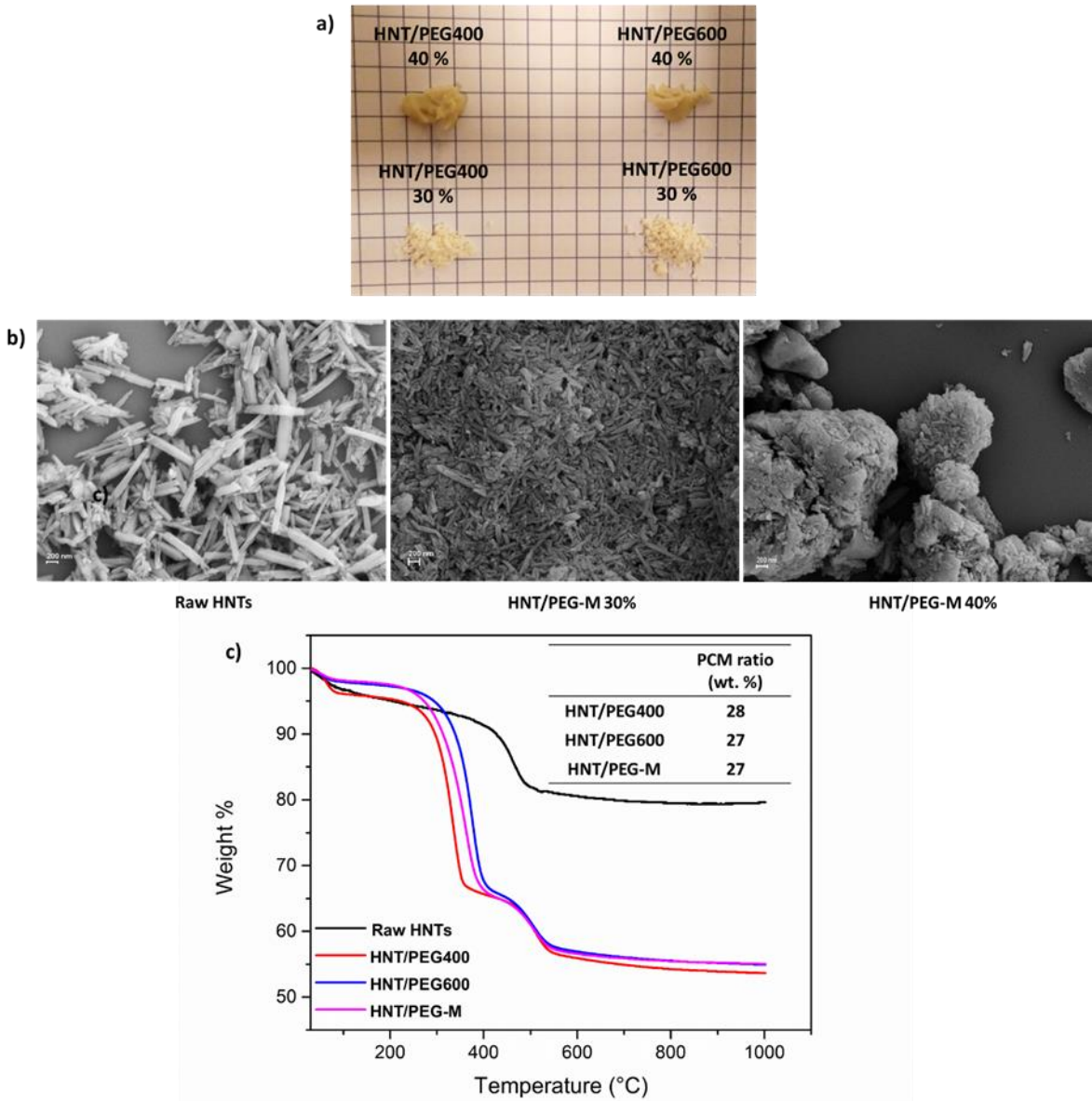


Figure 18. a) Photographs of HNT/PEG nanohybrids for different PCM impregnation ratios, b) SEM images of raw HNTs and HNT/PEG-M nanohybrids containing 30-40 wt.% PCM (scale bars represent 200 nm), c) Thermogravimetric analysis of raw HNTs and HNT/PCM nanohybrids containing 30 wt.% PCMs. Inset: PCM ratios as calculated by weight loss differences between nanohybrids and raw HNTs.

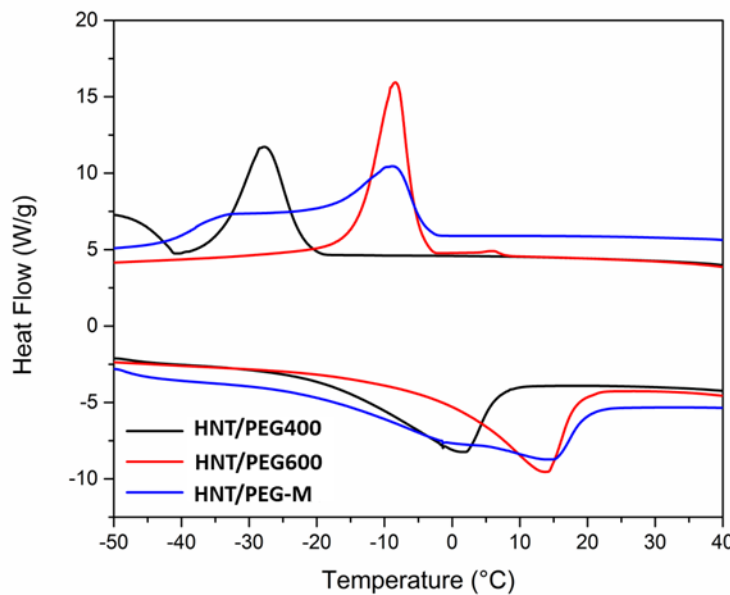


Figure 19. DSC curves of HNT/PCM nanohybrids.

Table 3. Transition temperatures and enthalpies of pure PCMs and HNT/PCM nanohybrids.

	Heating Cycle				Cooling Cycle			
	T _m peak (°C)	T _m onset (°C)	T _m offset (°C)	ΔH _m (J/g)	T _s peak (°C)	T _s onset (°C)	T _s offset (°C)	ΔH _s (J/g)
PEG400	4.6	-26.8	14.5	111.5	-15.3	-9.3	-33.6	96.7
PEG600	21.0	-3.8	31.1	129.7	7.7	12.3	-11.7	122.2
HNTPEG400	1.3	-22.0	6.4	22.5	-27.8	-17.2	-41.0	22.1
HNTPEG600	13.9	-6.0	19.0	24.8	-8.3	-2.2	-21.9	24.2
HNTPEG-M	8.5	-21.8	21.7	23.4	-16.2	-1.4	-46.2	23.1

The thermal reliability of HNT/PEG-M nanohybrids was evaluated by accelerated DSC cycles and results were presented in Figure 20A. Only a negligible decrease in melting and solidifying enthalpies (only 0.05 J/g for the melting; 0.17 J/g for the cooling process) between 1st and 21st thermal cycles was observed. These results have put forward that HNTs acted as effective shape-stabilizers and have kept PCMs successfully inside/outside the tubular shape through strong capillary forces, and hindered leakage of PCMs from nanohybrids during heating cycles.

To ensure that prepared HNT/PCM nanohybrids would remain stable during high temperature conditions required for the melt compounding, their thermal stability was investigated before and after heat treatment at 160°C via FT-IR analysis. Figure 20B demonstrates that characteristic peaks of PEG at 3436 cm⁻¹, 2868 cm⁻¹ and 1462-1354 cm⁻¹ corresponding to the terminal hydroxyl groups, -CH₂ stretching and C-H bending, respectively, are visible on the spectrum of HNT/PEG-M composites both before and after the heat treatment. Photographs of HNT/PEG-M nanohybrid powders also confirmed that heat treatment did not lead to leakage as the powders retained their dry appearance. The PEG content of the nanohybrids remained unaffected even under high temperature conditions, ensuring leak-proof use of HNT/PEG-M nanohybrids in melt compounding process for food packaging film production.

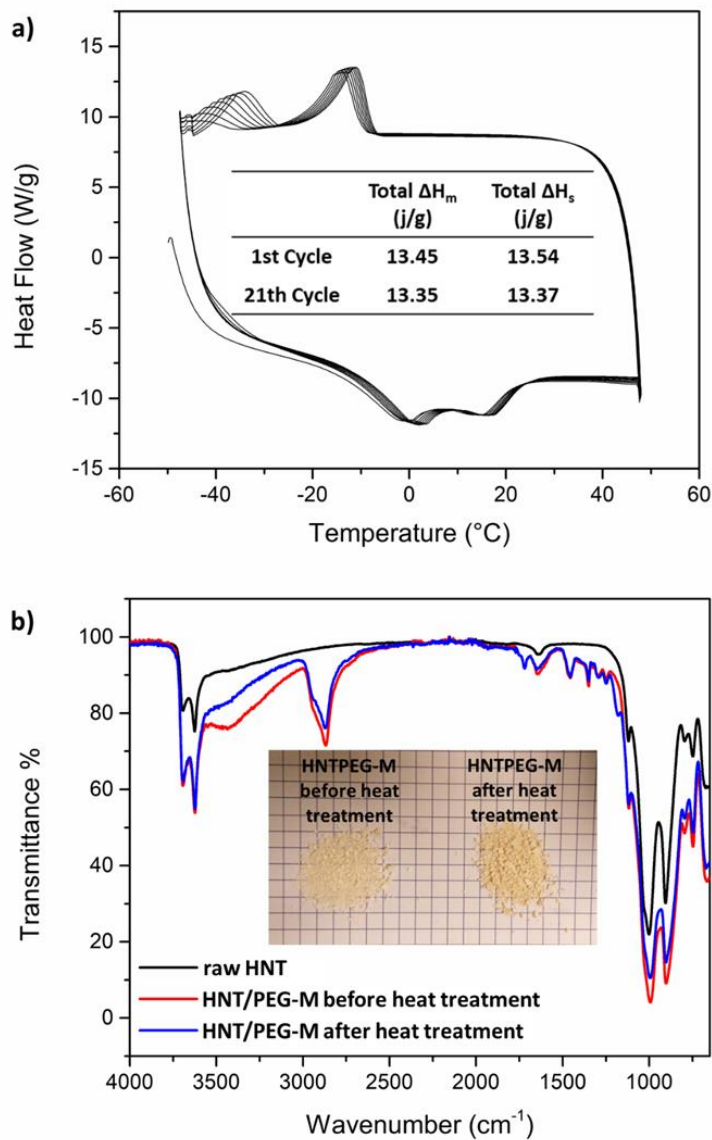


Figure 20. a) Accelerated DSC heating/cooling cycles of HNT/PEG-M nanohybrids, inset: total $\Delta\text{H}_m/\text{s}$ calculated for the -20°C to 20°C temperature range, b) FT-IR spectra of raw HNTs and HNT/PEG-M nanohybrids before and after heat application at 160°C for 5 min, inset: photographs of HNT/PEG-M nanohybrid powders before and after heat treatment.

3.4.3 PE-HNT/PCM nanocomposite films

PE based nanocomposite films were prepared by embedding HNT/PEG-M nanohybrids into the polymer matrix by melt processing. As the amount of absorbed latent heat and buffering capacity of nanocomposite films were directly related to the amount of embedded HNT/PEG-M nanohybrids, a maximum possible nanohybrid concentration was aimed. HNT/PEG-M concentration in the PE matrix was selected as 20 wt.% and whether the nanocomposite films would have the appropriate mechanical properties for being used as food packaging materials at this concentration was studied. It is well known that there usually is a concentration limitation of fillers in polymeric nanocomposite films. While mechanical properties improve up to a certain filler content, they decline at higher concentrations.^{267,268} Mechanical properties of PE-HNT/PEG-M nanocomposite films prepared at 20 wt.% filler content were determined relative to neat PE films (Table 4). Despite the high nanoparticle concentration in the polymer matrix, mechanical properties decreased only by 4.3%, 6.6%, 10.1 % and 10.9% for young's modulus, tensile strength, elongation at break and yield strength, respectively. Impregnation of HNTs with PEG400 and PEG600 potentially modified the HNTs surface chemistry and improved the compatibility between HNTs and LDPE. The enhanced compatibility compensated for the high filler content and the deterioration in mechanical properties was minimal. Contrary to another study where the incorporation of microencapsulated wax into high density polyethylene matrix significantly deteriorated mechanical properties due to immiscibility of fillers in the polymer matrix, in our work the nanoparticle entrapped PCMs were finely dispersed in the PE matrix resulting in mechanically strong nanocomposite films²⁶⁹. Besides, mechanical properties of PE-HNT/PEG400 and PE-HNT/PEG600 nanocomposite films were statistically similar to mechanical properties of PE-HNT/PEG-M films demonstrating that nanohybrids prepared with PCMs of close molecular weight presented similar dispersion behavior in the LDPE matrix. Characterization of mechanical properties of PE-HNT/PEG-M films confirmed that they have acceptable mechanical properties for being utilized as food packaging materials^{260,270,271}.

Table 4. Mechanical properties of neat PE and PE-HNT/PEG nanocomposite films.

	Young's Modulus (MPa)	Tensile Strength (MPa)	Elongation at Break %	Yield Strength (MPa)
Neat PE Film	161.2 ±12 ^a	12.1 ±2.0 ^a	318.1 ±36 ^a	9.1 ±0.6 ^a
PE-HNT/PEG400	152.4 ±14 ^a	13.0 ±0.8 ^a	270.2 ±42 ^{a,b}	8.4 ±0.4 ^{a,b}
PE-HNT/PEG600	148.6 ±17 ^a	13.2 ±1.4 ^a	238.5 ±57 ^b	8.6 ±0.5 ^{a,b}
PE-HNT/PEG-M	154.3 ±10 ^a	11.3 ±0.4 ^a	284.5 ±23 ^{a,b}	8.1 ±0.4 ^b

Values sharing a common letter (a–b) within the same column are not significantly different

PE-HNT/PEG-M nanocomposite films were studied by DSC to evaluate their melting transition temperatures and melting enthalpies of PEG400 and PEG600 contained in them. In accordance with results obtained for the melting transitions of HNT/PEG-M nanohybrids, nanocomposite films containing HNT/PEG-M nanohybrids presented a broad melting transition at temperatures between -16.6°C and 26.3°C covering the total melting transition temperature range of both PE-HNT/PEG400 and PE-HNT/PEG600 films. This broad melting transition would allow PE-HNT/PEG-M films to absorb latent heat and therefore present thermal buffering over a broad temperature interval covering cold storage temperatures. The latent heat of melting in the temperature interval of -16.6°C and 26.3°C was calculated to be 2.3 J/g (Table 5).

Table 5. Thermal properties of PE-HNT/PEG nanocomposite films in the melting transition range of PEG400 and PEG600.

	Heating Cycle			
	T _m peak (°C)	T _m onset (°C)	T _m offset (°C)	ΔH _m (J/g)
PE-HNT/PEG400	-4.2	-17.5	9.2	1.6
PE-HNT/PEG600	8.7	-6.8	21.6	1.2
PE-HNT/PEG-M	-0.8	-16.6	26.3	2.3

Thermal buffering capacity of PE-HNT/PEG-M nanocomposite films was determined by constructing time-temperature curves for film samples that have been kept at -18°C and were taken to room temperature. As demonstrated in Figure 21, the time elapsed for PE-HNT/PEG-M nanocomposite films to reach 0°C, 10°C and 15°C was more than two times

longer than the elapsed time for neat PE films to reach the same temperatures. PEG400 and PEG600 PCMs incorporated into the PE matrix through impregnation of HNTs allowed the resulting nanocomposite films to absorb latent heat and resist temperature increases during their melting transitions. Therefore, the nanocomposite films stayed colder than standard neat polymeric films as the ambient temperature increased. Moreover, PE-HNT/PEG-M nanocomposite films showed better temperature buffering performance than the nanocomposite films containing only HNT/PEG400 and HNT/PEG600. PE-HNT/PEG-M films absorbed latent heat at melting transition temperature ranges of both HNT/PEG400 and HNT/PEG600 nanohybrids present in the nanocomposite system and stayed colder for longer time.

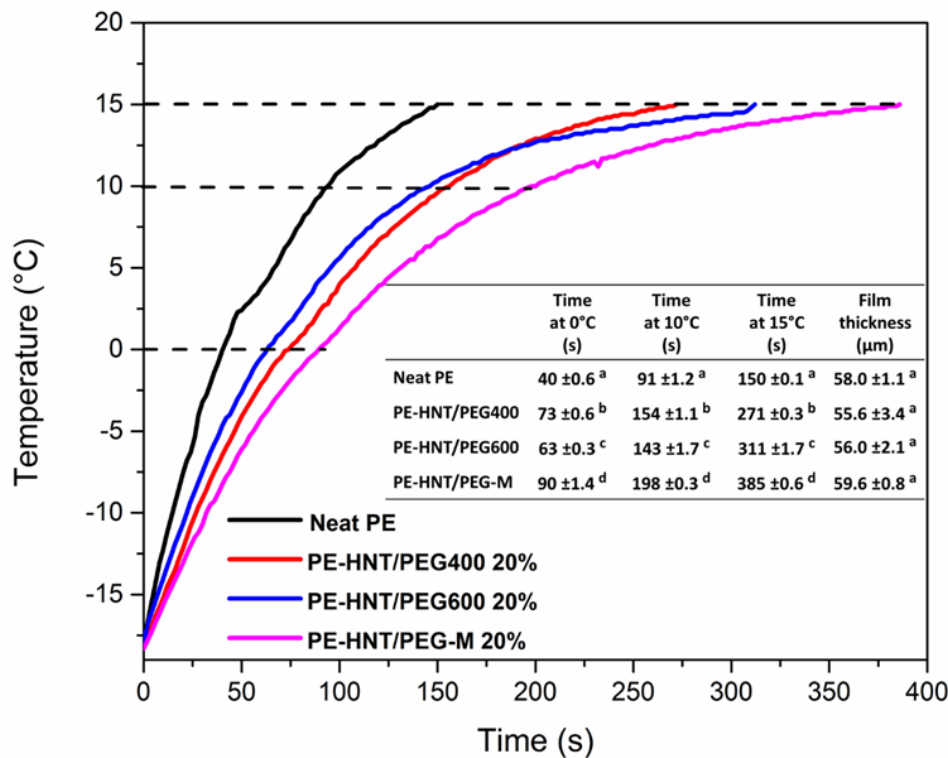


Figure 21. Time-temperature curves of neat PE film and PE-HNT/PEG nanocomposite films at -18°C which were taken to room temperature. Inset: Tabulated data showing elapsed time for the frozen films to reach 0°C, 10°C, 15°C and thickness of films. Values with different letters in the table (a-d) within the same column are significantly different.

3.4.4 Cold storage applications of PE-HNT/PCM nanocomposite films

Finally, the utilization of PE-HNT/PEG-M nanocomposite films as food packaging materials that can keep food cold for prolonged times was tested on food samples. Meatball samples were packaged with standard neat PE films and PE-HNT/PEG-M nanocomposite films by wrapping and kept in a deep-freezer (Figure 22A) before they were taken to room temperature and their time-temperature profiles were constructed. As seen in Figure 22B, meatball samples packaged with PE-HNT/PEG-M nanocomposite films reached 4°C after 44 min, while the elapsed time for the standard neat PE films to reach the same temperature was only 26 min. When packaged with PE-HNT/PEG-M nanocomposite films thawing of food products was significantly retarded relative to food products packaged with standard films lacking the PCMs impregnated into HNTs. The 18 min lag time for the frozen food to reach defrosting temperature was obtained thanks to the embedded PCM nanohybrids which absorb latent heat over a broad interval covering -17°C to 26°C. In a different experiment, meatball samples packaged with nanocomposite and standard films were kept in a refrigerator and their temperatures were monitored when they were taken out to room temperature (Figure 22C). Nanocomposite packaging films showed almost two times higher retarding performance on the warming of meatballs than standard neat PE packaging films. Meatball samples packaged with PE-HNT/PEG-M nanocomposite films reached 15°C in 43 min whereas meatball samples in standard neat PE packaging films reached the same temperature in 23 min. Nanocomposite films delayed the warming of a chilled food for 20 minutes without the use of any secondary container. PCMs embedded into the polymer matrix allowed the resulting nanocomposite films absorb latent heat in a wide temperature range and significantly slowed down the warming of frozen or chilled food products by presenting a significant buffering performance. Nano-entrapment of different PCMs within HNTs allowed their facile and leak-free incorporation into a polymer matrix and thereby allowed the exploitation of the thermal buffering capacity of PCMs for flexible packaging films that can keep food cold, for the first time.

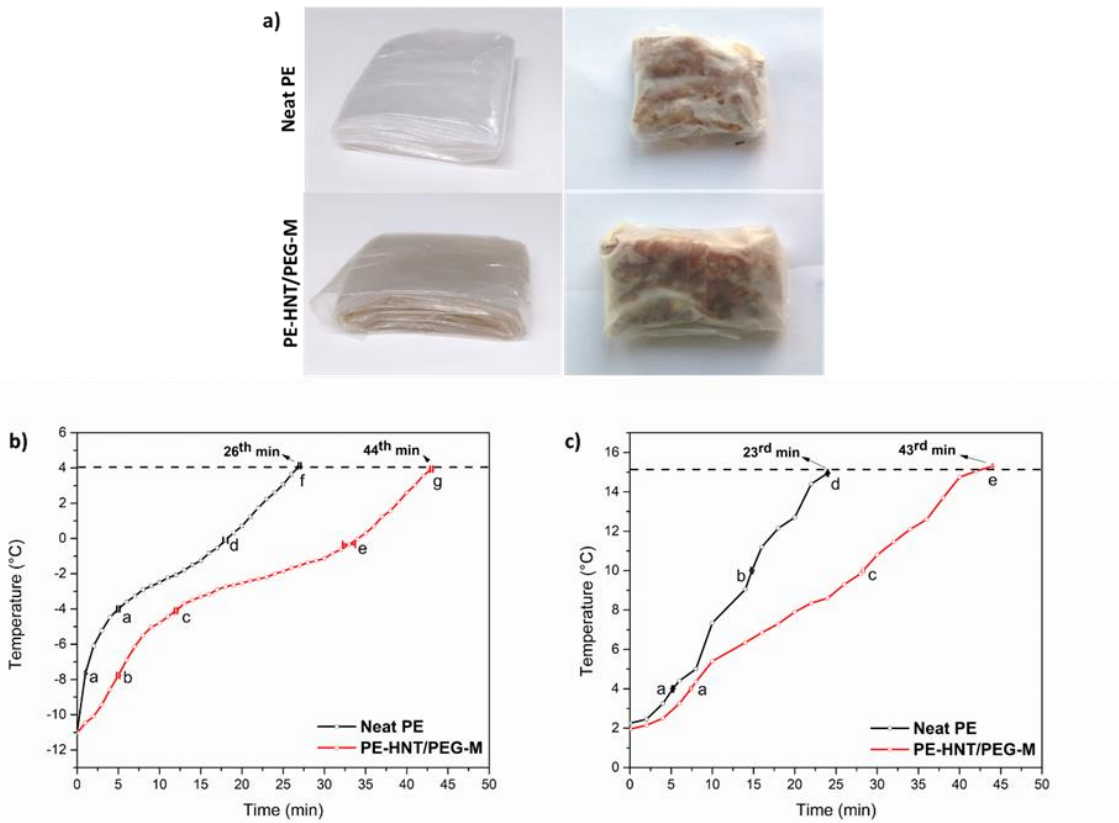


Figure 22. a) Photographs of packaged meatball samples, b) Time-temperature profiles of meatballs packaged with standard neat PE and PE-HNT/PEG-M films, curves constructed for frozen meatballs taken to room temperature (c) Time-temperature profiles of meatballs packaged with standard neat PE and PE-HNT/PEG-M films, curves constructed for chilled meatballs taken to room temperature. Time values with different letters in each graph (a-g) are significantly different.

3.5. Conclusions

Polyethylene based flexible nanocomposite food packaging films presenting thermal buffering performance in cold-chain temperatures was prepared by utilizing PCM impregnated HNTs as nanofillers. Nanocomposite films obtained by the incorporation of the mixture of HNT/PEG400 and HNT/PEG600 nanohybrids into PE films demonstrated acceptable mechanical properties for being used as food packaging materials and significant thermal buffering capacity in a temperature range covering cold-chain temperatures. The effectiveness of PE-HNT/PEG-M nanocomposite packaging films on keeping food products

colder for longer was demonstrated on food samples. The flexible packaging films prepared in this study significantly delayed the thawing of frozen meat samples and the warming of chilled meat samples. Incorporation of PCMs into polymers via nanocarriers allowed packaging films of only 60 μm thickness to significantly slow down temperature increases in cold foods. The nanocomposite films demonstrated here can be used for the protection of any material that is sensitive to undesired temperature fluctuation during transportation in cold chain and have great potential for the reduction of food waste and improvement of food safety.

CHAPTER 4: Purification and Sorting of Halloysite Nanotubes into Homogeneous, Agglomeration-Free Fractions by Polydopamine Functionalization

Reference Publication: Cüneyt Erdinç Taş, Emine Billur Seviniş Özbülut, Ömer Faruk Çeven, Buket Alkan Taş, Serkan Ünal and Hayriye Ünal, "Purification and Sorting of Halloysite Nanotubes into Homogeneous, Agglomeration-Free Fractions by Polydopamine Functionalization", *ACS Omega*, 2020, 5, 17962–17972.

4.1. Abstract

Halloysite nanotubes (HNTs) have attracted great attention in the field of nanotechnology as natural, high value-added nanomaterials. Despite their significant potential as carriers of active agents and fillers in nanocomposite structures, inhomogeneity of HNTs in terms of length and diameter along with their agglomeration tendency pose important obstacles for utilization of them in a wider range of applications. Here, a facile, three-step separation protocol that allows the sorting of HNTs into agglomeration-free, uniform size fractions is reported. The protocol consists of coating of HNTs with polydopamine to impart hydrophilicity and aqueous dispersibility, followed by their ultrasonication and centrifugation at varying velocities for size-based separation. Particle size distribution analysis by scanning electron microscopy and dynamic light scattering have demonstrated that the separation protocol resulted in uniform HNT fractions of varying agglomeration-states and particle sizes. The highest quality fraction obtained with 18% yield was free of agglomerations and consisted of HNTs of uniform length and diameters. The polydopamine coating on HNTs which facilitated the separation was demonstrated to be removed by a simple heat-treatment that preserved the crystal structure of HNTs. The impact of the separation protocol on the loading and functionalization capacity of halloysites was

investigated. Highest quality HNTs presented 4.1-fold increase in lumen loading and 1.9-fold increase in covalent surface coupling ratios compared to the loading and functionalization ratios obtained with raw HNTs. Similarly, sorted, high quality HNTs were demonstrated to be better dispersed in a polymeric matrix resulting in polymeric nanocomposites with significantly enhanced mechanical properties compared to nanocomposites prepared with raw HNTs. The three-step separation protocol presented here provides a toolbox that allows sorting of raw HNTs into uniform fractions of different size ranges, from which HNTs of desired qualities required by different applications can be selected.

4.2. Introduction

HNTs are abundant clay nanoparticles that have been utilized in a variety of scientific and industrial applications due to their intrinsic nanostructure, high thermal stability, acceptable mechanical strength, relatively low cost and biocompatibility. HNTs present a natural hollow tubular structure composed of tetrahedral silicone dioxide outside and octahedral aluminum oxide inside along with a high aspect ratio and a low hydroxyl group density¹⁸. Their unique structural properties make HNTs notable as reinforcing fillers for polymers and also as containers for active components²⁷², resulting in the utilization of HNTs in specific applications such as water purification^{11,273}, drug delivery¹², cancer cell isolation¹³, bone implants¹⁴, teeth fillers¹⁵ and cosmetics¹⁶.

HNTs naturally exist in a wide range of length and diameters²⁷⁴. Furthermore, they tend to agglomerate and cannot be individually dispersed in aqueous solutions and polymers. This inhomogeneity and agglomeration behavior of HNTs constitute a significant limiting factor in the final properties of their nanocomposites, which prevents their full potential utilization. HNTs have been incorporated into polymeric materials mainly to obtain polymer nanocomposites with enhanced mechanical and thermal properties. As for all polymeric nanocomposites, a homogeneous dispersion of the filler within the polymer matrix is one of the key requirements to achieve significant property improvements^{9,34,275}. However, the agglomeration tendency of HNTs in the polymer matrix may lead to the deterioration of thermal and mechanical properties²⁷⁶⁻²⁷⁸. The utilization of agglomeration-free HNTs with a homogenous size distribution in the nanoscale can improve their dispersion in the polymeric

matrix and provide a homogenous nanocomposite material. Furthermore, the wide distribution of the size of natural HNTs constitute critical problems in certain applications. For example, very long HNTs above the average length can induce cell injury and inflammation when injected into cells for medical applications²⁷⁹ or cause irritation to the skin in cosmetic applications²⁸⁰. Thus, a method that allows sorting of HNTs based on their size would improve their function and provide a toolbox for their efficient utilization in various applications.

Limited number of previous studies attempting the purification and size-separation of HNTs have focused on ultrasonic scission of HNTs followed by a viscosity-based centrifugation where HNTs were dispersed in water in the presence of a polymeric material and a surfactant, providing high density and stability, respectively^{7,281}. The potential of these methods might be limited due to the fact that these polymeric materials and surfactants cannot be completely removed at the end of the separation process and they might interfere with HNTs' functions.

Here, we demonstrate a facile method to obtain HNTs that are uniform in size and shape while preserving or improving their inherent properties. HNTs were functionalized with a polydopamine coating to impart hydrophilicity and enhance aqueous dispersibility, followed by ultrasonication and hydrophilicity gradient centrifugation that results in the purification of HNTs from other mineral impurities and sorting into different grades that are uniform in size and shape. The polydopamine coating that acts as an effective tool for the purification and separation of HNTs can be easily removed at the end of the separation process when needed. The proposed method provides a practical and useful way to obtain agglomeration free, uniform HNTs of desired aspect ratio which will allow the utilization of HNTs to their fullest potential.

4.3. Materials and Methods

4.3.1. Chemicals

Raw HNTs, sodium dodecyl sulfate, sodium hydroxide pellets and hydrochloric acid (ACS reagent, 37%) were purchased from Sigma-Aldrich Inc. Dopamine (3-hydroxytyramine hydrochloride) was purchased from Acros Organics Inc. Milli-Q purified water was used for all the synthesis and characterization stages. Carvacrol was purchased from Tokyo Chemical Industry Co., LTD. Ultrapure Tris base (Tris(hydroxymethyl)aminomethane) was purchased from MP Biomedicals, LLC. Low-density PE (LDPE) granules (PETİLEN F2-12) were provided by PETKİM Petrokimya A.Ş. All chemicals were used without any further purification.

4.3.2. Three-step separation of HNTs

HNTs were separated into three different grades of quality and size by following the three-step separation protocol. In the first step, HNTs were coated with polydopamine by dispersing 1g of raw HNTs in 100 mL of purified water (10mg/mL) with ultrasound sonication (Qsonica, Q700) for 30 min at 100% amplitude (120W) with 5 s pulse on and 2 s pulse off in an ice bath. Following the sonication, 0.2 g dopamine was added into the dispersion (2 mg/mL) and the pH was adjusted to 8.5 with Tris base powder. Prepared mixture was stirred at 30°C for 30 min. Then, polydopamine coated HNTs (PDHNTs) were separated from the reaction mixture with centrifugation at 5000 rpm for 5 min. Separated PDHNTs were washed with water and centrifuged five times to remove residual Tris base or unreacted dopamine molecule from the product. Obtained PDHNTs were dried at 50°C for 24 h in a vacuum oven.

In the second step, an aqueous PDHNT dispersion (20 mg/mL) was prepared using an Ultra-TURRAX T18 basic dispersion system at approximately 11000 rpm for 30 min and ultrasonicated for 45 min at 100% amplitude (120W) with 5 s pulse on and 2 s pulse off in an ice bath.

In the third step, obtained aqueous PDHNT dispersion was separated into three grades by applying centrifugation for 10 min at 2000 rpm. Following the 2000 rpm centrifugation, the precipitate was dried and labeled as “Grade 1 PDHNTs”. The supernatant was centrifuged

for 10 min at 6000 rpm, the precipitate was dried and labeled as “Grade 2 PDHNTs”. The supernatant was centrifuged at 11000 rpm, the precipitate was dried and labeled as “Grade 3 PDHNTs”.

For the removal of the polydopamine coating, Grade 1, Grade 2 and Grade 3 PDHNTs were heat treated for 48 hours at 290°C.

4.3.3. Functionalization of HNT surfaces with sodium dodecyl sulfate

Prior to the functionalization, HNTs were treated with NaOH to increase the amount of hydroxyl groups on the nanoparticle surface. 0.2 g HNTs (0.01g/ml) was stirred in 20 ml of NaOH solution overnight, then washed with distilled water several times to remove residual NaOH. 0.02 g SDS was added into 10 ml distilled water and 5 µl of HCl (37%) was added dropwise, the mixture was stirred for 15 min for the protonation of sodium sulfate groups on SDS. Finally, 0.2 g HNTs were gradually added into the mixture and the reaction was continued for 18 hours at 40°C.²⁸² The final product was obtained by centrifugation at 6000 rpm, which was then washed 5 times with distilled water and dried in a vacuum oven for 24 hours at 80°C.

4.3.4. Loading of HNTs with carvacrol

In order to load HNTs with carvacrol, 40 mg HNTs were dispersed in 20 mL carvacrol by using ultrasound sonication for 10 min at 60% amplitude (65W) with 2 s pulse on and 5 s pulse off in an ice bath. Then HNT-carvacrol dispersion was connected to a vacuum pump and vacuum (2 mbar) was applied for 20 min. The vacuum was released to bring the system to the atmospheric pressure and then vacuum was re-applied under the same conditions. At the end of the two-step vacuum cycle, HNTs were separated from the excess amount of carvacrol by centrifugation at 5000 rpm for 5min. Obtained carvacrol loaded HNTs (CHNT) were washed with ethanol to remove the residual carvacrol from the HNT surface. Finally, CHNTs were dried at room temperature for 24 hours²⁸³.

4.3.5. Preparation of polyethylene-HNT nanocomposite films

Mixture of polyethylene (99wt%) and HNT (1wt%) powders were fed into a twin-screw extruder (Zamac Mercator with a screw diameter of 12 mm and L/D of 40) and processed at

the zone temperature range between 160-180°C with the screw speed of 300 rpm. Nanocomposite melt flowing from the extrusion die was cooled in a water bath and pelletized. Afterward, pellet form of nanocomposite mixture was transferred to a single screw film blowing machine (Scientific Laboratory Ultra Micro Film Blowing Line Type LUMF-150 with L8-30/C, LabTech Engineering), processed at 150-160°C with a single screw speed of 80 rpm and blown into 55-65 µm thick films. The neat LDPE samples were processed through the blown film extrusion of LDPE granules under the same conditions.

4.3.6. Characterization Methods

Thermogravimetric analysis (TGA) of all samples was performed using Shimadzu Corp. DTG-60H (TGA/DTA) instrument by heating samples up to 1000°C with a rate of 10°C/min under nitrogen. Prior to the analysis, samples were dried for 30 min at 100°C in the instrument to remove all moisture from the samples.

Determination of the hydrodynamic diameter of samples was performed using a dynamic light scattering (DLS) instrument (Zetasizer Nano - ZS, Malvern Instruments Ltd., UK) at 25 °C at a sample concentration of 2mg/mL for each sample.

Nicolet IS10 Fourier Transform Infrared (FTIR) spectroscopy with an ATR system was utilized for the chemical analysis of raw samples.

Phase purity of samples was analyzed by X-ray diffraction patterns (XRD) from a Bruker D2 Phaser XRD instrument using CuKa radiation ($k = 1.5418 \text{ \AA}$, 40 kV, 200 mA) in the 2Theta range of 5–70°.

The samples were visualized using Zeiss LEO Supra 35VP scanning electron microscopy (SEM). HNT samples were prepared for visualization on silicon wafer by drying a drop of aqueous HNT dispersions (0.1mg/mL) obtained by ultrasonication for 2 min at 70% amplitude (75W) with 5 s pulse on and 2 s pulse off in an ice bath. For the visualization of HNT/PE nanocomposite films, samples were coated with Au-Pd and images were recorded using a secondary electron detector at 5kV under high vacuum. Size distribution of HNT specimens were analyzed using SEM images at 50K magnification by ImageJ software. For the statistical analysis, lengths were measured using at least 50-200 nanotubes for each grade, and they were presented as frequencies of nanotubes versus their lengths. Mechanical

properties of nanocomposite films were investigated using a universal testing machine Zwick Roell Z100 UTM, with a load cell of 200 N and a crosshead speed of 12.5 mm min⁻¹ according to the ASTM D1708–10 testing method. Dog-bone test specimens had a length of 38 mm and width of 15 mm, narrow section width of 5 mm and grip distance of 22 mm. An average of four replicates of each sample was reported. Thicknesses of films were measured using a digimatic micrometer (Mitutoyo Quicmike, no. 99MAB041M).

4.4. Results and Discussions

Polydopamine is a synthetic analog to mussels' strong adhesive protein containing repeated amine and catechol groups that is obtained by the autoxidation of the dopamine monomer⁷¹. It is well-established that polydopamine coating is applicable to nearly all substrates to impart biocompatibility, post functionality, adhesion and other targeted properties^{71,284,285}. Polydopamine coating of HNT surfaces has been previously reported for their functionalization with nanoparticles and enzymes^{43,286,287}.

The first step of the separation protocol was the coating of HNT surfaces with polydopamine in order to impart hydrophilicity and aqueous dispersibility for their centrifugation-based purification and separation. HNTs were simply mixed with the dopamine monomer in alkaline aqueous buffer which has mediated the self-polymerization of dopamine on the surface of HNTs (Figure 23A). The reaction mixture was then washed to remove unreacted dopamine and dried, resulting in polydopamine coated HNTs (PDHNTs) in black powder form. The presence of the polydopamine coating on PDHNTs was demonstrated by FT-IR spectroscopy (Figure 23B). Compared to raw HNTs' FT-IR spectrum, PDHNTs presented additional peaks appearing at 1337 cm⁻¹ due to symmetric and asymmetric -NH stretching vibrations and peaks at 1625 cm⁻¹, 1499 cm⁻¹ and 1276 cm⁻¹ corresponding to -NH bending, aromatic C=C bending and C-N stretching, respectively²⁸⁸, confirming the presence of the polydopamine coating on HNTs. Figure 23C shows the thermogravimetric analysis of raw HNTs and PDHNTs. While both samples had similar decomposition behaviors, PDHNTs presented an additional weight loss of 5.9 wt% starting at 220°C due to the decomposition of the polydopamine coating. These results further confirmed that HNT surfaces were successfully coated with polydopamine.

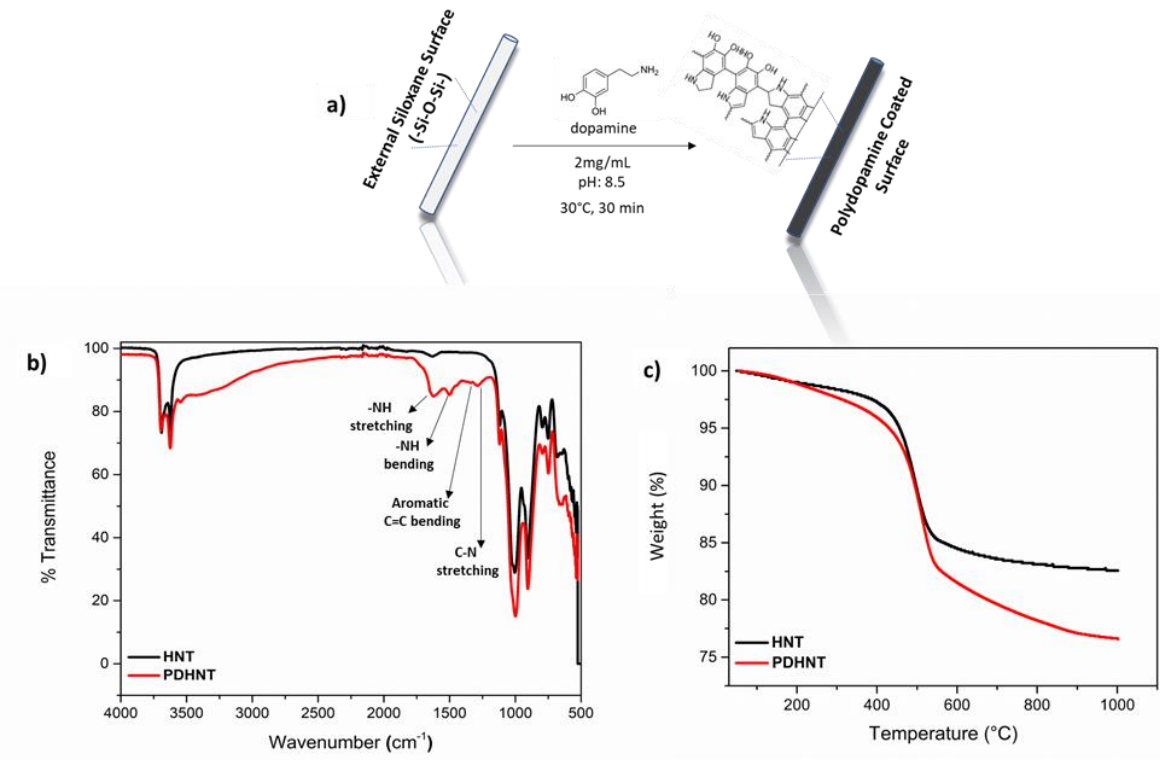


Figure 23. Coating of HNTs with polydopamine (a), FT-IR (b) and TGA (c) analysis of raw HNTs and PDHNTs.

In the second step of the separation protocol, PDHNTs were treated with ultrasonication to break large agglomerations into individual nanotubes. Application of ultrasound energy is an effective and widely applied method to facilitate disruption of large particle agglomerates into nanosizes.²⁸⁹ Polydopamine coated HNTs were treated with the optimal ultrasonication power and duration that minimize the destructive effect of ultrasound but also provide the sufficient energy to break up large agglomerations. In the third step of the separation, aqueous dispersions of ultrasonicated PDHNTs were subjected to consecutive centrifugations at increasing velocities. The precipitate obtained at 2,000 rpm constituted grade 1 PDHNTs, where the supernatant was centrifuged again at 6,000 rpm, resulting in the second precipitate constituting the grade 2 PDHNTs. The supernatant was further centrifuged at 11,000 rpm and the third precipitate constituted grade 3 PDHNTs (Figure 24).

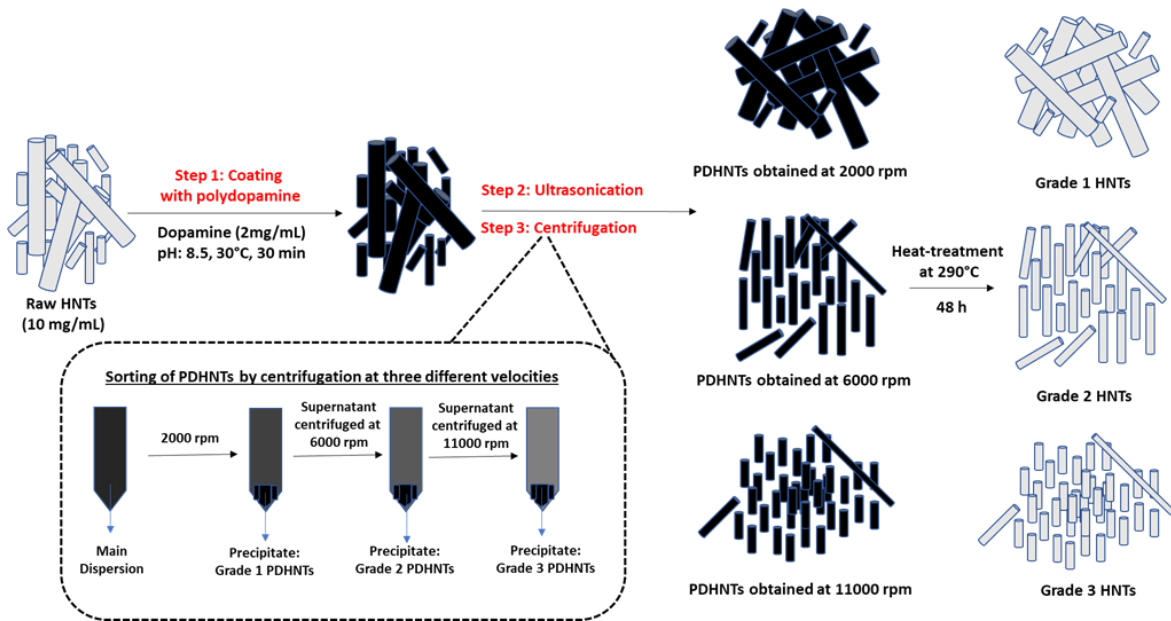


Figure 24. Schematic representation of the three-step separation protocol for HNTs.

In order to assess the effect and importance of the polydopamine coating and ultrasonication steps on the separation efficiency of HNTs, the yields of grade 1, grade 2 and grade 3 PDHNTs obtained through (i) polydopamine coating alone and (ii) through both polydopamine coating and ultrasonication were calculated along with the yields of raw HNTs obtained through the same centrifugation conditions. Figure 25A demonstrates the yields of PDHNTs obtained through polydopamine coating of HNTs followed by centrifugation at varying velocities without the ultrasonication step in comparison to yields of raw HNTs that were processed through the same centrifugation protocol. Raw HNTs that were not functionalized with polydopamine did not show any separation as almost all raw HNTs (97.4 wt%) precipitated upon centrifugation at the lowest velocity of 2000 rpm and negligible amount of HNTs remained in the supernatant. Large aggregates that are already present or have formed due to strong intermolecular interactions in raw HNTs have prevented the aqueous colloidal stability as expected. In contrast, when polydopamine coated HNTs were dispersed in water without ultrasonication, they presented a significantly enhanced colloidal stability as only 74 % of PDHNTs precipitated in the first centrifugation application at 2000 rpm and 24 % remained in the aqueous supernatant. Apparently, the polydopamine coating on HNTs has resulted in more stable aqueous dispersions of HNTs due to the highly hydrophilic character of the polydopamine²⁹⁰. While PDHNTs were able to be separated into

different quality grades without the ultrasonication step, the efficiency of separation was very low. The improved hydrophilicity of PDHNTs improved the colloidal stability to a certain extent, but large agglomerations of PDHNTs that cannot be disintegrated limited the efficiency of the centrifugation-based separation.

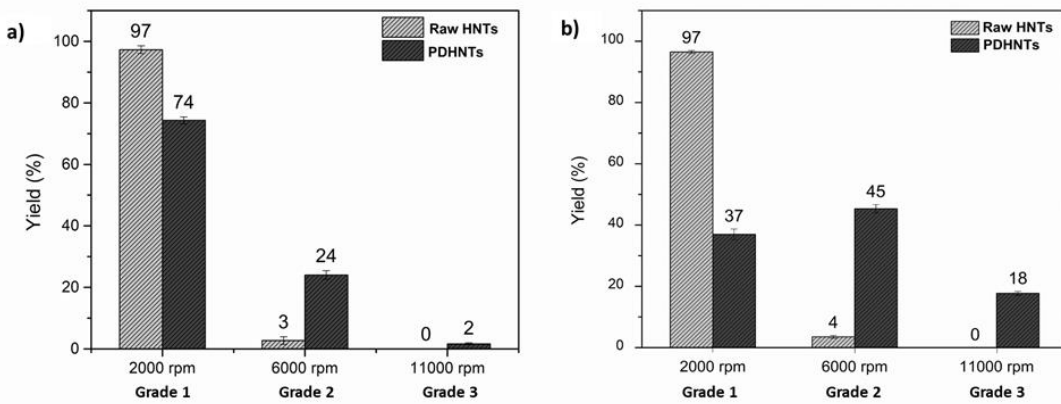


Figure 25. Yields of grade 1, grade 2 and grade 3 PDHNTs obtained at 2000, 6000 and 11000 rpm centrifugation, respectively, in comparison to yields of raw HNTs obtained by centrifugation at the same velocities. a) two-step separation protocol; polydopamine coating and centrifugation, b) three-step separation; polydopamine coating, ultrasonication and centrifugation.

On the other hand, when PDHNTs were further treated with the ultrasonication step, the yield of PDHNTs obtained at higher centrifugation velocities, which are supposedly the pure and agglomeration-free PDHNTs has improved (Figure 25B). While the yield of grade 1 PDHNTs obtained at 2000 rpm centrifugation significantly decreased, the yield of grade 2 and grade 3 PDHNTs obtained at 6000 rpm and 11000 rpm centrifugation increased and reached 45% and 18%, respectively. The increase in the yield of grade 2 and grade 3 quality can be explained with the ultrasound scission stage that physically breaks down the PDHNT agglomerations through sound waves. The fact that 96.5 % of raw HNTs without the polydopamine coating precipitated at 2000 rpm centrifugation and negligible yields were obtained at 6000 and 11000 rpm demonstrates that the hydrophilicity imparted through the polydopamine coating is essential for the centrifugation-based separation of HNTs. As it can be clearly seen, when both polydopamine coating and ultrasound sonication were applied,

the colloidal stability of PDHNTs was enhanced which allowed the centrifugation-based separation of PDHNTs in increased yields.

The relationship between the amount of the polydopamine coating on HNTs and the aqueous colloidal stability it imparts to HNTs was investigated by comparing PDHNTs separated at different centrifugation velocities. Photographs of PDHNTs obtained by the three-step separation showed that different quality grades of PDHNT powders (Figure 26A) had different intensities of a black tint that is known to be caused by the polydopamine coating⁴³. While the initial PDHNT powder had a homogenous black color; following the separation, grade 1, grade 2 and grade 3 PDHNTs had brown, gray and black colors, respectively, demonstrating that different grades of HNTs possessed different amounts of polydopamine coating, depending on their level of agglomeration. The amount of polydopamine coating on PDHNTs calculated by TGA further demonstrated that HNTs were inhomogeneously coated with polydopamine. Grade 1, grade 2 and grade 3 PDHNTs were calculated to have 1.51 wt%, 1.70 wt% and 3.63 wt% polydopamine coating, respectively. Apparently, agglomeration-free, smaller HNTs were coated with polydopamine in higher percentages than HNTs in larger agglomerated forms, potentially due to larger surface areas of agglomeration-free HNTs relative to the surface areas of agglomerated HNTs. Thus, HNTs of different agglomeration states were imparted different extents of hydrophilic character and aqueous colloidal stability which allowed the sorting of HNTs into different quality grades by a simple centrifugation.

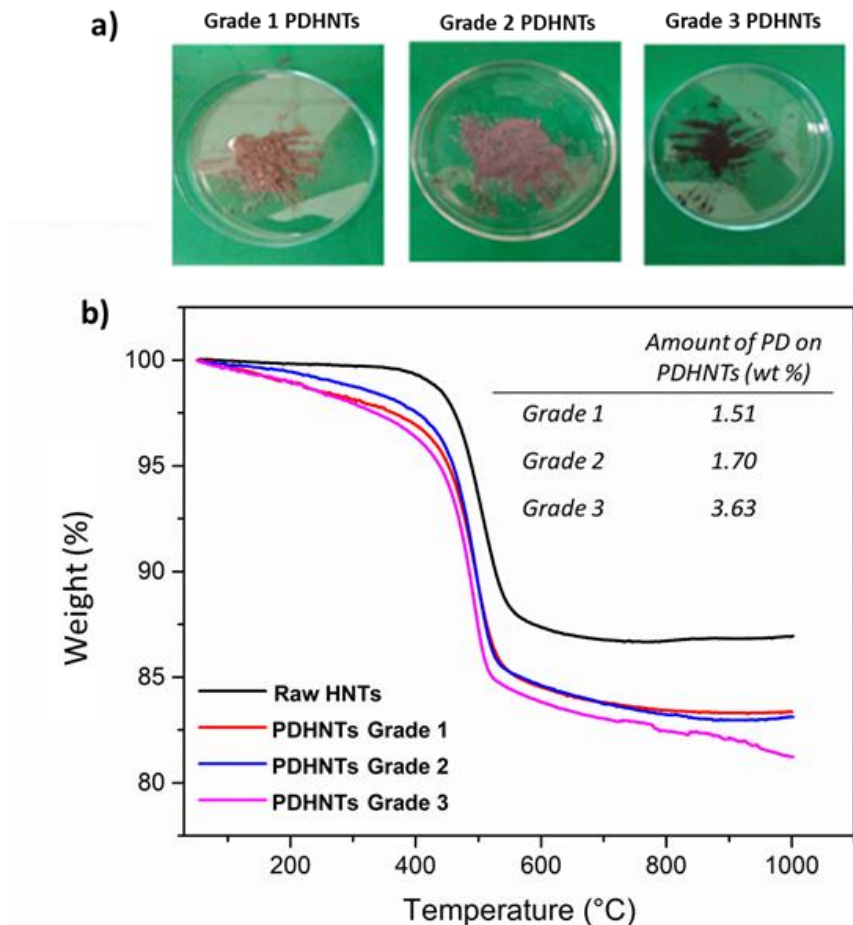


Figure 26. a) Photographs of grade 1, grade 2 and grade 3 PDHNTs, b) TGA analysis of separated PDHNTs.

The size distribution and agglomeration state of PDHNTs obtained through the three-step separation protocol were characterized by SEM and DLS analysis (Figure 27). Raw HNTs presented a wide distribution of nanotube lengths and diameters along with micron-sized aggregates of nanotubes. Following the three-step separation protocol, the polydisperse mixture of HNTs were separated into fractions of PDHNTs with more homogeneous distributions of sizes with minimum amount of aggregates. While grade 1 PDHNTs included longer nanotubes and occasional aggregates, grade 2 PDHNTs included shorter nanotubes and grade 3 PDHNTs included only individually separated nanotubes of shortest lengths (Figure 27A-B). Statistical analysis of PDHNT length distributions on the SEM images also demonstrated that the wide length distribution of raw HNTs ranging from 1200 nm to 400 nm was shifted to narrower distributions with significantly shorter average lengths for Grade

2 and Grade 3 PDHNTs (Figure 27C). The second step of the separation protocol which is the ultrasonication of polydopamine coated HNTs to break large agglomerations, resulted in the scission of nanotubes to different extents, as expected. Following the third step, which comprises the centrifugation of PDHNT dispersions at different velocities, PDHNTs were sorted based on their sizes where longest nanotubes were collected in Grade 1 and shortest nanotubes were collected in Grade3. DLS analysis was also performed on aqueous dispersions for a qualitative comparison of length distributions and demonstrated a significant shift from wider length distributions at larger hydrodynamic diameters for raw HNTs to narrower distributions at shorter hydrodynamic diameters for Grade 3 PDHNTs (Figure 27D). It is known that DLS cannot be safely used for the determination of actual length and diameters of nanotubular structures since it handles nanotubes as spherical particles within a hydrodynamic approximation. However, for well dispersed individual nanotubes that can freely rotate, the length distributions obtained from DLS analysis are expected to corroborate well with actual length distributions. Thus, the agreement between DLS sizes and actual sizes can be interpreted as the absence of agglomerations in the dispersion. While the DLS size distributions of raw HNTs did not match the size, distributions obtained from SEM due to presence of large agglomerations, for separated Grade 3 PDHNTs, both distributions were in good agreement suggesting an agglomeration-free dispersion. These results further confirmed that the separation method provides a facile route towards obtaining monodisperse and agglomeration-free fractions of HNTs from a polydisperse HNT mixture dominated by agglomerations.

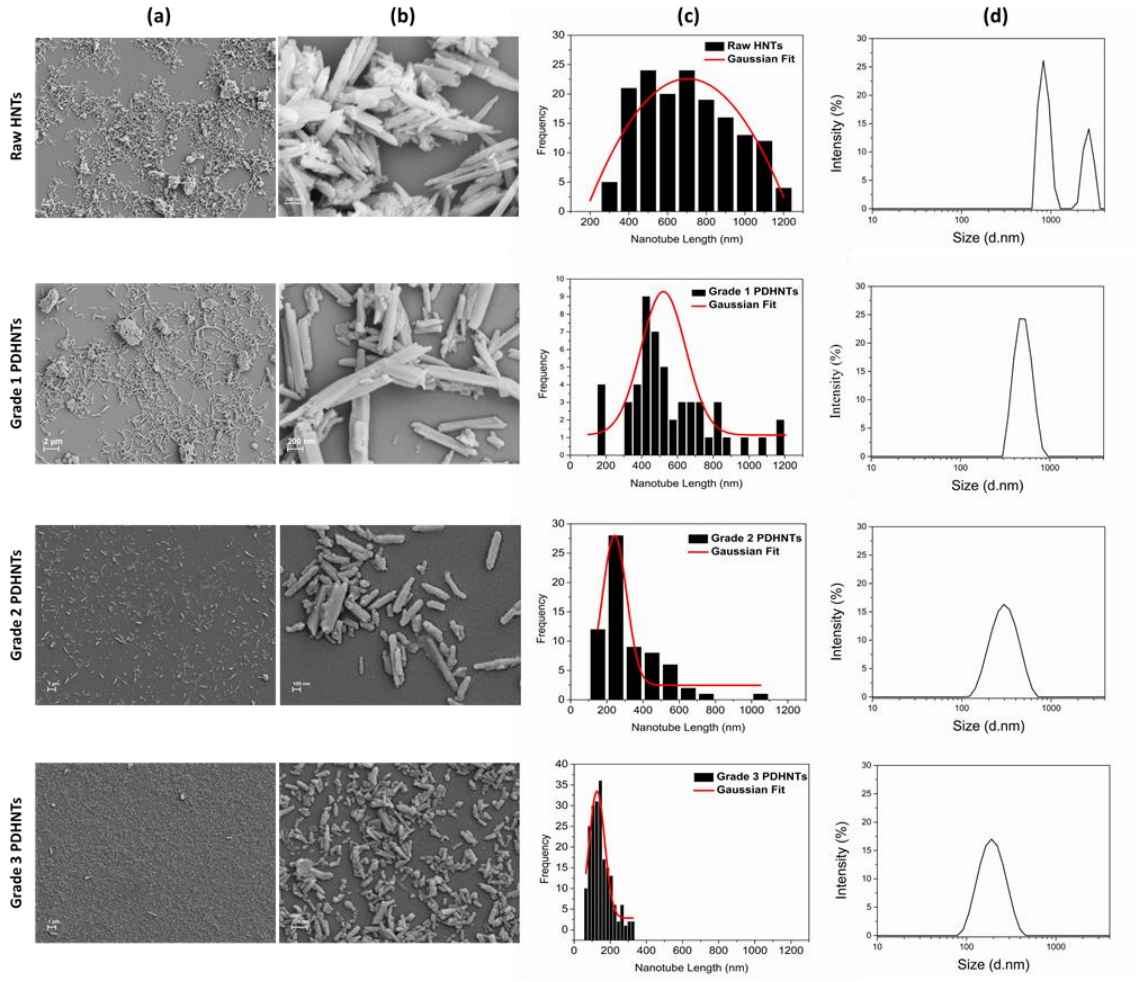


Figure 27. SEM and DLS characterization of raw HNTs and separated PDHNTs. a) representative SEM images at 10K magnification, b) representative SEM images at 100K magnification, c) nanotube length distributions histograms from SEM image analysis, d) size distribution histograms obtained by DLS.

The removability of the polydopamine coating on HNTs was investigated. In order to remove the polydopamine coating, separated PDHNTs were heat treated at 290° for 48 hours under ambient atmosphere. The removal of the polydopamine coating was confirmed by the disappearance of the black tint on HNTs (Figure 28A). Furthermore, TGA analysis of PDHNTs that were heat treated showed that all of the polydopamine coating was removed as the treated nanotubes presented a similar thermo-gravimetric behavior as raw HNTs (Figure 28B).

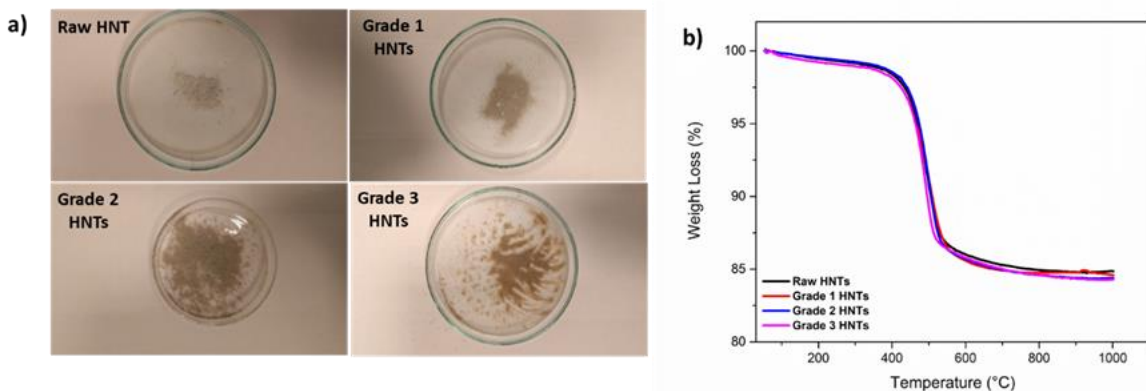


Figure 28. a) Photographs and b) TGA analysis of Raw HNTs and separated HNTs (Grade -1,2,3) after polydopamine coating removed.

Figure 29 A-D demonstrates the SEM and DLS analysis of grade 1, grade 2 and grade 3 HNTs obtained following the removal of the polydopamine coating. The heat treatment did not exert any damage on the tubular shape of HNTs and they retained their monodisperse and agglomeration free morphology. The removal of the polydopamine coating by heat-treatment did not negatively affect the aqueous dispersibility of separated HNTs (Figure 29E). Grade 1, grade 2 and grade 3 HNTs obtained with the three-step separation protocol followed by the polydopamine coating removal were easily dispersed in water and presented colloidal stability for at least six hours. These results demonstrated that the three-step separation protocol to obtain uniform and agglomeration free HNT fractions can safely be followed with a heat treatment step to remove the polydopamine coating in cases where the polydopamine coating would interfere with the desired application.

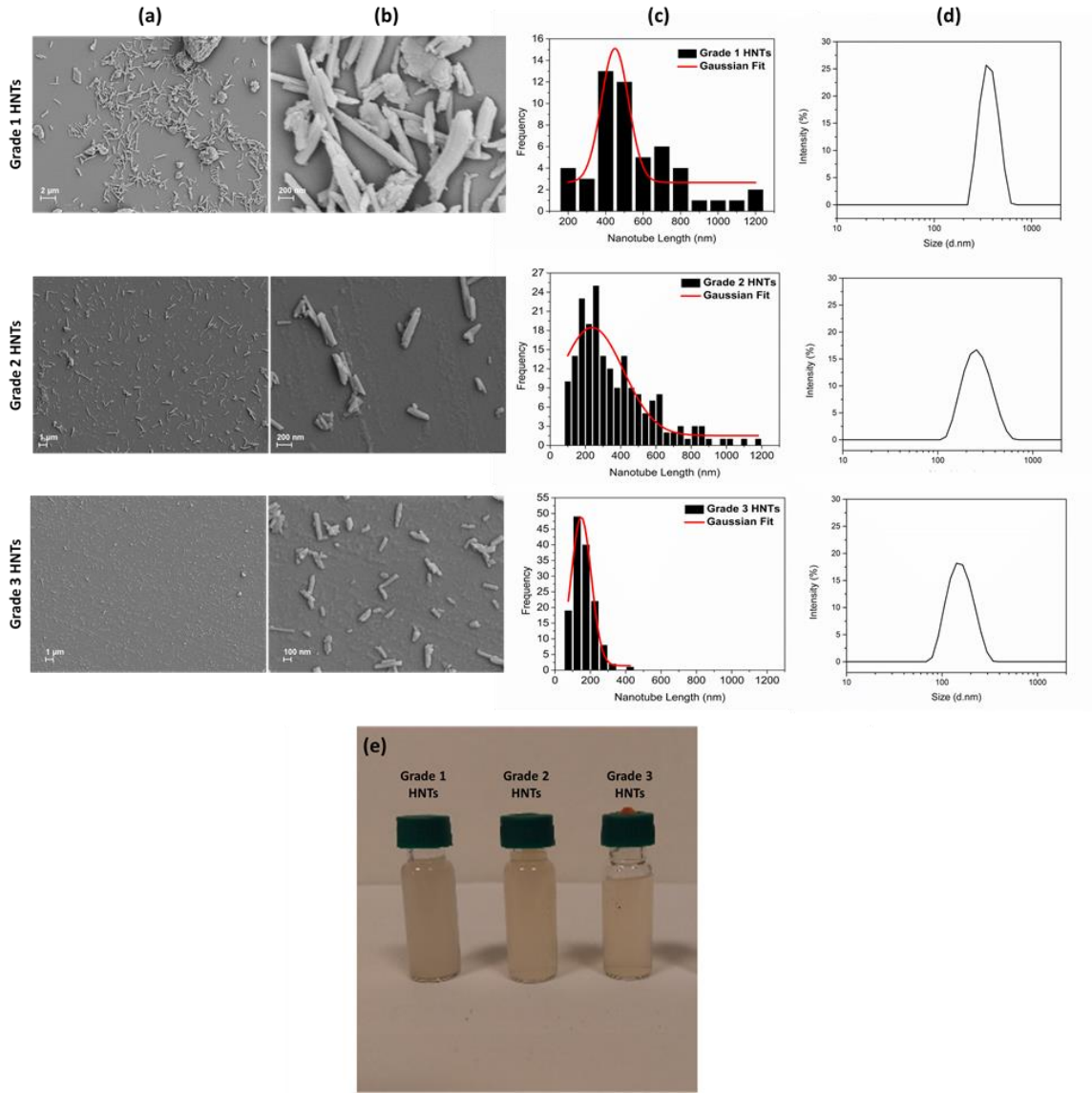


Figure 29. Analysis of grade 1, grade 2 and grade 3 HNTs following the removal of the polydopamine coating by heat-treatment, a) representative SEM images at 10K magnification, b) representative SEM images at 100K magnification, c) nanotube length distributions histograms from SEM image analysis, d) size distribution histograms obtained by DLS, e) Aqueous dispersions of HNTs after six hours of storage at room temperature.

The effect of the treatments applied during the three-step separation protocol and removal of the polydopamine coating on the crystal structure of HNTs was also investigated (Figure 30). The XRD pattern of raw HNTs reflected the characteristic crystal structure of Halloysite-10Å, which included the (001) peak at 2θ of 11.91° , (100) peak at 2θ of 20.17° indicative of the tubular halloysite structure and the (002) peak at 2θ of 24.8° ²⁹¹. The XRD pattern of HNTs did not change following the treatments, indicating that the crystal structure of HNTs was not affected and the tubular nanostructure was retained. Furthermore, peaks corresponding to quartz (*) and kaolinite (#) impurities²⁷⁴ visible in the patterns of raw HNTs and in grade 1 HNTs were not present in the XRD pattern of grade 2 and grade 3 HNTs demonstrating that the three-step separation protocol also facilitated the purification of impurities in raw HNTs. Removal of impurities in HNTs via centrifugation of surfactant-assisted dispersions has been demonstrated before^{7,292}. In our work, without the use of any surfactants, HNTs were well dispersed in water due to the polydopamine modification which allowed centrifugation-based removal of non-tubular clay impurities. These results demonstrated that the three-step separation protocol provides a tool for not only the preparation of agglomeration-free, monodisperse fractions but also the removal of impurities from raw HNTs.

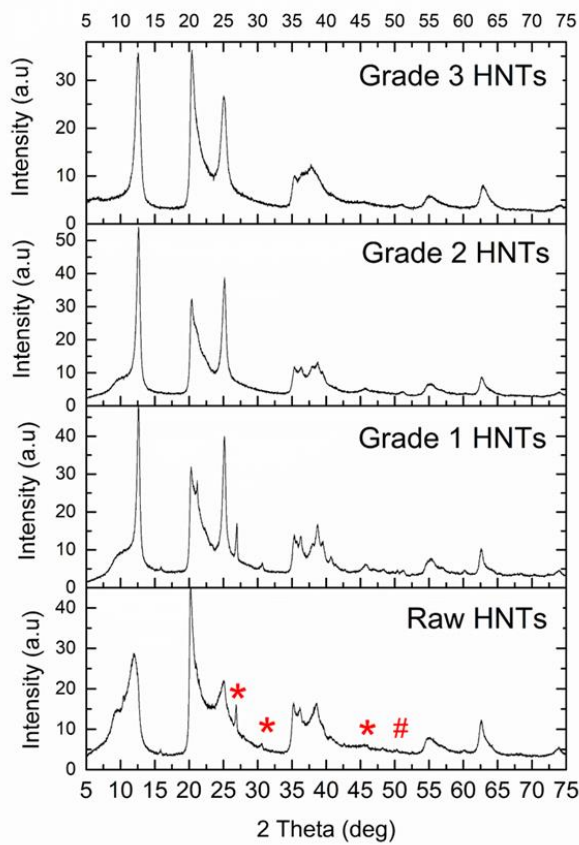


Figure 30. XRD analysis of raw HNTs; grade 1, grade 2, and grade 3 HNTs following the removal of the polydopamine coating.

The effect of the three-step separation on the covalent functionalization and loading capacity of HNTs was critical to understand. In order to investigate the loading capacity of separated HNTs obtained by the three-step separation method followed by the removal of the polydopamine coating; they were loaded with carvacrol as a representative active component through vacuum application. The weight percentage of the loaded carvacrol for separated HNTs was calculated through TGA analysis (Figure 31A). While raw HNTs were loaded with 5.8 wt% carvacrol, under the same experimental conditions, the loading capacity of grade 1 HNTs was slightly lower, where they were loaded with 3.5 wt % carvacrol. Apparently, grade 1 HNTs included an increased content of quartz and kaolinite impurities that had been observed in the XRD spectrum of both raw and grade 1 HNTs. On the other hand, the loading capacity of grade 2 and grade 3 HNTs significantly increased and reached 23.8 wt% for grade 3 HNTs which is four times higher than the loading capacity of

unseparated raw HNTs. This significant increase in the loading capacity can be explained with the fact that grade 2 and 3 HNTs have been purified from agglomerated nanotubes and other impurities which cannot be loaded to their fullest capacity due to inadequate dispersion in carvacrol and reduced surface area. The three-step separation method provided an effective tool to obtain agglomeration-free and uniform HNTs that can be loaded with active materials at significantly higher contents that were not reported before.

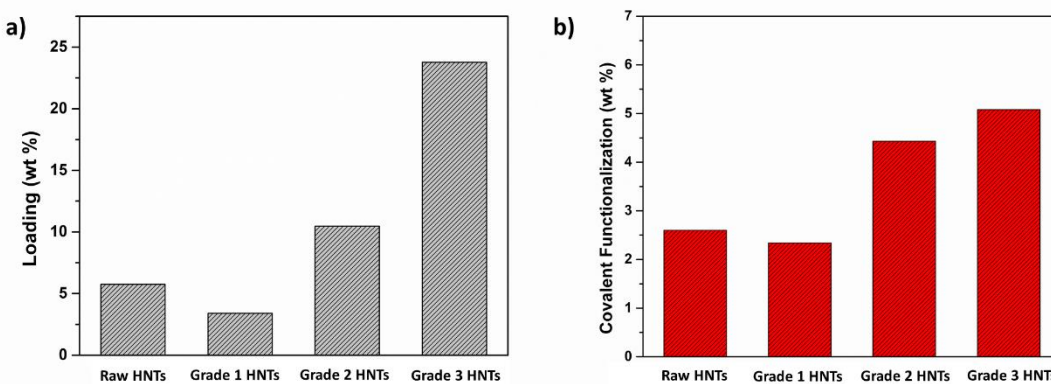


Figure 31. Functionalization yields of separated HNTs of different quality grades along with raw HNTs calculated by TGA analysis. a) Yields of loading with carvacrol (b) Yields of covalent functionalization with SDS.

The impact of the three-step separation on the covalent functionalization yield of HNTs was also investigated. The content of reactive hydroxyl groups on separated HNT surfaces was increased through alkaline treatment²⁹³, which were then reacted with sodium dodecyl sulfate (SDS) through a condensation reaction. The functionalization reaction was followed and verified by FTIR analysis (Figure 32). The amount of covalently attached SDS on HNTs was determined by TGA (Figure 31B). While raw HNTs were functionalized with SDS by 2.6 wt.% only, grade 2 and grade 3 HNTs were functionalized by 4.4 wt.% and 5.1 wt. %, respectively. As the monodispersity of HNTs increased and agglomerations were minimized, more functional groups were available on the outer surface of HNTs, by which the functionalization efficiency increased more than two-fold compared to the functionalization rate of unprocessed raw HNTs. The relatively low yield for grade 3 HNTs may correspond to increased costs for such materials, despite the relatively low cost of commercially available

raw HNTs. However, the three-step separation method presented in this study would now allow the use of these high purity HNTs with significantly increased loading and functionalization capacities as well as better defined size distributions as nanocontainers in various high value-added applications such as active food packaging and drug delivery.

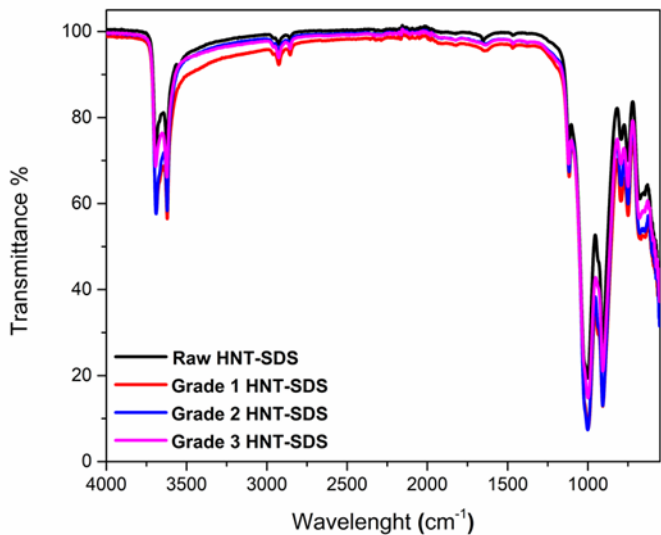


Figure 32. FT-IR spectrum of SDS functionalized raw HNTs and separated HNTs (Grade 1,2,3).

The effect of the monodisperse and agglomeration-free character of separated HNTs on the characteristics of polymeric HNT nanocomposites was also studied. HNTs separated into different quality grades and heat treated for the removal of the polydopamine coating were incorporated into low density polyethylene (LDPE) through melt compounding and nanocomposite blown films were prepared. The HNT content in the prepared nanocomposite films was chosen to be 1 wt% as an optimum value based on our previous study that focused on the effect of HNT content on LDPE-based nanocomposite film properties.²⁶⁰ SEM visualization of resulting film surfaces demonstrated that the separation process applied to raw HNTs positively affected the dispersion quality of HNTs within the polymer matrix (Figure 33A). While nanocomposite films containing raw HNTs presented an inhomogeneous distribution of nanoparticles with several agglomerations, nanocomposite films prepared with grade 2 and grade 3 HNTs presented a significantly better dispersion in

the LDPE matrix. The films containing the highest quality HNT fraction, grade 3 HNTs, was almost free of agglomerations. The improved dispersibility of higher quality monodisperse HNTs has also positively impacted the mechanical properties of resulting nanocomposite films (Figure 33B). While nanocomposite films prepared with raw HNTs did not present any improvement in Young's modulus, tensile strength and elongation at break values compared to neat LDPE films, mechanical properties of nanocomposite films significantly increased as a function of the separated HNT grade quality when compared to raw HNT reinforced nanocomposite films. Compared to less uniformly dispersed, agglomerated raw HNTs present in the LDPE matrix as evidenced by SEM analysis, the uniform dispersion of individual, significantly less agglomerated HNTs, especially grade 2 and grade 3 HNTs, resulted in the improvement of the Young's Modulus and the tensile strength, demonstrating the true nano-scale reinforcement effect.

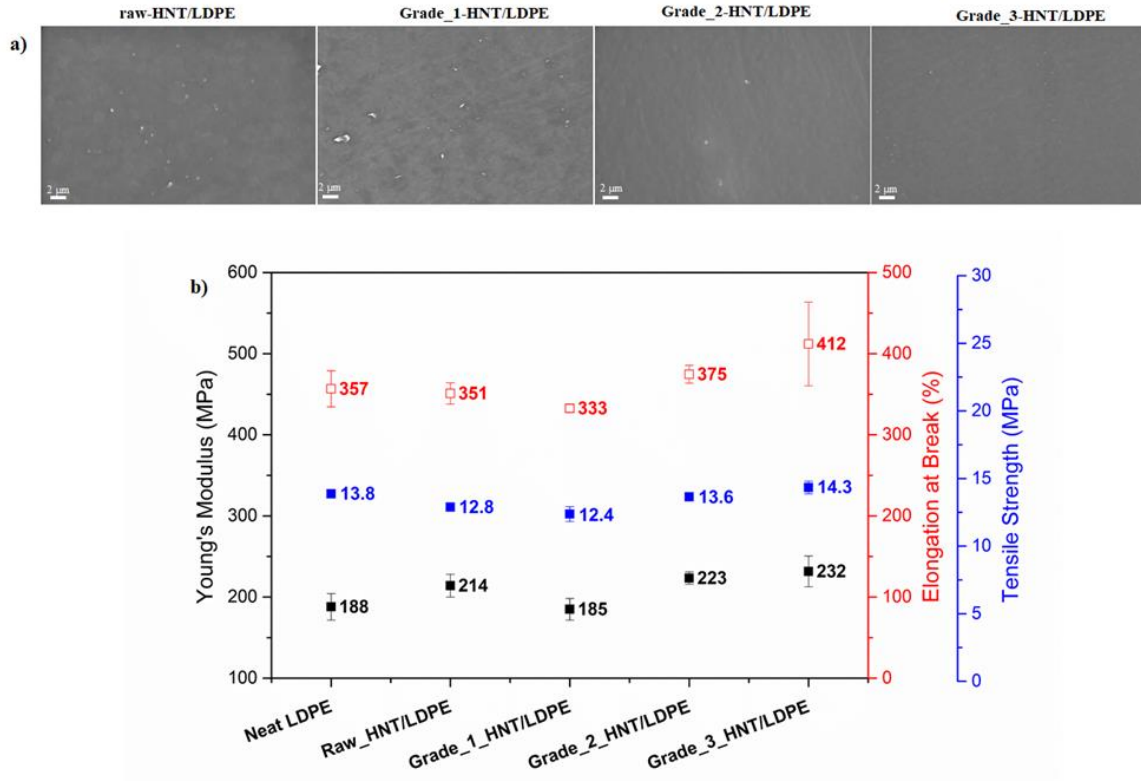


Figure 33. a) SEM images of surfaces of nanocomposite films composed of LDPE and HNTs, b) Mechanical parameters of HNT/LDPE nanocomposite films containing different quality grade HNTs in comparison to neat LDPE films.

4.5. Conclusion

Halloysite nanotubes were successfully separated into monodisperse, agglomeration-free fractions of different sizes through a facile three-step separation process that includes (i) coating of HNT surfaces with polydopamine, (ii) ultrasonication and (iii) hydrophilicity-based centrifugation. The polydopamine coating on the surface of HNTs imparted hydrophilicity and aqueous dispersibility which allowed the sorting of HNTs via centrifugation. Following the separation process, the polydopamine coating was completely removed through a simple heat treatment step. Resulting fractions of HNTs were demonstrated to be uniform in size and shape and preserved their intact nanotubular forms and crystal structures. The method allowed the sorting of raw polydisperse HNTs into fractions of different quality grades based on the velocity of centrifugation; while grade 1 HNTs obtained at low centrifugation velocity presented larger diameters with more

agglomerations, grade 3 HNTs obtained at higher centrifugation velocity presented smaller diameters with almost no agglomerations. High quality grade HNTs obtained through the separation protocol were shown to present significantly higher lumen loading and covalent surface functionalization capacity compared to raw HNTs. Furthermore, separated higher quality grade HNTs showed better dispersibility in a polymeric matrix and resulting nanocomposite films.

CHAPTER 5: Waterborne Polydopamine/Polyurethane Photothermal Polymer Matrix for Light-to-Heat Conversion

Reference Un-published Journal Article: Cüneyt Erdinç Taş, Ekin Berksun, Deniz Köken, Serkan Ünal and Hayriye Ünal, " Waterborne polydopamine/polyurethane photothermal polymer matrix for light-to-heat conversion".

5.1. Abstract

A novel polydopamine-polyurethane based polymeric matrix with efficient light-to-heat conversion properties, which can initiate light-activated temperature elevations is presented. The polymerization of dopamine monomer in a pre-synthesized aqueous polyurethane dispersion results in hybrid polyurethane-polydopamine particles via the encapsulation of discrete waterborne polyurethane (WPU) particles with photothermal polydopamine. Resulting polydopamine-polyurethane (PDA-WPU) dispersions presented a unimodal particle size distribution and particle sizes that increased as a function of the initial dopamine concentration and polymerization time. Films cast from PDA-WPU dispersions were black-colored and presented a homogeneous morphology with contact angles that decreased with increasing PDA content. While the thermal decomposition behavior and thermal conductivity values of hybrid PDA-WPU films were improved relative to neat WPU films, the glass transition temperatures remained unaffected and films presented acceptable mechanical properties. Light-to-heat conversion capacity of PDA-WPU films was investigated under solar and near-infrared (NIR) laser light irradiation. PDA-WPU films prepared with the highest amount of polydopamine reached 105.8°C when irradiated with solar light at 3 SUN for 20 minutes. Five minutes of irradiation with NIR laser light at 800 mW/cm² elevated the temperatures of the PDA-WPU films from room temperature to 138.6 °C. Moreover, PDA-WPU dispersions were molded in the form of a container to investigate their potential in

solar-driven water-evaporation applications. 3.17 kg/m^2 water was evaporated from PDA-WPU containers under solar irradiation in one hour. The hybrid PDA-WPU polymer matrix prepared via a facile post-synthesis modification of WPU dispersions offers strong photothermal activity and ease of applicability without the need of supporting-materials for polydopamine, such as nanoparticles; thus, can be viewed as a promising candidate for a wide range of photo-driven applications.

5.2. Introduction

Photothermal materials can efficiently convert light-to-heat by the non-emissive deactivation of harvested light resulting in significant local temperature elevations. The heat generated by the light-activation of photothermal materials can trigger a multitude of thermal processes which are easily controllable. Light-to-heat conversion properties of photothermal materials can be utilized in a wide range of critical applications including the disruption of tumors by laser light²⁹⁴⁻²⁹⁶, light-activated sterilization of surfaces by killing microbes^{297,298}, solar-driven water evaporation for desalination/purification^{113,299}, light-activated controlled release of molecules³⁰⁰⁻³⁰² and design of light-activated shape-memory/self-healing materials^{123,303}.

Photothermal materials are commonly designed by the incorporation of photothermal nanoparticles into a main matrix that is selected according to the requirements of the application. Photothermal nanoparticles, which impart light-to-heat conversion properties to the matrix they are incorporated, can be categorized as metallic nanoparticles such as gold and silver nanoparticles; carbon-based nanoparticles such as graphene oxide, carbon nanotubes, and inorganic semi-conductors such as black titania, copper phosphate and SnSe⁵⁶. Although the above-mentioned nanoparticles present significant photothermal conversion capacities, many disadvantages such as toxicity, incompatibility with polymer matrices, dispersion problems, environmental issues, concerns about the reliability/reproducibility and increased cost restrict the wide range application of the final nanocomposites³⁰⁴⁻³⁰⁶. Some semiconducting organic polymers with strong light absorption capacities such as polyaniline, polypyrrole and polydopamine are also well-known for having light-to-heat conversion capacities and applied as key components of photothermal materials^{112,307,308}. Photothermal polymers absorb light via their delocalized π -electrons and

convert it to heat likely via nonradiative relaxations and molecular vibrations in the polymer backbone⁶⁴.

Among other photothermal polymers, polydopamine (PDA), the mussel-inspired polymer, stands out with its distinct physical properties in addition to its intrinsic photothermal capacity. PDA, synthesized by the oxidative self-polymerization of dopamine, has strong adhesive properties due to its catechol groups³⁰⁹, which enable it to be coated to almost any kind of surfaces ranging from wood³¹⁰ and oil droplets³¹¹ to polymers^{312,313} for a wide variety of applications⁷¹. Since the polymerization of dopamine occurs either on a substrate resulting in PDA coated surfaces or via the aggregate formation resulting in PDA particles, it is generally employed as a component in a hybrid system rather than a monolithic, homogeneous polymer matrix in light-to-heat conversion systems^{114,115,120,121}. PDA containing polymeric composites have been typically prepared by either coating bulk polymeric material surfaces with PDA or the incorporation of PDA functionalized nanoparticles into the polymer matrix and have been utilized in various applications ranging from solar driven vapor generation to self-healing materials^{53,117,314-317}. While composites of PDA and polymers have been demonstrated to present significant photothermal properties, they are all in multi-component, heterogeneous forms, which are difficult to fabricate and restrict eco-friendliness, cost-effectiveness, and the ease of applicability of resulting materials. To the best of our knowledge, a monolithic polymer matrix, which can be obtained from a one-component aqueous dispersion and presents strong light-to-heat conversion capacity without the incorporation of any secondary particles has not been previously reported in the literature.

In this study, the preparation and characterization of a novel hybrid polymer matrix composed of waterborne polyurethane (WPU) and PDA is demonstrated. WPU dispersions are prepared from discrete polyurethane solid particles synthesized and dispersed in a continuous aqueous phase and provide a safe, eco-friendly, volatile-organic-compound-free system³¹⁸. Waterborne polydopamine-polyurethane (PDA-WPU) polymer matrix with light-to-heat conversion ability was obtained by coating WPU solid particles with PDA in an aqueous dispersion. PDA-WPU hybrid polymer matrix presented here synergistically combines the characteristics of WPUs and PDA in a feasible way, resulting in photothermal

materials that can be easily applied as single component films or coatings for a variety of applications.

5.3. Materials and Methods

5.3.1. Chemicals

Ethylenediamine (EDA) and acetone (99.5%) were purchased from Sigma-Aldrich Inc. Hexamethylene diisocyanate (Desmodur H) (HDI), and polyester polyol (Desmophen 1652, Mn= 1060 g/mol) were purchased from Covestro AG. Sodium 2-[(2-aminoethyl) amino] ethane sulphonate (AEAS, 50 wt% in water) was kindly donated by Evonik Industries. Polyester polyol was dried at 100 °C under vacuum (~2 mbar) for 15 min prior to use. Dopamine (3-hydroxytyramine hydrochloride) was purchased from Acros Organics Inc. Ultrapure Tris base (Tris(hydroxymethyl)aminomethane) was purchased from MP Biomedicals, LLC. Milli-Q purified water was used for all of the synthesis and characterization stages. All chemicals were used without any further purification.

5.3.2. Synthesis of waterborne polyurethane dispersion

The WPU dispersion was synthesized using the acetone method, in a four-necked, 1-L glass round-bottomed-flask equipped with a heating mantle, stirrer, condenser and a thermocouple. The NCO-terminated polyurethane prepolymer was synthesized from 170.8 g of polyester polyol and 29.0 g of HDI, allowing the mixture to polymerize at 80 °C until reaching the theoretical NCO content, which was determined by the standard di-butyl amine back titration method (ASTM D2572-97). Once the theoretical NCO value was achieved, the reaction temperature was dropped to 50 °C while dissolving the prepolymer in acetone to obtain 40 wt% solid content. Upon the complete dissolution of the prepolymer in acetone, the chain extension step was carried out by adding the mixture of 13.3 g AEAS (50 wt% in water) and 1.9 g EDA dropwise into the solution at 50 °C. The prepared polyurethane polymer was dispersed in water by slowly adding 110.00 g of distilled water into the flask while cooling the mixture to 40 °C. Finally, acetone was removed from the reaction mixture by vacuum distillation, and the complete removal of acetone was ensured at 45 °C, 50 mbar. A WPU dispersion product with the solid content of approximately 35 wt% and pH value of 7.0 was obtained by filtering the final dispersion through a 50-micron filter.

5.3.3. Preparation of PDA-WPU dispersion

PDA-WPU dispersion was synthesized by following a typical PDA coating procedure⁷⁰. 15 g of WPU dispersion with a 35% solids content was diluted with distilled water to 20% solids. 0.042 g of dopamine was dissolved in 2 mL of distilled water (2mg/ml) and the solution was added into the WPU dispersion dropwise using a 5 ml syringe to avoid precipitation/agglomeration. The pH value of the reaction mixture was adjusted to 7.5 using ultrapure Tris base. Three parallel reactions were set-up with reaction times of 24-, 48-, and 72-hours, all at 40 °C. Another set of reactions was repeated with three-fold higher dopamine amount (0.126 g: 6 mg/ml) in the mixture, while all other reaction conditions were kept constant. Dark gray dispersions of PDA-PU were obtained at the end of all coating reactions.

5.3.4. Preparation of PDA-WPU films

Following the PDA-WPU dispersion preparation, reaction mixtures were directly cast onto Teflon molds (15x5 cm²) at room temperature and dried under ambient conditions for three days followed by a 1 hr. drying in an oven at 100 °C. Bubble-free, uniform cast films were removed from the mold and washed with excess amount of distilled water to remove any chemical residues from the surface. Finally, washed films were kept in an oven at 80°C for two hours and stored in a desiccator under dark. The final film thicknesses were measured to be approximately 0.5 ± 0.08 mm.

5.3.5. Characterization

Determination of the hydrodynamic diameter and zeta potential of dispersed WPU and PDA-WPU particles in water was performed using a Dynamic Light Scattering (DLS) instrument (Zetasizer Nano - ZS, Malvern Instruments Ltd., UK) equipped with laser diffraction and polarized light detectors at three wavelengths. Dispersions were diluted with distilled water to an adequate concentration in the cell and measured at room temperature. Zeta potential was measured at the pH value of 7.5 using Helmholtz-Smoulchowski equation.

WPU and PDA-WPU solid particles in aqueous dispersions were imaged using cryogenic transmission electron microscopy (Hitachi HT7800 cryo-TEM). 1–3 µL of freshly prepared dispersion samples were applied to a 200-mesh lacey carbon TEM grid which was subjected to plasma glow discharge with a DV-502A vacuum system for 1 min to increase its wettability. The grid was placed into a Mark III Vitrobot chamber at 22°C with a relative

humidity of 95–100% and blotted to create an electron-transmissible specimen thickness. Then, the specimen was plunged into liquid ethane and cooled by liquid nitrogen to vitrify (Leica EM-GP 2) the sample following 3–5 s of relaxation time. The vitrified specimen was imaged utilizing an FEI Tecnai Spirit BioTWIN at 120 kV with an Eagle 2048×2048 CCD camera. The imaging was performed below -178°C in the microscope, under the focus of 1–6 μm and low-dose mode (<20 e⁻/Å²). The images were processed with the TEM Imaging and Analysis 4.2 software.

Static contact angle measurements on cast WPU and PDA-WPU film specimens under ambient conditions were performed with the sessile-drop method using a Theta Lite Contact Angle Measurement System with an optical tensiometer. The shapes of water droplets were recorded by the optical tensiometer and automatically analyzed from a high-quality image from a high-resolution digital camera, and the accuracy of the drop fitting method. The measurements were taken from five different spots of each sample and average contact angle values were reported.

The surface morphology and cross-section of cast WPU and PDA-WPU films were examined using Zeiss LEO Supra 35VP scanning electron microscope (SEM) employing a secondary electron detector at 3 kV by coating with Au–Pd. Films were cryo-fractured by immersion in liquid nitrogen to obtain cross sections.

A Nicolet IS10 FT-IR spectroscope with an attenuated total reflection system was used for the chemical analysis of film samples.

Thermogravimetric analysis (TGA) of all samples was performed using a Shimadzu Corp. DTG-60H (TGA/DTA) instrument by heating samples of films up to 600 °C with a rate of 10 °C/min under nitrogen atmosphere.

Glass transition temperatures (T_g) of the prepared film samples were investigated using differential scanning calorimetry (DSC; Thermal Analysis MDSC TAQ2000) with a heating rate of 10 °C/min and heat-cool-heat cycles between 120 °C and 150 °C under nitrogen atmosphere. Reported T_g values were taken from the second heating cycle.

The thermal conductivity of films was measured using the Hot Disk Thermal Constant Analyzer (TPS2500 S).

Mechanical properties of films were determined using a universal testing machine Zwick Roell Z100 UTM, with a load cell of 200 N and a crosshead speed of 25 mm/min according to ASTM D1708-10 standard. An average of at least four replicates was reported for each sample.

Evaluation of light to thermal energy conversion performance of PDA-WPU films

The time-temperature profiles of PDA-WPU films were constructed under solar simulator and NIR laser light irradiation. For sunlight exposure, WPU and PDA-WPU film samples of 4x4 cm² with a thickness of 0.5 ± 0.08 mm were irradiated with Oriel LCS-100 solar simulator at 100 mW/cm² and 300 mW/cm² flux density for 20 minutes while recording the temperature of films in one-minute intervals. For NIR laser light exposure, 1x1 cm² WPU and PDA-WPU film samples with a thickness of 0.5 ± 0.08 mm were irradiated with an 800 nm laser module (STEMINC, SMM22808E1200) (Doral, FL USA) at 800 mW/cm² flux density for 5 minutes while recording the temperature of films in 5 seconds intervals. Temperature recordings and thermal camera photographs were taken using FLIR E6XT 2.1L thermal camera. Irradiations for the construction of time-temperature profiles of WPU and PDA-WPU films were repeated three times; measurement data were taken from three different points on the samples, and average values were reported.

Solar-assisted water evaporation using PDA-WPU films

WPU and PDA-WPU (6mg/ml)/72h was molded into a container (2.6 cm diameter) shape using a cylindrical Teflon mold. Prepared containers with an inside volume of 7 cm³ and based thickness of 1.5 mm were filled with 2.32 g of distilled water and exposed to 300 mW/cm² solar irradiation for 60 min. The real-time mass loss over the entire irradiation duration was recorded in 10 min intervals using an electronic mass balance (Shimadzu, BL-320H) with an accuracy of 1 mg. All experiments were performed at room temperature (23 ± 0.5 °C) and humidity of approximately 51.8%.

5.4. Results and Discussions

5.4.1. Synthesis and particle size distribution of PDA-WPU dispersions

PDA-WPU dispersions were prepared by a facile post-synthesis modification of pre-synthesized WPU dispersions with dopamine which resulted in the coating of WPU solid particles in water with PDA. WPU particles were coated with dopamine through an efficient one-pot reaction in water to obtain an aqueous dispersion of solid PDA-WPU particles. Although the oxidative self-polymerization of dopamine has generally been carried out at a pH of 8.5, lower pH values have also been demonstrated to be practical²⁸⁷. In this study, the pH value of the reaction medium during the oxidative self-polymerization of dopamine was adjusted to pH 7.5 to preserve the characteristics of the WPU dispersions. The chemical structure of the WPU along with the synthesis pathway for PDA-WPU matrix is presented in Figure 34.

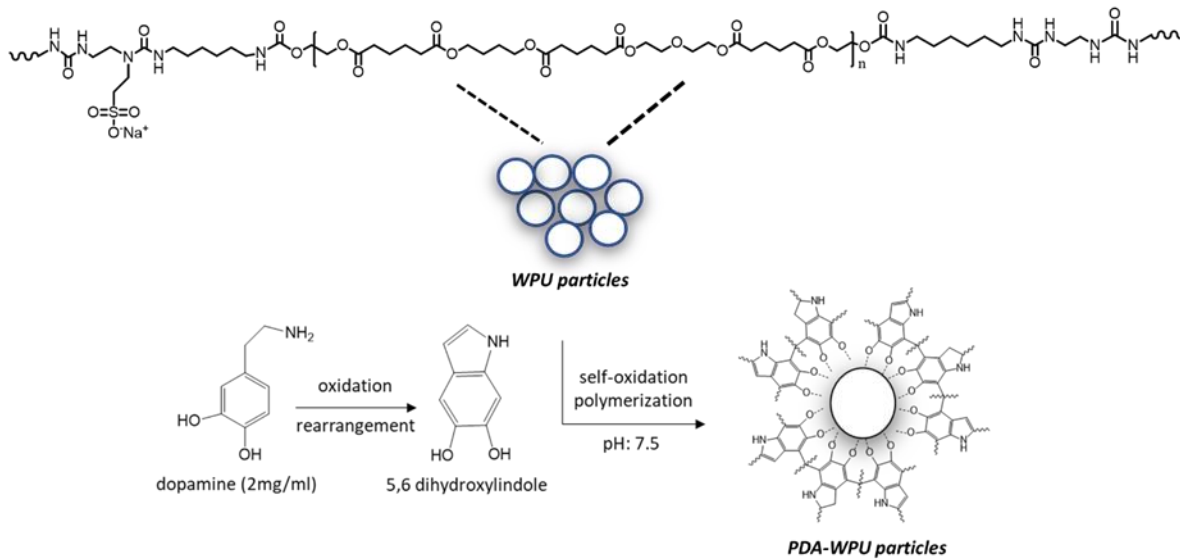


Figure 34. Structure of synthesized WPU and the synthesis pathway for PDA-WPU particles.

The particle size of WPU particles in the dispersion has a significant impact on the ultimate morphology and quality of films and coatings prepared from these dispersions³¹⁹. The particle size and zeta potential of PDA-WPU dispersions prepared with varying initial dopamine concentrations and reaction times were investigated (Figure 35). Just like the neat WPU dispersion, all PDA-WPU dispersions prepared at varying reaction conditions presented a unimodal size distribution (Figure 35A). The lack of an additional peak on the

particle size distribution graph demonstrated that dopamine polymerization took place on WPU particle surfaces acting as a substrate, resulting in hybrid PDA-PU particles and the self-polymerization of dopamine leading to pure PDA particles did not occur. The z-average diameter of PDA-WPU particles were significantly larger than WPU particles and the diameter of PDA-WPU particles increased with increasing initial dopamine concentration and polymerization times, further confirming that the PDA forms a coating layer on PDA-WPU particles, thickness of which can be controlled by the polymerization reaction conditions (Figure 35B). A similar trend in increasing solid particle diameters upon PDA coating was demonstrated in studies in which PDA polymerization was performed on different solid particles^{311,313}.

The zeta potential provides two important pieces of information on the properties of dispersed particles including surface charge in relation to the pH value of the medium and colloidal stability of particles in the dispersion³²⁰. Results presented in Figure 35C show that zeta potential values increased with increasing amount of PDA coating on WPU solid particle surfaces. While the differences in zeta potential values were not significant for PDA-WPUs, which were synthesized with an initial dopamine concentration of 2mg/ml at increasing reaction times, three-fold increase in the initial dopamine concentration (6 mg/ml) resulted in a significant increase in zeta potential values. Apparently, the strong ionic content of WPU particle surfaces was screened with the quinone, catechol and amine groups of the PDA coating layer³²¹⁻³²³. While the PDA coating on WPU surfaces resulted in higher zeta potential values, particle surfaces remained negatively charged. Moreover, the zeta potential value of PDA-WPU (6mg/ml)/72h almost passed to incipient instability level³²⁴, probably due to the interaction between PDA-WPU particles caused by the substantial adhesion property of the PDA making particles slightly stick to each other³²⁵. All DLS results confirmed the formation of a PDA layer on WPU particle surfaces instead of formation of individual PDA particles. The PDA coating on PU particle was visualized with cryo-TEM (Figure 35D). When coated with PDA, the smooth surface of PU particles became textured and irregular presenting a darker color due to a denser electron density confirming the formation of PDA-WPU particles.

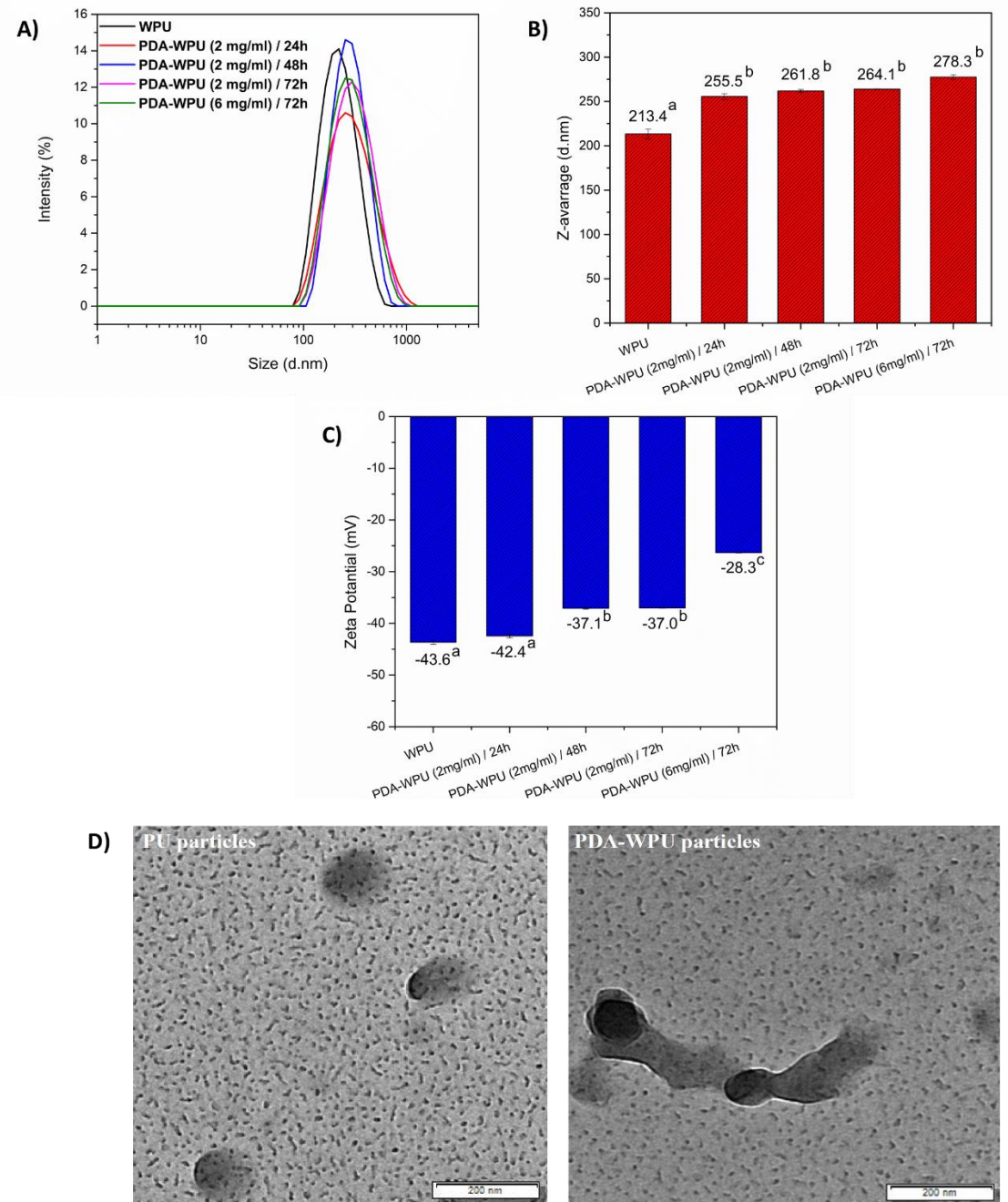


Figure 35. Particle size distribution (a), z-average diameter (b) and zeta potential (c) values of WPU and PDA-WPU dispersions by DLS analysis (Values sharing a common letter (a–c) within the same bar are not significantly different). TEM images of WPU and PDA-WPU solid particles (d).

5.4.2. Physicochemical and morphological properties of PDA-WPU films

The general appearance of WPU and PDA-WPU films cast from aqueous dispersions are presented in Figure 36A. While WPU films have a white/transparent appearance, PDA-WPU films are black-colored due to the PDA content.

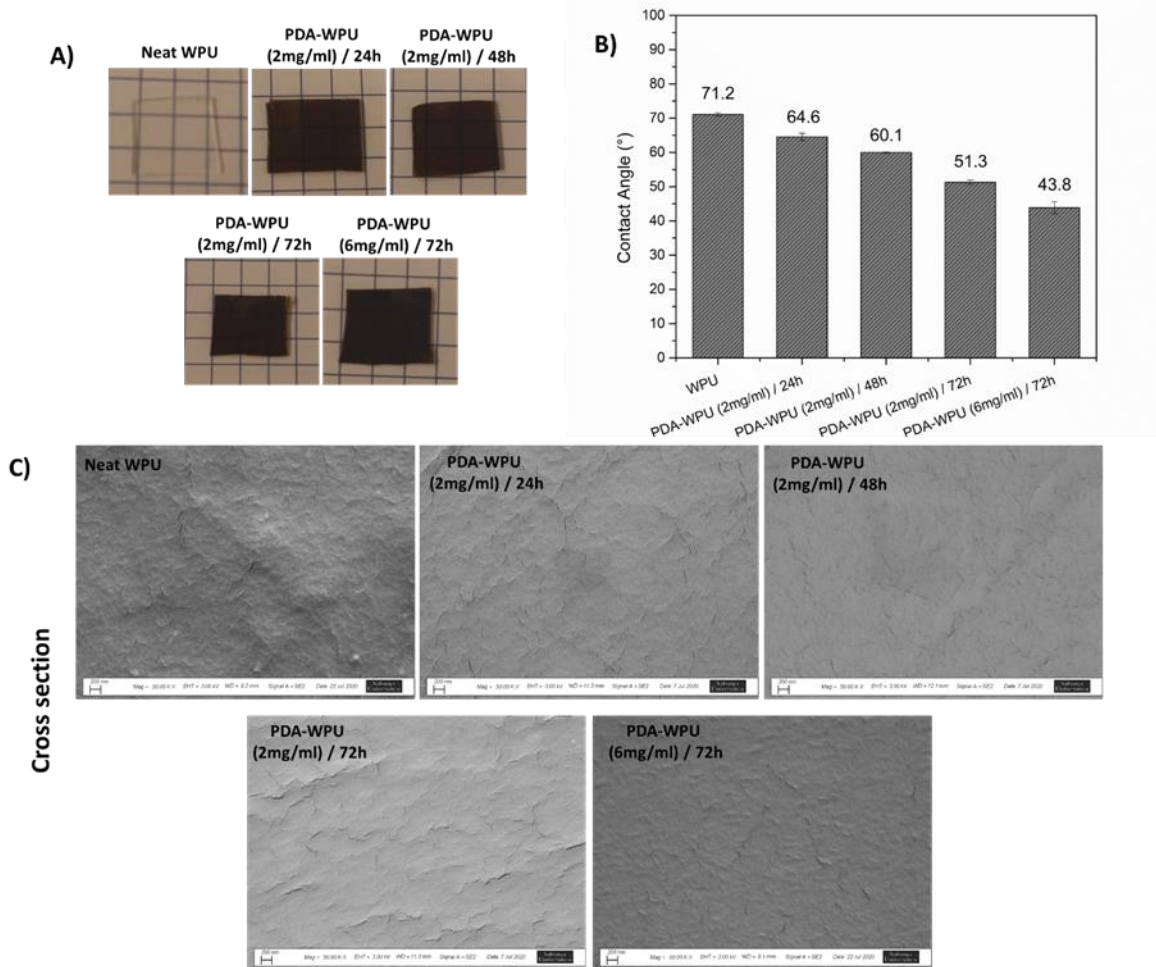


Figure 36. Photographs (A) contact angle values (B) and cross-section SEM images (C) of WPU and PDA-WPU films.

Surface wetting properties of PDA-WPU films were investigated via water contact angle measurements (Figure 36B). As expected, increasing the PDA content of prepared films by increasing the polymerization time and initial concentration of dopamine reduced water

contact angle values, which indicates an increased hydrophilic character for film surfaces due to the hydrophilic nature of the PDA layer³²⁶⁻³²⁸.

The morphology of WPU and PDA-WPU films were studied by SEM imaging. While cross-section images of WPU and PDA-WPU did not display any significant differences as shown in Figure 36C, the fact that free polydopamine particles were not observed in any of the PDA-WPU cast films was an important observation confirming the formation of PDA layers only on WPU particles rather than individually crosslinked, immiscible PDA particles¹²³.

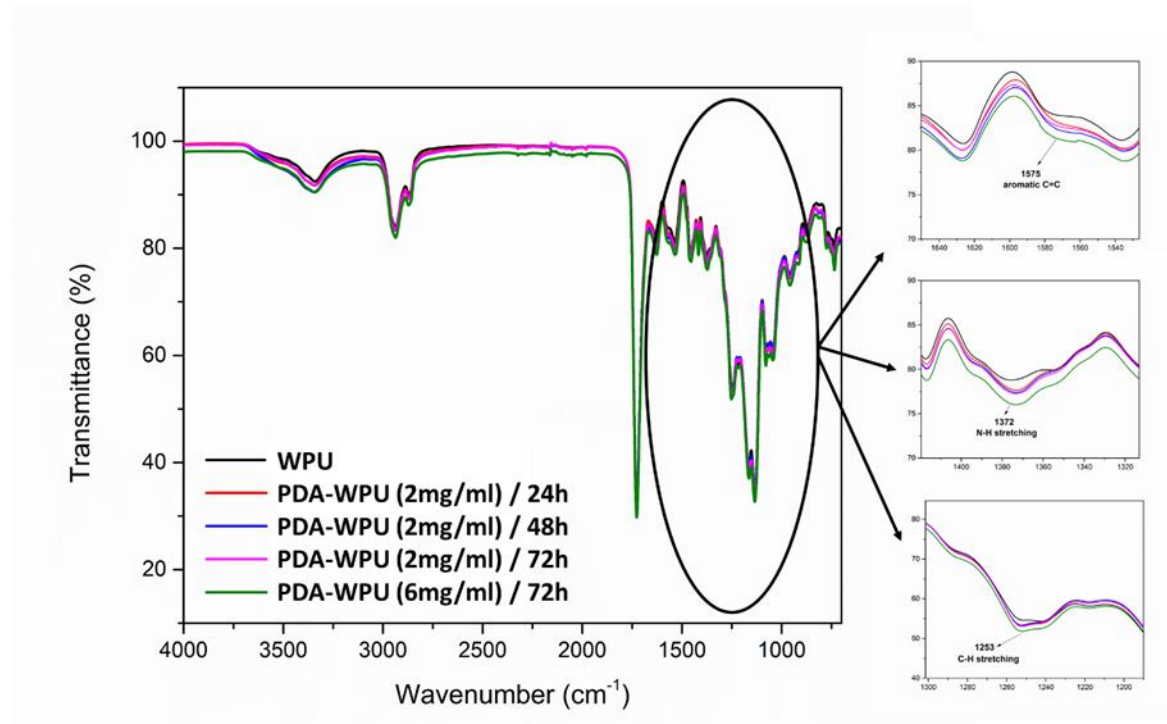


Figure 37. FT-IR analysis of WPU and PDAPU films.

The chemical analysis of WPU and PDA-WPU films was performed by FT-IR analysis (Figure 37). On the FT-IR spectrum of WPU, characteristic peaks at around 3365-3385 cm⁻¹ were observed arising from -NH bonds of urea and urethane groups. The peaks at 2870-2940 cm⁻¹ region correspond to the -CH stretching and the strong absorption bands around 1725 cm⁻¹ were attributed to the carbonyl stretching region³²⁹. For the PDA-WPU films, new peaks originating from PDA content appeared on the spectrum, which can be listed as the aromatic C=C double bond at 1575 cm⁻¹, symmetric and asymmetric -NH stretching vibrations at

1372 cm⁻¹ and C–N stretching at 1253 cm⁻¹, confirming the presence of the PDA in the cast films.

5.4.3. Thermal properties of PDA-WPU films

Thermal properties of PDA-WPU films were analyzed and summarized in Table 6. The decomposition temperatures calculated for all PDA-WPU films prepared with increasing PDA content were significantly higher than decomposition temperatures of neat WPU films. The increased thermal stability of PDA-WPU films was ascribed to the presence of PDA in the polymer matrix³¹³. Because the T_g of WPU matrices is one of the major factors that reflects their morphology and determines mechanical properties³³⁰, the effect of PDA content on the T_g values of film samples was examined by DSC analysis. No significant changes were found in the T_g values of PDA-WPU films when compared to WPU films. Results demonstrated that PDA-WPU matrices preserved their low temperature T_g values, which is an important property for PU-based elastomeric coatings and films.

Table 6. Thermal decomposition, glass transition temperature and thermal conductivity values of WPU and PDA-WPU films. Values having a different letter (a–d) within the same column are significantly different.

	T_D (10 wt.%) (°C)	T_D (50 wt.%) (°C)	T_D (80 wt.%) (°C)	T_g DSC (°C)	Thermal Conductivity (W/m°K)
WPU	314.1	379.8	402.6	-42.9	0.1462 a
PDA-WPU (2mg/ml) / 24h	320.1	399.1	414.3	-42.3	0.2078 b
PDA-WPU (2mg/ml) / 48h	324.8	403.8	419.5	-43.1	0.2088 b
PDA-WPU (2mg/ml) / 72h	330.3	407.1	423.3	-43.3	0.2249 c
PDA-WPU (6mg/ml) / 72h	323.3	395.6	412.4	-43.8	0.2316 d

The thermal conductivity of materials is always a critical phenomenon in systems designed with the concept of light-to-heat conversion. An intrinsically low thermal conductivity is favorable for heat management and prevention of thermal energy loss and thermal transfer so that generated heat can be utilized effectively³³¹. The thermal conductivity of neat WPU films, which was measured to be 0.1462 W/m°K almost doubled for PDA-WPU (6 mg/ml)/72h films and was read as 0.2316 W/m°K. Enhancement of thermal conductivity of

films with the PDA content can be explained by the hydrogen bonding and π - π stacking tendencies, as well as the increased aromatic content originating from the PDA structure⁷¹. Hydrogen bonding may improve the inter-chain coupling to form continuous thermal networks resulting in heat-transferring pathways. The existence of sp^2 hybridization in the PDA structure might also be providing higher thermal conductivity due to the bonding energy and formation of delocalized conjugated π -bonds. Moreover, strong noncovalent inter-chain interactions due to the aromatic structure of the PDA may be further enabling π - π stacking. Consequently, due to the fact that thermal conductivity of chains with aromatic-backbone networks is much higher than that of aliphatic-backbone structures, thermal conductivity of prepared PDA-WPU films was found to be higher than WPU films³³².

5.4.4. Mechanical properties of PDA-WPU cast films.

The mechanical properties of PDA-WPU films were investigated by the measurement of Young's Modulus (YM), Tensile Strength (TS), and Elongation at Break (EB) values in comparison with the mechanical properties of WPU films (Figure 38). It is known that elastomeric materials have weak intermolecular forces, thus they exhibit generally low YM and high strain at break compared to other materials³³³. While the YM values of PDA-WPU films were measured to be lower than the YM values of WPU films in general, there was no correlation with the amount of PDA in the films. Conversely, EB values of PDA-WPU films proportionally increased with respect to dopamine polymerization times. While the EB value of WPU was found as 1824 %, the elongation of PDA-WPU films gradually reached 2178 % as a function of the dopamine polymerization time at constant initial dopamine concentration of 2 mg/ml. The results indicate that PDA-WPU films exhibited a more flexible character than WPU films, which ascribed to the disruption of the intermolecular forces between the hard segments (urethane and urea) of PU chains by the introduction of PDA into the matrix. Therefore, PDA-WPU films prepared with the PDA coated particles using 2 mg/ml dopamine solution showed lower TS and YM values than WPU films but higher elongation at break values¹²². Increasing the PDA content by three-fold increase in the initial dopamine concentration from 2 mg/ml to 6 mg/ml was presumed to result in further disruption of the polyurethane morphology, yielding decreased YM, EB and TS values compared to the neat WPU film. Potentially, the contribution of cohesive forces arising from the increasing PDA content leads to this observed change in mechanical properties³³⁴.

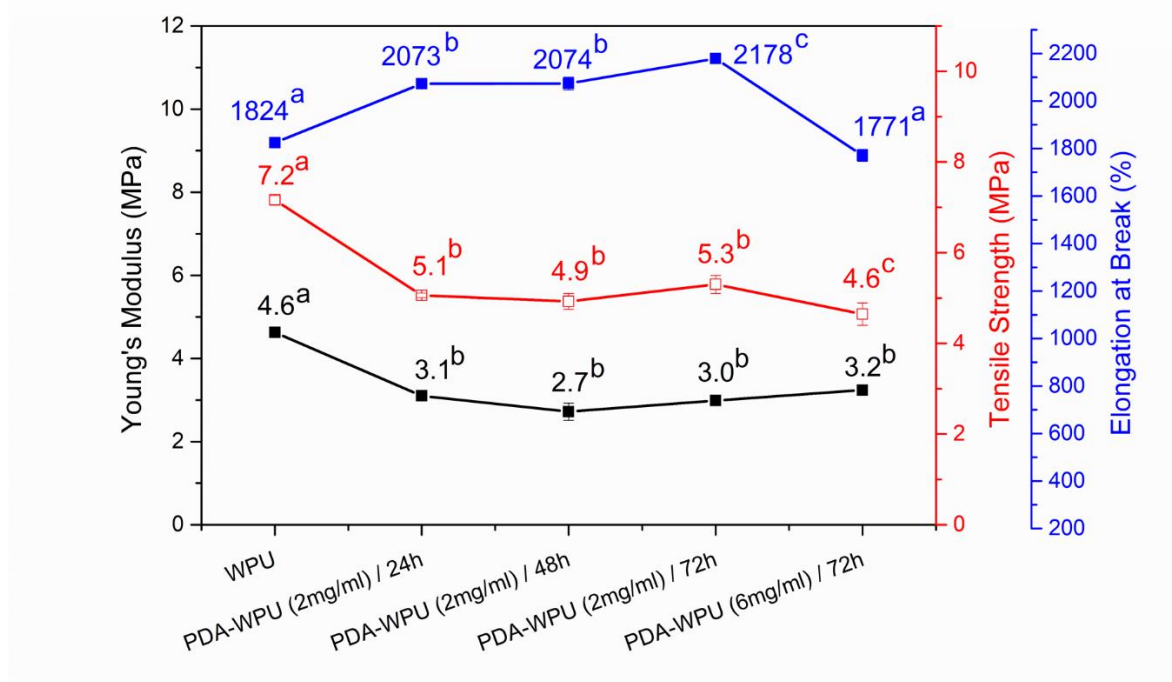


Figure 38. Mechanical properties of WPU and PDA-WPU films. Values in the same group sharing a common letter (a-c) are not significantly different.

5.4.5. Light-to-heat conversion in PDA-WPU films

The light-to-heat conversion ability of PDA-WPU films were investigated under different light sources and irradiance values. Figure 39A shows time-temperature profiles of WPU and PDA-WPU films with varying PDA contents which were irradiated with sunlight under 1 SUN (100 mW/cm^2) and 3 SUN (300 mW/cm^2) intensity. PDA-WPU films presented significant temperature elevations under sunlight irradiation and reached temperatures which were 15°C to 25°C and 40°C to 65°C higher than temperatures reached by control WPU films under 1 SUN and 3 SUN, respectively. The temperature elevation in PDA-WPU films was proportional to the PDA content in the films. The PDA-WPU (6mg/ml)/72h film sample prepared with the highest initial dopamine content presented the highest temperature increase and reached 115.4°C in 20 min under solar irradiation at 3 SUN.

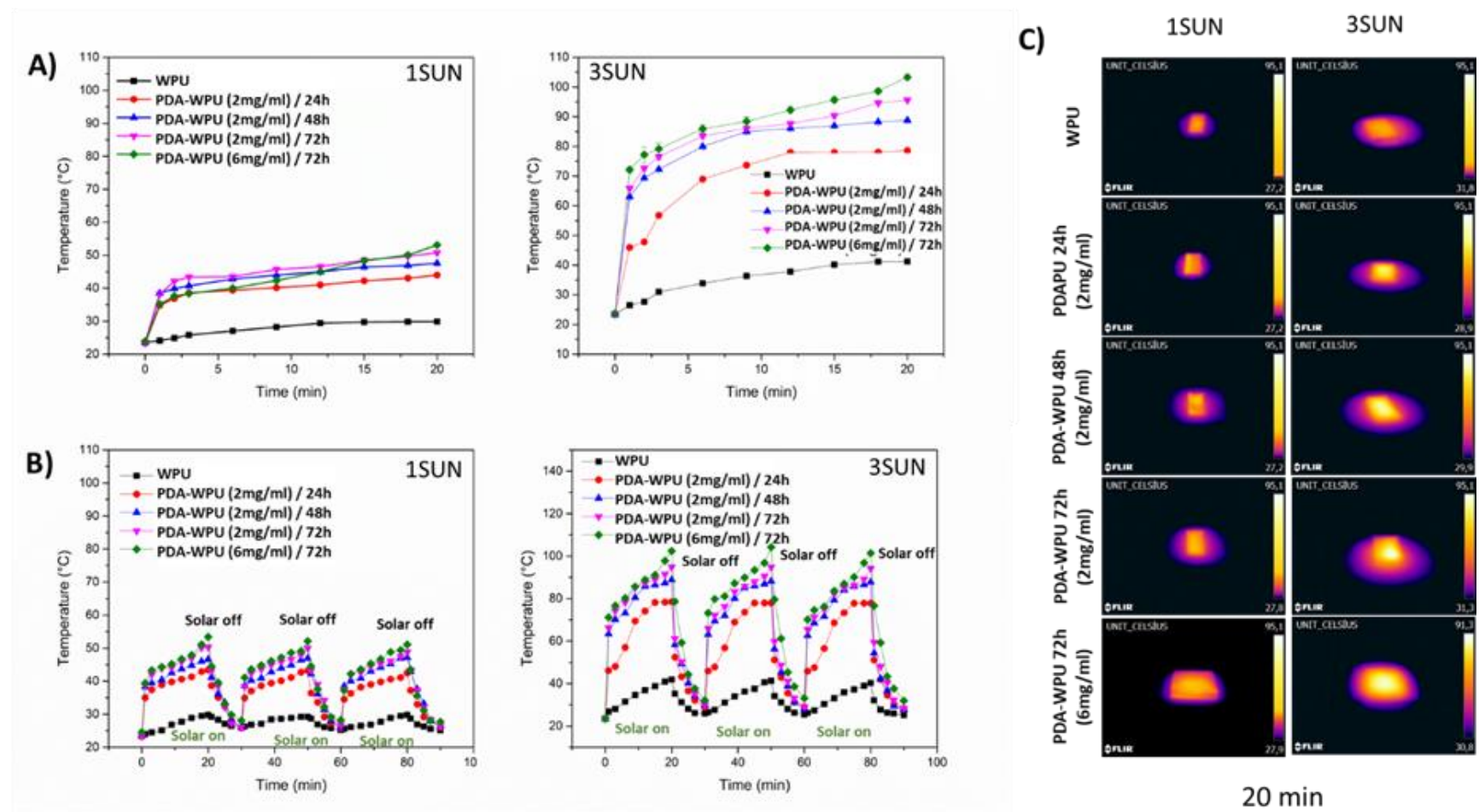


Figure 39. Time-temperature profiles (a), solar irradiation cycles (b) and thermal camera images (c) of WPU and PDA-WPU films under sunlight at 1SUN and 3SUN irradiance.

Under the same conditions, WPU films, which did not have any PDA content scarcely attained 39.4 °C, which highlighted the effect of PDA content on solar to thermal energy conversion capacity of PDA-WPU films. Thus, it was demonstrated that a typical WPU was converted to a photothermal polymer matrix by coating WPU solid particles in the aqueous dispersion form with a PDA layer. Repeatable use of PDA-WPU films was also tested and results were presented in Figure 39B. Photothermal heating ability of all PDA-WPU films remained robust after three cycles of solar light exposure, meaning that they exhibited adequate stability under reported photothermal heating conditions, which is a critical requirement in many different applications of such materials. Thermal camera images of films taken at the end of the 20 minutes irradiation under sunlight further demonstrated the sunlight-activated heating of PDA-WPU films (Figure 39C).

Although the main focus of scientific studies in the light-to-heat conversion concept has been intensified on solar energy because of its abundance and being a natural resource, the activation of photothermal materials with near infrared (NIR) laser light has found critical applications especially in the field of medical science³³⁵⁻³³⁸ or antimicrobial materials³³⁹⁻³⁴¹. Laser light to thermal energy conversion capacity of PDA-WPU films was also investigated in this study. Similar to the results obtained with solar light irradiation, the PDA-WPU (6mg/ml)/72h film samples achieved the highest measured temperature after 5 min and reached 138.6 °C, while the temperature of the control WPU film remained unchanged for the same exposure time (Figure 40A). Just like their stability under sunlight irradiation, all film samples presented stability under photothermal heating conditions after three cycles of NIR laser light exposure (Figure 40B). Thermal camera images of WPU and PDA-WPU films taken at the end of 5 min irradiation under NIR laser demonstrated the increased photothermal heating of films with increasing PDA content. The fact that the warming area of the samples enlarged from the WPU toward PDA-WPU (6mg/ml)/72h film samples further indicated enhancement in the thermal conductivity of PDA-WPU films.

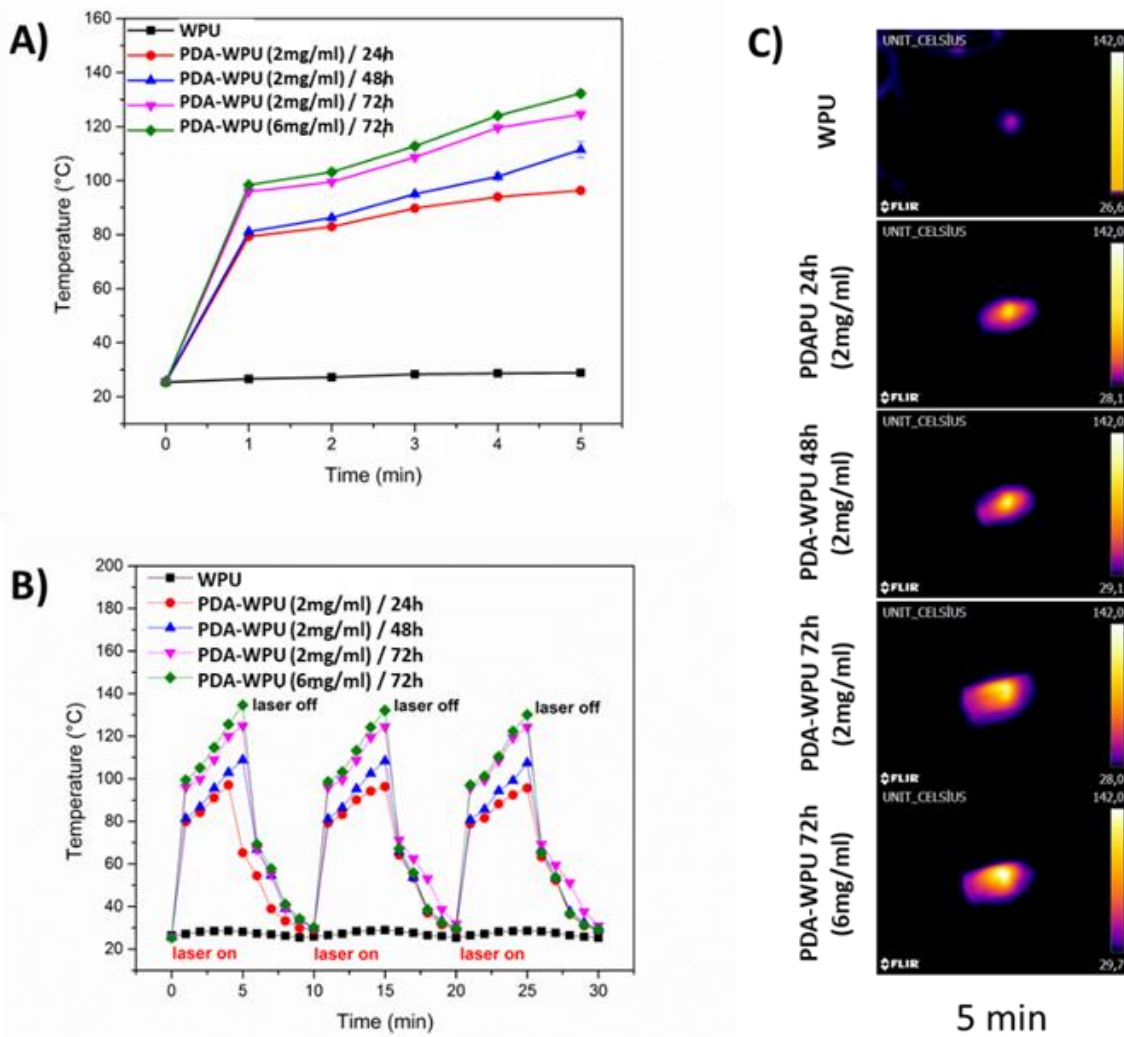


Figure 40. Time-temperature profiles (a), NIR laser light irradiation cycles (b) and thermal camera images (c) of WPU and PDA-WPU films under 808 nm laser light at 800 mW/cm² irradiance.

A comparison of the properties of photothermal materials for similar applications such as energy storage, water evaporation or antimicrobial systems reported in the literature along with the properties of the PDA-WPU materials developed in this study is summarized in Table 7. Various materials were designed by combining different nanoparticles and polymeric structures to create photothermal composite materials for light-to-heat conversion. It should be noted that PDA-WPU dispersions reported in this study offer cost effective, environmentally, and user-friendly solutions to develop photothermal materials due to their

nanoparticle and catalyst free, waterborne nature without any toxic components. Unlike other photothermal systems reported in the literature, these PDA-WPU dispersions can be easily applied as one-component systems to obtain coatings or free-standing films. In addition to these advantages in terms of the ease of synthesis and applicability, the photothermal conversion capacity of PDA-WPU polymer matrix is also superior or comparable to many different photothermal systems. Despite having a relatively lower thermal conductivity, PDA-WPU films display a very promising light-to-heat conversion with both sunlight at 1 SUN and 3 SUN irradiance and NIR laser light, and present significant light-activated temperature elevations which could not be reached by other multi-component complex photothermal systems. Thus, PDA-WPU, as a monolithic photothermal polymer matrix, can open a great window in the field of light-to-heat conversion either solely or as a strong and effective component of a composite system.

Table 7. Comparison of light to thermal energy conversion performance of PDAPU (6mg/ml)/72h with photothermal materials presented in the literature for different applications.

Components	Max. Temperature (°C)	Time (min)	Irradiation density of the sunlight (mW/cm ²)	Thermal conductivity (W/m°K)	Reference
n-Eicosane/TiO ₂ /CuS	~54.7	6.5	100	0.730	342
Stearic acid/MWCNT	80.0	10.2	100	7.159	343
NH ₂ -SWCNT	81.1	18.2	250	0.421	344
Ti ₃ C ₂ T _x /PDA	86.6	21.2	250	0.471	345
hexadecyl acrylate -MWCNT	~51.0	33.3	100	0.877	169
Polystyrene-CNT	~64.1	18.0	110	0.390	346
Lauric acid/graphene	49.8	37.0	100	1.037	347
PDA/PVDF	35.0	10.0	75	-	114
Hydroxyapatite/PDA	43.0	2.0	100	0.147	115
Fluorophore/CNT	120	2.0	1000	-	298
PDAPU(6mg/ml)/72h	53.2 115.4 138.6	20 20 5	100 300 800	0.232	This study

5.4.6. Solar-driven water evaporation capacity of PDA-WPU-based container

One of the most popular and attractive application fields of the photothermal conversion phenomenon is solar–driven water evaporation, which has received significant interest in recent years as reported in pioneering studies^{348,349}. With the purpose of examining the potential applications of photothermal PDA-WPU materials developed in this study, their utilization for solar-driven water evaporation was studied.

In general, water evaporation systems are designed by placing solar-absorbing materials on water surface as floaters, which usually allows the passage of water to the surface and heating the water at the surface⁴⁹. Here, the system was designed in reverse of the general approach to show the effect of the thickness of the material on light-to-heat conversion capacity and offer a practical product design for water evaporation systems. PDA-WPU (6 mg/ml)/72h, which is the photothermal polymer that has reached the highest temperature under solar irradiation and the control WPU dispersion were cast into container-shaped molds presented in Figure 41A. The time-temperature profiles of WPU and PDA-WPU containers under 3 SUN solar irradiance were constructed by measuring the temperature of inner surfaces of empty containers. The inner surface of the PDA-WPU (6mg/ml)/72h container reached 118.7°C at the end of 20 min irradiation with sunlight, whereas the temperature of the WPU container was measured as 43.6 °C under the same irradiation conditions. When the WPU and PDA-WPU containers were filled with water corresponding to about 3.2 kg/m² and irradiated with sunlight for 30 minutes, temperature of the water in the containers were read as 49.6 °C and 78.2 °C, respectively (Figure 41C).

Mass loss and the evaporation rates of water inside the WPU and PDA-WPU containers were recorded by measuring the mass loss as a function of time for an hour under sunlight irradiation. As seen in Figure 41D, while an average of 1.29 kg/m² water evaporated from the WPU container in 60 minutes, an average of 3.17 kg/m² water, almost the entire amount of water in the PDA-WPU container, was consumed in 60 minutes. The average evaporation rate of water from the WPU container was calculated as 1.18 kg/m²·h, whereas the evaporation rate of water from the PDA-WPU container was found to be 2.81 kg/m²·h on, demonstrating more than two-fold increase in the water evaporation rate relative to the WPU container. The solar-driven evaporation rate obtained with PDA-WPU container was

comparable to other solar-driven evaporation systems obtained with much more complicated material designs reported in the literature¹¹⁶.

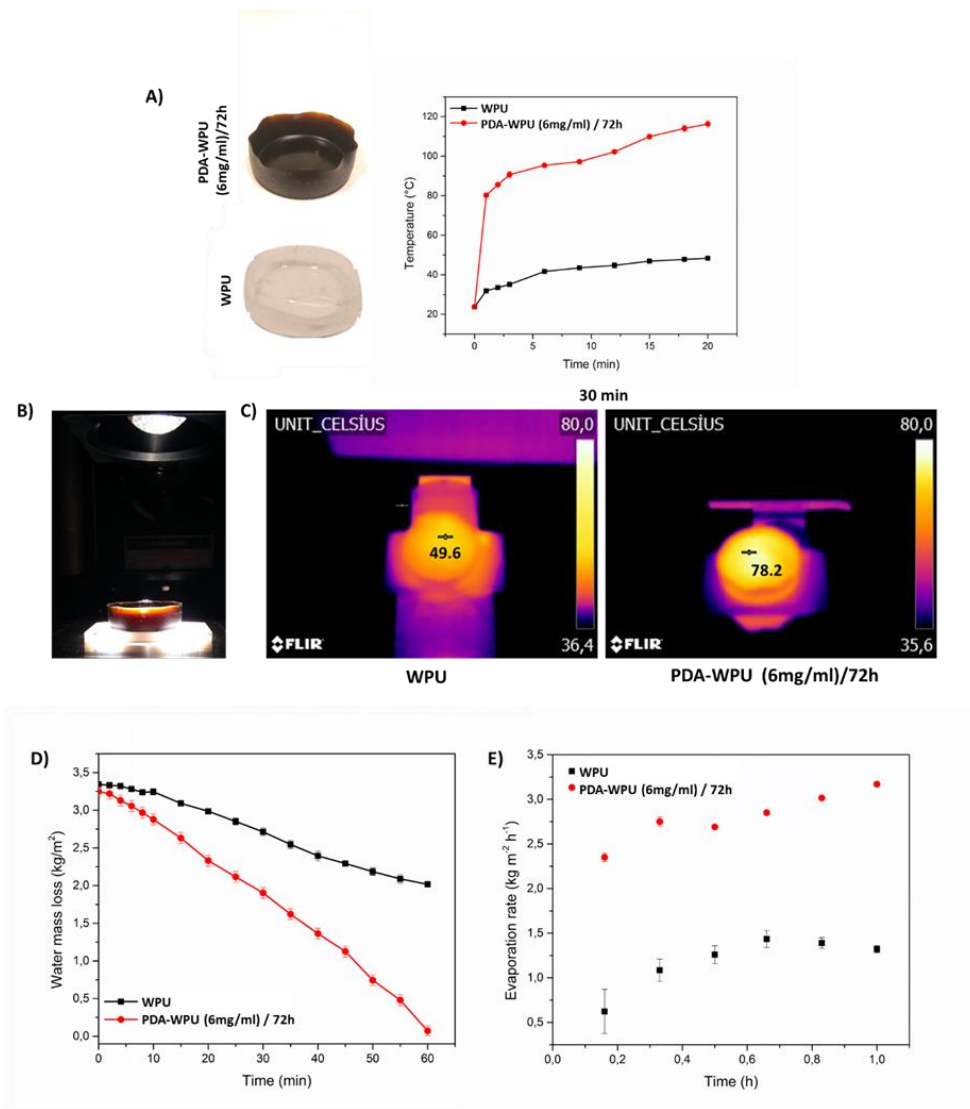


Figure 41. Photographs and solar-irradiation based time-temperature profiles of WPU and PDA-WPU (6mg/ml)/72h cast in the form of a container (A), experimental setup of water evaporation experiment under solar simulator (B), thermal camera images of WPU and PDA-WPU (6mg/ml)/72h container filled with water and exposed to sunlight for 60 min (C), water mass loss (D) and evaporation rates (E) of water in WPU and PDA-WPU containers under 3 SUN solar irradiance.

5.5. Conclusions

Polyurethane matrices from waterborne dispersions were converted to photothermal materials by simply coating WPU solid particles with PDA in the dispersion state. The monodisperse particle size distribution along with increased particle size and decreased zeta potential values of the PDA-WPU dispersions pointed out the successful coating of WPU particle surfaces with PDA, as also visualized in TEM images. Films cast from PDA-WPU dispersions presented enhanced thermal stability and thermal conductivity behaviors, similar glass transition temperatures and acceptable mechanical properties relative to neat WPU film samples. PDA-WPU films presented significant temperature elevations when irradiated with sunlight and NIR laser demonstrating their photothermal character. When compared to other photothermal materials reported in literature, PDA-WPU films stand out with their simple design, cost-effectiveness, and easy applicability. As exemplary potential applications for PDA-WPU materials, containers cast from PDA-WPU dispersions were utilized for solar-driven water evaporation and demonstrated to provide higher water evaporation capacity. The design approach demonstrated here provides a facile method to obtain a monolithic hybrid photothermal material that synergistically combines the advantages of a photothermal polymer and waterborne polyurethanes in the form of a one-component system that is easy to apply in various forms.

CHAPTER 6: Improved Latent Heat Storage Properties through Mesopore-Enrichment of a Zeolitic Shape Stabilizer

Reference Publication: Cüneyt Erdinç Taş, Oznur Karaoğlu, Buket Alkan Taş, Erdal Ertaş, Hayriye Ünal and Hakan Bildirir, 'Improved Latent Heat Storage Properties after Mesopore-Enrichment of a Zeolitic Shape Stabilizer", *Solar Energy Materials & Solar Cells* 216 (2020) 110677.

6.1. Abstract

Latent heat storage systems are applied to keep temperature of a local environment within a constant range. The process takes place via release/storage of latent heat during freezing/melting of a corresponding phase change material embedded in a shape stabilizer, which is the scaffold keeping the phase change material stationary in its molten form. In this work, a highly siliceous ZSM-5 and modified versions thereof were chosen as shape stabilizers for molecular and polymeric phase change materials (namely lauric acid and polyethylene glycol), to be impregnated using solvent assisted vacuum impregnation. The dominantly microporous analogues, parent ZSM-5 and its acid-treated derivative, were limited to 40% uptake for each phase change material. Contrastingly, a mesopore rich analogue (as formed under basic conditions) reached 65% impregnation for lauric acid and 70% for polyethylene glycol, without any leakage at 70 °C, resulting in latent heats of 106.9 J/g and 118.6 J/g for each composite, respectively. A simple prototypical real-world application demonstrated that the prepared lauric acid and polyethylene glycol composites of mesopore enriched ZSM-5 could maintain their temperatures up to 27% and 22% lower than the ambient environment under solar heating, as well as up to 20% and 26% higher when solar heating stops. The presented findings indicate mesopore enrichment improves phase

change material uptake in these low cost, non-toxic zeolitic shape stabilizers, hence making them good candidates as isolation materials to address energy loss during heating/cooling of household environments.

6.2. Introduction

Producing energy in a sustainable manner, without causing pollution is necessary to keep the Earth as a livable planet since conventional production processes result in significant environmental issues. Unfortunately, environmentally unfriendly energy sources are still generally preferred essentially as a consequence of costs, with significant improvements in efficiency and reductions in costs at scale required for green energy production alternatives.³⁵⁰⁻³⁵² Positively, a considerable volume of research has been reported with regard to addressing challenges and demonstrating improved performance of alternative energy systems, a viable solution is unlikely to be presented in the near future.³⁵³ Therefore, reducing energy consumption is considered as a highly beneficial complementary approach, leading to a reduction in pollution resulting from excess energy use, but also a decrease the required energy-per-capita to be reached by the prospective alternative energy solution.³⁵⁴

Heating is the most energy-consuming process according to International Energy Agency,³⁵⁵ with the use of facile techniques such as proper isolation leading to reductions in energy demand.³⁵⁶ In this context, Phase Change Materials (PCMs) are interesting since their use in latent heat storage systems aims to keep the local environment within a constant temperature window.³⁵⁷⁻³⁵⁹ Essentially, heat buffering process occurs via consumption of excess heat at temperatures above the melting point or the release of the stored heat at temperatures below the freezing point of the corresponding PCM. Since the latent heat of the PCM compensates for the heat change, the PCM should be selected in accordance with the aimed application. Thus, organic compounds with long alkyl chains such as fatty acids or polymeric materials like polyethylene glycols with different molecular weights can be utilized as useful PCMs since several of their derivatives offer different melting/freezing points.³⁶⁰ Additionally, their non-toxicity, easy processability, relatively low-costs, and inert nature also make them desirable for such use.³⁶¹

The biggest challenge in the application of PCMs is keeping the molten form stationary at elevated temperatures.¹⁹² To solve this issue, PCMs are embedded in shape stabilizers, which

are mostly porous scaffolds such as zeolites, porous carbons, metal-organic frameworks, or porous polymers.³⁶²⁻³⁶⁷ Aside from having excellent thermal stability and conductivity, a good shape stabilizer should be able to host a large amount of PCM to have better thermal properties since the latent heat is stored by those compounds. In the literature, mesopore-rich, hierarchically porous materials are promoted as useful shape stabilizers since the mobility of long alkyl chain PCMs can be limited for microporous materials due to steric hindrance, while keeping the adsorbed PCM in the shape stabilizer (i.e. avoiding leakage) can be hard for macroporous scaffolds due to poor capillary effect.^{258,262,368,369}

Since their discovery in the 19th century, zeolites have been used in various fields from water softening to high-temperature catalytic cracking.³⁷⁰⁻³⁷³ Indeed, there are examples of zeolites used in latent heat storage systems as shape stabilizers. For instance, Goitandia et al.²⁶² compared Zeolite Y with various inorganic shape stabilizers possessing different pore sizes. They reported the domination of the mesoporous silica over ultra-microporous zeolite Y with an impregnation of 45% for hexadecane as PCM without any leakage.²⁶² In another study, a frequently used zeolite, namely ZSM-5, was used as the shape stabilizer for polyethylene glycol and showed a remarkable performance with a 50% impregnation and excellent thermal conductivity.²⁶⁵ In this context, introduction of mesopores among the skeleton of ZSM-5 seems interesting. Thus, in this work, we present the effect of mesopore enrichment on PCM uptake for ZSM-5 and in turn the final latent heat storage properties. Comparing the shape stabilizing performance of a pristine microporous ZSM-5 with its post-synthetically modified versions possessing altered porosity allow us to investigate specifically the effect of pore size on latent heat storage properties, via eliminating the effects of other variables (e.g. thermal conductivity difference) since the scaffolds have essentially the same backbone. Moreover, the choice of a molecular fatty acid (lauric acid (LA)) and a polymeric material (polyethylene glycol 4000 (PEG)) as PCMs facilitate the monitoring of structural differences such as size, shape and the number of heteroatoms on PCM loading and latent heat storage properties.

6.3. Materials and Methods

6.3.1. Chemicals

ZSM-5 type Zeolite ($\text{SiO}_2/\text{Al}_2\text{O}_3$ ratio of 469) was received from Acros Organics. Poly (ethylene glycol) with an average molecular weight 3500-4500 g/mol (PEG4000), lauric acid and potassium hydroxide pellets were purchased from Merck. Extra pure methanol (99.8%) was purchased from Tekkim Ltd. (Bursa/Turkey). Pure water was obtained using a Milli-Q Plus system. All chemicals were used without further purification.

6.3.2. General procedure for the synthesis of ZSM-A

The preparation and characterization of ZSM-A and ZSM-B were explained in detail elsewhere.³⁷⁴ The acidic treatment of ZSM-5 for the dealumination was performed in 2.5 M HCl (aq). Briefly, 50.0 g ZSM-5 was placed in a flask and 250 mL 2.5 M HCl (aq) was added. Following stirring for 6 h at 150 °C, the mixture was diluted two-fold with water. The solid was filtered and washed two times with 250 mL deionized water. Finally, the solid was dried at 120 °C overnight (under vacuum) and ZSM-A was obtained.

6.3.3. General procedure for the synthesis of ZSM-B

Desilicated ZSM-5 was prepared by using nearly the same method above. 50.0 g ZSM-5 and 250 mL 2M KOH (aq) were put in a flask, and the reaction performed 110 °C for 6 h. Subsequently, the solution was diluted with 250 mL deionized water, and the precipitate then filtered. The collected precipitate was twice washed with 250 mL water and dried at 120 °C overnight (under vacuum) to yield ZSM-B.

6.3.4. General procedure for preparation of PCM composites

Solvent assisted impregnation under vacuum was used to obtain ZSM-5, ZSM-A and ZSM-B-based PCM (LA and PEG) composites. By adjusting the total amount to 0.3 g for desired composite percentage (i.e. 0.12 g of PCM to 0.18 g shape stabilizer for 40% loading), the mixture of corresponding PCM and dried ZSM-X (in vacuum oven at 150 °C for 24 h) were added into 7.5 mL MeOH in 50 mL centrifuge tube. The charged tube was then placed in an ultrasonic water bath for 15 min and transferred to the vacuum impregnation system. Solvent removal was conducted gradually by reducing the pressure to 7-9 mb first at room

temperature by stopping the vacuum after 5 min and stirring for 5 min and repeated three times. Heating to 70 °C was then used to remove the solvent completely (in order to improve the impregnation). After solvent removal, the obtained powders were further dried in a vacuum oven for 24 h at 40 °C.

6.3.5. Characterizations

Surface area measurements were performed by using the Quantachome Instrument Nova4000e (Florida, USA). Fourier Transform Infrared (FTIR) spectroscopy with an ATR system was utilized for the analysis of PCM composites. Amount of embedded PCM in composite was measured with Shimadzu Corp. DTG-60H (TGA/DTA) instrument by heating samples up to 1000 °C with a rate of 20 °C/min. Thermal properties of the PCM composites were investigated using differential scanning calorimetry (DSC; Thermal Analysis MDSC TAQ2000). Heat storage performance of PCM composites were carried out at the rate of 10 °C/min with a heating and cooling cycle between 0 - 100 °C. Stability tests were also performed using DSC from 10 to 80 °C at a rate of 20 °C/min for each cycle. All thermal measurement was carried out under nitrogen atmosphere. Thermal behaviour of PCM composites under solar power light were evaluated using an Oriel LCS-100 solar simulator at 0.404 W/cm². Temperature changes were measured by a Hanna thermometer attached to a K-type thermocouple.

6.3.6. Solar simulator experiments.

The prepared LA and PEG containing PCM composites were irradiated in the solar simulator at 0.404 W/cm² power. Time-temperature curves were obtained by recording the temperatures of environment (blank), neat ZSM-B, and the corresponding composite every two seconds during heating and cooling. The measurements were repeated three times, and the calculated average values were used for time-temperature graphs.

6.4. Results and Discussions

6.4.1. Comparison of shape stability of ZSM-5, ZSM-A and ZSM-B PCM composites

The properties of zeolitic structures can change significantly after simple dealumination or desilication of the framework.³⁷⁵ Such modifications might lead to hierarchical porosity, which results in altered diffusion dynamics as a consequence of removal of the corresponding network unit. In this context, introducing mesopore-rich hierarchical porosity to the backbone of ZSM-5 is expected to provide favorable properties in latent heat storage systems since mesoporosity is an asset for such scaffolds in latent heat storage systems,²⁶² and also because pristine ZSM-5 has been previously highlighted as a promising shape stabilizer for PCMs due to its good thermal conductivity, even in its microporous form.²⁶⁵

Alteration to the parent ZSM-5 after acidic and basic treatments were investigated thoroughly, and explained in our previous publication.³⁷⁴ Briefly, dealumination of the highly siliceous ZSM-5 (Si/Al ratio = 938) was not successful, yet the acid exposure resulted in highly microporous ZSM-A. On the other hand, base treatment of the parent material to obtain ZSM-B yielded a hierarchically porous material possessing a dominantly mesoporous character and containing less silicon (Figure 42).³⁷⁵⁻³⁷⁷ Moreover, a lower specific surface area (BET) for ZSM-B ($180 \text{ m}^2\text{g}^{-1}$) was recorded in comparison to ZSM-5 ($356 \text{ m}^2\text{g}^{-1}$) and ZSM-A ($359 \text{ m}^2\text{g}^{-1}$) probably due to increased mesoporosity (Figure 43 and Figure 44).

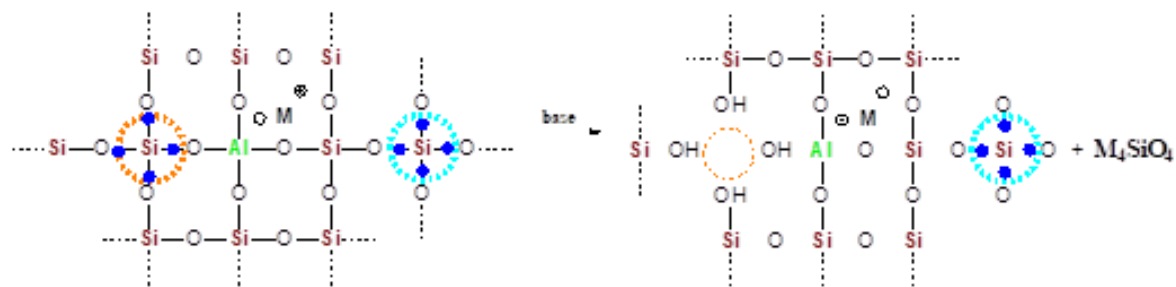


Figure 42. A basic description of desilication of ZSM-5. M^+ can be H^+ , Na^+ or K^+ depending on the composition of the parent zeolite and the applied base.

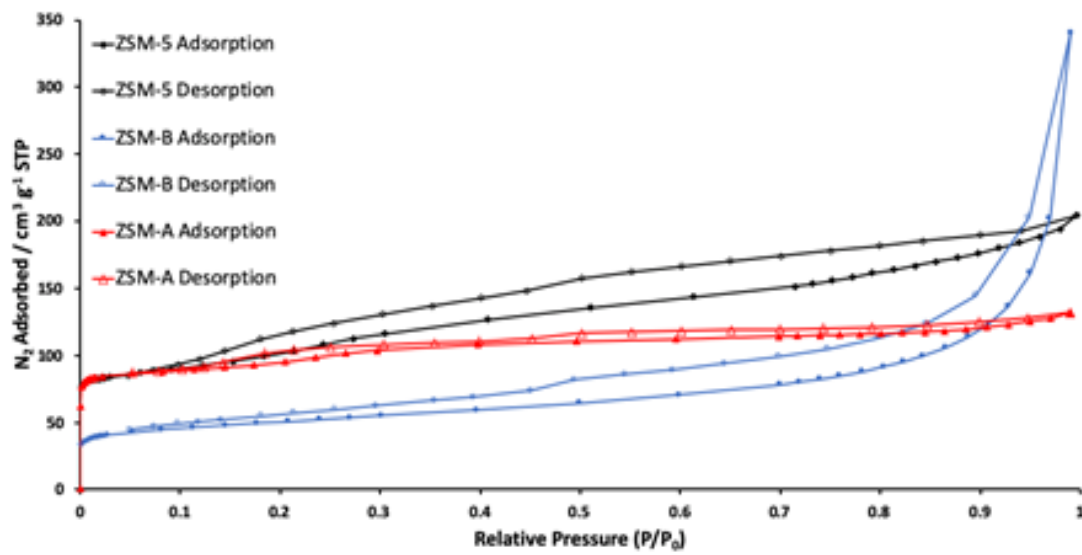


Figure 43. Gas absorption measurement of ZSM-A, ZSM-B and ZSM-5.

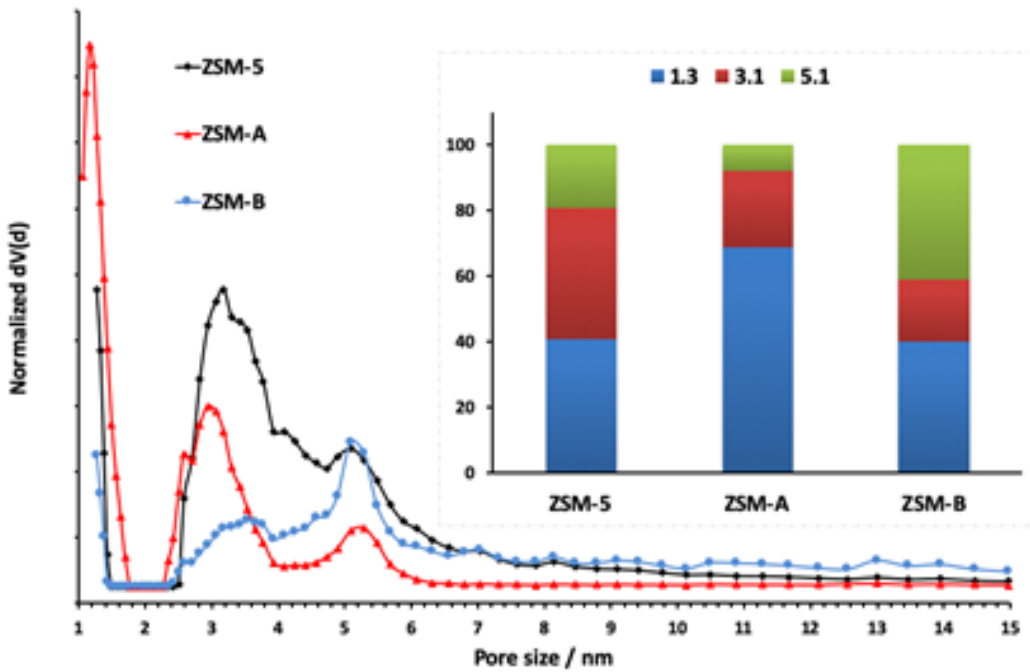


Figure 44. NL-DFT predictions for pore size distributions of the zeolitic materials, and relative pore size contributions near 1.3 nm, 3.1 nm, and 5.1 nm derived from the NL-DFT calculations as inset.

Shape stabilizers were loaded with LA and PEG through vacuum impregnation method by mixing ZSM-X (X= 5 or A or B) and corresponding quantities of PCMs dissolved in methanol at 40-80%, (w/w) ratios, followed by ultrasonication and solvent removal under reduced pressure (Figure 45). Composite ZSM-X/PCM powders obtained are shown in Figure 46A.

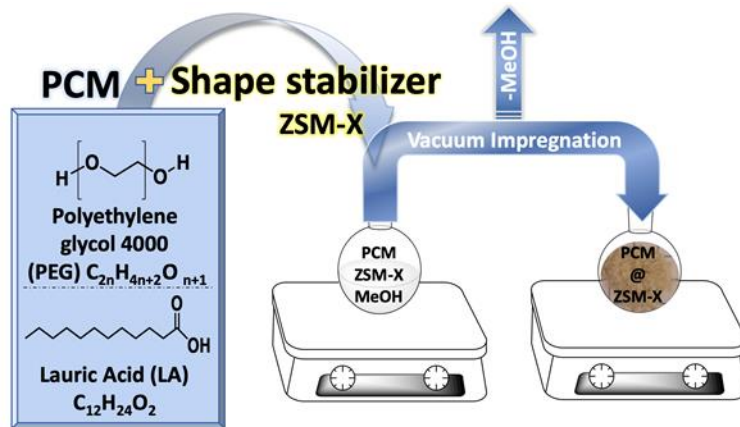


Figure 45. Schematic representation of the composite preparation.

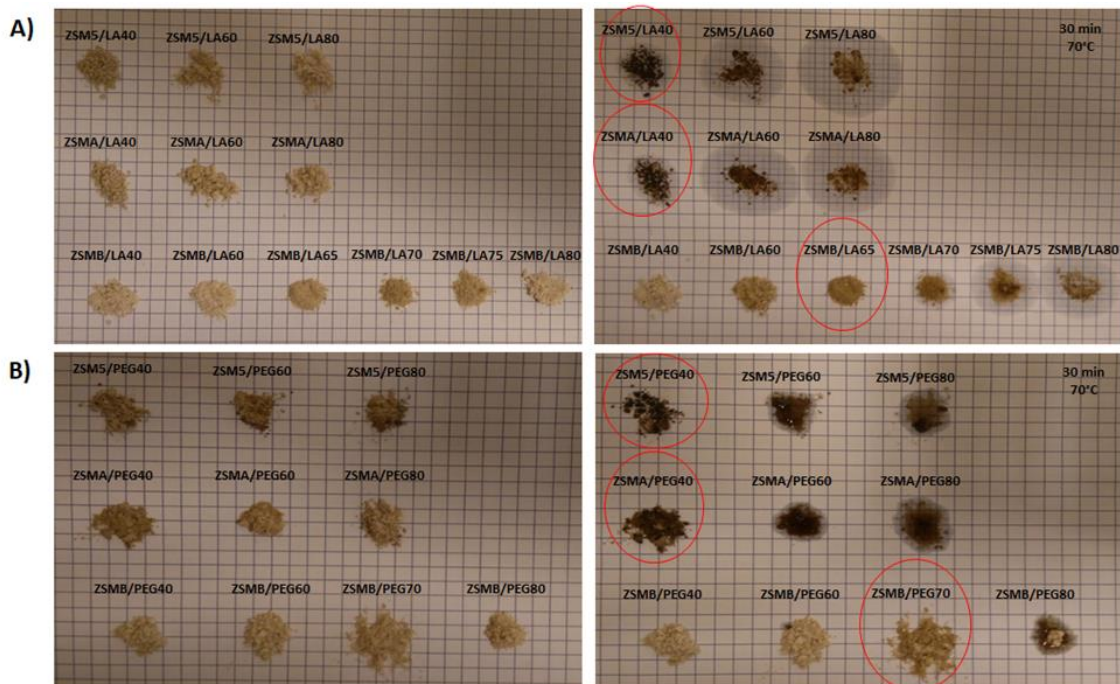


Figure 46. The physical states of prepared ZSM-X/PCM composites before (A) and after (B) heat treatment.

Since impregnating shape stabilizers with the highest amount PCM without any leakage is a highly desired feature to yield optimum latent heat storage properties,³⁷⁸ the non-exudative maximum PCM uptake capacities of the shape stabilizers were determined via performing a leakage test at elevated temperatures. Briefly, ZSMX/PCM composites were placed on a regular paper and heated in an oven at 70 °C for 30 min, and the area below the powder was checked whether it was wet or not. As can be seen in Figure 46B, impregnation of ZSM-A and ZSM-5 with both PCMs at ratios of 40% and above resulted in leakage, whereas the ZSM-B composites did not leak any LA and PEG even at 65% and 70% impregnation, respectively. Moreover, the actual amounts of organic PCMs loaded into ZSM-B composites were verified by thermal gravimetric analysis (TGA) under ambient atmosphere. Impregnation ratios determined by the weight losses in ZSMB/LA and ZSMB/PEG due to decomposition of organic components (for LA around 220 °C and for PEG near 410 °C) were in good agreement with theoretical values (Figure 47 and Table 8). Based on these results, the composites formed from ZSM-B were conducted for further investigations.

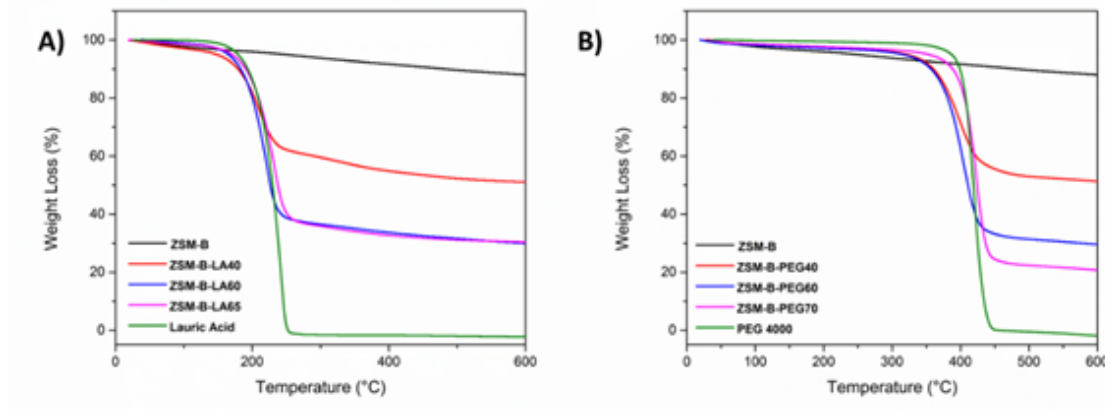


Figure 47. TGA Analysis of (A) ZSMB/LA (40%, 60%, 65% loading ratio), (B) ZSMB/PEG (40%, 60%, 70%).

Table 8. TGA Results of ZSM-B Based PCM Nanocomposites.

	Theoretical Composition (%)	Experimental Composition (%)	%Δ
LA	100	100	0
ZSMB/LA40	40	38.49	3.78
ZSMB/LA60	60	59.62	0.64
ZSMB/LA65	65	62.84	3.33
PEG 4000	100	100	0
ZSMB/PEG40	40	37.37	6.58
ZSMB/PEG60	60	58.64	2.19
ZSMB/PEG70	70	63.72	8.98

%Δ: Differences between theoretical composition % and experimental (TGA) composition %.

The exudation stability of ZSMB/LA composite at 65% impregnation (ZSMB/LA65) and ZSMB/PEG composite at 70% impregnation (ZSMB/PEG70) were evaluated by performing DSC experiments to confirm the results after the abovementioned macro-level leakage tests. Briefly, the samples were placed in a DSC sample holder and scanned for four times, during which the powders were removed from the DSC pan and put in the oven at 70 °C for 30 min after each cycle. The melting and solidifying patterns of ZSMB/LA65 and ZSMB/PEG70 were nearly the same for each cycle (Figure 48A and Figure 48B). Both melting and cooling curves of ZSMB/LA65 became slightly narrower with respect to the first cycle. This was probably due to the small amount of LA that evaporated from the composite powder at elevated temperatures during the DSC scan due to weak capillary forces.^{262,379} Nevertheless, the change on the melting/solidifying enthalpies can be regarded as insignificant (Figure 48B). On the other hand, such evaporation did not occur in case of ZSMB/PEG70 which is composed of a polymeric PCM (Figure 48C and Figure 48D).

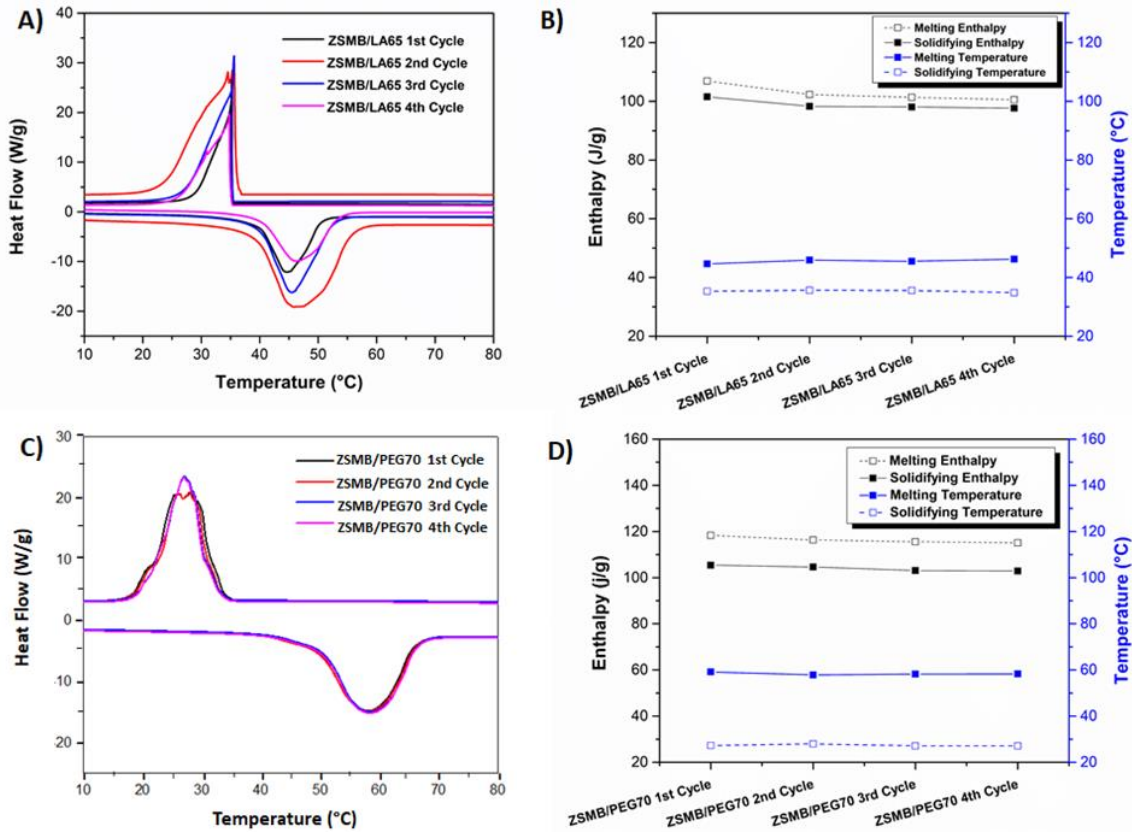


Figure 48. DSC curves of the thermal cycle for (a) ZSMB/LA65, (c) ZSMB/LA70; (b-d) their enthalpy and transition temperature changing graphs.

Extended thermal stability tests of ZSMB/LA65 and ZSMB/PEG70 were employed by subjecting samples to 45 consecutive thermal cycles, during which the samples were transferred to a new pan after every 15th cycle (Table 9, Figure 49). The melting temperature of ZSMB/LA65 was detected to be only 1.5 °C lower than its initial state while its solidifying temperature remained nearly constant. On the other hand, solidifying temperature of ZSMB/PEG70 changed by only 0.9 °C while its melting temperature remained almost the same. Moreover, the melting and solidifying enthalpies also changed insignificantly, where they decreased by 4.3 J/g and 4.1 J/g, for ZSMB/LA65 and by 9.1 J/g and 5.7 J/g for ZSMB/PEG70. The negligible changes (%ΔH values; Table 9) showed that both of the prepared composites were stable after more than several melting/solidifying processes, indicating their long-term stability. Additionally, the infrared spectra of the composites before and after 45 thermal cycles also demonstrated the structural stability of the PCMs by

showing nearly the same responses, particularly at ca. 2900 cm^{-1} and 900 cm^{-1} which are the vibrations of the C-H groups of the organic PCMs (Figure 50).

Table 9. The long-term stability of the prepared ZSM-B composites.

PCM	T_m ($^{\circ}\text{C}$)	ΔH_m (J/g)	$\% \Delta H_m$	T_s ($^{\circ}\text{C}$)	Δs (J/g)	$\% \Delta H_s$
ZSMB/LA65 1 st cycle	44.67	106.9	100	35.29	98.7	100
ZSMB/LA65 15 th cycle	45.18	104.6	97.8	35.35	96.3	97.6
ZSMB/LA65 30 th cycle	45.39	103.1	96.4	35.18	95.2	96.5
ZSMB/LA65 45 th cycle	46.02	102.6	96.0	35.09	94.6	95.8
ZSMB/PEG70 1 st cycle	59.33	118.6	100	29.17	103.9	100
ZSMB/PEG70 15 th cycle	59.45	114.3	96.4	29.06	101.9	98.1
ZSMB/PEG70 30 th cycle	59.16	111.6	94.1	28.71	100.5	96.7
ZSMB/PEG70 45 th cycle	59.79	109.5	92.3	28.24	98.2	94.5

ΔH_m : melting enthalpy; ΔH_s : solidifying enthalpy; T_m : melting temperature; T_s : solidifying temperature

% indicates the change with respect to the first cycle

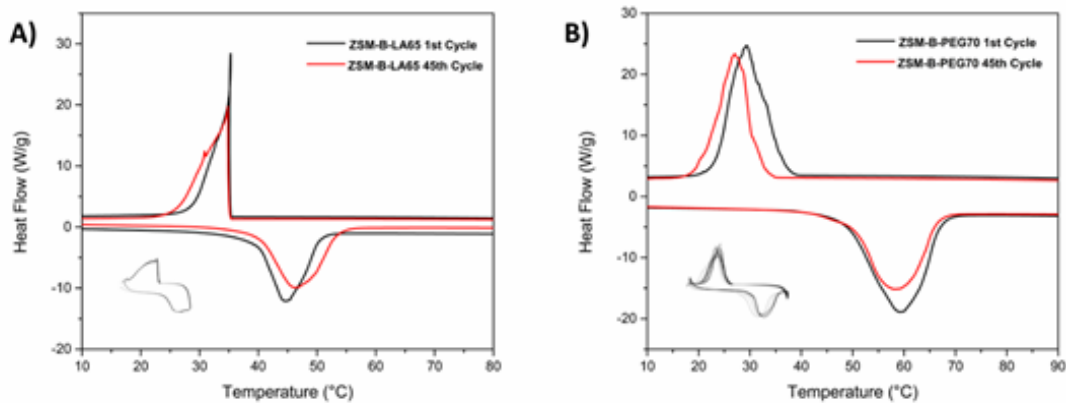


Figure 49. DSC curves of accelerated thermal cycles for (A) ZSM-B-LA65 and ZSM-B-PEG70 (B). The insets show the full measurements for each case.

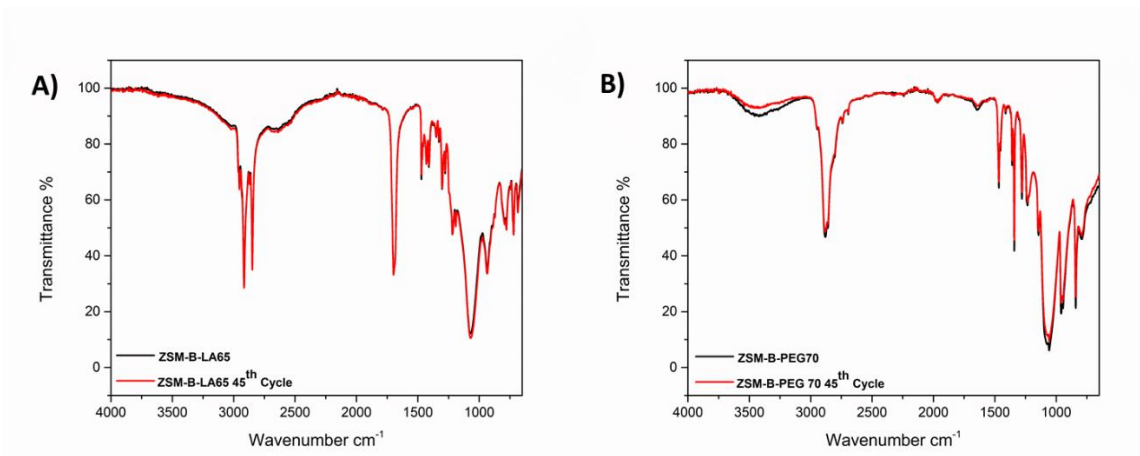


Figure 50. FT-IR analysis of accelerated thermal cycles for (A) ZSM-B-LA65 and ZSM-B-PEG70 (B) end of 45 cycles.

6.4.2. Thermal energy storage performance of ZSM-B based PCM composites

Latent heat storage properties of the prepared ZSM-B composites containing LA and PEG at impregnation ratios of 40% and above were investigated by DSC in order to monitor the effect of higher PCM uptake on latent heat storage properties (Figure 51). The melting and solidifying temperatures of all composites was found to slightly shift to lower values with respect to pure LA and PEG. This was potentially caused by weak molecular interactions of PCMs with the porous shape stabilizer (e.g. capillary forces, hydrogen bonding interactions, etc.), which affect the required energies for phase transitions.^{380,381} Moreover, melting and solidifying enthalpies of the prepared composites changed proportionally with respect to their PCM impregnation ratios, confirming the successful impregnation to ZSM-B (Figure 51C and Figure 51D). The melting enthalpies of composites prepared at highest impregnation ratios, ZSMB/LA65 and ZSMB/PEG70, reached 106.9 J/g and 118.6 J/g, respectively, which are comparable enthalpies reported for similar shape stabilized PCM composites (Table 10).^{265,382-388} Especially, the composite prepared in this work via impregnation of ZSM-B with PEG presented 35.5% higher latent heat than the composite prepared with ZSM-5²⁶⁵ (also with PEG 4000) confirming the potential of ZSM-B as a high capacity PCM shape stabilizer. Notably, the actual enthalpies of all ZSM-B composites were found to be lower than the theoretical values to different extents. A significant difference was observed for

ZSMB/LA40, for which the LA molecules should be hindered in the core of the scaffold as a result of the low mass fraction. Therefore, the big deviation can either be due to the possible gap between the PCM and the exterior area of the scaffold^{173,389} or altered phase change behavior of the LA in such highly confined spaces.³⁹⁰

Table 10. Comparison of phase change temperature and latent heat of ZSM-B-LA65 and ZSM-B-PEG70 with other literature studies which are in similar concept.

PCM	Phase Change Temperature (°C)	Latent Heat (J/g)	References
Paraffin(60wt%)/expanded perlite	27.5	80.9	5
Paraffin(50wt%)/diatomite	36.5	53.1	6
Lauric acid (48 wt.%)/intercalated kaolinite	43.7	72.5	7
Lauric acid (60 wt.%)/expanded perlite	41.1	93.4	8
Lauric acid (60 wt.%)/sepiolite	42.5	125.2	9
Lauric Acid (65wt.%)/ZSM-5-B	44.67	106.9	This Work
PEG4000(79.3 wt%)/SiO ₂	58.1	151.8	10
PEG-4000(80 wt%)/Radial mesoporous silica	57.22	129.6	11
PEG4000(50wt.%)/ZSM-5	56.3	76.4	12
PEG4000 (70 wt%)/ZSM-5-B	60.7	118.6	This Work

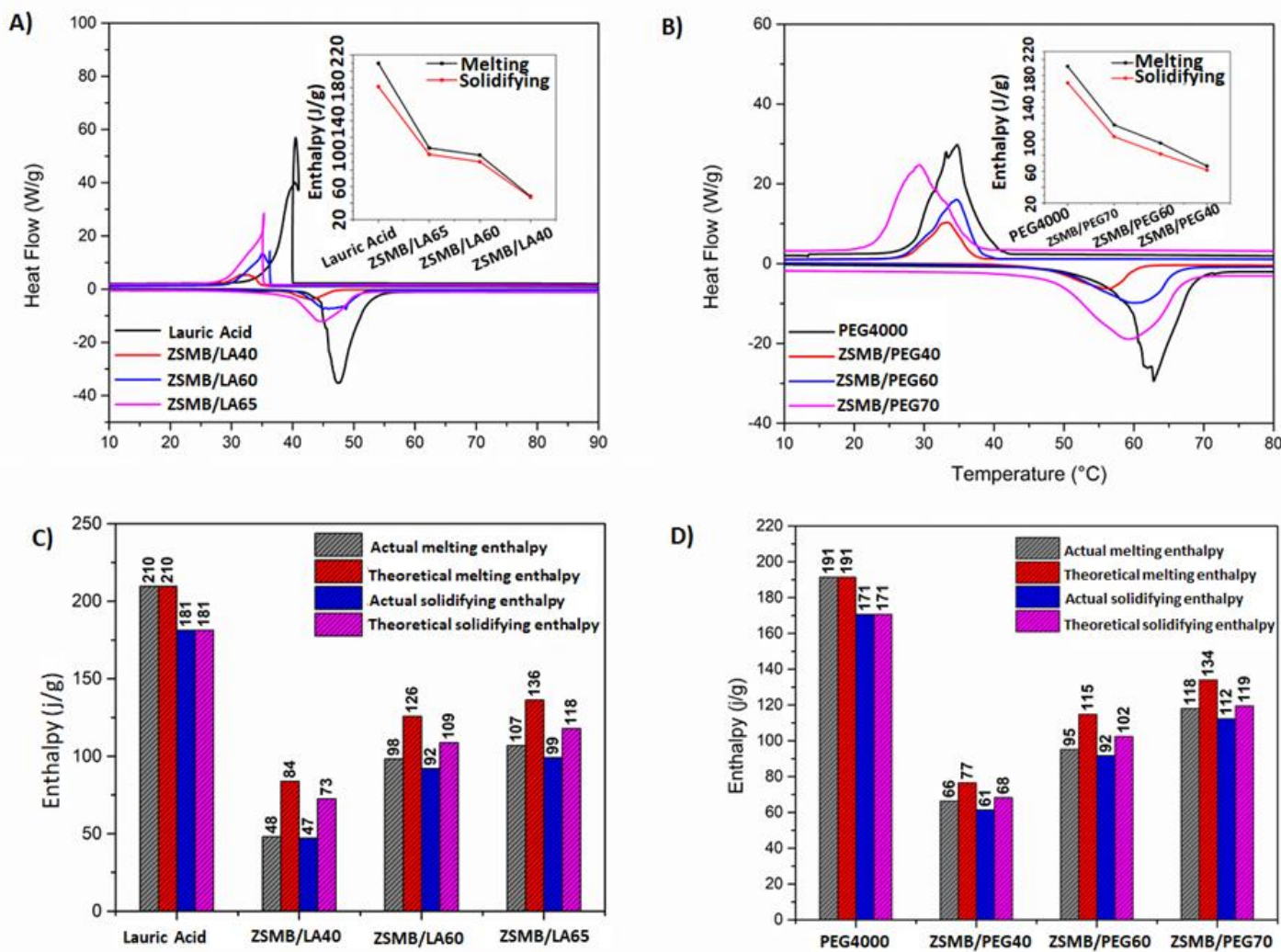


Figure 51. DSC curves of (a) ZSMB/LA and (b) ZSMB/PEG during melting and solidifying process; Enthalpies of melting and solidifying of (c) ZSMB/LA and (d) ZSMB/PEG with different PCM contents.

Theoretical enthalpies of ZSMB/PCM composites were calculated by using Eq. 2. The actual enthalpies of pure PCMs (100% PCM content) were accepted as their theoretical enthalpies to make comparison with the ZSMB/PCM composite system.

$$\Delta H_{\text{theo.}} : (1-w) \Delta H_{m/s} \quad \text{Eq.2}$$

where “ $\Delta H_{\text{theo.}}$ ” is theoretical latent enthalpy, “ $H_{m/s}$ ” is the melting or solidifying enthalpy of pure PCMs, and “ w ” denotes the content of ZSM-B.

On the other hand, the variations between actual and theoretical values were less significant for the composites of PEG. Presumably, the higher heteroatom content (oxygen) of PEG or its bulkier polymeric structure ($M_w: \approx 4000$ g/mol) result in strong interactions with the skeleton of zeolitic framework might reduce the strength of the capillary forces to confine the material through the core of the scaffold as deep as LA. Nevertheless, such interactions should also be limiting the (re)crystallization of the molten phase in the low loadings, hence yielding lower actual enthalpies than the theoretical.³⁸¹

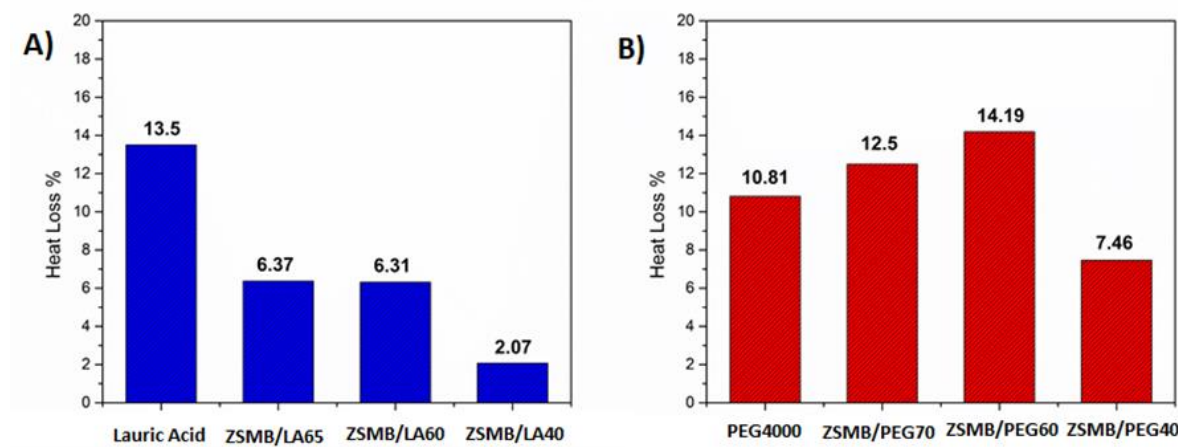


Figure 52. Heat loss percentages of (A) ZSMB/LA and (B) ZSMB/PEG composites.

The differences between melting and solidifying enthalpies (heat loss) of the prepared composites were calculated to monitor their relative latent heating and cooling performances (Figure 52). The heat loss calculated for pure LA was considerably higher than the heat loss

calculated for its composites indicating that the capillary forces of the shape stabilizer limits its evaporation³⁹¹ at elevated temperatures. Indeed, the composite with the lowest loading of LA, ZSMB/LA40, showed nearly minimal heat loss as a consequence of the hindrance of such low amount of LA through the network. In case of the composites of the polymeric PEG, the heat loss occurs due to energy differences between melting and crystallization, which even occurs in case of the neat PEG.^{258,388}

6.4.3. Latent heat storage performances of ZSM-B based PCM composites under solar irradiation

The composites containing the highest amount of the PCMs were subjected to heating-cooling cycles by using a solar simulator as a prototype of real-world applications. Temperatures of ZSMB/LA65 and ZSMB/PEG70 composite powders were recorded under solar irradiation and also after the simulator was switched off. Even though the composites demonstrated nearly homogeneous heat buffering until their saturation points, maximum performances were highlighted in Figure 53 (Table 11 for more information).

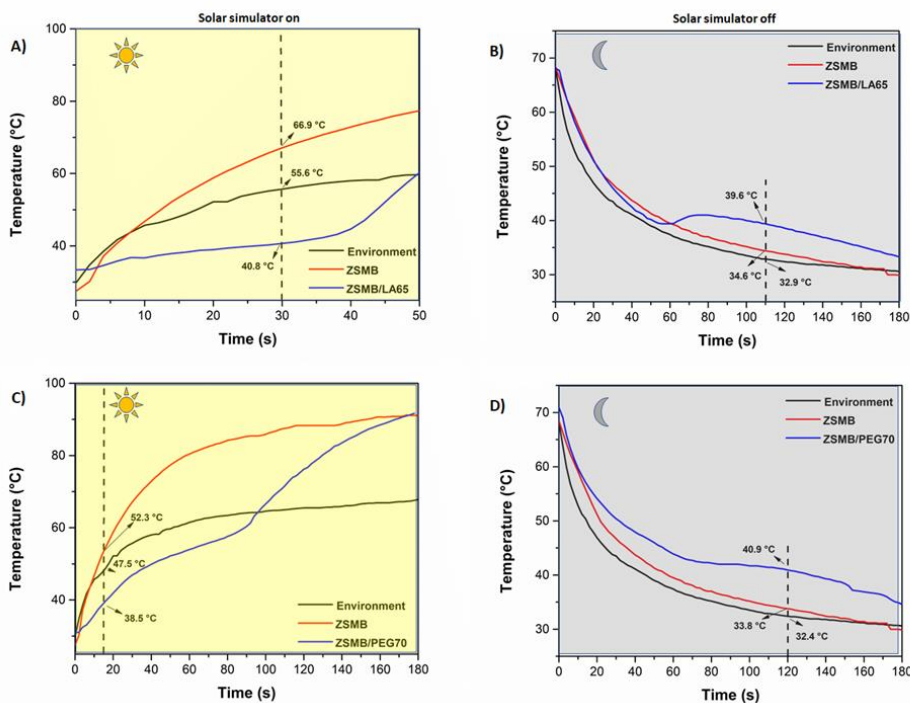


Figure 53. Thermal behavior of (A-B) ZSMB/LA65 and (C-D) ZSMB/PEG70 composites under solar simulator irradiation.

Table 11. Solar simulator results.

Parameters	Heating					Cooling				
	Time (s)	Environment (°C)	ZSM-B (°C)	Composite (°C)	%Δ	Time (s)	Environment (°C)	ZSM-B (°C)	Composite (°C)	%Δ
<u>Initiation</u> ZSMB/LA65	8	44.9	45.9	36.8	18	68	36.0	38.2	40.5	13
<u>Max. %Δ</u> ZSMB/LA65	30	55.6	66.9	40.8	27	110	32.9	34.6	39.6	20
<u>Saturation</u> ZSMB/LA65	39	57.5	73.1	44.6	22	160	30.9	31.3	35.2	14
<u>Initiation</u> ZSMB/PEG70	2	34.8	30.2	31.1	11	90	34.3	35.9	42.1	23
<u>Max. %Δ</u> ZSMB/PEG70	14	47.5	52.3	38.5	22	120	32.4	33.8	40.9	26
<u>Saturation</u> ZSMB/PEG70	90	64.3	85.6	60.3	6	160	30.9	31.3	36.7	19

%Δ: Corresponds to temperature differences between environment and composite

The temperatures of both composites were compared to the temperature of the environment in the absence of the composites and the temperature of PCM-free ZSM-B powder as references under the same solar irradiation conditions. Accordingly, when the environment control temperature reached 55.6 °C, the temperature of ZSMB/LA65 powder was only 40.8 °C, providing 27% cooling. At this time point, the temperature of neat ZSM-B powder was 66.9 °C showing that the medium of ZSMB/LA65 composite powder was 39% cooler. Similarly, the temperature of ZSMB/PEG70 composite powder was 38.5 °C, at the time when the temperature of the environment reached 47.5 °C meaning that ZSMB/PEG70 composite powder keeps the system 22% cooler than the ambient temperature.

Thermal behavior of both composites after the solar simulator was switched off was also evaluated. For ZSMB/LA65, at the time the environment temperature was 32.9 °C, the temperature of ZSMB/LA65 was 39.6 °C which corresponds to a 20% warmer medium than the environment. Similarly, ZSMB/PEG70 composite powder allowed a 26% warmer medium since its temperature was 40.9 °C while it was 32.4 °C for the blank. The results indicated that ZSMB/LA65 and ZSMB/PEG70 successfully perform latent heat storage by providing significantly cooler environments during solar heating and significantly warmer environments when the solar heating is disrupted through corresponding phase transitions.

6.5. Conclusions

Desilication was applied to a microporous zeolitic shape stabilizer, ZSM-5, in order to yield a mesopore rich hierarchical porous backbone in the framework to increase the amount of PCM impregnation. Even though the specific surface area dropped after the treatment, ZSM-B was able to hold nearly twice the amount of PCMs inside the framework with respect to other analogues. The optimum non-exudative composites of ZSM-B containing 65% LA and 70% PEG were able to store latent heat up to 106.9 J/g and 118.6 J/g, respectively. Moreover, the solar simulator tests of ZSMB/LA65 and ZSMB/PEG70 indicated the latent heat storage potential of the composites via buffering the temperature change up to 27% and 22% when the solar simulator was on as well as 20% and 26% during the cooling, respectively. Our results demonstrate that the introduction of mesopore rich hierarchical porosity to microporous ZSM-5 improved the PCM impregnation capacity, hence the latent heat storage properties of the zeolitic shape stabilizer. Additionally, the solar simulator tests indicate how

promising the latent heat storage systems are to keep an environment in a constant temperature to save energy spent for heating and its significant *lab-to-fab* potential via hereby presented combination of non-toxic PCMs with low-cost shape stabilizers.

CHAPTER 7: Waterborne Polydopamine-Polyurethane/Polyethylene Glycol Phase Change Composites for Solar-to-Thermal Energy Conversion

Reference Un-published Journal Article: Cüneyt Erdinç Taş, Ekin Berksun, Deniz Köken, Serkan Ünal and Hayriye Ünal “Waterborne polydopamine-polyurethane/polyethylene glycol phase change composites for solar-to-thermal energy conversion”.

7.1. Abstract

Form-stable phase change composite films composed of novel polydopamine-polyurethane polymer matrix with photothermal conversion properties and PEG4000 phase change material are presented. Waterborne polyurethane (WPU), which is a safe and environmentally friendly coating material was synthesized in the form of an aqueous dispersion. Surfaces of WPU particles were coated with polydopamine to create waterborne polydopamine-polyurethane (PDA-WPU) polymer matrix which presents significant photothermal conversion properties without using any other secondary particles. PEG4000 was directly integrated into the PDA-WPU matrix at different ratios by simple mixing in the dispersion form resulting in form-stable phase change composites. The thermal, mechanical, morphological properties, form stability and thermal conductivity of prepared composite films were investigated. Reliability of films in repeated thermal application, as well as melting/solidifying enthalpies of PEG4000 in cast films were evaluated by differential scanning calorimeter. For the composite film with the highest amount of PEG4000 without any leakage (PDA-WPU/PCM 1:1), the melting and solidifying enthalpies were calculated as 81.1°J/g and 77.9 J/g , respectively. The temperature of the composite film reached 74.8°C under 20-minutes solar irradiation at 150 mW/cm^2 with a solar-to-thermal energy conversion efficiency of 72.9%. Under cold weather conditions, PDA-WPU/PCM films were shown to heat up significantly more than control neat WPU films under solar light irradiation and to

stay significantly warmer when the solar irradiation stopped, demonstrating that PDA-WPU/PCM films can efficiently harvest and store sunlight and have strong potential as solar-driven thermoregulating materials.

7.2.Introduction

Photothermal materials, which can effectively harvest light from a light source and convert it into heat, can be utilized in various photo-driven applications as products that generate thermal energy³⁹². To create a system having light-to-thermal energy conversion ability, two main strategies can generally be applied, which are incorporation of nanomaterials such as metallic nanostructures or carbon-based nanoparticles into the system and coating of a substrate surface with a photothermal polymer such as polyaniline, polypyrrole and polydopamine⁵⁶. Mussel inspired polydopamine (PDA) is one of the most considerable photothermal polymers due to its strong NIR absorbance capacity, good biocompatibility, the feasibility of functional group modification and its ability to be coated onto almost any object surface^{71,393}. Thanks to its exceptional properties PDA has been widely utilized in material systems that produce heat by employing solar irradiation.

Phase change materials (PCMs) are invaluable in the concept of thermal energy storage and have attracted attention in various energy-related applications in recent years³⁹⁴. PCMs can be categorized into fatty acids²³⁹, paraffins³⁹⁵, salt hydrates³⁹⁶, inorganic materials³⁹⁷ and polymeric materials³⁹⁸⁻⁴⁰⁰. The main ability of PCMs is to store heat during their melting transition and release stored latent heat in the solidifying process. With this property, they can be used for thermal energy storage¹²⁴ or thermal buffering systems⁴⁰¹. Therefore, PCM-containing systems have been utilized in different application fields such as solar energy storage⁴⁰², smart buildings,⁴⁰³ textiles⁴⁰⁴, photovoltaics⁴⁰⁵ and thermoregulating food packaging.²⁵³

Incorporation of photothermal materials and PCMs into a single system provides an effective way to obtain a composite design consisting of harvesting of light, conversion of light to heat and the storage of heat. Fundamentally, composites of carbon-based photothermal agents and PCMs have been demonstrated as an attractive framework to achieve photothermal conversion and heat storage due to their large energy storage density and effective photon harvesting capacity⁴⁰⁶. Different photothermal agent/PCM composites involving carbon

nanotubes⁴⁰⁷⁻⁴⁰⁹, reduced graphene oxide⁴¹⁰⁻⁴¹², carbon fibers⁴¹³⁻⁴¹⁵ and carbon aerogels⁴¹⁶⁻⁴¹⁸ as photothermal fillers have been reported.

In solid-liquid PCM systems, one of the major challenges is the proper encapsulation of the PCM in a supporting material to prevent leakage during the melting transition. To do this, PCMs have been integrated into supporting materials such as inorganic porous materials⁴¹⁹ and cross-linking polymers⁴²⁰ or encapsulated in emulsions^{238,421,422} resulting in form-stable phase change materials that stay intact when the ambient temperature is higher than the melting temperature of the PCM. In addition to the form-stability of PCM composites, other vital criteria which should be met by the composites can be listed as high thermal conductivity, thermal stability/reliability, high latent heat capacity, higher encapsulating/impregnating capacity and lower supercooling degree⁴²³. Clay minerals such as diatomite,¹⁸³ sepiolite,¹⁸⁴ bentonite,¹⁸⁵ perlite,¹⁸⁶ SiO₂,¹⁸⁷ attapulgite,¹⁸⁸ vermiculite,¹⁸⁹ fly ash,¹⁹⁰ zeolite,¹⁹¹ halloysite,³² have been widely studied as PCM composites that meet most of these criteria due to their porous structures, excellent absorbability, high thermal stability and thermal conductivity. However, the main disadvantage with form-stable encapsulated PCMs is that their thermal performances may diminish when they are incorporated into a matrix relative to their bulk performances along with the problems arising from potential incompatibilities between the PCM encapsulating agent and the matrix⁴²⁴.

Form-stable PCM systems where PCMs are directly integrated into polymer matrices without any other encapsulating agent are very limited. Fang et al. prepared polyethylene glycol/epoxy resin composites as a form-stable PCM and examined their fundamental properties⁴²⁵. In another study, Wang et al. obtained fatty acid eutectic/polymethyl methacrylate (PMMA) form-stable PCM composites by incorporating the melted PCMs into the system during PMMA synthesis and tested the final composite properties in terms of thermal energy storage performance¹⁴⁸.

In this study, polydopamine, a photothermal polymer; a PCM and waterborne polyurethane dispersions were combined via a novel design approach to result in environmentally friendly and safe composite films that intrinsically present photothermal activity, energy storage capacity and thermal buffering properties. Waterborne polydopamine-polyurethane (PDA-WPU) polymer was synthesized by coating polyurethane solid particles with polydopamine

in aqueous dispersion and PEG4000 was incorporated into PDA-WPU dispersion by simple blending without using any other encapsulating agent. The strong potential of obtained form-stable phase change films as sunlight-activated thermoregulating materials that can be applied for real-life problems has been investigated.

7.3. Materials and Methods

7.3.1. Chemicals

Ethylenediamine (EDA), polyethylene glycol ($M_n=4000$ g/mol) and acetone (99.5%) were purchased from Sigma-Aldrich Inc. Hexamethylene diisocyanate (Desmodur H) (HDI) and polyester polyol (Desmophen 1652, $M_n=1060$ g/mol) were supplied from Covestro AG. Sodium 2-[2-aminoethyl] amino ethane sulphonate (AEAS, 50 wt% in water) was kindly donated by Evonik Industries. Polyester polyol was dried at 100 °C under vacuum (~2 mbar) for 15 min prior to use. Dopamine (3-hydroxytyramine hydrochloride) was purchased from Acros Organics Inc. Ultrapure Tris base (Tris(hydroxymethyl)aminomethane) was purchased from MP Biomedicals, LLC. Milli-Q purified water was used for all the synthesis and characterization stages. All chemicals were used without any further purification.

7.3.2. Synthesis of WPU dispersion

The WPU dispersion was synthesized using the acetone method, in a four-necked, 1-L glass round-bottomed-flask equipped with a heating mantle, stirrer, condenser and a thermocouple. The NCO-terminated polyurethane prepolymer was synthesized from 170.8 g of polyester polyol and 29.0 g of HDI, allowing the mixture to polymerize at 80 °C until reaching the theoretical NCO content, which was determined by the standard di-butyl amine back titration method (ASTM D2572-97). Once the theoretical NCO value was achieved, the reaction temperature was dropped to 50 °C while dissolving the prepolymer in acetone to obtain 40 wt% solid content. Upon the complete dissolution of the prepolymer in acetone, the chain extension step was carried out by adding the mixture of 13.3 g AEAS (50 wt% in water) and 1.9 g EDA dropwise into the solution at 50 °C. Afterwards, the prepared polyurethane polymer was dispersed in water by slowly adding 110.00 g of distilled water into the flask while cooling the mixture to 40 °C. Finally, the acetone was removed from the reaction mixture by vacuum distillation and complete removal of acetone was ensured at 45 °C, 50

mbar. WPU dispersion product with approximately 35 wt% solid content with a pH of 7.0 was obtained by filtering the final dispersion through a 50-micron filter.

7.3.3. Preparation of PDA-WPU dispersion

PDA-WPU was synthesized by applying the general polydopamine coating procedure⁷⁰. 50 g of WPU dispersion having 35% solid particle content was diluted with distilled water to 20% solid content to decrease the viscosity of the reaction medium. 0.126 g of dopamine was dissolved in 2 mL of distilled water (6mg/ml) and added into WPU dispersion dropwise using a 5 ml syringe to avoid particle agglomeration. Then, the pH value of the reaction system was adjusted to 8.5 by using ultrapure Tris base. Reaction was carried out at 40°C for 96 hours and dispersions of brown color were obtained.

7.3.4. Preparation of PDA-WPU/PCM films

Following the PDA-WPU dispersion preparation, various amounts of PEG4000 were directly added into the PDA-WPU dispersion and dissolved in water part of the dispersion by mixing the system for four hours. PDA-WPU/PCM mixtures with PDA-WPU solid content to PEG4000 ratio of 1:1.2, 1:1, 1:0.7 and 1:0.5 were prepared. Films were cast from these dispersions on Teflon molds (15x5 cm²) at room temperature and dried under ambient conditions for three days with slow water evaporation. Cast films were removed from the mold, kept in an oven at 30°C overnight and stored in a desiccator at dark. The final film thicknesses were measured to be approximately 0.7 ± 0.12 mm.

7.3.5. Characterizations

Hydrodynamic diameter and zeta potential values of WPU and PDA-WPU dispersions were measured by using a dynamic light scattering (DLS) instrument (Zetasizer Nano - ZS, Malvern Instruments Ltd., UK) provided with laser diffraction and polarized light detectors at three wavelengths. Dispersions were diluted with distilled water to an adequate concentration in the cell and measured at room temperature. Zeta potential was measured at pH 8.5 using Helmholtz-Smoulchowski equation.

A Nicolet IS10 FT-IR spectrometer with an attenuated total reflection system was utilized for the chemical analysis of PDA-WPU/PCM film samples.

The surface and cross-section morphology of the films were investigated using Zeiss LEO Supra 35VP scanning electron microscope (SEM) employing a secondary electron detector at 3 kV by coating with Au–Pd before imaging. Films were cryo-fractured by immersion in liquid nitrogen to obtain cross sections.

Thermogravimetric analysis (TGA) of films was performed using a Shimadzu Corp. DTG-60H (TGA/DTA) instrument by heating samples up to 600 °C at a rate of 10 °C/min under nitrogen atmosphere.

Glass transition temperatures (T_g) and the melting/solidifying transition enthalpies of PCM containing film samples were investigated using differential scanning calorimetry (DSC; Thermal Analysis MDSC TAQ2000) with a heating rate of 10°C/min with heat-cool cycles between -80°C and 100°C under nitrogen atmosphere.

Thermal reliability of PDA-WPU/PCM films was analyzed with accelerated DSC cycles and performing 60 consecutive cycles in the temperature range of -20°C to 100°C with a heating rate of 20°C/min under nitrogen atmosphere. Transition temperatures and enthalpies were calculated by using TA Universal Analysis software.

Theoretical enthalpies of PDAPU/PCM film composites were calculated by using equation below. The actual enthalpies of pure PCMs obtained from DSC analysis for 100% PCM content were utilized as their theoretical enthalpies to make comparisons with the PDAPU/PCM composite films.

$$\Delta H_{theo.} : (1-w) \Delta H_{m/s} \quad Eq.3$$

where “ $\Delta H_{theo.}$ ” is theoretical latent enthalpy, “ $\Delta H_{m/s}$ ” is the melting or solidifying enthalpy of pure PCMs and “ w ” denotes the wt. % (mass fraction) of the PDAPU solid particles in the final film composite.

The thermal conductivity of films was measured by the Hot Disk Thermal Constant Analyser (TPS2500 S).

The mechanical properties of PDA-WPU/PCM films were tested by a universal testing machine Zwick Roell Z100 UTM, with a load cell of 200 N and a crosshead speed of 25

mm/min according to the testing method determined by ASTM D1708-10. An average of at least four replicates of each sample was reported.

Thicknesses of nanocomposite films were measured with a digimatic micrometer (Mitutoyo Quicmike, no. 99MAB041M).

The crystal structure of PDA-WPU/PCM films was analyzed by X-ray diffraction patterns (XRD) from a Bruker D2 Phaser XRD instrument using CuKa radiation ($k = 1.5418 \text{ \AA}$, 40 kV, 200 mA) in the 2Theta range of 5–90°.

Light to thermal energy conversion performance of PDA-WPU films

Time-temperature profiles of PDA-WPU/PCM films were constructed under solar light irradiation at room temperature ($23 \pm 0.5 \text{ }^{\circ}\text{C}$) and humidity of about 51.8%. WPU and PDA-WPU/PCM films of 1.6 cm x 1.4 cm with a thickness of $0.7 \pm 0.12 \text{ mm}$ were irradiated with Oriel LCS-100 solar simulator at 150 mW/cm^2 on a Teflon pad. The film temperature was allowed to rise for 20 minutes and cooled for 10 minutes by switching off the solar simulator. Data were collected with one-minute intervals.

The solar to thermal energy conversion and storage efficiency (η) of PDA-WPU/PCM composite films were calculated by using the formula given below,

$$\eta = \frac{m\Delta H}{PAx(t_e - t_o)} \times 100\% \quad \text{Eq.4}$$

where m is the weight of the film sample, ΔH is the phase change enthalpy of PEG4000, P is the intensity of the applied light irradiation, A is the area of film sample which was irradiated with solar simulator, and t_o and t_e are the onset and end phase transition time of PEG4000, respectively.

Temperature recordings and thermal camera photographs were taken by FLIR E6XT 2.1L thermal imaging camera. All thermal tests of WPU and PDA-WPU/PCM films were repeated three times.

Thermoregulation properties of PDA-WPU/PCM films

To investigate solar light to thermal energy conversion properties of the PDA-WPU/PCM composite films in a cooled environment, a simple experimental setup was constructed. 500 ml of a crystallizing dish was filled with ice. Meanwhile, PDA-WPU/PCM and WPU films

with a surface area of 24 cm^2 ($6\text{cm} \times 4\text{cm}$) were placed onto the inside surface of a beaker having an area of 76 cm^2 and volume of 226 cm^3 . With this design, the $1/3$ of the surface area of the cylindric beaker was covered with film samples. Then, prepared beakers covered with film samples were placed into the ice bath so that the surface of the beaker covered with films was completely immersed in ice. The whole experiment setup was exposed to solar light irradiation at 150 mW/cm^2 by a solar simulator for 30 minutes and naturally cooled by switching-off the solar light for 30 minutes. The temperature of film samples was recorded with the IR sensor of a thermal camera. Time-temperature profiles of films were constructed with data points collected at one-minute intervals. All thermal tests were repeated three times.

During the experiment, the temperature of the inside of the beaker was also followed by placing a K-type thermocouple into the cylindrical environment. To do this, a thermocouple was located to the center of the beaker at 3 cm distance from the film and the temperature of the environment was recorded. All thermal tests were repeated three times. The experimental setup was illustrated in Figure 54.

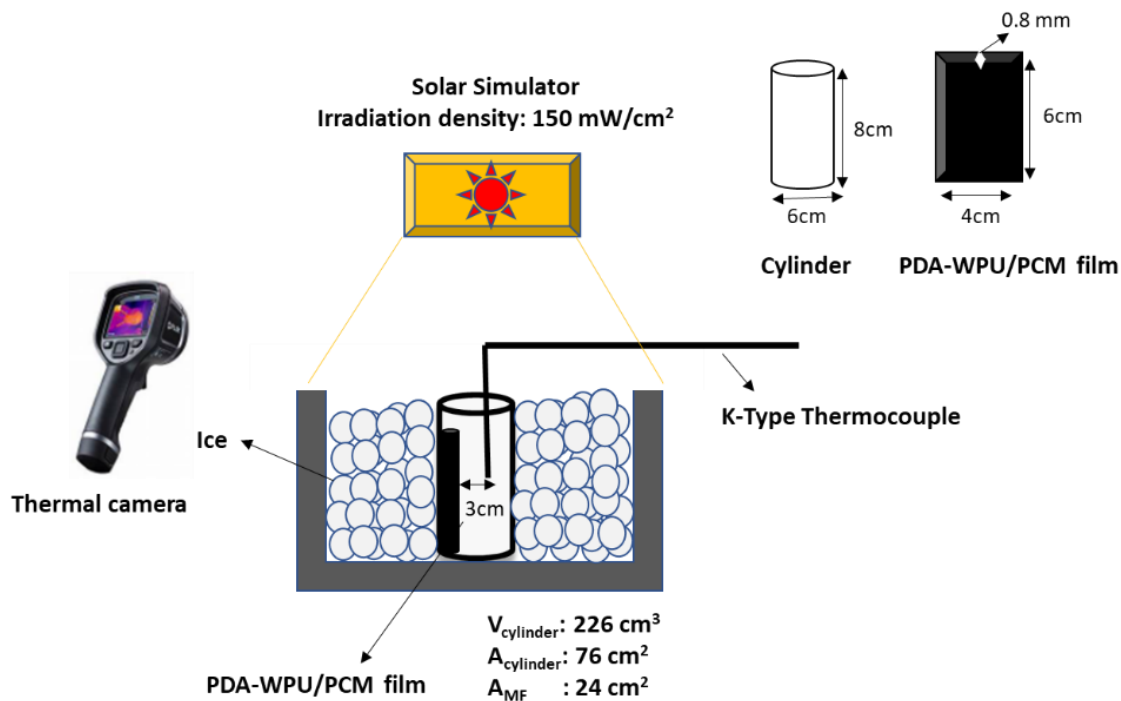


Figure 54. Experimental setup for the evaluation of thermoregulation properties of PDA-WPU/PCM films.

7.4. Results and Discussions

7.4.1. Synthesis and characterization of WPU and PDA-WPU dispersions/cast films

The surfaces of the synthesized WPU particles which were synthesized via the reaction of an isocyanate and a polyester polyol followed by chain extension with a diamine, were coated with polydopamine by a facile and efficient one-pot post-synthesis reaction. At the end of the coating reaction, an aqueous dispersion of PDA-WPU particles were obtained as illustrated in Figure 55A.

Both WPU and PDA-WPU dispersions presented a unimodal size distribution (Figure 55B). The lack of an additional peak on the size distribution graph was an important indicator of dopamine polymerization on WPU particles instead of self-polymerization of dopamine leading to individual PDA capsules in the system. Z-average values of WPU and PDA-WPU dispersions demonstrated an increase in the particle size of WPU particles after PDA surface coating (Figure 55C). While synthesized WPU particles presented an average diameter of 210 nm, PDA-WPU particles presented a 60 nm increase in diameter indicating coating of WPU solid particles with PDA layer. Similar increases in solid particle diameters were reported in studies involving PDA polymerization on different solid particles³¹¹⁻³¹³. Zeta potential values also increased with PDA coating on WPU solid particle surfaces potentially arising from the strong ionic content of WPU particle surfaces due to the quinone, catechol and amine groups of the PDA layer^{321,323}. Although the PDA coating on WPU surfaces shifted zeta potential values to a higher level, particle surfaces still stayed negatively charged. All DLS results strongly supported the formation of a PDA layer on WPU particle surfaces instead of the formation of individual PDA capsules.

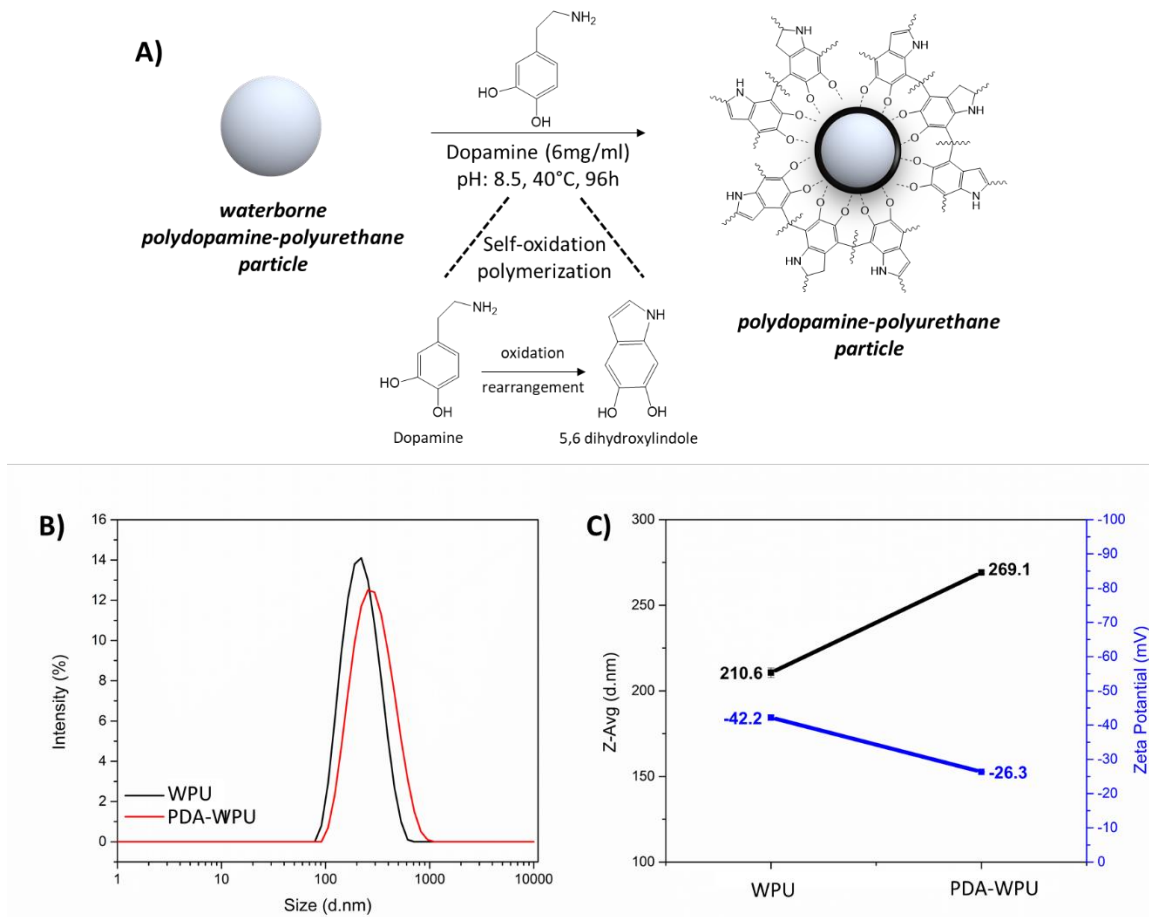


Figure 55. Synthesis of PDA-WPU particles (A), DLS diagram (B) and Z-Avg size and zeta potential values (C) of WPU and PDA-WPU.

Cast films of WPU and PDA-WPU were prepared and analyzed by FT-IR to evaluate the chemical content of films. On the FT-IR spectrum of WPU in Figure 56, characteristic peaks were observed at around $3365\text{-}3385\text{ cm}^{-1}$ due to hydrogen bonds between -NH and C=O groups of urea and urethane. Also, the peaks at $2870\text{-}2940\text{ cm}^{-1}$ region and the strong absorption bands around 1725 cm^{-1} were attributed to -CH stretching and the carbonyl stretching region, respectively. For PDA-WPU films, it was observed that new peaks originating from PDA content appeared. Assigned peaks at 1575 cm^{-1} , 1372 cm^{-1} , and 1253 cm^{-1} corresponding to aromatic C=C double bonds, symmetric and asymmetric -NH stretching vibrations and C-N stretching, respectively, confirmed the presence of the PDA in the cast films.

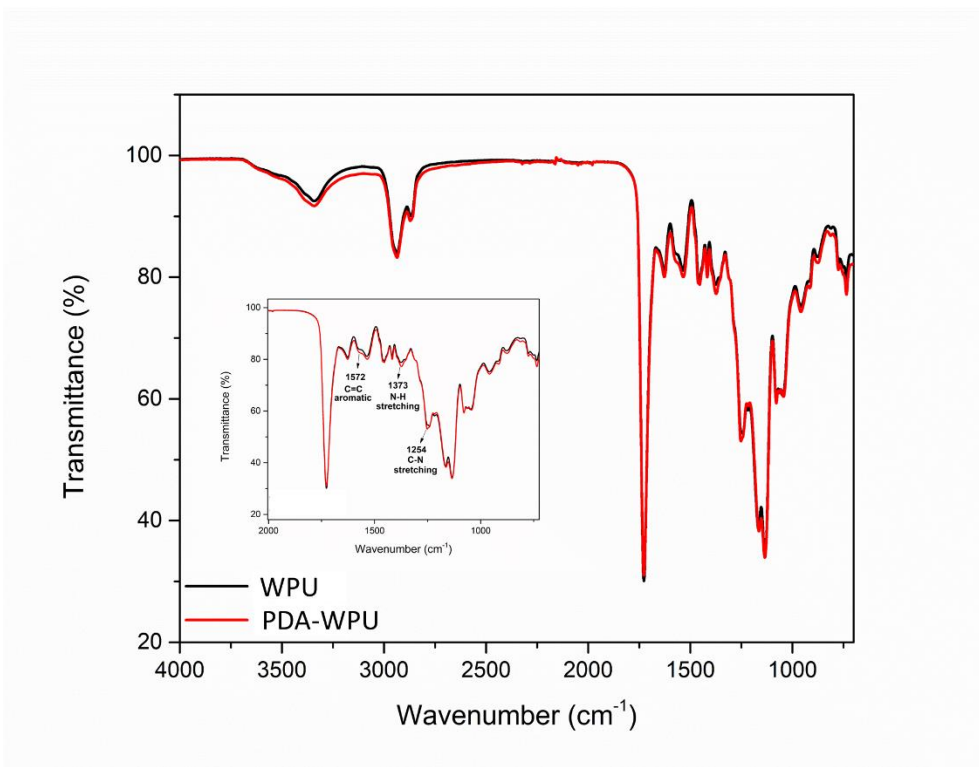


Figure 56. FT-IR spectrum of WPU and PDA-WPU cast films.

7.4.2. Preparation and characterization of shape-stable PDA-WPU/PCM composite films

PEG4000, which is utilized as the PCM in this study was directly added to PDA-WPU dispersion at desired ratios and allowed to mix followed by molding and drying for the film formation (Figure 57).

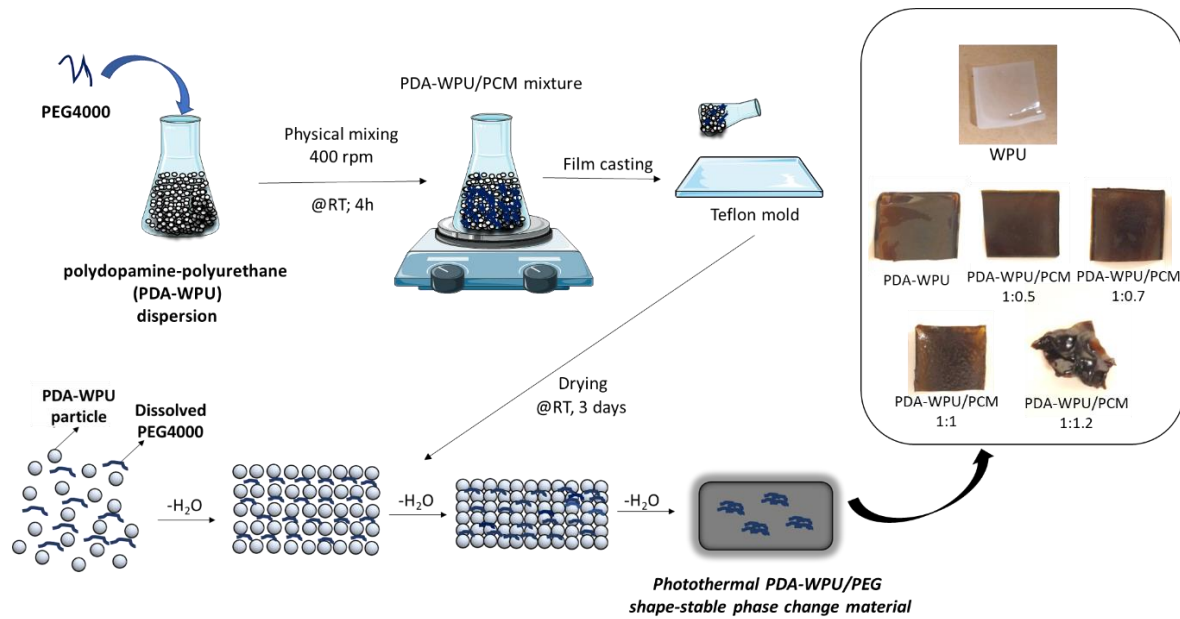


Figure 57. Preparation of PDA-WPU/PCM cast films and photographs of films at different PDA-WPU:PCM ratios.

Successful film formation was demonstrated for dispersions prepared at PDA-WPU:PCM ratios of 1:0.5, 1:0.7 and 1:1. However, the dispersion prepared at the ratio of 1:1.2 did not form a proper cast film and the film remained sticky with PEG4000 leaking out of the film. These preliminary findings showed that there is a limit for the amount of PEG4000 that can be incorporated into the polymer matrix above which the excess PEG4000 could not be trapped between PDA-WPU solid particles during the film formation. The highly hydrophobic character of PEG4000⁴²⁶ may also have prevented interactions with the hydrophilic polymer matrix at increased ratios. For dispersions prepared at PDA-WPU:PCM ratios of 1:1 and below, which resulted in shape-stable film formation, PEG4000 molecules were probably first trapped between PDA-WPU particles due to the strong adhesive property of the PDA layer⁴²⁷, possible hydrogen bonding interactions⁴²⁸ and structural compatibility with polyurethane-based particles⁴²⁹ and later have diffused/coalesced into PDA-WPU particles⁴³⁰ as schematized in Figure 57.

Surface and cross-section morphologies of prepared PDA-WPU/PCM films were examined by SEM (Figure 58). A three-dimensional network structure was observed for films containing PEG4000 both on the surface and on cross-section images, whereas neat PDA-WPU films did not present such morphologies. The fact that the PDA-WPU/PCM 1:1 which

contained the highest amount of PCM presented a more distinct network structure with higher number of dark-colored spots might indicate that the deformed network structure and dark spots represent the PDA-WPU matrix and the PEG4000, respectively. Similar morphologies were reported before for various polymer matrices doped with PCMs in different studies^{149,151,431,432}. Most likely, the solidification of embedded PEG4000 during the drying process required for film formation resulted in stretching and deformation of the PDA-WPU polymer film and three-dimensional network structures have formed on areas where PEG4000 had accumulated.

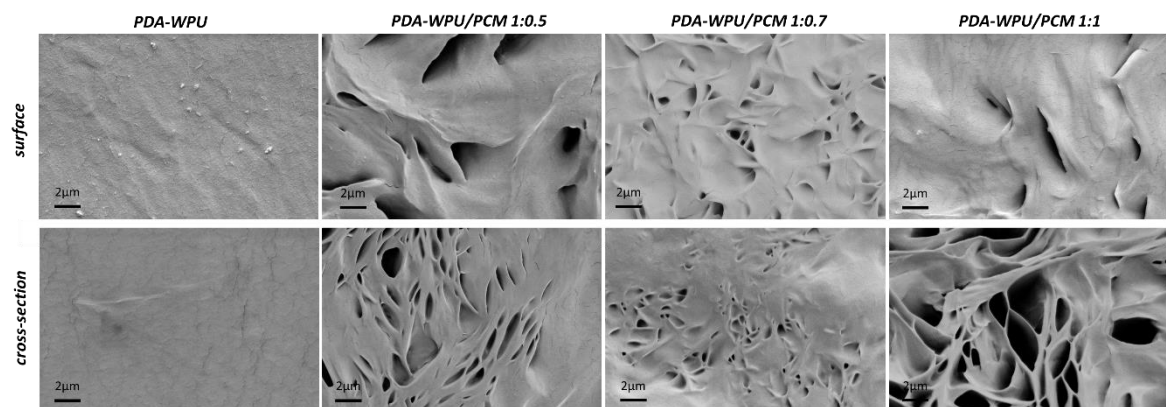


Figure 58. Surface and cross-section SEM images of PDA-WPU and PDA-WPU/PCM with different PEG4000 contents.

Existence of PEG4000 in the PDA-WPU films and their crystal structures were analyzed by XRD and presented in Figure 59A. The broad peak on the XRD spectrum of WPU at $2\theta = 20.1^\circ$ could be attributed to the diffraction of the amorphous structures of the WPU⁴³³. It was observed that the broad peak for the PDA-WPU film sample prepared from PDA coated WPU particles was slightly shifted to the 2θ value of 19.5° ⁴³⁴. Also, new broad peaks at the 2θ of 29.9° and 41.3° appeared on the XRD spectrum of PDA-WPU films due to the amorphous PDA coating. On the XRD spectrum of PEG4000, major diffraction peaks at 2θ of 19.2° and 23.5° as well as some minor peaks at 26.7° , 36.5° and 40.6° indicated crystallinity of PEG4000 as also reported in different studies^{435,436}. Sharp peaks of PEG4000 were also obviously seen on the spectra of PDA-WPU/PCM films at the same 2θ values. It was also interesting that broadness of the peak between 15° and 25° originated from PDA-WPU matrix was narrowed with increasing PEG4000 content in composite films, which

could imply well integration of PEG4000 in/between PDA-WPU solid particles. These results demonstrated the crystalline nature of PDA-WPU/PCM films due to the presence of PEG4000 and its well integration into the composite film by means of possible intermolecular hydrogen bonding via interpenetration of PEG and PDA-WPU particles⁴³⁷.

As shown in Figure 59B, the general mechanical behavior of WPU and PDA-WPU has definitely changed with the PEG 4000 content in the prepared films. The Young's modulus of PDA-WPU, which was 3.21 MPa, increased almost 7-fold and reached 20.9 MPa when PEG400 was incorporated at 1:1 ratio. The increase of Young's modulus with PEG4000 content was most likely because of the increased stiffness of the composite films due to the integration of crystalline PEG4000 into the polymer matrix. On the contrary, tensile strength and elongation at break values of the composite films have sharply decreased with increasing PEG4000 content in the polymer matrix. A similar impact of high concentrations of PEG4000 in the polymer matrix was reported before^{438,439}. These findings were undoubtedly obtained due to the increase of the brittle character and the drop of elasticity of the final composite film originating from the PEG4000 content. Created voids in the films due to the stretching of the polymer matrix by solidified PEG4000 could be also a factor that decreased tensile strength and elongation at break values⁴⁴⁰. WPU film formation occurs in three steps, which are evaporation of water and ordering of particles, deformation of particles and interdiffusion of particles across particle-particle boundaries⁴⁴¹. Dissolved PEG4000 in the system could have hindered these processes, especially the interdiffusion stage, due to stacking of PEG4000 molecules on the particle surfaces. Thus, some weak points could have formed in the polymer matrix and pulled down tensile strength and elongation at break values. One more reason could be the interpenetration of PEG4000 toward the amorphous PDA-WPU polymer matrix. PEG4000 inside the amorphous region of the polymer matrix may have hindered the stretching of the polymer chains and reduced the elongation ability of the polymer film.

The thermal stability of PEG4000 and PDA-WPU/PCM films were analyzed via TGA (Figure 59C). The decomposition temperature of PDA-WPU films was higher than WPU films by 9°C probably due to the PDA coating on WPU particles which acted as a protecting layer³¹³. As to PDA-WPU/PCM composite films, it was found that decomposition temperatures were between the decomposition temperatures of pure PEG4000 and PDA-

WPU films, demonstrating an enhanced thermal stability as the PEG4000 content incorporated into polymer matrix increased.

The thermal conductivity of prepared films was measured and presented in Figure 59D. The thermal conductivity of PDA-WPU was found to be almost two times higher than the WPU film. A number of reasons such as hydrogen bonding, aromatic content, and π - π stacking abilities of PDA structure⁷¹ may have caused the enhancement of the thermal conductivity of the PDA-WPU film³³². Addition of PEG4000 into the PDA-WPU system has further increased the thermal conductivity of composite films relative to the PDA-WPU films and thermal conductivity of PDA-WPU/PCM 1:1 composite film reached 0.301 W/m°K, potentially due to the contribution of PEG4000⁴⁴².

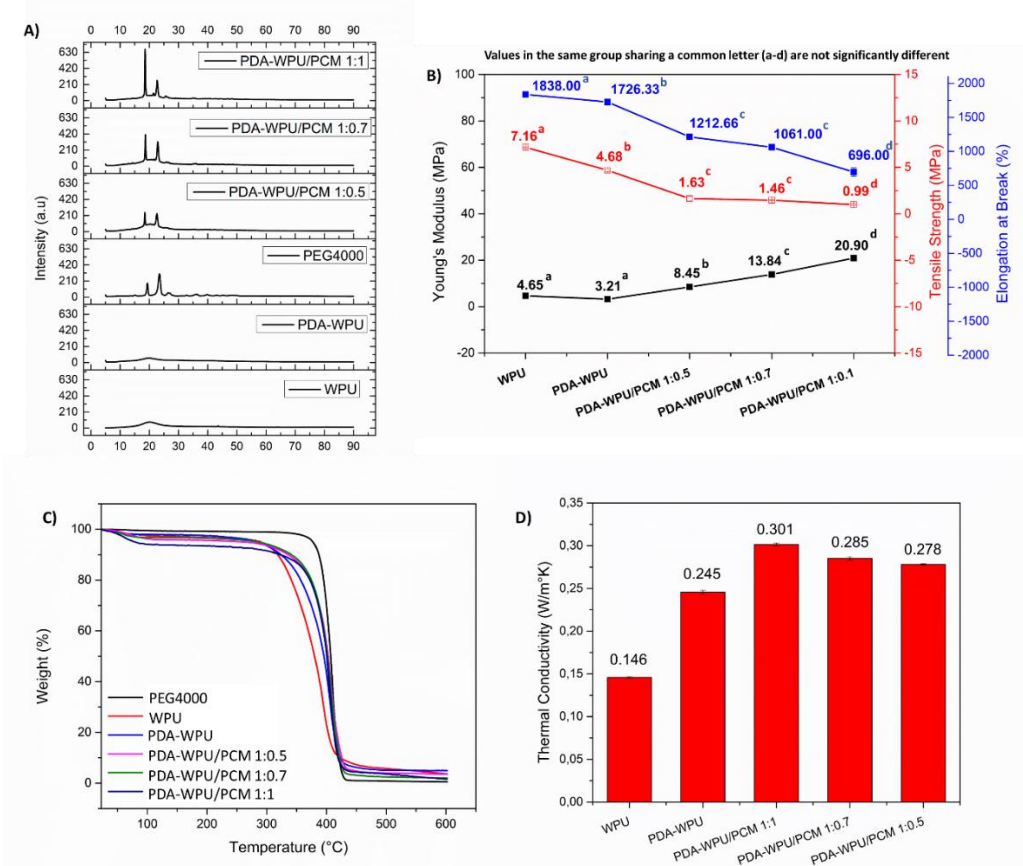


Figure 59. XRD spectra of PDA-WPU, PEG4000 and PDA-WPU/PCM films with different PEG4000 contents (A). Mechanical parameters (B) and thermal properties (C) and thermal conductivity values (D) of WPU, PDA-WPU and PDA-WPU/PCM film composites.

7.4.3. Thermal properties of PDA-WPU/PCM composite films

The thermal properties of PDA-WPU/PCM composite films were investigated by DSC analysis (Figure 60A). Glass transition temperatures (T_g) of PDA-WPU/PCM composite films with different PEG4000 contents were not significantly different than neat WPU films. The onset/offset melting/solidifying temperatures of PEG4000 in composite films are critical to determine the maximum temperatures at which composite films can be handled for the thermal energy storage and the temperature range at which films will release the stored latent heat to the environment. The melting temperature of PEG4000 had shifted to lower temperatures when it was embedded in the composite films, where the shift was found to be shorter as the PEG4000 content in the composite increased (Figure 60B). The melting transition occurred at lower temperatures due to the confinement of PEG4000 within the PDA-WPU matrix caused by physical interactions such as surface tension or hydrogen bonding^{381,443}. As the amount of the PEG 4000 integrated into the polymer matrix increased, accumulation of PEG molecules in the different locations of the film matrix decreased these interactions, whereby acting more like pure PEG4000. Similarly, solidifying temperatures of PDA-WPU/PCM composites shifted to lower temperatures and a solidifying transition for PDA-WPU/PCM 1:0.5, the composite with the lowest PEG4000 content, was not observed (Figure 60C). Probably, when the PEG4000 amount was much below the amount of PDA-WPU solid particles, better coalescence occurred between PEG4000 and PDA-WPU particles; thus PDA-WPU polymer matrix hindered the crystal arrangement of PEG molecular chains. The thermal insulator character of WPU may have also led to the absorption of the heat released during the solidifying process so that the solidifying transition was not observed at low PEG4000 content. Nevertheless PDA-WPU/PCM 1:1 presented a melting transition that started at 33.3°C and completed at 3.6°C meaning that the composite

film will release the stored heat in this temperature range, which would be very suitable for a variety of applications.

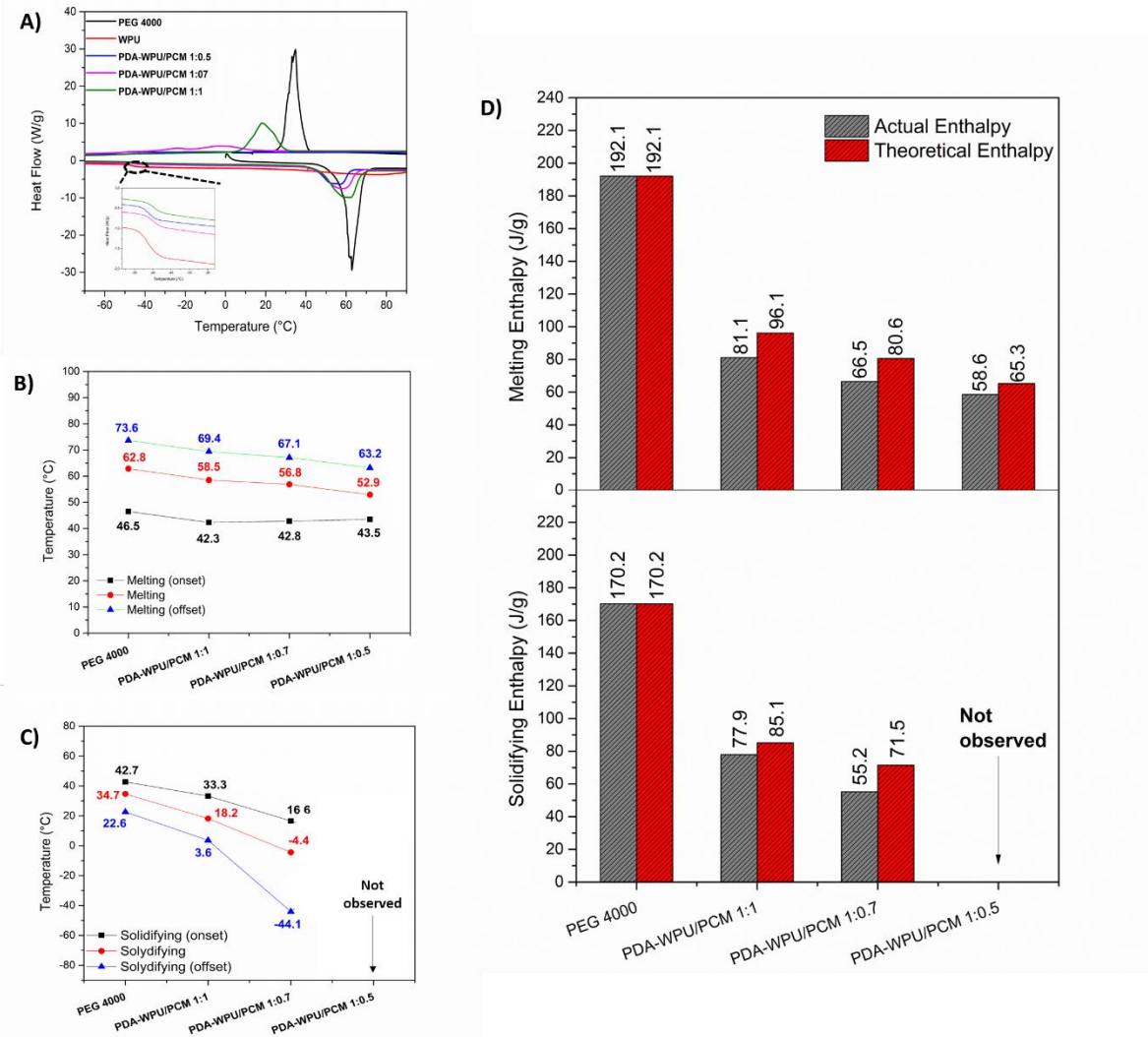


Figure 60. DSC curves (A), melting (B) and solidifying (C) temperatures with onset, peak and offset points, and melting/solidifying enthalpies (D) of PEG4000 and PDA-WPU/PCM film composites.

The melting/solidifying enthalpies of PEG4000 in the PDA-WPU/PCM composite films along with the transition enthalpies of pure PEG4000 was demonstrated in Figure 60D.

It should be noted that PDAPU/PCM 1:1 composes of 50:50 wt. % of PDAPU solid particles and PEG4000 in the final film composite system. These ratios are 58:42 wt. % and 66:33 wt. % for PDAPU/PCM 1:0.7 and 1:0.5, respectively.

As seen in Figure 60D, melting and solidifying enthalpies of pure PEG4000 were calculated as 192.1 J/g and 170.2 J/g, respectively. The melting enthalpy of PCM in the PDAPU film matrix for the ratio of 1:1, 1:0.7, and 1:0.5 was found as 81.1 J/g, 66.5 J/g, and 58.6 J/g, respectively. It was seen that actual enthalpies were lower than theoretical enthalpies, which were 15.6%, 17.5%, and 10.2%, respectively. A fair amount of differences between actual and theoretical enthalpies of PCM in the film composite system could be because of material losses during the film preparation or analysis processes (Ex; PEG 4000 remained on the surface part of film composite may have been kept by the Teflon mold).

As to the solidifying enthalpies of PEG4000 in the PDA-WPU matrix, it was found that solidifying enthalpies were decreased more than expected by integrating lower amount of PEG4000 than PDA-WPU solid particles into the polymer matrix. As seen in Figure 60D, the solidifying enthalpy of PDA-WPU/PCM 1:1 was calculated as 77.9 J/g. This value showed a more decreasing trend for the PDA-WPU/PCM 1:0.7 film composite that solidifying enthalpy of the film composite was measured as 55.2 J/g, while having melting enthalpy of 66.5 J/g.

Results obtained by the DSC analysis demonstrated that PDA-WPU/PCM 1:1 composite film was the most optimal film in terms of suitable melting/solidifying temperature ranges and high latent heat of the end-product which can directly be utilized in real-life applications.

7.4.4. Shape stability and thermal reliability of PDA-WPU/PCM composite films

Shape stability of the composite system is an important parameter in the concept of latent heat energy storage for practical applications. The designed material loaded with solid-liquid PCMs should prevent leakage of PCMs when the ambient temperature reaches the melting temperature of PCMs. A typical leakage test⁴⁴⁴⁻⁴⁴⁶ was applied to PDA-WPU/PCM films to investigate their shape stabilities, in which PDA-WPU/PCM composite films were incubated at a temperature above the melting temperature of PEG4000. While pure PEG4000 has transitioned to its liquid form at the end of the incubation period, under the same conditions,

any leakage or any sticky appearance was not observed for PDA-WPU/PCM films (Figure 61A). These results exhibited shape-stability of PDA-WPU/PCM composite films at all tested PEG4000 ratios.

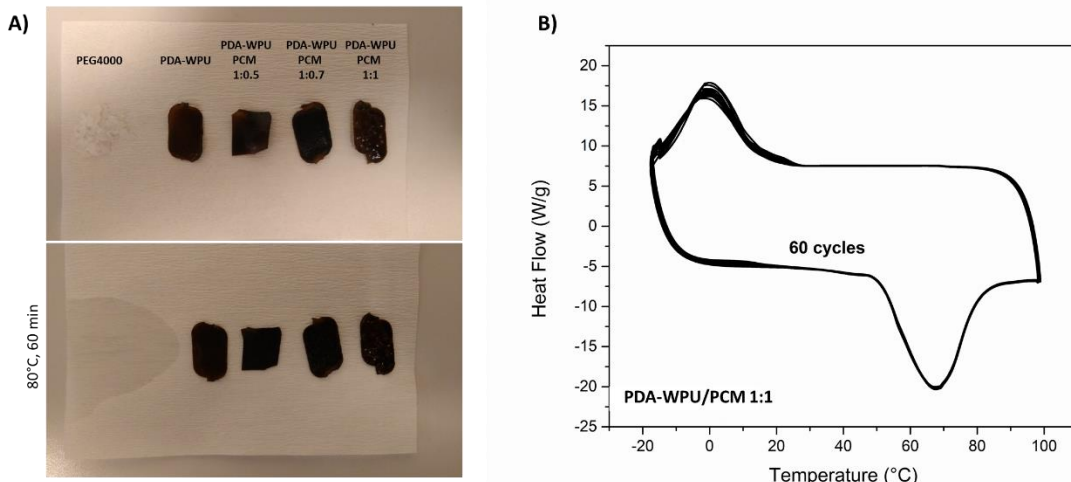


Figure 61. The physical states of prepared PDA-WPU/PCM composite films before and after heat treatment (A) and DSC curves of consecutive thermal cycles for thermal reliability of films (B).

The thermal reliability tests of PDA-WPU/PCM composite films were employed by subjecting samples to 60 consecutive thermal cycles (Figure 61B)²⁶². Significant differences were not observed in the melting/solidifying temperatures and enthalpies of the PDA-WPU/PCM 1:1 composite film. Results demonstrated that the prepared composite films remained stable after several melting/solidifying processes, indicating their long-term operational stability.

7.4.5. Solar-to-thermal energy conversion and storage performance of PDA-WPU/PCM films

Sunlight-activated heating and cooling curves of WPU, PDA-WPU and PDA-WPU/PCM film samples was constructed by collecting temperatures under sunlight irradiation (Figure 62A). While the temperature of the PDA-WPU film at room temperature increased to 61.3°C at the end of 20-minute irradiation, the temperature of the neat WPU film barely reached 30.4°C under the same conditions. The WPU particles were imparted photothermal character

via the PDA coating resulting in PDA-WPU composite films with strong photothermal activity. Furthermore, sunlight-activated temperature increases were observed to be higher at increasing PEG4000 contents, where the PDA-WPU/PCM 1:1 film with the highest PEG4000 content reached 74.8°C under 20-minute sunlight irradiation. This was undoubtedly arising from the enhancement of the thermal conductivity of film samples by the PEG4000 content. Films having higher thermal conductivity led to more rapid transmission of the same amount of heat, thereby the temperature of PEG4000 containing films raised faster⁴⁴⁷. Thermal camera images of film samples at the end of sunlight irradiation also demonstrated sunlight-activated heating of composite films (Figure 62B).

The energy storage efficiency of PDA-WPU/PCM composite films was calculated based on the duration of phase transitions determined by tangential method (Figure 62C) and the energy balance equation⁴²⁴. To evaluate the energy storage performance of prepared composite films in real-life conditions, films were exposed directly to solar irradiation under ambient conditions. Obviously, PDA-WPU/PCM 1:0.5 and 1:0.7 had low energy storage efficiencies due to the lower PEG4000 content. However, the PDA-WPU/PCM 1:1 composite film had an acceptable energy storage efficiency despite many disadvantages, such as their lower thermal conductivities relative to different designs in the literature^{263,448-450}, the experiment design under ambient conditions without any insulator and the relatively low solar irradiation density applied. It should be emphasized that the energy storage efficiency of 72.9 % obtained with PDA-WPU/PCM 1:1 is significantly promising when compared with some studies in the literature^{120,123,169,344,347,451,452} especially since the composite film is not a semi-finished material, but rather it is an end-product that can be directly used in the desired application.

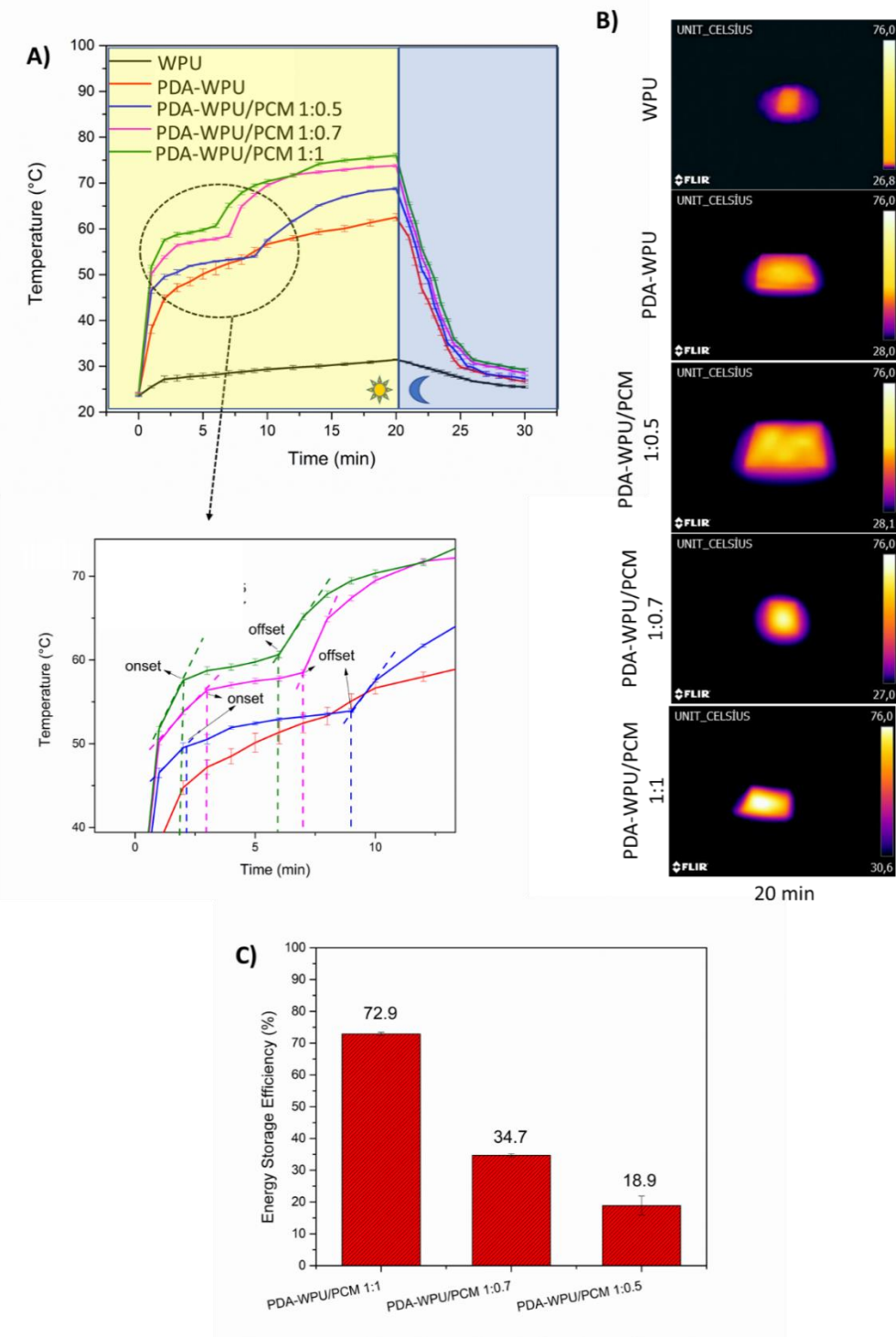


Figure 62. Thermal behavior of film samples under 150 mW/cm² solar light irradiation (A). Thermal camera imaging of film samples at 20 min solar irradiation (B). Energy storage efficiencies of PDA-WPU/PCM composite films (C).

7.4.6. Demonstration of PDA-WPU/PCM 1:1 composite film as a solar heat storage-release material effective under cold weather conditions

The effect of film samples on the applied environment in terms of heat absorbed under sunlight irradiation and thermal buffering capacity during the cooling process was studied by preparing a simple real-world test setup. PDA-WPU/PCM 1:1 film was utilized to partially cover the inside surface of a glass beaker which was placed in ice. While the ice allowed to simulate cold weather conditions, the PDA-WPU/PCM 1:1 film simulated a solar heat storage/release material that was applied at the border between outside and inside.

Thermal camera images of the setup before and after 30-minutes sunlight irradiation and during the cooling when the sunlight was switched off are shown in Figure 63A. Time-temperature curves constructed by the film surface temperatures (Figure 63B) have demonstrated that the temperature of PDA-WPU and PDA-WPU/PCM 1:1 films, which were 12.0°C prior to irradiation increased significantly and reached 38.2° and 45.3°C, respectively. Under the same conditions, the temperature of the neat WPU film only increased to 17.8°C. Furthermore, temperatures of both PDA-WPU and PDA-WPU/PCM 1:1 films reached a plateau approximately between 20°C and 30°C probably because they have reached their maximum solar-to-thermal energy conversion capacity. When the sunlight irradiation was switched off, the PDA-WPU film returned to starting temperature of 12.0°C within 30 minutes, whereas the PDA-WPU/PCM 1:1 stayed warmer at 17.9°C. During cooling, PDA-WPU/PCM 1:1 exhibited significant thermal buffering which began around 20°C because of the releasing of heat stored by the PCM content of the film, hence the temperature of the film stayed almost stable throughout 15 min resulting in slowing down of the cooling process.

Simultaneously, the temperature inside the beakers covered with film samples was followed to examine the effect of changes in film temperatures on the applied environment (Figure 63C). Impressively, the inside temperature of beakers covered with PDA-WPU and PDA-WPU/PCM 1:1 film increased to 21.6°C and 24.8°C, respectively, while the temperature attained for the beaker covered with neat WPU film was only 14.2°C. The PDA component of the hybrid films increased the amount of harvested sunlight resulting in more heat

produced by the films and more elevated temperatures around the environment of the films. After the sunlight source was switched off, the beaker covered with the PDA-WPU film returned to 2.8°C in 7 minutes and reached, whereas the temperature inside the beaker covered with PDA-WPU/PCM 1:1 film at remained significantly higher at 13.1°C. Again, the PCM containing film released the stored heat around its solidification transition resulting in a slower cooling and higher temperatures.

These results have demonstrated the sunlight-activated heat storage-release properties of PDA-WPU/PCM 1:1 composite film at cold weather conditions and their strong potential as materials for thermal management applied in buildings, textiles, or any other suitable fields.

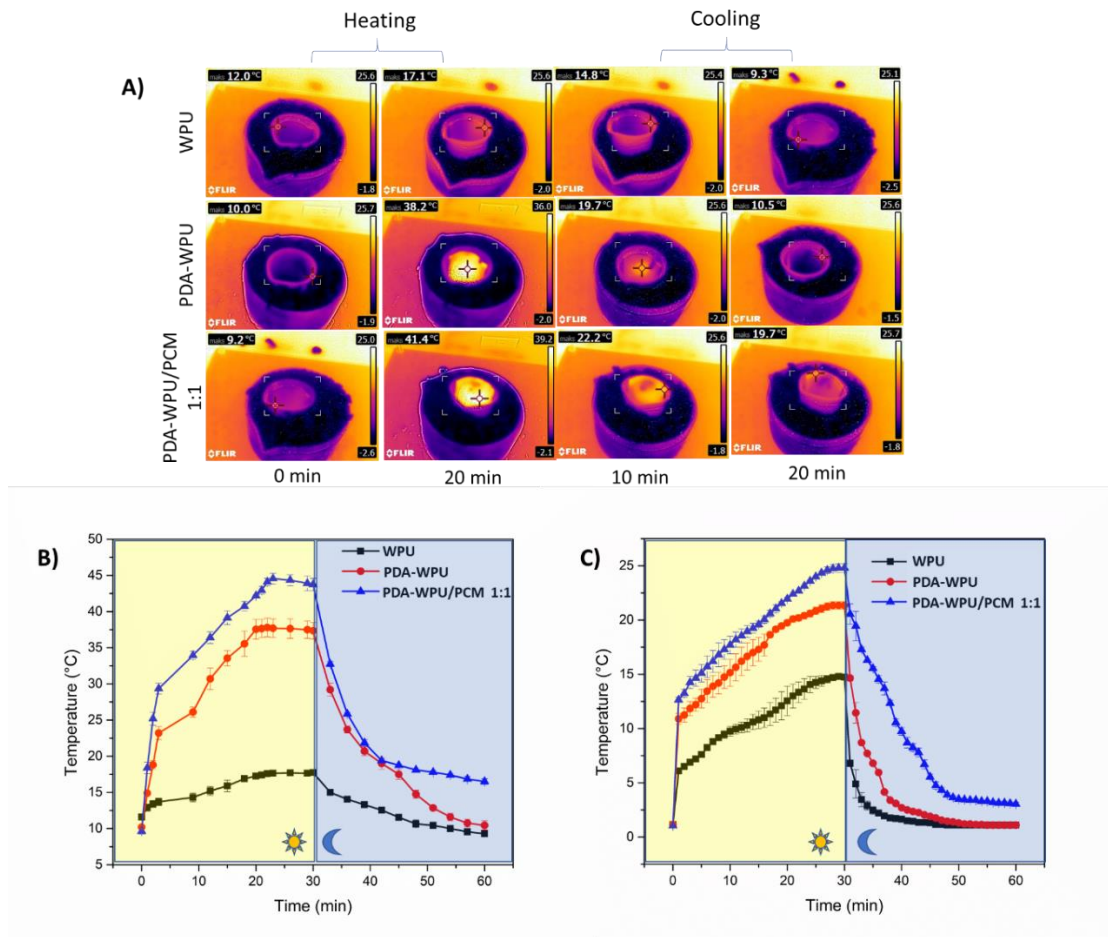


Figure 63. Thermal camera images (A) and thermal behavior graph (B) of film samples in the cold environment. Temperature changing inside of beakers having film samples (C).

7.5. Conclusions

In this study, neat WPU dispersions were turned into polymeric films, which intrinsically possess solar-to-thermal energy conversion capability by coating WPU particles with PDA in an aqueous dispersion. PEG4000, which is commonly used as a phase change material, was directly integrated into the polymer matrix in different ratios without utilization of any other encapsulation material. Prepared composite films were analyzed in terms of their mechanical, thermal and morphological properties and demonstrated to present similar behaviors as their neat counterparts. Latent heat storage and release performance of composite films were examined by DSC analysis. The melting and solidifying enthalpies of PDA-WPU/PCM 1:1 composite film, which had the highest PEG4000 amount without any leakage, was calculated as 81.1 J/g and 77.9 J/g, respectively. The PDA-WPU/PCM 1:1 composite film was heated to 74.8°C in 20-minutes sunlight irradiation at 150 mW/cm², with a solar-to-thermal energy conversion efficiency of 72.9%. The composite films were also tested in cold weather conditions in terms of their sunlight-activated temperature elevations and thermal buffering performance during the natural cooling process. PDA-WPU/PCM 1:1 composite film was demonstrated to reach significantly higher temperatures than neat WPU films under sunlight irradiation and to remain significantly warmer when the sunlight irradiation stopped. The sunlight-activated heat storage/release properties of the composite films were shown to affect the temperature of the applied environment where an environment insulated with these composite films heated up more by sunlight and remained warmer in the absence of sunlight. PDA-WPU/PCM composite films, which synergistically combined light harvesting/photothermal conversion properties of PDA and heat storage properties of PEG4000 have strong potential as shape-stable phase change materials that can be utilized in a broad range of heat management applications.

CHAPTER 8: Overall conclusions and future perspectives

8. 1. Overall conclusions

The general conclusions of the thesis study according to the order of chapters flow can be listed as below:

- HNT/PE nanocomposite films were prepared as potential active food packaging materials. It was found that PE prepared with HNTs presented significantly higher ethylene adsorption capacity in comparison with neat PE films. Moreover, the torturous path arising from HNTsin the polymer matrix resulted in decreased permeability of oxygen and water vapor, thus, slowed down processes that lead to senescence of food products. It was demonstrated that the shelf life of bananas and tomatoes packaged with the nanocomposite film having 5 wt.% HNT concentration increased relative to food samples packaged with neat films. As to oxygen and water vapor barrier properties, HNT/PE films with 1 wt.% HNT content presented the optimum performance, resulting in the improved shelf life of strawberries and fresh-cut chicken samples.
- Flexible nanocomposite food packaging films having thermal buffering performance in cold-chain temperatures were prepared by PE polymer matrix and PCM/HNT nanofillers. HNTs were impregnated with PEG 400 and PEG 600 PCMs at 30 wt.% without any leakage. Melting enthalpies of HNT/PEG400, HNT/PEG600, and HNT/PEG-M nanohybrids were measured as 22.5 J/g, 24.8 J/g, and 21.7 J/g respectively. HNT/PEG-M was demonstrated to have the buffering capacity at the temperature range of -21.8°C-21.7°C. Prepared PE/HNTPEG-M nanocomposite films have demonstrated significant thermal buffering capacity in a temperature range covering cold-chain temperatures. The effectiveness of PE-HNT/PEG-M

nanocomposite packaging films on keeping food products colder for longer times was investigated by using meatball samples. Frozen meatballs packaged with nanocomposite films warmed up to 4°C two-times slower than meatballs packaged with standard PE films. Similarly, chilled meatballs at the temperature of 2°C reached 15°C more than two times slower than when they were packaged with nanocomposite films.

- HNTs were successfully separated into monodisperse, agglomeration-free fractions of different sizes through the 3-stage separation method. The yields of separated HNTs into three quality -grades which were Grade-1, Grade-2, and Grade-3 were calculated as 37%, 45% and 17 %, respectively. It was also showed that the applied protocol for removing the PDA layer on HNT surfaces through a simple heat treatment did not disrupt nanotubular forms, chemical and crystal structures. Results revealed that high-quality grade HNTs presented significantly higher lumen loading, covalent surface functionalization capacity and better dispersibility in a polymeric matrix compared to raw HNTs.
- Classical waterborne WPU was converted into a novel photothermal polymer matrix by coating WPU solid particle surfaces with PDA in the dispersion state. Films cast from PDA-WPU dispersions containing different amounts of PDA were prepared and investigated in terms of their thermal, mechanical, morphological properties and surface hydrophilicity. PDA-WPU (6mg/ml)/72h, which has the highest PDA content among the other formulations, presented an xx temperature increase when irradiated with infrared laserlight. PDA-WPU (6mg/ml)/72h was also studied in terms of its solar-driven water evaporation performance and demonstrated to have an evaporation rate of 2.81 kg/m² with a solar-vapor generation efficiency of 58.61%.
- A mesopore rich hierarchical porous backbone was obtained via desilication to increase the amount of PCM impregnation capacity. The optimum non-exudative composites of ZSM-B having 65% LA and 70% PEG presented latent heat storage performance up to 106.9 J/g and 118.6 J/g, respectively. Moreover, The latent heat storage potential of the composites were demonstrated via solar simulation tests representing natural sunlight-activated heating and cooling cycles.

- PEG4000, which is commonly used as a PCM, was directly integrated into the PDA-WPU photothermal polymer matrix in different ratios without utilization of any other encapsulation agent. The melting and solidifying enthalpies of PDA-WPU/PCM composite films having the highest PEG4000 amount without any leakage was calculated as 81.1 J/g and 77.9 J/g, respectively. The PDA-WPU/PCM composite film having the highest PEG4000 amount reached 74.8°C in 20 min under solar light irradiation with a solar to the thermal energy conversion efficiency of 72.9%. Composite films have also been demonstrated to have significant thermoregulating properties.

8. 2. Future perspectives

HNT/PE-based nanocomposite films and HNT separation studies which were presented as Chapters 2-4 will have significant impact on various other HNT-related studies and on food packaging materials in the concept of food safety. Since the dispersion of HNTs into PE matrix was studied with both empty and impregnated HNTs, various strategies can be derived from these findings. For example, HNTs can be impregnated with antimicrobial agents and incorporated into the PE matrix together with empty HNTs. In this way, a multifunctional food packaging system having ethylene scavenging, barrier and antimicrobial properties can be designed. Besides, this technology can be easily applied to industrial manufacturing by scale-up studies and specific food products can be targeted by incorporating proper agents into the nanocomposite film. For example, by preparing HNT nanohybrids with an ethylene oxidation agent, not only ethylene scavenging but also ethylene inhibiting property can be added to packaging film. Moreover, different designs comprising HNTs alone can be applied in refrigerator parts that are able to capture released ethylene gas from fruits and vegetables during cold storage. HNT separation study can be used as a background for this goal due to higher loading capacities obtained.

Studies that have been presented as Chapters 4-7 can open a way to produce many critical and effective designs relating to light to thermal energy conversion applications. Because PDA presents photothermal properties, natural photothermal clay minerals by a polydopamine surface coating of HNT nanotubes can be created and offered as nanoparticles

that can be utilized in different application fields ranging from controlled release applications to photothermal therapy. As one of many potential ideas in this concept, the surface of driveways/highways can be transformed into an anti-icing surfaces integrating photothermal clay minerals into the asphalt/bitumen.

As to PDAPU, which is a photothermal polymer matrix, it can be the background of a great number of studies on its own, such as antibacterial surface coating materials, self-healing applications, self-sterilization materials, shape memory execution and thermal management in the textile industry. More specifically, for instance, the material can be applied as thermally buffering exterior insulation coating/block materials on buildings by buffering inside temperature to reduce energy consumption. Or, because the material is also a coating material, different membranes can be incorporated into a composite system produced by photothermal PU material. In this way, a high-water evaporation rate with strong salt rejection ability can be obtained. The composite system designed to float on the water surface can provide effective use for the desalination seawater or purification of wastewater revealed from industrial applications.

REFERENCES

- (1) Terry, L. A.; Ilkenhans, T.; Poulston, S.; Rowsell, L.; Smith, A. W. Development of new palladium-promoted ethylene scavenger. *Postharvest Biology and Technology* 2007, *45* (2), 214.
- (2) Wills, R.; Warton, M. Efficacy of potassium permanganate impregnated into alumina beads to reduce atmospheric ethylene. *Journal of the american society for horticultural science* 2004, *129* (3), 433.
- (3) Cui, Y.; Kumar, S.; Kona, B. R.; van Houcke, D. Gas barrier properties of polymer/clay nanocomposites. *Rsc Advances* 2015, *5* (78), 63669.
- (4) Sweeney, S. F.; Woehrle, G. H.; Hutchison, J. E. Rapid purification and size separation of gold nanoparticles via diafiltration. *Journal of the American Chemical Society* 2006, *128* (10), 3190.
- (5) Hanauer, M.; Pierrat, S.; Zins, I.; Lotz, A.; Sönnichsen, C. Separation of nanoparticles by gel electrophoresis according to size and shape. *Nano letters* 2007, *7* (9), 2881.
- (6) Duesberg, G.; Burghard, M.; Muster, J.; Philipp, G. Separation of carbon nanotubes by size exclusion chromatography. *Chemical Communications* 1998, (3), 435.
- (7) Rong, R.; Xu, X.; Zhu, S.; Li, B.; Wang, X.; Tang, K. Facile preparation of homogeneous and length controllable halloysite nanotubes by ultrasonic scission and uniform viscosity centrifugation. *Chemical Engineering Journal* 2016, *291*, 20.
- (8) Kamble, R.; Ghag, M.; Gaikawad, S.; Panda, B. K. Halloysite Nanotubes and Applications: A Review. *Journal of advanced scientific research* 2012, *3* (2).
- (9) Liu, M.; Jia, Z.; Jia, D.; Zhou, C. Recent advance in research on halloysite nanotubes-polymer nanocomposite. *Progress in polymer science* 2014, *39* (8), 1498.
- (10) Lvov, Y.; Wang, W.; Zhang, L.; Fakhrullin, R. Halloysite clay nanotubes for loading and sustained release of functional compounds. *Advanced Materials* 2016, *28* (6), 1227.
- (11) Peng, Q.; Liu, M.; Zheng, J.; Zhou, C. Adsorption of dyes in aqueous solutions by chitosan-halloysite nanotubes composite hydrogel beads. *Microporous and Mesoporous Materials* 2015, *201*, 190.
- (12) Lun, H.; Ouyang, J.; Yang, H. Natural halloysite nanotubes modified as an aspirin carrier. *RSC Advances* 2014, *4* (83), 44197.
- (13) Massaro, M.; Piana, S.; Colletti, C. G.; Noto, R.; Riela, S.; Baiamonte, C.; Giordano, C.; Pizzolanti, G.; Cavallaro, G.; Milioto, S. et al. Multicavity halloysite-amphiphilic

cyclodextrin hybrids for co-delivery of natural drugs into thyroid cancer cells. *Journal of Materials Chemistry B* 2015, 3 (19), 4074.

- (14) Lvov, Y. M.; DeVilliers, M. M.; Fakhrullin, R. F. The application of halloysite tubule nanoclay in drug delivery. *Expert Opinion on Drug Delivery* 2016, 13 (7), 977.
- (15) Alkatheeri, M. S.; Palasuk, J.; Eckert, G. J.; Platt, J. A.; Bottino, M. C. Halloysite nanotube incorporation into adhesive systems—effect on bond strength to human dentin. *Clinical Oral Investigations* 2015, 19 (8), 1905.
- (16) Suh, Y. J.; Kil, D. S.; Chung, K. S.; Abdullayev, E.; Lvov, Y. M.; Mongayt, D. Natural Nanocontainer for the Controlled Delivery of Glycerol as a Moisturizing Agent. *Journal of Nanoscience and Nanotechnology* 2011, 11 (1), 661.
- (17) Zhang, H. Selective modification of inner surface of halloysite nanotubes: A review. *Nanotechnology Reviews* 2017, 6 (6), 573.
- (18) Zhang, Y.; Tang, A.; Yang, H.; Ouyang, J. Applications and interfaces of halloysite nanocomposites. *Applied Clay Science* 2016, 119, 8.
- (19) Suh, Y.; Kil, D.; Chung, K.; Abdullayev, E.; Lvov, Y.; Mongayt, D. Natural nanocontainer for the controlled delivery of glycerol as a moisturizing agent. *Journal of nanoscience and nanotechnology* 2011, 11 (1), 661.
- (20) Ramadass, K.; Singh, G.; Lakhi, K. S.; Benzigar, M. R.; Yang, J.-H.; Kim, S.; Almajid, A. M.; Belperio, T.; Vinu, A. Halloysite nanotubes: Novel and eco-friendly adsorbents for high-pressure CO₂ capture. *Microporous and Mesoporous Materials* 2019, 277, 229.
- (21) Jin, J.; Zhang, Y.; Ouyang, J.; Yang, H. Halloysite nanotubes as hydrogen storage materials. *Physics and Chemistry of Minerals* 2014, 41 (5), 323.
- (22) Das, S.; Maity, A.; Pradhan, M.; Jana, S. Assessing atmospheric CO₂ entrapped in clay nanotubes using residual gas analyzer. *Analytical chemistry* 2016, 88 (4), 2205.
- (23) Palantöken, S.; Tekay, E.; Şen, S.; Nugay, T.; Nugay, N. A novel nonchemical approach to the expansion of halloysite nanotubes and their uses in chitosan composite hydrogels for broad-spectrum dye adsorption capacity. *Polymer Composites* 2016, 37 (9), 2770.
- (24) Gaikwad, K. K.; Singh, S.; Lee, Y. S. High adsorption of ethylene by alkali-treated halloysite nanotubes for food-packaging applications. *Environmental Chemistry Letters* 2018, 16 (3), 1055.
- (25) Massaro, M.; Cavallaro, G.; Colletti, C. G.; D'Azzo, G.; Guernelli, S.; Lazzara, G.; Pieraccini, S.; Riela, S. Halloysite nanotubes for efficient loading, stabilization and controlled release of insulin. *Journal of colloid and interface science* 2018, 524, 156.
- (26) Lee, Y.; Jung, G.-E.; Cho, S. J.; Geckeler, K. E.; Fuchs, H. Cellular interactions of doxorubicin-loaded DNA-modified halloysite nanotubes. *Nanoscale* 2013, 5 (18), 8577.
- (27) Shamsi, M. H.; Geckeler, K. E. The first biopolymer-wrapped non-carbon nanotubes. *Nanotechnology* 2008, 19 (7), 075604.

- (28) Maruthupandy, M.; Seo, J. Allyl isothiocyanate encapsulated halloysite covered with polyacrylate as a potential antibacterial agent against food spoilage bacteria. *Materials Science and Engineering: C* 2019, *105*, 110016.
- (29) Tas, B. A.; Sehit, E.; Tas, C. E.; Unal, S.; Cebeci, F. C.; Menceloglu, Y. Z.; Unal, H. Carvacrol loaded halloysite coatings for antimicrobial food packaging applications. *Food Packaging and Shelf Life* 2019, *20*, 100300.
- (30) Tan, D.; Yuan, P.; Annabi-Bergaya, F.; Dong, F.; Liu, D.; He, H. A comparative study of tubular halloysite and platy kaolinite as carriers for the loading and release of the herbicide amitrole. *Applied Clay Science* 2015, *114*, 190.
- (31) Seven, S. A.; Tastan, Ö. F.; Tas, C. E.; Ünal, H.; Ince, İ. A.; Menceloglu, Y. Z. Insecticide-releasing LLDPE films as greenhouse cover materials. *Materials Today Communications* 2019, *19*, 170.
- (32) Thanakkasaranee, S.; Seo, J. Effect of halloysite nanotubes on shape stabilities of polyethylene glycol-based composite phase change materials. *International Journal of Heat and Mass Transfer* 2019, *132*, 154.
- (33) Zhang, J.; Zhang, X.; Wan, Y.; Mei, D.; Zhang, B. Preparation and thermal energy properties of paraffin/halloysite nanotube composite as form-stable phase change material. *Solar energy* 2012, *86* (5), 1142.
- (34) Du, M.; Guo, B.; Jia, D. Newly emerging applications of halloysite nanotubes: a review. 2010, *59* (5), 574.
- (35) Tully, J.; Fakhru'llin, R.; Lvov, Y. In *Nanomaterials and Nanoarchitectures*; Springer, 2015.
- (36) Rawtani, D.; Agrawal, Y. Multifarious applications of halloysite nanotubes: a review. *Rev. Adv. Mater. Sci* 2012, *30* (3), 282.
- (37) Yang, Y.; Chen, Y.; Leng, F.; Huang, L.; Wang, Z.; Tian, W. Recent advances on surface modification of halloysite nanotubes for multifunctional applications. *Applied Sciences* 2017, *7* (12), 1215.
- (38) Vahedi, V.; Pasbakhsh, P. Instrumented impact properties and fracture behaviour of epoxy/modified halloysite nanocomposites. *Polymer Testing* 2014, *39*, 101.
- (39) Bediako, E. G.; Nyankson, E.; Dodoo-Arhin, D.; Agyei-Tuffour, B.; Łukowiec, D.; Tomiczek, B.; Yaya, A.; Efavi, J. K. Modified halloysite nanoclay as a vehicle for sustained drug delivery. *Heliyon* 2018, *4* (7), e00689.
- (40) Lisuzzo, L.; Cavallaro, G.; Parisi, F.; Milioto, S.; Lazzara, G. Colloidal stability of halloysite clay nanotubes. *Ceramics International* 2019, *45* (2), 2858.
- (41) Zeng, G.; Ye, Z.; He, Y.; Yang, X.; Ma, J.; Shi, H.; Feng, Z. Application of dopamine-modified halloysite nanotubes/PVDF blend membranes for direct dyes removal from wastewater. *Chemical Engineering Journal* 2017, *323*, 572.
- (42) Carrillo, A.; Carriazo, J. Cu and Co oxides supported on halloysite for the total oxidation of toluene. *Applied Catalysis B: Environmental* 2015, *164*, 443.

- (43) Chao, C.; Liu, J.; Wang, J.; Zhang, Y.; Zhang, B.; Zhang, Y.; Xiang, X.; Chen, R. Surface modification of halloysite nanotubes with dopamine for enzyme immobilization. *ACS applied materials & interfaces* 2013, 5 (21), 10559.
- (44) Cavallaro, G.; Lazzara, G.; Milioto, S.; Parisi, F. Hydrophobically modified halloysite nanotubes as reverse micelles for water-in-oil emulsion. *Langmuir* 2015, 31 (27), 7472.
- (45) Lin, Y.; Ng, K. M.; Chan, C.-M.; Sun, G.; Wu, J. High-impact polystyrene/halloysite nanocomposites prepared by emulsion polymerization using sodium dodecyl sulfate as surfactant. *Journal of colloid and interface science* 2011, 358 (2), 423.
- (46) Tang, Y.; Deng, S.; Ye, L.; Yang, C.; Yuan, Q.; Zhang, J.; Zhao, C. Effects of unfolded and intercalated halloysites on mechanical properties of halloysite–epoxy nanocomposites. *Composites Part A: Applied Science and Manufacturing* 2011, 42 (4), 345.
- (47) Wu, F.; Zheng, J.; Li, Z.; Liu, M. Halloysite nanotubes coated 3D printed PLA pattern for guiding human mesenchymal stem cells (hMSCs) orientation. *Chemical Engineering Journal* 2019, 359, 672.
- (48) Liu, C.; Luo, Y.; Jia, Z.; Zhong, B.; Li, S.; Guo, B.; Jia, D. Enhancement of mechanical properties of poly (vinyl chloride) with polymethyl methacrylate-grafted halloysite nanotube. *Express Polymer Letters* 2011, 5 (7).
- (49) Pang, Y.; Zhang, J.; Ma, R.; Qu, Z.; Lee, E.; Luo, T. Solar–thermal water evaporation: a review. *ACS Energy Letters* 2020, 5 (2), 437.
- (50) Li, Z.; Chen, Y.; Yang, Y.; Yu, Y.; Zhang, Y.; Zhu, D.; Yu, X.; Ouyang, X.; Xie, Z.; Zhao, Y. Recent advances in nanomaterials-based chemo-photothermal combination therapy for improving cancer treatment. *Frontiers in bioengineering and biotechnology* 2019, 7, 293.
- (51) Yougbaré, S.; Mutualik, C.; Krisnawati, D. I.; Kristanto, H.; Jazidie, A.; Nuh, M.; Cheng, T.-M.; Kuo, T.-R. Nanomaterials for the photothermal killing of bacteria. *Nanomaterials* 2020, 10 (6), 1123.
- (52) Liu, B.; Chen, C.; Wang, R.; Dong, S.; Li, J.; Zhang, G.; Cai, D.; Zhai, S.; Wu, Z. Near-infrared light-responsively controlled-release herbicide using biochar as a photothermal agent. *ACS Sustainable Chemistry & Engineering* 2019, 7 (17), 14924.
- (53) Yang, S.; Du, X.; Du, Z.; Zhou, M.; Cheng, X.; Wang, H.; Yan, B. Robust, stretchable and photothermal self-healing polyurethane elastomer based on furan-modified polydopamine nanoparticles. *Polymer* 2020, 190, 122219.
- (54) Hu, Z.; Shao, Q.; Huang, Y.; Yu, L.; Zhang, D.; Xu, X.; Lin, J.; Liu, H.; Guo, Z. Light triggered interfacial damage self-healing of poly (p-phenylene benzobisoxazole) fiber composites. *Nanotechnology* 2018, 29 (18), 185602.
- (55) Herath, M.; Epaarachchi, J.; Islam, M.; Fang, L.; Leng, J. Light activated shape memory polymers and composites: A review. *European Polymer Journal* 2020, 109912.

- (56) Wu, X.; Chen, G. Y.; Owens, G.; Chu, D.; Xu, H. Photothermal materials: A key platform enabling highly efficient water evaporation driven by solar energy. *Materials Today Energy* 2019, *12*, 277.
- (57) Schuller, J. A.; Barnard, E. S.; Cai, W.; Jun, Y. C.; White, J. S.; Brongersma, M. L. Plasmonics for extreme light concentration and manipulation. *Nature materials* 2010, *9* (3), 193.
- (58) Comin, A.; Manna, L. New materials for tunable plasmonic colloidal nanocrystals. *Chemical Society Reviews* 2014, *43* (11), 3957.
- (59) Kuznetsov, V.; Moseenkov, S.; Elumeeva, K.; Larina, T.; Anufrienko, V.; Romanenko, A.; Anikeeva, O.; Tkachev, E. Comparative study of reflectance properties of nanodiamonds, onion-like carbon and multiwalled carbon nanotubes. *physica status solidi (b)* 2011, *248* (11), 2572.
- (60) Tomlin, N. A.; Curtin, A.; White, M.; Lehman, J. Decrease in reflectance of vertically-aligned carbon nanotubes after oxygen plasma treatment. *Carbon* 2014, *74*, 329.
- (61) Koppens, F. H.; Chang, D. E.; Garcia de Abajo, F. J. Graphene plasmonics: a platform for strong light–matter interactions. *Nano letters* 2011, *11* (8), 3370.
- (62) Jung, H. S.; Verwilst, P.; Sharma, A.; Shin, J.; Sessler, J. L.; Kim, J. S. Organic molecule-based photochemical agents: an expanding photochemical therapy universe. *Chemical Society Reviews* 2018, *47* (7), 2280.
- (63) Jaque, D.; Maestro, L. M.; Del Rosal, B.; Haro-Gonzalez, P.; Benayas, A.; Plaza, J.; Rodriguez, E. M.; Sole, J. G. Nanoparticles for photochemical therapies. *nanoscale* 2014, *6* (16), 9494.
- (64) Xiao, L.; Chen, X.; Yang, X.; Sun, J.; Geng, J. Recent Advances in Polymer-Based Photochemical Materials for Biological Applications. *ACS Applied Polymer Materials* 2020, *2* (10), 4273.
- (65) Bhattacharai, D. P.; Kim, B. S. NIR-Triggered Hyperthermal Effect of Polythiophene Nanoparticles Synthesized by Surfactant-Free Oxidative Polymerization Method on Colorectal Carcinoma Cells. *Cells* 2020, *9* (9), 2122.
- (66) Abel, S. B.; Molina, M. A.; Rivarola, C. R.; Kogan, M. J.; Barbero, C. A. Smart polyaniline nanoparticles with thermal and photochemical sensitivity. *Nanotechnology* 2014, *25* (49), 495602.
- (67) Wang, M. Emerging multifunctional NIR photochemical therapy systems based on polypyrrole nanoparticles. *Polymers* 2016, *8* (10), 373.
- (68) Farokhi, M.; Mottaghitalab, F.; Saeb, M. R.; Thomas, S. Functionalized theranostic nanocarriers with bio-inspired polydopamine for tumor imaging and chemo-photochemical therapy. *Journal of Controlled Release* 2019, *309*, 203.
- (69) Lee, H.; Dellatore, S. M.; Miller, W. M.; Messersmith, P. B. Mussel-inspired surface chemistry for multifunctional coatings. *science* 2007, *318* (5849), 426.
- (70) Ryu, J. H.; Messersmith, P. B.; Lee, H. Polydopamine surface chemistry: a decade of discovery. *ACS applied materials & interfaces* 2018, *10* (9), 7523.

- (71) Liu, Y.; Ai, K.; Lu, L. Polydopamine and Its Derivative Materials: Synthesis and Promising Applications in Energy, Environmental, and Biomedical Fields. *Chemical Reviews* 2014, **114** (9), 5057.
- (72) Mrówczyński, R.; Markiewicz, R.; Liebscher, J. Chemistry of polydopamine analogues. *Polymer International* 2016, **65** (11), 1288.
- (73) d'Ischia, M.; Napolitano, A.; Ball, V.; Chen, C.-T.; Buehler, M. J. Polydopamine and eumelanin: From structure–property relationships to a unified tailoring strategy. *Accounts of chemical research* 2014, **47** (12), 3541.
- (74) Liebscher, J. r.; Mrówczyński, R.; Scheidt, H. A.; Filip, C.; Hădade, N. D.; Turcu, R.; Bende, A.; Beck, S. Structure of polydopamine: a never-ending story? *Langmuir* 2013, **29** (33), 10539.
- (75) Della Vecchia, N. F.; Avolio, R.; Alfè, M.; Errico, M. E.; Napolitano, A.; d'Ischia, M. Building-block diversity in polydopamine underpins a multifunctional eumelanin-type platform tunable through a quinone control point. *Advanced Functional Materials* 2013, **23** (10), 1331.
- (76) Ham, H. O.; Liu, Z.; Lau, K. A.; Lee, H.; Messersmith, P. B. Facile DNA immobilization on surfaces through a catecholamine polymer. *Angewandte Chemie* 2011, **123** (3), 758.
- (77) Lee, H.; Rho, J.; Messersmith, P. B. Facile conjugation of biomolecules onto surfaces via mussel adhesive protein inspired coatings. *Advanced Materials* 2009, **21** (4), 431.
- (78) Kang, S. M.; Rho, J.; Choi, I. S.; Messersmith, P. B.; Lee, H. Norepinephrine: material-independent, multifunctional surface modification reagent. *Journal of the American Chemical Society* 2009, **131** (37), 13224.
- (79) Shin, Y. M.; Jun, I.; Lim, Y. M.; Rhim, T.; Shin, H. Bio-inspired Immobilization of Cell-Adhesive Ligands on Electrospun Nanofibrous Patches for Cell Delivery. *Macromolecular Materials and Engineering* 2013, **298** (5), 555.
- (80) Preuss, C. M.; Goldmann, A. S.; Trouillet, V.; Walther, A.; Barner-Kowollik, C. Biomimetic Dopamine-Diels–Alder Switches. *Macromolecular rapid communications* 2013, **34** (8), 640.
- (81) Ryu, J.; Ku, S. H.; Lee, H.; Park, C. B. Mussel-inspired polydopamine coating as a universal route to hydroxyapatite crystallization. *Advanced Functional Materials* 2010, **20** (13), 2132.
- (82) Long, Y.; Wu, J.; Wang, H.; Zhang, X.; Zhao, N.; Xu, J. Rapid sintering of silver nanoparticles in an electrolyte solution at room temperature and its application to fabricate conductive silver films using polydopamine as adhesive layers. *Journal of Materials Chemistry* 2011, **21** (13), 4875.
- (83) Mi, Y.; Wang, Z.; Liu, X.; Yang, S.; Wang, H.; Ou, J.; Li, Z.; Wang, J. A simple and feasible in-situ reduction route for preparation of graphene lubricant films applied to a variety of substrates. *Journal of Materials Chemistry* 2012, **22** (16), 8036.

- (84) Wu, J.; Zhang, L.; Wang, Y.; Long, Y.; Gao, H.; Zhang, X.; Zhao, N.; Cai, Y.; Xu, J. Mussel-inspired chemistry for robust and surface-modifiable multilayer films. *Langmuir* 2011, 27 (22), 13684.
- (85) Satarkar, N. S.; Biswal, D.; Hilt, J. Z. Hydrogel nanocomposites: a review of applications as remote controlled biomaterials. *Soft Matter* 2010, 6 (11), 2364.
- (86) McCloskey, B. D.; Park, H. B.; Ju, H.; Rowe, B. W.; Miller, D. J.; Chun, B. J.; Kin, K.; Freeman, B. D. Influence of polydopamine deposition conditions on pure water flux and foulant adhesion resistance of reverse osmosis, ultrafiltration, and microfiltration membranes. *Polymer* 2010, 51 (15), 3472.
- (87) Zhang, X.; Wang, S.; Xu, L.; Feng, L.; Ji, Y.; Tao, L.; Li, S.; Wei, Y. Biocompatible polydopamine fluorescent organic nanoparticles: facile preparation and cell imaging. *Nanoscale* 2012, 4 (18), 5581.
- (88) Chien, H.-W.; Kuo, W.-H.; Wang, M.-J.; Tsai, S.-W.; Tsai, W.-B. Tunable micropatterned substrates based on poly (dopamine) deposition via microcontact printing. *Langmuir* 2012, 28 (13), 5775.
- (89) Sun, K.; Xie, Y.; Ye, D.; Zhao, Y.; Cui, Y.; Long, F.; Zhang, W.; Jiang, X. Mussel-inspired anchoring for patterning cells using polydopamine. *Langmuir* 2012, 28 (4), 2131.
- (90) Hong, S.; Kim, K. Y.; Wook, H. J.; Park, S. Y.; Lee, K. D.; Lee, D. Y.; Lee, H. Attenuation of the in vivo toxicity of biomaterials by polydopamine surface modification. *Nanomedicine* 2011, 6 (5), 793.
- (91) Sileika, T. S.; Kim, H.-D.; Maniak, P.; Messersmith, P. B. Antibacterial performance of polydopamine-modified polymer surfaces containing passive and active components. *ACS applied materials & interfaces* 2011, 3 (12), 4602.
- (92) Zhou, Y.-Z.; Cao, Y.; Liu, W.; Chu, C. H.; Li, Q.-L. Polydopamine-Induced Tooth Remineralization. *ACS Applied Materials & Interfaces* 2012, 4 (12), 6901.
- (93) Wu, C.; Fan, W.; Chang, J.; Xiao, Y. Mussel-inspired porous SiO₂ scaffolds with improved mineralization and cytocompatibility for drug delivery and bone tissue engineering. *Journal of Materials Chemistry* 2011, 21 (45), 18300.
- (94) Ku, S. H.; Park, C. B. Human endothelial cell growth on mussel-inspired nanofiber scaffold for vascular tissue engineering. *Biomaterials* 2010, 31 (36), 9431.
- (95) Black, K. C.; Yi, J.; Rivera, J. G.; Zelasko-Leon, D. C.; Messersmith, P. B. Polydopamine-enabled surface functionalization of gold nanorods for cancer cell-targeted imaging and photothermal therapy. *Nanomedicine* 2013, 8 (1), 17.
- (96) Liu, Y.; Ai, K.; Liu, J.; Deng, M.; He, Y.; Lu, L. Dopamine-Melanin Colloidal Nanospheres: An Efficient Near-Infrared Photothermal Therapeutic Agent for In Vivo Cancer Therapy. *Advanced Materials* 2013, 25 (9), 1353.
- (97) Yu, B.; Wang, D. A.; Ye, Q.; Zhou, F.; Liu, W. Robust polydopamine nano/microcapsules and their loading and release behavior. *Chemical Communications* 2009, DOI:10.1039/B910679K 10.1039/B910679K(44), 6789.

- (98) Farnad, N.; Farhadi, K.; Voelcker, N. H. Polydopamine nanoparticles as a new and highly selective biosorbent for the removal of copper (II) ions from aqueous solutions. *Water, Air, & Soil Pollution* 2012, 223 (6), 3535.
- (99) Iqbal, Z.; Alsudir, S.; Miah, M.; Lai, E. P. Rapid CE-UV binding tests of environmentally hazardous compounds with polymer-modified magnetic nanoparticles. *Electrophoresis* 2011, 32 (16), 2181.
- (100) Huang, S.; Yang, L.; Liu, M.; Phua, S. L.; Yee, W. A.; Liu, W.; Zhou, R.; Lu, X. Complexes of Polydopamine-Modified Clay and Ferric Ions as the Framework for Pollutant-Absorbing Supramolecular Hydrogels. *Langmuir* 2013, 29 (4), 1238.
- (101) Zhang, L.; Wu, J.; Wang, Y.; Long, Y.; Zhao, N.; Xu, J. Combination of Bioinspiration: A General Route to Superhydrophobic Particles. *Journal of the American Chemical Society* 2012, 134 (24), 9879.
- (102) Han, G.; Zhang, S.; Li, X.; Widjojo, N.; Chung, T.-S. Thin film composite forward osmosis membranes based on polydopamine modified polysulfone substrates with enhancements in both water flux and salt rejection. *Chemical Engineering Science* 2012, 80, 219.
- (103) Wang, A.-J.; Liao, Q.-C.; Feng, J.-J.; Yan, Z.-Z.; Chen, J.-R. In situ synthesis of polydopamine–Ag hollow microspheres for hydrogen peroxide sensing. *Electrochimica Acta* 2012, 61, 31.
- (104) Ruan, C.; Shi, W.; Jiang, H.; Sun, Y.; Liu, X.; Zhang, X.; Sun, Z.; Dai, L.; Ge, D. One-pot preparation of glucose biosensor based on polydopamine–graphene composite film modified enzyme electrode. *Sensors and Actuators B: Chemical* 2013, 177, 826.
- (105) Wang, G.; Huang, H.; Zhang, X.; Wang, L. Electrically contacted enzyme based on dual hairpin DNA structure and its application for amplified detection of Hg²⁺. *Biosensors and Bioelectronics* 2012, 35 (1), 108.
- (106) Kang, S. M.; Ryou, M.-H.; Choi, J. W.; Lee, H. Mussel- and Diatom-Inspired Silica Coating on Separators Yields Improved Power and Safety in Li-Ion Batteries. *Chemistry of Materials* 2012, 24 (17), 3481.
- (107) Nam, H. J.; Kim, B.; Ko, M. J.; Jin, M.; Kim, J. M.; Jung, D.-Y. A New Mussel-Inspired Polydopamine Sensitizer for Dye-Sensitized Solar Cells: Controlled Synthesis and Charge Transfer. *Chemistry – A European Journal* 2012, 18 (44), 14000.
- (108) Jiang, H.; Yang, L.; Li, C.; Yan, C.; Lee, P. S.; Ma, J. High-rate electrochemical capacitors from highly graphitic carbon-tipped manganese oxide/mesoporous carbon/manganese oxide hybrid nanowires. *Energy & Environmental Science* 2011, 4 (5), 1813.
- (109) Yu, Y. M.; Zhang, J. H.; Xiao, C. H.; Zhong, J. D.; Zhang, X. H.; Chen, J. H. High Active Hollow Nitrogen-Doped Carbon Microspheres for Oxygen Reduction in Alkaline Media. *Fuel Cells* 2012, 12 (3), 506.

- (110) Ko, J. W.; Kim, J. H.; Park, C. B. Synthesis of visible light-active CeO₂ sheets via mussel-inspired CaCO₃ mineralization. *Journal of Materials Chemistry A* 2013, 1 (2), 241.
- (111) Zeng, T.; Zhang, X.-l.; Niu, H.-y.; Ma, Y.-r.; Li, W.-h.; Cai, Y.-q. In situ growth of gold nanoparticles onto polydopamine-encapsulated magnetic microspheres for catalytic reduction of nitrobenzene. *Applied Catalysis B: Environmental* 2013, 134-135, 26.
- (112) Xu, Y.; Wang, J.; Yu, F.; Guo, Z.; Cheng, H.; Yin, J.; Yan, L.; Wang, X. Flexible and efficient solar thermal generators based on polypyrrole coated natural latex foam for multi-media purification. *ACS Sustainable Chemistry & Engineering* 2020.
- (113) Ni, F.; Xiao, P.; Qiu, N.; Zhang, C.; Liang, Y.; Gu, J.; Xia, J.; Zeng, Z.; Wang, L.; Xue, Q. et al. Collective behaviors mediated multifunctional black sand aggregate towards environmentally adaptive solar-to-thermal purified water harvesting. *Nano Energy* 2020, 68, 104311.
- (114) Wu, X.; Jiang, Q.; Ghim, D.; Singamaneni, S.; Jun, Y.-S. Localized heating with a photothermal polydopamine coating facilitates a novel membrane distillation process. *Journal of Materials Chemistry A* 2018, 6 (39), 18799.
- (115) Cao, S.; Wu, X.; Zhu, Y.; Gupta, R.; Tan, A.; Wang, Z.; Jun, Y.-S.; Singamaneni, S. Polydopamine/hydroxyapatite nanowire-based bilayered membrane for photothermal-driven membrane distillation. *Journal of Materials Chemistry A* 2020, 8 (10), 5147.
- (116) Zhao, X.; Zha, X.-J.; Tang, L.-S.; Pu, J.-H.; Ke, K.; Bao, R.-Y.; Liu, Z.-y.; Yang, M.-B.; Yang, W. Self-assembled core-shell polydopamine@ MXene with synergistic solar absorption capability for highly efficient solar-to-vapor generation. *Nano Research* 2020, 13 (1), 255.
- (117) Ma, S.; Chiu, C. P.; Zhu, Y.; Tang, C. Y.; Long, H.; Qarony, W.; Zhao, X.; Zhang, X.; Lo, W. H.; Tsang, Y. H. Recycled waste black polyurethane sponges for solar vapor generation and distillation. *Applied energy* 2017, 206, 63.
- (118) Shao, L.; Zhang, R.; Lu, J.; Zhao, C.; Deng, X.; Wu, Y. Mesoporous Silica Coated Polydopamine Functionalized Reduced Graphene Oxide for Synergistic Targeted Chemo-Photothermal Therapy. *ACS Applied Materials & Interfaces* 2017, 9 (2), 1226.
- (119) Ge, J.; Wang, Y.; Wang, H.; Mao, H.; Li, J.; Shi, H. Thermal properties and shape stabilization of epoxidized methoxy polyethylene glycol composite PCMs tailored by polydopamine-functionalized graphene oxide. *Solar Energy Materials and Solar Cells* 2020, 208, 110388.
- (120) Yang, J.; Qi, G.-Q.; Tang, L.-S.; Bao, R.-Y.; Bai, L.; Liu, Z.-Y.; Yang, W.; Xie, B.-H.; Yang, M.-B. Novel photodriven composite phase change materials with bioinspired modification of BN for solar-thermal energy conversion and storage. *Journal of Materials Chemistry A* 2016, 4 (24), 9625.

- (121) Qu, K.; Wang, Y.; Vasileff, A.; Jiao, Y.; Chen, H.; Zheng, Y. Polydopamine-inspired nanomaterials for energy conversion and storage. *Journal of Materials Chemistry A* 2018, 6 (44), 21827.
- (122) Han, L.; Yan, L.; Wang, K.; Fang, L.; Zhang, H.; Tang, Y.; Ding, Y.; Weng, L.-T.; Xu, J.; Weng, J. Tough, self-healable and tissue-adhesive hydrogel with tunable multifunctionality. *NPG Asia Materials* 2017, 9 (4), e372.
- (123) Wu, H.-y.; Chen, R.-t.; Shao, Y.-w.; Qi, X.-d.; Yang, J.-h.; Wang, Y. Novel flexible phase change materials with mussel-inspired modification of melamine foam for simultaneous light-actuated shape memory and light-to-thermal energy storage capability. *ACS Sustainable Chemistry & Engineering* 2019, 7 (15), 13532.
- (124) Sharma, A.; Tyagi, V. V.; Chen, C.; Buddhi, D. Review on thermal energy storage with phase change materials and applications. *Renewable and Sustainable energy reviews* 2009, 13 (2), 318.
- (125) Nazir, H.; Batool, M.; Osorio, F. J. B.; Isaza-Ruiz, M.; Xu, X.; Vignarooban, K.; Phelan, P.; Kannan, A. M. Recent developments in phase change materials for energy storage applications: a review. *International Journal of Heat and Mass Transfer* 2019, 129, 491.
- (126) Kahwaji, S.; Johnson, M. B.; Kheirabadi, A. C.; Groulx, D.; White, M. A. A comprehensive study of properties of paraffin phase change materials for solar thermal energy storage and thermal management applications. *Energy* 2018, 162, 1169.
- (127) Wu, Y.; Zhang, X.; Xu, X.; Lin, X.; Liu, L. A review on the effect of external fields on solidification, melting and heat transfer enhancement of phase change materials. *Journal of Energy Storage* 2020, 31, 101567.
- (128) Song, Y.; Zhang, N.; Yuan, Y.; Yang, L.; Cao, X. Prediction of the solid effective thermal conductivity of fatty acid/carbon material composite phase change materials based on fractal theory. *Energy* 2019, 170, 752.
- (129) Graham, M.; Shchukina, E.; De Castro, P. F.; Shchukin, D. Nanocapsules containing salt hydrate phase change materials for thermal energy storage. *Journal of Materials Chemistry A* 2016, 4 (43), 16906.
- (130) Kalaiselvam, S. Bifunctional nanoencapsulated eutectic phase change material core with SiO₂/SnO₂ nanosphere shell for thermal and electrical energy storage. *Materials & Design* 2018, 154, 291.
- (131) Sundararajan, S.; Samui, A. B.; Kulkarni, P. S. Versatility of polyethylene glycol (PEG) in designing solid–solid phase change materials (PCMs) for thermal management and their application to innovative technologies. *Journal of Materials Chemistry A* 2017, 5 (35), 18379.
- (132) Kou, Y.; Wang, S.; Luo, J.; Sun, K.; Zhang, J.; Tan, Z.; Shi, Q. Thermal analysis and heat capacity study of polyethylene glycol (PEG) phase change materials for thermal energy storage applications. *The Journal of Chemical Thermodynamics* 2019, 128, 259.

- (133) Hawlader, M.; Uddin, M.; Khin, M. M. Microencapsulated PCM thermal-energy storage system. *Applied energy* 2003, *74* (1-2), 195.
- (134) Chen, Z.; Wang, J.; Yu, F.; Zhang, Z.; Gao, X. Preparation and properties of graphene oxide-modified poly (melamine-formaldehyde) microcapsules containing phase change material n-dodecanol for thermal energy storage. *Journal of Materials Chemistry A* 2015, *3* (21), 11624.
- (135) Kaygusuz, K.; Alkan, C.; Sari, A.; Uzun, O. Encapsulated fatty acids in an acrylic resin as shape-stabilized phase change materials for latent heat thermal energy storage. *Energy Sources, Part A* 2008, *30* (11), 1050.
- (136) Su, J.; Wang, L.; Ren, L. Fabrication and thermal properties of microPCMs: used melamine-formaldehyde resin as shell material. *Journal of applied polymer science* 2006, *101* (3), 1522.
- (137) Yoo, Y.; Martinez, C.; Youngblood, J. P. Synthesis and characterization of microencapsulated phase change materials with poly (urea– urethane) shells containing cellulose nanocrystals. *ACS applied materials & interfaces* 2017, *9* (37), 31763.
- (138) Park, S.; Lee, Y.; Kim, Y. S.; Lee, H. M.; Kim, J. H.; Cheong, I. W.; Koh, W.-G. Magnetic nanoparticle-embedded PCM nanocapsules based on paraffin core and polyurea shell. *Colloids and Surfaces A: Physicochemical and Engineering Aspects* 2014, *450*, 46.
- (139) Latibari, S. T.; Mehrali, M.; Mehrali, M.; Mahlia, T. M. I.; Metselaar, H. S. C. Synthesis, characterization and thermal properties of nanoencapsulated phase change materials via sol–gel method. *Energy* 2013, *61*, 664.
- (140) Cao, L.; Tang, F.; Fang, G. Preparation and characteristics of microencapsulated palmitic acid with TiO₂ shell as shape-stabilized thermal energy storage materials. *Solar energy materials and solar cells* 2014, *123*, 183.
- (141) Yu, S.; Wang, X.; Wu, D. Microencapsulation of n-octadecane phase change material with calcium carbonate shell for enhancement of thermal conductivity and serving durability: synthesis, microstructure, and performance evaluation. *Applied energy* 2014, *114*, 632.
- (142) Li, F.; Wang, X.; Wu, D. Fabrication of multifunctional microcapsules containing n-eicosane core and zinc oxide shell for low-temperature energy storage, photocatalysis, and antibiosis. *Energy Conversion and Management* 2015, *106*, 873.
- (143) Song, Q.; Li, Y.; Xing, J.; Hu, J.; Marcus, Y. Thermal stability of composite phase change material microcapsules incorporated with silver nano-particles. *Polymer* 2007, *48* (11), 3317.
- (144) Jiang, F.; Wang, X.; Wu, D. Design and synthesis of magnetic microcapsules based on n-eicosane core and Fe₃O₄/SiO₂ hybrid shell for dual-functional phase change materials. *Applied energy* 2014, *134*, 456.

- (145) Yang, Y.; Ye, X.; Luo, J.; Song, G.; Liu, Y.; Tang, G. Polymethyl methacrylate based phase change microencapsulation for solar energy storage with silicon nitride. *Solar Energy* 2015, **115**, 289.
- (146) Sari, A.; Alkan, C.; Kolemen, U.; Uzun, O. Eudragit S (methyl methacrylate methacrylic acid copolymer)/fatty acid blends as form-stable phase change material for latent heat thermal energy storage. *Journal of applied polymer science* 2006, **101** (3), 1402.
- (147) Sarı, A.; Alkan, C.; Karaipekli, A.; Uzun, O. Poly (ethylene glycol)/poly (methyl methacrylate) blends as novel form-stable phase-change materials for thermal energy storage. *Journal of applied polymer science* 2010, **116** (2), 929.
- (148) Wang, L.; Meng, D. Fatty acid eutectic/polymethyl methacrylate composite as form-stable phase change material for thermal energy storage. *Applied Energy* 2010, **87** (8), 2660.
- (149) Kaygusuz, K.; Sarı, A. High density polyethylene/paraffin composites as form-stable phase change material for thermal energy storage. *Energy Sources, Part A* 2007, **29** (3), 261.
- (150) Wang, Y.; Wang, S.; Wang, J.; Yang, R. Preparation, stability and mechanical property of shape-stabilized phase change materials. *Energy and buildings* 2014, **77**, 11.
- (151) Alkan, C.; Kaya, K.; Sarı, A. Preparation, thermal properties and thermal reliability of form-stable paraffin/polypropylene composite for thermal energy storage. *Journal of Polymers and the Environment* 2009, **17** (4), 254.
- (152) Song, S.; Feng, J.; Wu, P. A New Strategy to Prepare Polymer-based Shape Memory Elastomers. *Macromolecular rapid communications* 2011, **32** (19), 1569.
- (153) Peng, S.; Fuchs, A.; Wirtz, R. Polymeric phase change composites for thermal energy storage. *Journal of applied polymer science* 2004, **93** (3), 1240.
- (154) Xiao, M.; Feng, B.; Gong, K. Thermal performance of a high conductive shape-stabilized thermal storage material. *Solar Energy Materials and Solar Cells* 2001, **69** (3), 293.
- (155) Liang, X.-H.; Guo, Y.-Q.; Gu, L.-Z.; Ding, E.-Y. Crystalline-amorphous phase transition of poly (ethylene glycol)/cellulose blend. *Macromolecules* 1995, **28** (19), 6551.
- (156) Ding, E.-Y.; Jiang, Y.; Li, G.-K. Comparative studies of the structures and transition characteristics of cellulose diacetate modified with polyethylene glycol prepared by chemical bonding and physical blending methods. *Journal of Macromolecular Science, Part B* 2001, **40** (6), 1053.
- (157) Şentürk, S. B.; Kahraman, D.; Alkan, C.; Gökçe, İ. Biodegradable PEG/cellulose, PEG/agarose and PEG/chitosan blends as shape stabilized phase change materials for latent heat energy storage. *Carbohydrate Polymers* 2011, **84** (1), 141.

- (158) Chen, K.; Yu, X.; Tian, C.; Wang, J. Preparation and characterization of form-stable paraffin/polyurethane composites as phase change materials for thermal energy storage. *Energy conversion and management* 2014, 77, 13.
- (159) Wang, Y.; Tang, B.; Zhang, S. Light–thermal conversion organic shape-stabilized phase-change materials with broadband harvesting for visible light of solar radiation. *RSC advances* 2012, 2 (30), 11372.
- (160) Wang, Y.; Tang, B.; Zhang, S. Single-walled carbon nanotube/phase change material composites: sunlight-driven, reversible, form-stable phase transitions for solar thermal energy storage. *Advanced Functional Materials* 2013, 23 (35), 4354.
- (161) Balandin, A. A.; Ghosh, S.; Bao, W.; Calizo, I.; Teweldebrhan, D.; Miao, F.; Lau, C. N. Superior Thermal Conductivity of Single-Layer Graphene. *Nano Letters* 2008, 8 (3), 902.
- (162) Zhang, Y.; Zheng, X.; Wang, H.; Du, Q. Encapsulated phase change materials stabilized by modified graphene oxide. *Journal of Materials Chemistry A* 2014, 2 (15), 5304.
- (163) Xiong, W.; Chen, Y.; Hao, M.; Zhang, L.; Mei, T.; Wang, J.; Li, J.; Wang, X. Facile synthesis of PEG based shape-stabilized phase change materials and their photo-thermal energy conversion. *Applied Thermal Engineering* 2015, 91, 630.
- (164) Liu, L.; Kong, L.; Wang, H.; Niu, R.; Shi, H. Effect of graphene oxide nanoplatelets on the thermal characteristics and shape-stabilized performance of poly(styrene-co-maleic anhydride)-g-octadecanol comb-like polymeric phase change materials. *Solar Energy Materials and Solar Cells* 2016, 149, 40.
- (165) Yang, J.; Tang, L.-S.; Bao, R.-Y.; Bai, L.; Liu, Z.-Y.; Xie, B.-H.; Yang, M.-B.; Yang, W. Hybrid network structure of boron nitride and graphene oxide in shape-stabilized composite phase change materials with enhanced thermal conductivity and light-to-electric energy conversion capability. *Solar Energy Materials and Solar Cells* 2018, 174, 56.
- (166) Yang, J.; Tang, L.-S.; Bao, R.-Y.; Bai, L.; Liu, Z.-Y.; Yang, W.; Xie, B.-H.; Yang, M.-B. An ice-templated assembly strategy to construct graphene oxide/boron nitride hybrid porous scaffolds in phase change materials with enhanced thermal conductivity and shape stability for light–thermal–electric energy conversion. *Journal of Materials Chemistry A* 2016, 4 (48), 18841.
- (167) Han, W.; Ge, C.; Zhang, R.; Ma, Z.; Wang, L.; Zhang, X. Boron nitride foam as a polymer alternative in packaging phase change materials: Synthesis, thermal properties and shape stability. *Applied Energy* 2019, 238, 942.
- (168) Zhu, X.; Han, L.; Lu, Y.; Wei, F.; Jia, X. Geometry-induced thermal storage enhancement of shape-stabilized phase change materials based on oriented carbon nanotubes. *Applied Energy* 2019, 254, 113688.
- (169) Cao, R.; Chen, S.; Wang, Y.; Han, N.; Liu, H.; Zhang, X. Functionalized carbon nanotubes as phase change materials with enhanced thermal, electrical conductivity, light-to-thermal, and electro-to-thermal performances. *Carbon* 2019, 149, 263.

- (170) Putra, N.; Rawi, S.; Amin, M.; Kusrini, E.; Kosasih, E. A.; Indra Mahlia, T. M. Preparation of beeswax/multi-walled carbon nanotubes as novel shape-stable nanocomposite phase-change material for thermal energy storage. *Journal of Energy Storage* 2019, 21, 32.
- (171) Li, Y.; Samad, Y. A.; Polychronopoulou, K.; Alhassan, S. M.; Liao, K. From biomass to high performance solar–thermal and electric–thermal energy conversion and storage materials. *Journal of Materials Chemistry A* 2014, 2 (21), 7759.
- (172) Wei, Y.; Li, J.; Sun, F.; Wu, J.; Zhao, L. Leakage-proof phase change composites supported by biomass carbon aerogels from succulents. *Green Chemistry* 2018, 20 (8), 1858.
- (173) Wang, J.; Jia, X.; Atinifu, D. G.; Wang, M.; Wang, G.; Lu, Y. Synthesis of “graphene-like” mesoporous carbons for shape-stabilized phase change materials with high loading capacity and improved latent heat. *Journal of Materials Chemistry A* 2017, 5 (46), 24321.
- (174) Lin, Y.; Zhu, C.; Alva, G.; Fang, G. Palmitic acid/polyvinyl butyral/expanded graphite composites as form-stable phase change materials for solar thermal energy storage. *Applied Energy* 2018, 228, 1801.
- (175) Al-Shannaq, R.; Farid, M. M. A novel graphite-PCM composite sphere with enhanced thermo-physical properties. *Applied Thermal Engineering* 2018, 142, 401.
- (176) Kim, D.; Jung, J.; Kim, Y.; Lee, M.; Seo, J.; Khan, S. B. Structure and thermal properties of octadecane/expanded graphite composites as shape-stabilized phase change materials. *International Journal of Heat and Mass Transfer* 2016, 95, 735.
- (177) Liang, S.; Zhu, Y.; Wang, H.; Wu, T.; Tian, C.; Wang, J.; Bai, R. Preparation and Characterization of Thermoregulated Rigid Polyurethane Foams Containing Nanoencapsulated Phase Change Materials. *Industrial & Engineering Chemistry Research* 2016, 55 (10), 2721.
- (178) Qu, L.; Li, A.; Gu, J.; Zhang, C. Thermal Energy Storage Capability of Polyurethane Foams Incorporated with Microencapsulated Phase Change Material. *ChemistrySelect* 2018, 3 (11), 3180.
- (179) Aydin, A. A.; Okutan, H. Polyurethane rigid foam composites incorporated with fatty acid ester-based phase change material. *Energy Conversion and Management* 2013, 68, 74.
- (180) Tang, B.; Wei, H.; Zhao, D.; Zhang, S. Light-heat conversion and thermal conductivity enhancement of PEG/SiO₂ composite PCM by in situ Ti₄O₇ doping. *Solar Energy Materials and Solar Cells* 2017, 161, 183.
- (181) Tang, B.; Wu, C.; Qiu, M.; Zhang, X.; Zhang, S. PEG/SiO₂–Al₂O₃ hybrid form-stable phase change materials with enhanced thermal conductivity. *Materials Chemistry and Physics* 2014, 144 (1), 162.
- (182) Tang, B.; Cui, J.; Wang, Y.; Jia, C.; Zhang, S. Facile synthesis and performances of PEG/SiO₂ composite form-stable phase change materials. *Solar Energy* 2013, 97, 484.

- (183) Wen, R.; Zhang, X.; Huang, Z.; Fang, M.; Liu, Y.; Wu, X.; Min, X.; Gao, W.; Huang, S. Preparation and thermal properties of fatty acid/diatomite form-stable composite phase change material for thermal energy storage. *Solar Energy Materials and Solar Cells* 2018, *178*, 273.
- (184) Konuklu, Y.; Ersoy, O. Preparation and characterization of sepiolite-based phase change material nanocomposites for thermal energy storage. *Applied Thermal Engineering* 2016, *107*, 575.
- (185) Sarı, A. Thermal energy storage characteristics of bentonite-based composite PCMs with enhanced thermal conductivity as novel thermal storage building materials. *Energy Conversion and Management* 2016, *117*, 132.
- (186) Karaipekli, A.; Biçer, A.; Sarı, A.; Tyagi, V. V. Thermal characteristics of expanded perlite/paraffin composite phase change material with enhanced thermal conductivity using carbon nanotubes. *Energy conversion and management* 2017, *134*, 373.
- (187) Wu, X.; Fan, M.; Cui, S.; Tan, G.; Shen, X. Novel Na₂SO₄@ SiO₂ phase change material with core-shell structures for high temperature thermal storage. *Solar Energy Materials and Solar Cells* 2018, *178*, 280.
- (188) Wang, Y.; Qin, Z.; Zhang, T.; Zhang, D. Preparation and thermophysical properties of three-dimensional attapulgite based composite phase change materials. *Journal of Energy Storage* 2020, *32*, 101847.
- (189) Zhang, X.; Yin, Z.; Meng, D.; Huang, Z.; Wen, R.; Huang, Y.; Min, X.; Liu, Y.; Fang, M.; Wu, X. Shape-stabilized composite phase change materials with high thermal conductivity based on stearic acid and modified expanded vermiculite. *Renewable Energy* 2017, *112*, 113.
- (190) Pilehvar, S.; Cao, V. D.; Szczotok, A. M.; Carmona, M.; Valentini, L.; Lanzón, M.; Pamies, R.; Kjønksen, A.-L. Physical and mechanical properties of fly ash and slag geopolymers concrete containing different types of micro-encapsulated phase change materials. *Construction and Building Materials* 2018, *173*, 28.
- (191) Tas, C. E.; Karaoglu, O.; Tas, B. A.; Ertas, E.; Unal, H.; Bildirir, H. Improved latent heat storage properties through mesopore enrichment of a zeolitic shape stabilizer. *Solar Energy Materials and Solar Cells* 2020, *216*, 110677.
- (192) Umair, M. M.; Zhang, Y.; Iqbal, K.; Zhang, S.; Tang, B. Novel strategies and supporting materials applied to shape-stabilize organic phase change materials for thermal energy storage—A review. *Applied Energy* 2019, *235*, 846.
- (193) Brody, A. L.; Strupinsky, E.; Kline, L. R. *Active packaging for food applications*; CRC press, 2001.
- (194) Ozdemir, M.; Floros, J. D. Active food packaging technologies. *Critical reviews in food science and nutrition* 2004, *44* (3), 185.
- (195) Abeles, F. B.; Morgan, P. W.; Saltveit Jr, M. E. *Ethylene in plant biology*; Academic press, 2012.
- (196) Rooney, M. In *Active food packaging*; Springer, 1995.

- (197) Srithammaraj, K.; Magaraphan, R.; Manuspiya, H. Modified porous clay heterostructures by organic–inorganic hybrids for nanocomposite ethylene scavenging/sensor packaging film. *Packaging Technology and Science* 2012, 25 (2), 63.
- (198) Alexandre, M.; Dubois, P. Polymer-layered silicate nanocomposites: preparation, properties and uses of a new class of materials. *Materials science and engineering: R: Reports* 2000, 28 (1-2), 1.
- (199) Choudalakis, G.; Gotsis, A. Permeability of polymer/clay nanocomposites: a review. *European polymer journal* 2009, 45 (4), 967.
- (200) Alexandre, B.; Langevin, D.; Médéric, P.; Aubry, T.; Couderc, H.; Nguyen, Q.; Saiter, A.; Marais, S. Water barrier properties of polyamide 12/montmorillonite nanocomposite membranes: structure and volume fraction effects. *Journal of Membrane Science* 2009, 328 (1-2), 186.
- (201) Gorrasi, G.; Tortora, M.; Vittoria, V.; Pollet, E.; Lepoittevin, B.; Alexandre, M.; Dubois, P. Vapor barrier properties of polycaprolactone montmorillonite nanocomposites: effect of clay dispersion. *Polymer* 2003, 44 (8), 2271.
- (202) Morawiec, J.; Pawlak, A.; Slouf, M.; Galeski, A.; Piorkowska, E.; Krasnikowa, N. Preparation and properties of compatibilized LDPE/organo-modified montmorillonite nanocomposites. *European Polymer Journal* 2005, 41 (5), 1115.
- (203) Picard, E.; Vermogen, A.; Gérard, J.-F.; Espuche, E. Barrier properties of nylon 6-montmorillonite nanocomposite membranes prepared by melt blending: influence of the clay content and dispersion state: consequences on modelling. *Journal of Membrane Science* 2007, 292 (1-2), 133.
- (204) Joshi, A.; Abdullayev, E.; Vasiliev, A.; Volkova, O.; Lvov, Y. Interfacial modification of clay nanotubes for the sustained release of corrosion inhibitors. *Langmuir* 2013, 29 (24), 7439.
- (205) Owoseni, O.; Nyankson, E.; Zhang, Y.; Adams, S. J.; He, J.; McPherson, G. L.; Bose, A.; Gupta, R. B.; John, V. T. Release of surfactant cargo from interfacially-active halloysite clay nanotubes for oil spill remediation. *Langmuir* 2014, 30 (45), 13533.
- (206) Vergaro, V.; Lvov, Y. M.; Leporatti, S. Halloysite clay nanotubes for resveratrol delivery to cancer cells. *Macromolecular bioscience* 2012, 12 (9), 1265.
- (207) Forsgren, J.; Jämstorp, E.; Bredenberg, S.; Engqvist, H.; Strømme, M. A ceramic drug delivery vehicle for oral administration of highly potent opioids. *Journal of pharmaceutical sciences* 2010, 99 (1), 219.
- (208) Shemesh, R.; Krepker, M.; Natan, M.; Danin-Poleg, Y.; Banin, E.; Kashi, Y.; Nitzan, N.; Vaxman, A.; Segal, E. Novel LDPE/halloysite nanotube films with sustained carvacrol release for broad-spectrum antimicrobial activity. *RSC advances* 2015, 5 (106), 87108.
- (209) Ward, C. J.; Song, S.; Davis, E. W. Controlled release of tetracycline–HCl from halloysite–polymer composite films. *Journal of nanoscience and nanotechnology* 2010, 10 (10), 6641.

- (210) Wunderlich, B.; Czornyj, G. A study of equilibrium melting of polyethylene. *Macromolecules* 1977, **10** (5), 906.
- (211) Ahmadi, S. J.; Huang, Y.; Li, W. Fabrication and physical properties of EPDM–organoclay nanocomposites. *Composites science and technology* 2005, **65** (7-8), 1069.
- (212) Cui, L.; Cho, H. Y.; Shin, J. W.; Tarte, N. H.; Woo, S. I. Macromolecular symposia, 2007; p 49.
- (213) Visakh, P.; Morlanes, M. J. M. *Polyethylene-based blends, composites and nanocomposites*; John Wiley & Sons, 2015.
- (214) Du, M.; Guo, B.; Jia, D. Thermal stability and flame retardant effects of halloysite nanotubes on poly (propylene). *European Polymer Journal* 2006, **42** (6), 1362.
- (215) Lecouvet, B.; Sclavons, M.; Bourbigot, S.; Devaux, J.; Bailly, C. Water-assisted extrusion as a novel processing route to prepare polypropylene/halloysite nanotube nanocomposites: structure and properties. *Polymer* 2011, **52** (19), 4284.
- (216) Marcilla, A.; Gómez, A.; Menargues, S.; Ruiz, R. Pyrolysis of polymers in the presence of a commercial clay. *Polymer degradation and stability* 2005, **88** (3), 456.
- (217) Du, M.; Guo, B.; Liu, M.; Jia, D. Preparation and characterization of polypropylene grafted halloysite and their compatibility effect to polypropylene/halloysite composite. *Polymer journal* 2006, **38** (11), 1198.
- (218) Liu, M.; Guo, B.; Du, M.; Chen, F.; Jia, D. Halloysite nanotubes as a novel β -nucleating agent for isotactic polypropylene. *Polymer* 2009, **50** (13), 3022.
- (219) Pedrazzoli, D.; Pegoretti, A.; Thomann, R.; Kristof, J.; Karger-Kocsis, J. Toughening linear low-density polyethylene with halloysite nanotubes. *Polymer Composites* 2015, **36** (5), 869.
- (220) Zhao, S.; Cai, Z.; Xin, Z. A highly active novel β -nucleating agent for isotactic polypropylene. *Polymer* 2008, **49** (11), 2745.
- (221) Handge, U. A.; Hedicke-Höchstötter, K.; Altstädt, V. Composites of polyamide 6 and silicate nanotubes of the mineral halloysite: influence of molecular weight on thermal, mechanical and rheological properties. *Polymer* 2010, **51** (12), 2690.
- (222) Jia, Z.; Luo, Y.; Guo, B.; Yang, B.; Du, M.; Jia, D. Reinforcing and flame-retardant effects of halloysite nanotubes on LLDPE. *Polymer-Plastics Technology and Engineering* 2009, **48** (6), 607.
- (223) Prashantha, K.; Lacrampe, M.-F.; Krawczak, P. Processing and characterization of halloysite nanotubes filled polypropylene nanocomposites based on a masterbatch route: effect of halloysites treatment on structural and mechanical properties. *Express Polymer Letters* 2011, **5** (4).
- (224) Singh, V. P.; Vimal, K.; Kapur, G.; Sharma, S.; Choudhary, V. High-density polyethylene/halloysite nanocomposites: morphology and rheological behaviour under extensional and shear flow. *Journal of Polymer Research* 2016, **23** (3), 43.

- (225) Saltveit, M. E. Effect of ethylene on quality of fresh fruits and vegetables. *Postharvest biology and technology* 1999, *15* (3), 279.
- (226) Abeles, F. B.; Morgan, P.; Saltveit, M. Ethylene in plant biology Academic press. *San Diego* 1992.
- (227) Gustavsson, J.; Cederberg, C.; Sonesson, U.; Van Otterdijk, R.; Meybeck, A. *Global food losses and food waste*; FAO Rome, 2011.
- (228) Xue, L.; Liu, G.; Parfitt, J.; Liu, X.; Van Herpen, E.; Stenmarck, Å.; O'Connor, C.; Östergren, K.; Cheng, S. Missing food, missing data? A critical review of global food losses and food waste data. *Environmental Science & Technology* 2017, *51* (12), 6618.
- (229) Nychas, G. J. E.; Panagou, E. In *Food and Beverage Stability and Shelf Life*; Kilcast, D.;Subramaniam, P., Eds.; Woodhead Publishing, 2011, DOI:<https://doi.org/10.1533/9780857092540.1.3>
<https://doi.org/10.1533/9780857092540.1.3>.
- (230) Singh, S.; ho Lee, M.; Park, I.; Shin, Y.; Lee, Y. S. J. J. o. F. S.; Technology. Antimicrobial seafood packaging: a review. 2016, *53* (6), 2505.
- (231) Křížek, M.; Matějková, K.; Vácha, F.; Dadáková, E. Biogenic amines formation in high-pressure processed pike flesh (*Esox lucius*) during storage. *Food Chemistry* 2014, *151*, 466.
- (232) Gaikwad, K. K.; Singh, S.; Lee, Y. S. J. E. C. L. Oxygen scavenging films in food packaging. 2018, *16* (2), 523.
- (233) Likar, K.; Jevšnik, M. Cold chain maintaining in food trade. *Food control* 2006, *17* (2), 108.
- (234) Singh, S.; Gaikwad, K. K.; Lee, Y. S. J. E. C. L. Phase change materials for advanced cooling packaging. 2018, *16* (3), 845.
- (235) Singh, S.; Gaikwad, K. K.; Lee, M.; Lee, Y. S. Temperature-regulating materials for advanced food packaging applications: a review. *Journal of Food Measurement and Characterization* 2018, *12* (1), 588.
- (236) Silvestre, C.; Duraccio, D.; Cimmino, S. Food packaging based on polymer nanomaterials. *Progress in Polymer Science* 2011, *36* (12), 1766.
- (237) Zhou, D.; Zhao, C. Y.; Tian, Y. Review on thermal energy storage with phase change materials (PCMs) in building applications. *Applied Energy* 2012, *92*, 593.
- (238) Alehosseini, E.; Jafari, S. M. Micro/nano-encapsulated phase change materials (PCMs) as emerging materials for the food industry. *Trends in Food Science & Technology* 2019, *91*, 116.
- (239) Yuan, Y.; Zhang, N.; Tao, W.; Cao, X.; He, Y. Fatty acids as phase change materials: a review. *Renewable and Sustainable Energy Reviews* 2014, *29*, 482.
- (240) Vakhshouri, A. R.; Intechopen, 2019, DOI:DOI: 10.5772/intechopen.90487 DOI: 10.5772/intechopen.90487.

- (241) Xie, N.; Huang, Z.; Luo, Z.; Gao, X.; Fang, Y.; Zhang, Z. Inorganic salt hydrate for thermal energy storage. *Applied Sciences* 2017, *7* (12), 1317.
- (242) Zhang, N.; Yuan, Y.; Cao, X.; Du, Y.; Zhang, Z.; Gui, Y. Latent heat thermal energy storage systems with solid–liquid phase change materials: a review. *Advanced Engineering Materials* 2018, *20* (6), 1700753.
- (243) Jacob, R.; Bruno, F. Review on shell materials used in the encapsulation of phase change materials for high temperature thermal energy storage. *Renewable and Sustainable Energy Reviews* 2015, *48*, 79.
- (244) Zhao, P.-P.; Deng, C.; Zhao, Z.-Y.; Huang, S.-C.; Lu, P.; Wang, Y.-Z. Nanoflakes-Constructed Supramolecular Hierarchical Porous Microsphere for the Fire-Safety and Highly Efficient Thermal Energy Storage. *ACS Applied Materials & Interfaces* 2020.
- (245) Sarbu, I.; Dorca, A. Review on heat transfer analysis in thermal energy storage using latent heat storage systems and phase change materials. *International Journal of Energy Research* 2019, *43* (1), 29.
- (246) Gin, B.; Farid, M. M. The use of PCM panels to improve storage condition of frozen food. *Journal of Food Engineering* 2010, *100* (2), 372.
- (247) Lu, Y. L.; Zhang, W. H.; Yuan, P.; Xue, M. D.; Qu, Z. G.; Tao, W. Q. Experimental study of heat transfer intensification by using a novel combined shelf in food refrigerated display cabinets (Experimental study of a novel cabinets). *Applied Thermal Engineering* 2010, *30* (2), 85.
- (248) Oró, E.; Cabeza, L. F.; Farid, M. M. Experimental and numerical analysis of a chilly bin incorporating phase change material. *Applied Thermal Engineering* 2013, *58* (1), 61.
- (249) Singh, S. P.; Burgess, G.; Singh, J. Performance comparison of thermal insulated packaging boxes, bags and refrigerants for single-parcel shipments. 2008, *21* (1), 25.
- (250) Oró, E.; de Gracia, A.; Cabeza, L. F. Active phase change material package for thermal protection of ice cream containers. *International Journal of Refrigeration* 2013, *36* (1), 102.
- (251) Singh, S.; Gaikwad, K. K.; Lee, M.; Lee, Y. S. Thermally buffered corrugated packaging for preserving the postharvest freshness of mushrooms (*Agaricus bisporus*). *Journal of Food Engineering* 2018, *216*, 11.
- (252) Melone, L.; Altomare, L.; Cigada, A.; De Nardo, L. Phase change material cellulosic composites for the cold storage of perishable products: From material preparation to computational evaluation. *Applied Energy* 2012, *89* (1), 339.
- (253) Chalco-Sandoval, W.; Fabra, M. J.; López-Rubio, A.; Lagaron, J. M. Use of phase change materials to develop electrospun coatings of interest in food packaging applications. *Journal of Food Engineering* 2017, *192*, 122.
- (254) Bonadies, I.; Izzo Renzi, A.; Cocca, M.; Avella, M.; Carfagna, C.; Persico, P. Heat Storage and Dimensional Stability of Poly(vinyl alcohol) Based Foams Containing Microencapsulated Phase Change Materials. *Industrial & Engineering Chemistry Research* 2015, *54* (38), 9342.

- (255) Johnston, J. H.; Grindrod, J. E.; Dodds, M.; Schimitschek, K. Composite nanostructured calcium silicate phase change materials for thermal buffering in food packaging. *Current Applied Physics* 2008, 8 (3), 508.
- (256) Tully, J.; Fakhrullin, R.; Lvov, Y. Nanomaterials and Nanoarchitectures, Dordrecht, 2015; p 87.
- (257) Mitran, R. A.; Berger, D.; Munteanu, C.; Matei, C. Evaluation of different mesoporous silica supports for energy storage in shape-stabilized phase change materials with dual thermal responses. *The Journal of Physical Chemistry C* 2015, 119 (27), 15177.
- (258) Feng, L.; Zhao, W.; Zheng, J.; Frisco, S.; Song, P.; Li, X. The shape-stabilized phase change materials composed of polyethylene glycol and various mesoporous matrices (AC, SBA-15 and MCM-41). *Solar Energy Materials and Solar Cells* 2011, 95 (12), 3550.
- (259) Qian, T.; Li, J.; Deng, Y. Pore structure modified diatomite-supported PEG composites for thermal energy storage. *Scientific reports* 2016, 6, 32392.
- (260) Tas, C. E.; Hendessi, S.; Baysal, M.; Unal, S.; Cebeci, F. C.; Menceloglu, Y. Z.; Unal, H. Halloysite Nanotubes/Polyethylene Nanocomposites for Active Food Packaging Materials with Ethylene Scavenging and Gas Barrier Properties. *Food and Bioprocess Technology* 2017, 10 (4), 789.
- (261) Hendessi, S.; Sevinis, E. B.; Unal, S.; Cebeci, F. C.; Menceloglu, Y. Z.; Unal, H. Antibacterial sustained-release coatings from halloysite nanotubes/waterborne polyurethanes. *Progress in Organic Coatings* 2016, 101, 253.
- (262) Goitandia, A. M.; Beobide, G.; Aranzabe, E.; Aranzabe, A. Development of content-stable phase change composites by infiltration into inorganic porous supports. *Solar Energy Materials and Solar Cells* 2015, 134, 318.
- (263) Chen, L.; Zou, R.; Xia, W.; Liu, Z.; Shang, Y.; Zhu, J.; Wang, Y.; Lin, J.; Xia, D.; Cao, A. Electro-and photodriven phase change composites based on wax-infiltrated carbon nanotube sponges. *ACS nano* 2012, 6 (12), 10884.
- (264) Mei, D.; Zhang, B.; Liu, R.; Zhang, Y.; Liu, J. Preparation of capric acid/halloysite nanotube composite as form-stable phase change material for thermal energy storage. *Solar Energy Materials and Solar Cells* 2011, 95 (10), 2772.
- (265) Li, C.; Yu, H.; Song, Y.; Zhao, M. Synthesis and characterization of PEG/ZSM-5 composite phase change materials for latent heat storage. *Renewable Energy* 2018, 121, 45.
- (266) Min, X.; Fang, M.; Huang, Z.; Liu, Y. g.; Huang, Y.; Wen, R.; Qian, T.; Wu, X. Enhanced thermal properties of novel shape-stabilized PEG composite phase change materials with radial mesoporous silica sphere for thermal energy storage. *Scientific Reports* 2015, 5 (1), 12964.
- (267) Voon, H. C.; Bhat, R.; Easa, A. M.; Liong, M. T.; Karim, A. A. J. F.; Technology, B. Effect of Addition of Halloysite Nanoclay and SiO₂ Nanoparticles on Barrier and Mechanical Properties of Bovine Gelatin Films. 2012, 5 (5), 1766.

- (268) Qiao, X.; Na, M.; Gao, P.; Sun, K. Halloysite nanotubes reinforced ultrahigh molecular weight polyethylene nanocomposite films with different filler concentration and modification. *Polymer Testing* 2017, 57, 133.
- (269) Krupa, I.; Nogelová, Z.; Špitalský, Z.; Janigová, I.; Boh, B.; Sumiga, B.; Kleinová, A.; Karkri, M.; AlMaadeed, M. A. Phase change materials based on high-density polyethylene filled with microencapsulated paraffin wax. *Energy Conversion and Management* 2014, 87, 400.
- (270) Rojas, A.; Torres, A.; Añazco, A.; Villegas, C.; Galotto, M. J.; Guarda, A.; Romero, J. Effect of pressure and time on scCO₂-assisted incorporation of thymol into LDPE-based nanocomposites for active food packaging. *Journal of CO₂ Utilization* 2018, 26, 434.
- (271) Dehghani, S.; Peighambarioust, S. H.; Peighambarioust, S. J.; Hosseini, S. V.; Regenstein, J. M. Improved mechanical and antibacterial properties of active LDPE films prepared with combination of Ag, ZnO and CuO nanoparticles. *Food Packaging and Shelf Life* 2019, 22, 100391.
- (272) Shchukina, E.; Shchukin, D. G. Nanocontainer-Based Active Systems: From Self-Healing Coatings to Thermal Energy Storage. *Langmuir* 2019, 35 (26), 8603.
- (273) Ormancı-Acar, T.; Celebi, F.; Keskin, B.; Mutlu-Salmanlı, O.; Agtas, M.; Turken, T.; Tufanı, A.; İmer, D. Y.; Ince, G. O.; Demir, T. U. et al. Fabrication and characterization of temperature and pH resistant thin film nanocomposite membranes embedded with halloysite nanotubes for dye rejection. *Desalination* 2018, 429, 20.
- (274) Joussein, E.; Petit, S.; Churchman, J.; Theng, B.; Righi, D.; Delvaux, B. In *Clay Minerals*, 2005; Vol. 40.
- (275) Kausar, A. Review on Polymer/Halloysite Nanotube Nanocomposite. *Polymer-Plastics Technology and Engineering* 2018, 57 (6), 548.
- (276) Makaremi, M.; De Silva, R. T.; Pasbakhsh, P. Electrospun Nanofibrous Membranes of Polyacrylonitrile/Halloysite with Superior Water Filtration Ability. *The Journal of Physical Chemistry C* 2015, 119 (14), 7949.
- (277) Gaaz, T. S.; Sulong, A. B.; Kadhum, A. A. H.; Nassir, M. H.; Al-Amiery, A. A. Absolute variation of the mechanical characteristics of halloysite reinforced polyurethane nanocomposites complemented by Taguchi and ANOVA approaches. *Results in Physics* 2017, 7, 3287.
- (278) Liu, W.; Hoa, S. V.; Pugh, M. Fracture toughness and water uptake of high-performance epoxy/nanoclay nanocomposites. *Composites Science and Technology* 2005, 65 (15), 2364.
- (279) Lvov, Y.; Abdullayev, E. Functional polymer-clay nanotube composites with sustained release of chemical agents. *Progress in Polymer Science* 2013, 38 (10), 1690.
- (280) López-Galindo, A.; Viseras, C.; Cerezo, P. Compositional, technical and safety specifications of clays to be used as pharmaceutical and cosmetic products. *Applied Clay Science* 2007, 36 (1), 51.

- (281) Zhao, J. M.; Chang, J. H.; Lee, Y. K.; Hwang, K. H.; Lee, J. K. Separation of Halloysite Nano Tubes (HNTs) by Homogenization of Quartz Contaminated Kaolins. *Journal of Nanoscience and Nanotechnology* 2019, 19 (2), 984.
- (282) Suppiah, K.; Teh, P. L.; Husseinsyah, S.; Rahman, R. Properties and characterization of carboxymethyl cellulose/halloysite nanotube bio-nanocomposite films: Effect of sodium dodecyl sulfate. *Polymer Bulletin* 2019, 76 (1), 365.
- (283) Alkan Tas, B.; Sehit, E.; Erdinc Tas, C.; Unal, S.; Cebeci, F. C.; Menceloglu, Y. Z.; Unal, H. Carvacrol loaded halloysite coatings for antimicrobial food packaging applications. *Food Packaging and Shelf Life* 2019, 20, 100300.
- (284) Zhan, Y.; Zhang, J.; Wan, X.; Long, Z.; He, S.; He, Y. Epoxy composites coating with Fe₃O₄ decorated graphene oxide: Modified bio-inspired surface chemistry, synergistic effect and improved anti-corrosion performance. *Applied Surface Science* 2018, 436, 756.
- (285) Zhan, Y.; He, S.; Wan, X.; Zhao, S.; Bai, Y. Thermally and chemically stable poly(arylene ether nitrile)/halloysite nanotubes intercalated graphene oxide nanofibrous composite membranes for highly efficient oil/water emulsion separation in harsh environment. *Journal of Membrane Science* 2018, 567, 76.
- (286) Liu, Y.; Guan, H.; Zhang, J.; Zhao, Y.; Yang, J.-H.; Zhang, B. Polydopamine-coated halloysite nanotubes supported AgPd nanoalloy: An efficient catalyst for hydrolysis of ammonia borane. *International Journal of Hydrogen Energy* 2018, 43 (5), 2754.
- (287) Feng, J.; Fan, H.; Zha, D.-a.; Wang, L.; Jin, Z. Characterizations of the Formation of Polydopamine-Coated Halloysite Nanotubes in Various pH Environments. *Langmuir* 2016, 32 (40), 10377.
- (288) Zhu, B.; Edmondson, S. Polydopamine-melanin initiators for Surface-initiated ATRP. *Polymer* 2011, 52 (10), 2141.
- (289) Taurozzi, J. S.; Hackley, V. A.; Wiesner, M. R. Ultrasonic dispersion of nanoparticles for environmental, health and safety assessment—issues and recommendations. *Nanotoxicology* 2011, 5 (4), 711.
- (290) Lynge, M. E.; van der Westen, R.; Postma, A.; Städler, B. Polydopamine—a nature-inspired polymer coating for biomedical science. *Nanoscale* 2011, 3 (12), 4916.
- (291) Gaaz, T. S.; Sulong, A. B.; Kadhum, A. A. H.; Nassir, M. H.; Al-Amiry, A. A. Impact of Sulfuric Acid Treatment of Halloysite on Physico-Chemic Property Modification. 2016, 9 (8), 620.
- (292) Liu, M.; Cao, X.; Liu, H.; Yang, X.; Zhou, C. In *Nanomaterials from Clay Minerals*; Wang, A.; Wang, W., Eds.; Elsevier, 2019, DOI:<https://doi.org/10.1016/B978-0-12-814533-3.00012-0>.
- (293) Zeng, S.; Reyes, C.; Liu, J.; Rodgers, P. A.; Wentworth, S. H.; Sun, L. Facile hydroxylation of halloysite nanotubes for epoxy nanocomposite applications. *Polymer* 2014, 55 (25), 6519.

- (294) Doughty, A. C.; Hoover, A. R.; Layton, E.; Murray, C. K.; Howard, E. W.; Chen, W. R. Nanomaterial applications in photothermal therapy for cancer. *Materials* 2019, *12* (5), 779.
- (295) Fernandes, N.; Rodrigues, C. F.; Moreira, A. F.; Correia, I. J. Overview of the application of inorganic nanomaterials in cancer photothermal therapy. *Biomaterials science* 2020.
- (296) Wang, J.; Qiu, J. A review of organic nanomaterials in photothermal cancer therapy. *Cancer Res. Front* 2016, *2* (1), 67.
- (297) Kim, S. H.; Kang, E. B.; Jeong, C. J.; Sharker, S. M.; In, I.; Park, S. Y. Light Controllable Surface Coating for Effective Photothermal Killing of Bacteria. *ACS Applied Materials & Interfaces* 2015, *7* (28), 15600.
- (298) Oruc, B.; Unal, H. Fluorophore-Decorated Carbon Nanotubes with Enhanced Photothermal Activity as Antimicrobial Nanomaterials. *ACS Omega* 2019, *4* (3), 5556.
- (299) Zhu, L.; Gao, M.; Peh, C. K. N.; Ho, G. W. Solar-driven photothermal nanostructured materials designs and prerequisites for evaporation and catalysis applications. *Materials Horizons* 2018, *5* (3), 323.
- (300) Xu, X.; Bai, B.; Wang, H.; Suo, Y. A near-infrared and temperature-responsive pesticide release platform through core–shell polydopamine@ PNIPAm nanocomposites. *ACS Applied Materials & Interfaces* 2017, *9* (7), 6424.
- (301) Yang, X.; Li, H.; Qian, C.; Guo, Y.; Li, C.; Gao, F.; Yang, Y.; Wang, K.; Oupicky, D.; Sun, M. Near-infrared light-activated IR780-loaded liposomes for anti-tumor angiogenesis and Photothermal therapy. *Nanomedicine: Nanotechnology, Biology and Medicine* 2018, *14* (7), 2283.
- (302) Cao, Z.; Ma, Y.; Sun, C.; Lu, Z.; Yao, Z.; Wang, J.; Li, D.; Yuan, Y.; Yang, X. ROS-sensitive polymeric nanocarriers with red light-activated size shrinkage for remotely controlled drug release. *Chemistry of Materials* 2018, *30* (2), 517.
- (303) Yu, P.; Guo, X.-S.; Bao, R.-Y.; Liu, Z.-Y.; Yang, M.-B.; Yang, W. Photo-Driven Self-Healing of Arbitrary Nondestructive Damage in Polyethylene-Based Nanocomposites. *ACS Applied Materials & Interfaces* 2019, *12* (1), 1650.
- (304) Jamkhande, P. G.; Ghule, N. W.; Bamer, A. H.; Kalaskar, M. G. Metal nanoparticles synthesis: An overview on methods of preparation, advantages and disadvantages, and applications. *Journal of Drug Delivery Science and Technology* 2019, *53*, 101174.
- (305) Bae, K.; Kang, G.; Cho, S. K.; Park, W.; Kim, K.; Padilla, W. J. Flexible thin-film black gold membranes with ultrabroadband plasmonic nanofocusing for efficient solar vapour generation. *Nature communications* 2015, *6* (1), 1.
- (306) Zhu, M.; Li, Y.; Chen, F.; Zhu, X.; Dai, J.; Li, Y.; Yang, Z.; Yan, X.; Song, J.; Wang, Y. Plasmonic wood for high-efficiency solar steam generation. *Advanced Energy Materials* 2018, *8* (4), 1701028.

- (307) Zou, Y.; Chen, X.; Guo, W.; Liu, X.; Li, Y. Flexible and Robust Polyaniline Composites for Highly Efficient and Durable Solar Desalination. *ACS Applied Energy Materials* 2020, 3 (3), 2634.
- (308) Pierini, F.; Nakielski, P.; Urbanek, O.; Pawłowska, S.; Lanzi, M.; De Sio, L.; Kowalewski, T. A. Polymer-based nanomaterials for photothermal therapy: from light-responsive to multifunctional nanoplates for synergistically combined technologies. *Biomacromolecules* 2018, 19 (11), 4147.
- (309) Zhao, Y.; Wu, Y.; Wang, L.; Zhang, M.; Chen, X.; Liu, M.; Fan, J.; Liu, J.; Zhou, F.; Wang, Z. Bio-inspired reversible underwater adhesive. *Nature communications* 2017, 8 (1), 1.
- (310) Duan, X.; Liu, S.; Huang, E.; Shen, X.; Wang, Z.; Li, S.; Jin, C. Superhydrophobic and antibacterial wood enabled by polydopamine-assisted decoration of copper nanoparticles. *Colloids and Surfaces A: Physicochemical and Engineering Aspects* 2020, 125145.
- (311) Jia, X.; Sheng, W.-b.; Li, W.; Tong, Y.-b.; Liu, Z.-y.; Zhou, F. Adhesive polydopamine coated avermectin microcapsules for prolonging foliar pesticide retention. *ACS applied materials & interfaces* 2014, 6 (22), 19552.
- (312) Park, J.; Brust, T. F.; Lee, H. J.; Lee, S. C.; Watts, V. J.; Yeo, Y. Polydopamine-based simple and versatile surface modification of polymeric nano drug carriers. *ACS nano* 2014, 8 (4), 3347.
- (313) Cong, Y.; Xia, T.; Zou, M.; Li, Z.; Peng, B.; Guo, D.; Deng, Z. Mussel-inspired polydopamine coating as a versatile platform for synthesizing polystyrene/Ag nanocomposite particles with enhanced antibacterial activities. *Journal of Materials Chemistry B* 2014, 2 (22), 3450.
- (314) Cheng, H.; Liu, X.; Zhang, L.; Hou, B.; Yu, F.; Shi, Z.; Wang, X. Self-floating Bi₂S₃/poly (vinylidene fluoride) composites on polyurethane sponges for efficient solar water purification. *Solar Energy Materials and Solar Cells* 2019, 203, 110127.
- (315) Yang, L.; Lu, X.; Wang, Z.; Xia, H. Diels–Alder dynamic crosslinked polyurethane/polydopamine composites with NIR triggered self-healing function. *Polymer Chemistry* 2018, 9 (16), 2166.
- (316) Yang, S.; Du, X.; Deng, S.; Qiu, J.; Du, Z.; Cheng, X.; Wang, H. Recyclable and Self-Healing Polyurethane Composites Based on Diels-Alder Reaction for Efficient Solar-to-Thermal Energy Storage. *Chemical Engineering Journal* 2020, 125654.
- (317) Yang, L.; Tong, R.; Wang, Z.; Xia, H. Polydopamine Particle-Filled Shape-Memory Polyurethane Composites with Fast Near-Infrared Light Responsibility. *ChemPhysChem* 2018, 19 (16), 2052.
- (318) Anıl, D.; Berksun, E.; Durmuş-Sayar, A.; Sevinis,-Özbulut, E. B.; Ünal, S. In *Handbook of Waterborne Coatings*; Zarras, P.; Soucek, M. D.; Tiwari, A., Eds.; Elsevier, 2020, DOI:<https://doi.org/10.1016/B978-0-12-814201-1.00011-1> <https://doi.org/10.1016/B978-0-12-814201-1.00011-1>.

- (319) Han, Y.; Hu, J.; Xin, Z. Facile preparation of high solid content waterborne polyurethane and its application in leather surface finishing. *Progress in Organic Coatings* 2019, *130*, 8.
- (320) Bhattacharjee, S. DLS and zeta potential—what they are and what they are not? *Journal of controlled release* 2016, *235*, 337.
- (321) Tejido-Rastrilla, R.; Ferraris, S.; Goldmann, W. H.; Grünewald, A.; Detsch, R.; Baldi, G.; Spriano, S.; Boccaccini, A. R. Studies on Cell Compatibility, Antibacterial Behavior, and Zeta Potential of Ag-Containing Polydopamine-Coated Bioactive Glass-Ceramic. *Materials* 2019, *12* (3), 500.
- (322) Xu, J.; Ma, A.; Liu, T.; Lu, C.; Wang, D.; Xu, H. Janus-like Pickering emulsions and their controllable coalescence. *Chemical Communications* 2013, *49* (92), 10871.
- (323) Lv, Y.; Yang, H.-C.; Liang, H.-Q.; Wan, L.-S.; Xu, Z.-K. Nanofiltration membranes via co-deposition of polydopamine/polyethylenimine followed by cross-linking. *Journal of membrane science* 2015, *476*, 50.
- (324) Kumar, A.; Dixit, C. K. In *Advances in Nanomedicine for the Delivery of Therapeutic Nucleic Acids*; Nimesh, S.; Chandra, R.; Gupta, N., Eds.; Woodhead Publishing, 2017, DOI:<https://doi.org/10.1016/B978-0-08-100557-6.00003-1>
- (325) Deng, Z.; Shang, B.; Peng, B. Polydopamine based colloidal materials: synthesis and applications. *The Chemical Record* 2018, *18* (4), 410.
- (326) Moazzam, P.; Tavassoli, H.; Razmjou, A.; Warkiani, M. E.; Asadnia, M. Mist harvesting using bioinspired polydopamine coating and microfabrication technology. *Desalination* 2018, *429*, 111.
- (327) Su, L.; Yu, Y.; Zhao, Y.; Liang, F.; Zhang, X. Strong antibacterial polydopamine coatings prepared by a shaking-assisted method. *Scientific reports* 2016, *6*, 24420.
- (328) Saraswathi, M. S. S. A.; Rana, D.; Alwarappan, S.; Gowrishankar, S.; Kanimozhi, P.; Nagendran, A. Cellulose acetate ultrafiltration membranes customized with bio-inspired polydopamine coating and in situ immobilization of silver nanoparticles. *New Journal of Chemistry* 2019, *43* (10), 4216.
- (329) Špírková, M.; Hodan, J.; Kredatusová, J.; Poręba, R.; Uchman, M.; Serkis-Rodzeń, M. Functional properties of films based on novel waterborne polyurethane dispersions prepared without a chain-extension step. *Progress in Organic Coatings* 2018, *123*, 53.
- (330) Overbeek, A. Polymer heterogeneity in waterborne coatings. *Journal of coatings technology and research* 2010, *7* (1), 1.
- (331) Wu, D.; Qu, D.; Jiang, W.; Chen, G.; An, L.; Zhuang, C.; Sun, Z. Self-floating nanostructured Ni–NiO x/Ni foam for solar thermal water evaporation. *Journal of Materials Chemistry A* 2019, *7* (14), 8485.
- (332) Huang, C.; Qian, X.; Yang, R. Thermal conductivity of polymers and polymer nanocomposites. *Materials Science and Engineering: R: Reports* 2018, *132*, 1.
- (333) Shanks, R. In *Thermoplastic elastomers*; IntechOpen, 2012.

- (334) Klosterman, L.; Ahmad, Z.; Viswanathan, V.; Bettinger, C. J. Synthesis and measurement of cohesive mechanics in polydopamine nanomembranes. *Advanced Materials Interfaces* 2017, **4** (10), 1700041.
- (335) Zhang, T.; Jiang, Z.; Xve, T.; Sun, S.; Li, J.; Ren, W.; Wu, A.; Huang, P. One-pot synthesis of hollow PDA@ DOX nanoparticles for ultrasound imaging and chemo-thermal therapy in breast cancer. *Nanoscale* 2019, **11** (45), 21759.
- (336) Li, Y.; Li, N.; Ge, J.; Xue, Y.; Niu, W.; Chen, M.; Du, Y.; Ma, P. X.; Lei, B. Biodegradable thermal imaging-tracked ultralong nanowire-reinforced conductive nanocomposites elastomers with intrinsical efficient antibacterial and anticancer activity for enhanced biomedical application potential. *Biomaterials* 2019, **201**, 68.
- (337) Borzenkov, M.; Pallavicini, P.; Chirico, G. Photothermally active inorganic nanoparticles: From colloidal solutions to photothermally active printed surfaces and polymeric nanocomposite materials. *European Journal of Inorganic Chemistry* 2019, **2019** (41), 4397.
- (338) Khoei, S.; Sadeghi, A. An NIR-triggered drug release and highly efficient photodynamic therapy from PCL/PNIPAm/porphyrin modified graphene oxide nanoparticles with the Janus morphology. *RSC Advances* 2019, **9** (68), 39780.
- (339) Sun, J.; Zhang, P.; Fan, Y.; Zhao, J.; Niu, S.; Song, L.; Ma, L.; Ren, L.; Ming, W. Near-infrared triggered antibacterial nanocomposite membrane containing upconversion nanoparticles. *Materials Science and Engineering: C* 2019, **103**, 109797.
- (340) Manivasagan, P.; Khan, F.; Hoang, G.; Mondal, S.; Kim, H.; Doan, V. H. M.; Kim, Y.-M.; Oh, J. Thiol chitosan-wrapped gold nanoshells for near-infrared laser-induced photothermal destruction of antibiotic-resistant bacteria. *Carbohydrate polymers* 2019, **225**, 115228.
- (341) Xu, J.-W.; Yao, K.; Xu, Z.-K. Nanomaterials with a photothermal effect for antibacterial activities: an overview. *Nanoscale* 2019, **11** (18), 8680.
- (342) Fan, X.; Qiu, X.; Lu, L.; Zhou, B. Fabrication and characteristics of solar-driven phase change microcapsules with crystalline TiO₂/CuS hybrid shell for solar energy conversion and storage. *Journal of Materials Research*, 1.
- (343) Chen, Y.; Zhang, Q.; Wen, X.; Yin, H.; Liu, J. A novel CNT encapsulated phase change material with enhanced thermal conductivity and photo-thermal conversion performance. *Solar Energy Materials and Solar Cells* 2018, **184**, 82.
- (344) Du, X.; Xu, J.; Deng, S.; Du, Z.; Cheng, X.; Wang, H. Amino-functionalized single-walled carbon nanotubes-integrated polyurethane phase change composites with superior photothermal conversion efficiency and thermal conductivity. *ACS Sustainable Chemistry & Engineering* 2019, **7** (21), 17682.
- (345) Du, X.; Qiu, J.; Deng, S.; Du, Z.; Cheng, X.; Wang, H. Ti₃C₂T_x@ PDA-Integrated Polyurethane Phase Change Composites with Superior Solar-Thermal Conversion Efficiency and Improved Thermal Conductivity. *ACS Sustainable Chemistry & Engineering* 2020, **8** (14), 5799.

- (346) Maleki, M.; Ahmadi, P. T.; Mohammadi, H.; Karimian, H.; Ahmadi, R.; Emrooz, H. B. M. Photo-thermal conversion structure by infiltration of paraffin in three dimensionally interconnected porous polystyrene-carbon nanotubes (PS-CNT) polyHIPE foam. *Solar Energy Materials and Solar Cells* 2019, *191*, 266.
- (347) Mu, B.; Li, M. Synthesis of novel form-stable composite phase change materials with modified graphene aerogel for solar energy conversion and storage. *Solar Energy Materials and Solar Cells* 2019, *191*, 466.
- (348) Neumann, O.; Urban, A. S.; Day, J.; Lal, S.; Nordlander, P.; Halas, N. J. Solar vapor generation enabled by nanoparticles. *ACS nano* 2013, *7* (1), 42.
- (349) Ghasemi, H.; Ni, G.; Marconnet, A. M.; Loomis, J.; Yerci, S.; Miljkovic, N.; Chen, G. Solar steam generation by heat localization. *Nature communications* 2014, *5*, 4449.
- (350) Liddle, B.; Sadorsky, P. How much does increasing non-fossil fuels in electricity generation reduce carbon dioxide emissions? *Applied Energy* 2017, *197*, 212.
- (351) Jackson, R. B.; Le Quéré, C.; Andrew, R. M.; Canadell, J. G.; Korsbakken, J. I.; Liu, Z.; Peters, G. P.; Zheng, B. Global energy growth is outpacing decarbonization. *Environmental Research Letters* 2018, *13* (12), 120401.
- (352) Chu, S.; Majumdar, A. Opportunities and challenges for a sustainable energy future. *Nature* 2012, *488* (7411), 294.
- (353) Davis, S. J.; Lewis, N. S.; Shaner, M.; Aggarwal, S.; Arent, D.; Azevedo, I. L.; Benson, S. M.; Bradley, T.; Brouwer, J.; Chiang, Y.-M. et al. Net-zero emissions energy systems. *Science* 2018, *360* (6396), eaas9793.
- (354) Amaral, C.; Vicente, R.; Marques, P. A. A. P.; Barros-Timmons, A. Phase change materials and carbon nanostructures for thermal energy storage: A literature review. *Renewable and Sustainable Energy Reviews* 2017, *79*, 1212.
- (355) Collier, U. “Renewable heat policies Delivering clean heat solutions for the energy transition,” 2018.
- (356) Asadi, E.; da Silva, M. G.; Antunes, C. H.; Dias, L. Multi-objective optimization for building retrofit strategies: A model and an application. *Energy and Buildings* 2012, *44*, 81.
- (357) Ahmad, M.; Bontemps, A.; Sallée, H.; Quenard, D. Thermal testing and numerical simulation of a prototype cell using light wallboards coupling vacuum isolation panels and phase change material. *Energy and Buildings* 2006, *38* (6), 673.
- (358) Abuelnuor, A. A. A.; Omara, A. A. M.; Saqr, K. M.; Elhag, I. H. I. Improving indoor thermal comfort by using phase change materials: A review. 2018, *42* (6), 2084.
- (359) Rao, Z.; Wang, S.; Zhang, Z. Energy saving latent heat storage and environmental friendly humidity-controlled materials for indoor climate. *Renewable and Sustainable Energy Reviews* 2012, *16* (5), 3136.
- (360) Pilichowska, K.; Pilichowski, K. Phase change materials for thermal energy storage. *Progress in Materials Science* 2014, *65*, 67.

- (361) Chadel, S. S.; Agarwal, T. Review of current state of research on energy storage, toxicity, health hazards and commercialization of phase changing materials. *Renewable and Sustainable Energy Reviews* 2017, *67*, 581.
- (362) Luan, Y.; Yang, M.; Ma, Q.; Qi, Y.; Gao, H.; Wu, Z.; Wang, G. Introduction of an organic acid phase changing material into metal–organic frameworks and the study of its thermal properties. *Journal of Materials Chemistry A* 2016, *4* (20), 7641.
- (363) Tang, J.; Yang, M.; Yu, F.; Chen, X.; Tan, L.; Wang, G. 1-Octadecanol@hierarchical porous polymer composite as a novel shape-stability phase change material for latent heat thermal energy storage. *Applied Energy* 2017, *187*, 514.
- (364) Li, J.; Cheng, Z.; Zhu, M.; Thomas, A.; Liao, Y. Facile Synthesis of Nitrogen-Rich Porous Organic Polymers for Latent Heat Energy Storage. *ACS Applied Energy Materials* 2018, *1* (11), 6535.
- (365) Yang, J.; Tang, L.-S.; Bai, L.; Bao, R.-Y.; Liu, Z.-Y.; Xie, B.-H.; Yang, M.-B.; Yang, W. High-performance composite phase change materials for energy conversion based on macroscopically three-dimensional structural materials. *Materials Horizons* 2019, *6* (2), 250.
- (366) Huang, X.; Chen, X.; Li, A.; Atinifu, D.; Gao, H.; Dong, W.; Wang, G. Shape-stabilized phase change materials based on porous supports for thermal energy storage applications. *Chemical Engineering Journal* 2019, *356*, 641.
- (367) Zhang, X.; Lin, Q.; Luo, H.; Luo, S. Three-dimensional graphitic hierarchical porous carbon/stearic acid composite as shape-stabilized phase change material for thermal energy storage. *Applied Energy* 2020, *260*, 114278.
- (368) Feng, D.; Feng, Y.; Qiu, L.; Li, P.; Zang, Y.; Zou, H.; Yu, Z.; Zhang, X. Review on nanoporous composite phase change materials: Fabrication, characterization, enhancement and molecular simulation. *Renewable and Sustainable Energy Reviews* 2019, *109*, 578.
- (369) Gao, H.; Wang, J.; Chen, X.; Wang, G.; Huang, X.; Li, A.; Dong, W. Nanoconfinement effects on thermal properties of nanoporous shape-stabilized composite PCMs: A review. *Nano Energy* 2018, *53*, 769.
- (370) Masters, A. F.; Maschmeyer, T. Zeolites – From curiosity to cornerstone. *Microporous and Mesoporous Materials* 2011, *142* (2), 423.
- (371) Thomas, A. Functional Materials: From Hard to Soft Porous Frameworks. 2010, *49* (45), 8328.
- (372) Kumar, K. V.; Preuss, K.; Titirici, M.-M.; Rodríguez-Reinoso, F. Nanoporous Materials for the Onboard Storage of Natural Gas. *Chemical Reviews* 2017, *117* (3), 1796.
- (373) Vogt, E. T. C.; Weckhuysen, B. M. Fluid catalytic cracking: recent developments on the grand old lady of zeolite catalysis. *Chemical Society Reviews* 2015, *44* (20), 7342.
- (374) Karaoglu, O.; Alpdogan, G.; Zor, S. D.; Bildirir, H.; Ertas, E. Efficient solid phase extraction of α -tocopherol and β -sitosterol from sunflower oil waste by improving the mesoporosity of the zeolitic adsorbent. *Food Chemistry* 2019,

DOI:<https://doi.org/10.1016/j.foodchem.2019.125890>
<https://doi.org/10.1016/j.foodchem.2019.125890>, 125890.

- (375) Pérez-Ramírez, J.; Christensen, C. H.; Egeblad, K.; Christensen, C. H.; Groen, J. C. Hierarchical zeolites: enhanced utilisation of microporous crystals in catalysis by advances in materials design. *Chemical Society Reviews* 2008, *37* (11), 2530.
- (376) Malola, S.; Svelle, S.; Bleken, F. L.; Swang, O. Detailed reaction paths for zeolite dealumination and desilication from density functional calculations. *Angewandte Chemie International Edition* 2012, *51* (3), 652.
- (377) Verboekend, D.; Pérez-Ramírez, J. Design of hierarchical zeolite catalysts by desilication. *Catalysis Science & Technology* 2011, *1* (6), 879.
- (378) Miró, L.; Barreneche, C.; Ferrer, G.; Solé, A.; Martorell, I.; Cabeza, L. F. Health hazard, cycling and thermal stability as key parameters when selecting a suitable phase change material (PCM). *Thermochimica Acta* 2016, 627-629, 39.
- (379) Yang, M.-H.; Choong, Y.-M. A rapid gas chromatographic method for direct determination of short-chain (C₂-C₁₂) volatile organic acids in foods. *Food Chemistry* 2001, *75* (1), 101.
- (380) Zhang, D.; Tian, S.; Xiao, D. Experimental study on the phase change behavior of phase change material confined in pores. *Solar Energy* 2007, *81* (5), 653.
- (381) Wang, C.; Feng, L.; Li, W.; Zheng, J.; Tian, W.; Li, X. Shape-stabilized phase change materials based on polyethylene glycol/porous carbon composite: The influence of the pore structure of the carbon materials. *Solar Energy Materials and Solar Cells* 2012, *105*, 21.
- (382) Lu, Z.; Xu, B.; Zhang, J.; Zhu, Y.; Sun, G.; Li, Z. Preparation and characterization of expanded perlite/paraffin composite as form-stable phase change material. *Solar Energy* 2014, *108*, 460.
- (383) Konuklu, Y.; Ersoy, O.; Gokce, O. Easy and industrially applicable impregnation process for preparation of diatomite-based phase change material nanocomposites for thermal energy storage. *Applied Thermal Engineering* 2015, *91*, 759.
- (384) Song, S.; Dong, L.; Zhang, Y.; Chen, S.; Li, Q.; Guo, Y.; Deng, S.; Si, S.; Xiong, C. Lauric acid/intercalated kaolinite as form-stable phase change material for thermal energy storage. *Energy* 2014, *76*, 385.
- (385) Zhang, D.; Zhou, J.; Wu, K.; Li, Z. Granular phase changing composites for thermal energy storage. *Solar Energy* 2005, *78* (3), 471.
- (386) Shen, Q.; Ouyang, J.; Zhang, Y.; Yang, H. Lauric acid/modified sepiolite composite as a form-stable phase change material for thermal energy storage. *Applied Clay Science* 2017, *146*, 14.
- (387) Qian, T.; Li, J.; Ma, H.; Yang, J. The preparation of a green shape-stabilized composite phase change material of polyethylene glycol/SiO₂ with enhanced thermal performance based on oil shale ash via temperature-assisted sol-gel method. *Solar Energy Materials and Solar Cells* 2015, *132*, 29.

- (388) Min, X.; Fang, M.; Huang, Z.; Liu, Y. g.; Huang, Y.; Wen, R.; Qian, T.; Wu, X. Enhanced thermal properties of novel shape-stabilized PEG composite phase change materials with radial mesoporous silica sphere for thermal energy storage. *Scientific Reports* 2015, 5, 12964.
- (389) Xia, L.; Zhang, P.; Wang, R. Z. Preparation and thermal characterization of expanded graphite/paraffin composite phase change material. *Carbon* 2010, 48 (9), 2538.
- (390) Radhakrishnan, R.; Gubbins, K. E.; Watanabe, A.; Kaneko, K. Freezing of simple fluids in microporous activated carbon fibers: Comparison of simulation and experiment. 1999, 111 (19), 9058.
- (391) Riesen, R.; Vogel, K.; Schubnell, M. DSC by the TGA/SDTA851e Considering Mass Changes. *Journal of Thermal Analysis and Calorimetry* 2001, 64 (1), 243.
- (392) Wang, P. Emerging investigator series: the rise of nano-enabled photothermal materials for water evaporation and clean water production by sunlight. *Environmental Science: Nano* 2018, 5 (5), 1078.
- (393) Huang, Q.; Chen, J.; Liu, M.; Huang, H.; Zhang, X.; Wei, Y. Polydopamine-based functional materials and their applications in energy, environmental, and catalytic fields: State-of-the-art review. *Chemical Engineering Journal* 2020, 387, 124019.
- (394) Tao, Y.; He, Y.-L. A review of phase change material and performance enhancement method for latent heat storage system. *Renewable and Sustainable Energy Reviews* 2018, 93, 245.
- (395) Gulfam, R.; Zhang, P.; Meng, Z. Advanced thermal systems driven by paraffin-based phase change materials—A review. *Applied energy* 2019, 238, 582.
- (396) Xie, N.; Luo, J.; Li, Z.; Huang, Z.; Gao, X.; Fang, Y.; Zhang, Z. Salt hydrate/expanded vermiculite composite as a form-stable phase change material for building energy storage. *Solar Energy Materials and Solar Cells* 2019, 189, 33.
- (397) Mohamed, S. A.; Al-Sulaiman, F. A.; Ibrahim, N. I.; Zahir, M. H.; Al-Ahmed, A.; Saidur, R.; Yıldırım, B.; Sahin, A. A review on current status and challenges of inorganic phase change materials for thermal energy storage systems. *Renewable and Sustainable Energy Reviews* 2017, 70, 1072.
- (398) Jia, X.; Li, Q.; Ao, C.; Hu, R.; Xia, T.; Xue, Z.; Wang, Q.; Deng, X.; Zhang, W.; Lu, C. High thermal conductive shape-stabilized phase change materials of polyethylene glycol/boron nitride@ chitosan composites for thermal energy storage. *Composites Part A: Applied Science and Manufacturing* 2020, 129, 105710.
- (399) Zhou, L.; Tang, L.-S.; Tao, X.-F.; Yang, J.; Yang, M.-B.; Yang, W. Facile fabrication of shape-stabilized polyethylene glycol/cellulose nanocrystal phase change materials based on thiol-ene click chemistry and solvent exchange. *Chemical Engineering Journal* 2020, 125206.
- (400) Wijesena, R. N.; Tissera, N. D.; Rathnayaka, V.; Rajapakse, H.; de Silva, R. M.; de Silva, K. N. Shape-stabilization of polyethylene glycol phase change materials with chitin nanofibers for applications in “smart” windows. *Carbohydrate Polymers* 2020, 116132.

- (401) Jankowski, N. R.; McCluskey, F. P. A review of phase change materials for vehicle component thermal buffering. *Applied Energy* 2014, *113*, 1525.
- (402) Kenisarin, M.; Mahkamov, K. Solar energy storage using phase change materials. *Renewable and sustainable energy reviews* 2007, *11* (9), 1913.
- (403) Kuznik, F.; David, D.; Johannes, K.; Roux, J.-J. A review on phase change materials integrated in building walls. *Renewable and Sustainable Energy Reviews* 2011, *15* (1), 379.
- (404) Mondal, S. Phase change materials for smart textiles—An overview. *Applied thermal engineering* 2008, *28* (11-12), 1536.
- (405) Ma, T.; Yang, H.; Zhang, Y.; Lu, L.; Wang, X. Using phase change materials in photovoltaic systems for thermal regulation and electrical efficiency improvement: a review and outlook. *Renewable and Sustainable Energy Reviews* 2015, *43*, 1273.
- (406) Sari, A.; Bicer, A.; Al-Ahmed, A.; Al-Sulaiman, F. A.; Zahir, M. H.; Mohamed, S. A. Silica fume/capric acid-palmitic acid composite phase change material doped with CNTs for thermal energy storage. *Solar Energy Materials and Solar Cells* 2018, *179*, 353.
- (407) Cheng, J.; Zhou, Y.; Ma, D.; Li, S.; Zhang, F.; Guan, Y.; Qu, W.; Jin, Y.; Wang, D. Preparation and characterization of carbon nanotube microcapsule phase change materials for improving thermal comfort level of buildings. *Construction and Building Materials* 2020, *244*, 118388.
- (408) Chen, X.; Gao, H.; Hai, G.; Jia, D.; Xing, L.; Chen, S.; Cheng, P.; Han, M.; Dong, W.; Wang, G. Carbon nanotube bundles assembled flexible hierarchical framework based phase change material composites for thermal energy harvesting and thermotherapy. *Energy Storage Materials* 2020, *26*, 129.
- (409) Bao, S.; Wei, Q.; Cao, J.; Li, H.; Ma, L.; An, J.; Lin, C.-T.; Luo, J.; Zhou, K. Hydrophilic modification of carbon nanotube to prepare a novel porous copper network-carbon nanotube/erythritol composite phase change material. *Composite Interfaces* 2020, *1*.
- (410) Wu, H.-y.; Li, S.-t.; Shao, Y.-w.; Jin, X.-z.; Qi, X.-d.; Yang, J.-h.; Zhou, Z.-w.; Wang, Y. Melamine foam/reduced graphene oxide supported form-stable phase change materials with simultaneous shape memory property and light-to-thermal energy storage capability. *Chemical Engineering Journal* 2020, *379*, 122373.
- (411) Ren, W.; Cao, L.; Zhang, D. Composite phase change material based on reduced graphene oxide/expanded graphite aerogel with improved thermal properties and shape-stability. *International Journal of Energy Research* 2020, *44* (1), 242.
- (412) Zhou, Y.; Li, C.; Wu, H.; Guo, S. Construction of hybrid graphene oxide/graphene nanoplates shell in paraffin microencapsulated phase change materials to improve thermal conductivity for thermal energy storage. *Colloids and Surfaces A: Physicochemical and Engineering Aspects* 2020, 124780.

- (413) Sheng, N.; Rao, Z.; Zhu, C.; Habazaki, H. Honeycomb carbon fibers strengthened composite phase change materials for superior thermal energy storage. *Applied Thermal Engineering* 2020, *164*, 114493.
- (414) Zhu, X.; Han, L.; Yang, F.; Jiang, J.; Jia, X. Lightweight mesoporous carbon fibers with interconnected graphitic walls for supports of form-stable phase change materials with enhanced thermal conductivity. *Solar Energy Materials and Solar Cells* 2020, *208*, 110361.
- (415) Sheng, N.; Zhu, R.; Nomura, T.; Rao, Z.; Zhu, C.; Aoki, Y.; Habazaki, H.; Akiyama, T. Anisotropically enhanced heat transfer properties of phase change material reinforced by graphene-wrapped carbon fibers. *Solar Energy Materials and Solar Cells* 2020, *206*, 110280.
- (416) Zou, Z.; Wu, W.; Wang, Y.; Drummer, D. Biomass derived carbon aerogel as an ultrastable skeleton of form-stable phase change materials for efficient thermal energy storage. *Materials Research Express* 2020, *7* (4), 045601.
- (417) Wang, C.; Liang, W.; Yang, Y.; Liu, F.; Sun, H.; Zhu, Z.; Li, A. Biomass carbon aerogels based shape-stable phase change composites with high light-to-thermal efficiency for energy storage. *Renewable Energy* 2020, *153*, 182.
- (418) Lin, P.; Xie, J.; He, Y.; Lu, X.; Li, W.; Fang, J.; Yan, S.; Zhang, L.; Sheng, X.; Chen, Y. MXene aerogel-based phase change materials toward solar energy conversion. *Solar Energy Materials and Solar Cells* 2020, *206*, 110229.
- (419) Zhang, X.; Wen, R.; Huang, Z.; Tang, C.; Huang, Y.; Liu, Y.; Fang, M.; Wu, X.; Min, X.; Xu, Y. Enhancement of thermal conductivity by the introduction of carbon nanotubes as a filler in paraffin/expanded perlite form-stable phase-change materials. *Energy and Buildings* 2017, *149*, 463.
- (420) Mu, S.; Guo, J.; Zhang, S.; An, Q.; Wang, D.; Liu, Y.; Guan, F. Preparation and thermal properties of cross-linked poly (acrylonitrile-co-itaconate)/polyethylene glycol as novel form-stable phase change material for thermal energy storage. *Materials Letters* 2016, *171*, 23.
- (421) Weinstock, L.; Sanguramath, R. A.; Silverstein, M. S. Encapsulating an organic phase change material within emulsion-templated poly (urethane urea) s. *Polymer Chemistry* 2019, *10* (12), 1498.
- (422) Cárdenas-Ramírez, C.; Jaramillo, F.; Gómez, M. Systematic review of encapsulation and shape-stabilization of phase change materials. *Journal of Energy Storage* 2020, *30*, 101495.
- (423) Lv, P.; Liu, C.; Rao, Z. Review on clay mineral-based form-stable phase change materials: preparation, characterization and applications. *Renewable and Sustainable Energy Reviews* 2017, *68*, 707.
- (424) Aftab, W.; Khurram, M.; Jinming, S.; Tabassum, H.; Liang, Z.; Usman, A.; Guo, W.; Huang, X.; Wu, W.; Yao, R. Highly efficient solar-thermal storage coating based on phosphorene encapsulated phase change materials. *Energy Storage Materials* 2020, *32*, 199.

- (425) Fang, Y.; Kang, H.; Wang, W.; Liu, H.; Gao, X. Study on polyethylene glycol/epoxy resin composite as a form-stable phase change material. *Energy Conversion and Management* 2010, 51 (12), 2757.
- (426) Madduru, S. R. C.; Shaik, K. S.; Velivila, R.; Karri, V. K. Hydrophilic and hydrophobic chemicals as self curing agents in self compacting concrete. *Journal of Building Engineering* 2020, 28, 101008.
- (427) Zhang, R.; Su, Y.; Zhao, X.; Li, Y.; Zhao, J.; Jiang, Z. A novel positively charged composite nanofiltration membrane prepared by bio-inspired adhesion of polydopamine and surface grafting of poly (ethylene imine). *Journal of membrane science* 2014, 470, 9.
- (428) Chen, Y.; Ding, H.; Wang, B.; Shi, Q.; Gao, J.; Cui, Z.; Wan, Y. Dopamine functionalization for improving crystallization behaviour of polyethylene glycol in shape-stable phase change material with silica fume as the matrix. *Journal of Cleaner Production* 2019, 208, 951.
- (429) Zarras, P.; Soucek, M. D.; Tiwari, A. *Handbook of Waterborne Coatings*; Elsevier, 2020.
- (430) Guo, Y.-h.; Li, S.-c.; Wang, G.-s.; Ma, W.; Huang, Z. Waterborne polyurethane/poly (n-butyl acrylate-styrene) hybrid emulsions: Particle formation, film properties, and application. *Progress in Organic Coatings* 2012, 74 (1), 248.
- (431) Zhang, L.; Zhu, J.; Zhou, W.; Wang, J.; Wang, Y. Characterization of polymethyl methacrylate/polyethylene glycol/aluminum nitride composite as form-stable phase change material prepared by in situ polymerization method. *Thermochimica acta* 2011, 524 (1-2), 128.
- (432) Mu, M.; Basheer, P.; Sha, W.; Bai, Y.; McNally, T. Shape stabilised phase change materials based on a high melt viscosity HDPE and paraffin waxes. *Applied Energy* 2016, 162, 68.
- (433) Wang, C.; Ma, C.; Mu, C.; Lin, W. Tailor-made zwitterionic polyurethane coatings: microstructure, mechanical property and their antimicrobial performance. *Rsc Advances* 2017, 7 (44), 27522.
- (434) Luo, H.; Gu, C.; Zheng, W.; Dai, F.; Wang, X.; Zheng, Z. Facile synthesis of novel size-controlled antibacterial hybrid spheres using silver nanoparticles loaded with poly-dopamine spheres. *RSC Advances* 2015, 5 (18), 13470.
- (435) Bhattacharyya, R.; Ray, S. K. Removal of congo red and methyl violet from water using nano clay filled composite hydrogels of poly acrylic acid and polyethylene glycol. *Chemical Engineering Journal* 2015, 260, 269.
- (436) Jayaramudu, T.; Raghavendra, G. M.; Varaprasad, K.; Reddy, G. V. S.; Reddy, A. B.; Sudhakar, K.; Sadiku, E. R. Preparation and characterization of poly (ethylene glycol) stabilized nano silver particles by a mechanochemical assisted ball mill process. *Journal of Applied Polymer Science* 2016, 133 (7).

- (437) Sundararajan, S.; Samui, A. B.; Kulkarni, P. S. Shape-stabilized poly (ethylene glycol)(PEG)-cellulose acetate blend preparation with superior PEG loading via microwave-assisted blending. *Solar Energy* 2017, *144*, 32.
- (438) Tawab, K. A.; Magida, M.; Ibrahim, S. M. Effect of ionizing radiation on the morphological, thermal and mechanical properties of polyvinyl alcohol/polyethylene glycol blends. *Journal of Polymers and the Environment* 2011, *19* (2), 440.
- (439) Falqi, F. H.; Bin-Dahman, O. A.; Hussain, M.; Al-Harthi, M. A. Preparation of miscible PVA/PEG blends and effect of graphene concentration on thermal, crystallization, morphological, and mechanical properties of PVA/PEG (10 wt%) blend. *International Journal of Polymer Science* 2018, *2018*.
- (440) Wang, X.; Zhao, L.; Fuh, J. Y. H.; Lee, H. P. Effect of porosity on mechanical properties of 3D printed polymers: Experiments and micromechanical modeling based on X-ray computed tomography analysis. *Polymers* 2019, *11* (7), 1154.
- (441) Bellotti, N.; Deyá, C. In *Handbook of Waterborne Coatings*; Elsevier, 2020.
- (442) Li, R.; Shan, Z. Enhancement of thermal conductivity of PEG-PPG-based waterborne polyurethane coating by incorporating ordered polyethylene glycol fragment. *Polymer Testing* 2018, *69*, 125.
- (443) Qian, T.; Li, J.; Ma, H.; Yang, J. Adjustable thermal property of polyethylene glycol/diatomite shape-stabilized composite phase change material. *Polymer Composites* 2016, *37* (3), 854.
- (444) Sun, K.; Kou, Y.; Zheng, H.; Liu, X.; Tan, Z.; Shi, Q. Using silicagel industrial wastes to synthesize polyethylene glycol/silica-hydroxyl form-stable phase change materials for thermal energy storage applications. *Solar Energy Materials and Solar Cells* 2018, *178*, 139.
- (445) Yang, L.; Yang, J.; Tang, L.-S.; Feng, C.-P.; Bai, L.; Bao, R.-Y.; Liu, Z.-Y.; Yang, M.-B.; Yang, W. Hierarchically porous PVA aerogel for leakage-proof phase change materials with superior energy storage capacity. *Energy & Fuels* 2020, *34* (2), 2471.
- (446) Shi, J.; Li, M. Synthesis and characterization of polyethylene glycol/modified attapulgite form-stable composite phase change material for thermal energy storage. *Solar Energy* 2020, *205*, 62.
- (447) Min, P.; Liu, J.; Li, X.; An, F.; Liu, P.; Shen, Y.; Koratkar, N.; Yu, Z. Z. Thermally Conductive Phase Change Composites Featuring Anisotropic Graphene Aerogels for Real-Time and Fast-Charging Solar-Thermal Energy Conversion. *Advanced Functional Materials* 2018, *28* (51), 1805365.
- (448) Qi, G.; Yang, J.; Bao, R.; Xia, D.; Cao, M.; Yang, W.; Yang, M.; Wei, D. Hierarchical graphene foam-based phase change materials with enhanced thermal conductivity and shape stability for efficient solar-to-thermal energy conversion and storage. *Nano Research* 2017, *10* (3), 802.
- (449) Zhang, L.; Zhou, K.; Wei, Q.; Ma, L.; Ye, W.; Li, H.; Zhou, B.; Yu, Z.; Lin, C.-T.; Luo, J. Thermal conductivity enhancement of phase change materials with 3D porous diamond foam for thermal energy storage. *Applied Energy* 2019, *233*, 208.

- (450) Xu, Y.; Li, M.-J.; Zheng, Z.-J.; Xue, X.-D. Melting performance enhancement of phase change material by a limited amount of metal foam: Configurational optimization and economic assessment. *Applied energy* 2018, *212*, 868.
- (451) Zhou, Y.; Wang, X.; Liu, X.; Sheng, D.; Ji, F.; Dong, L.; Xu, S.; Wu, H.; Yang, Y. Polyurethane-based solid-solid phase change materials with halloysite nanotubes-hybrid graphene aerogels for efficient light-and electro-thermal conversion and storage. *Carbon* 2019, *142*, 558.
- (452) Zhou, Y.; Liu, X.; Sheng, D.; Lin, C.; Ji, F.; Dong, L.; Xu, S.; Wu, H.; Yang, Y. Polyurethane-based solid-solid phase change materials with in situ reduced graphene oxide for light-thermal energy conversion and storage. *Chemical Engineering Journal* 2018, *338*, 117.

VITA of Cüneyt Erdinç TAŞ

Cüneyt Erdinç Taş was born on April 11, 1985, in İstanbul, Turkey. He graduated from Bülent Ecevit University with B.Sc. in Chemistry Department in June 2010 and graduated from İstanbul Technical University with M.Sc. in January 2013. Before he began his Ph.D. education in Material Science and Engineering Program at Sabancı University in İstanbul, he worked as a Project researcher at M-Pol Lt. Co. and as a R&D Department Specialist at Boytek Resins Co. between January 2011 and June 2015. During his Ph.D., he served as a teaching assistant in Introduction to Material Science (MAT205, two-semesters), Polymer Synthesis (MAT302, two semesters) and Polymer Synthesis and Physics (MAT511L, six semesters) courses.